UNIVERSITÀ DI PARMA

UNIVERSITÀ DEGLI STUDI DI PARMA

DOTTORATO DI RICERCA IN

"SCIENZE CHIMICHE"

CICLO XXXIII

Thiosemicarbazone metal complexes and ruthenium(II) photoactivatable compounds: two ever-expanding research fields in bioinorganic chemistry

Coordinatore:

Chiar.ma Prof.ssa Alessia Bacchi

Approved on June 7th 2021

Alessia Bacchi

Tutore:

Chiar.mo Prof. Franco Bisceglie

Dottorando: Dott. Nicolò Orsoni

Anni 2017/2020

Contents

Part one

Part two

PART ONE

Chapter one: thiosemicarbazones and their metal complexes as anticarcinogenic compounds

1 Introduction

1.1 Metals in medicine

Inorganic chemistry is commonly perceived like a “dead chemistry”, i.e., a branch of chemistry completely detached from biology, generally associated with organic chemistry [1]. In practice, inorganic elements are essential for a plethora of biological processes: in the osmotic balance (sodium and potassium), in structural roles (calcium, magnesium and zinc), in the transport of oxygen (copper and iron) and in all the enzymes involved in redox reactions (iron, copper, manganese, molybdenum, magnesium and nickel). At the same time, the metal elements can be introduced artificially in the human body, like salts or complexes, for diagnostic or therapeutic purposes. The use of metals to prevent or defeat diseases is not a recent application. In fact, is historically proven that in the ancient civilizations of Mesopotamia, Egypt, India and China metals were used in pharmaceutical potions [2-4]. Go forward in the modern age, salvarsan was one of the first therapeutic metallodrugs. Discovered in 1912 by Paul Ehrlich, is an arsenic-based antimicrobial agent (a mixture of 3-amino-4hydroxyphenyl-arsenic(III) compounds) used against syphilis [5]. With the advance of the research other metal-based drugs have been applied to treat a lot of diseases: lithium carbonate, used to stabilize the mood of people with manic-depressive disorders, bismuth subsalicylate which is an antidiarrheal agent, gold compounds (sodium aurothiomalate, auranofin and aurothioglucose) used against arthritis and vanadium compounds for the treatment of diabetes [6]. In our days, cisplatin is the most famous and used metallodrug. Cisplatin, cis-diamminodichloroplatinum(II), is one of the lead compound for the treatment of solid tumors thanks to its ability to bind DNA and therefore to inhibit the proliferation of the cancerous cells [7-8]. Primarily, cisplatin is used for the treatment of breast, ovarian and lung cancer, and especially for testicular cancer, for which it is considered an effective and definitive treatment. The wide success of this compound makes it the progenitor of a new class of platinum-based drugs (i.e. carboplatin and oxaliplatin) which are still the only drugs to fight against extremely aggressive tumors in colon and lungs. The activity of cisplatin is due by the exchange of chlorides, inside the cytoplasm, through aquation [9]. This substitution is induced by the low concentration of chlorides inside the cell compared to the blood, with the consequence that the aqueous form of cisplatin is unable to leave the cell thanks of the positive charge. Inside the cell the platinum of the $[Pt(NH_3)_2]^{2+}$ unit binds covalently the DNA, specifically in the N-7position of either guanine or adenine to form interstrand cross-links and 1,2- or 1,3-intrastrand cross-links [10]. Such cisplatin−DNA adducts lead to replication arrest, transcription inhibition, cell-cycle arrests, DNA repair, and apoptosis [11] (figure 1).

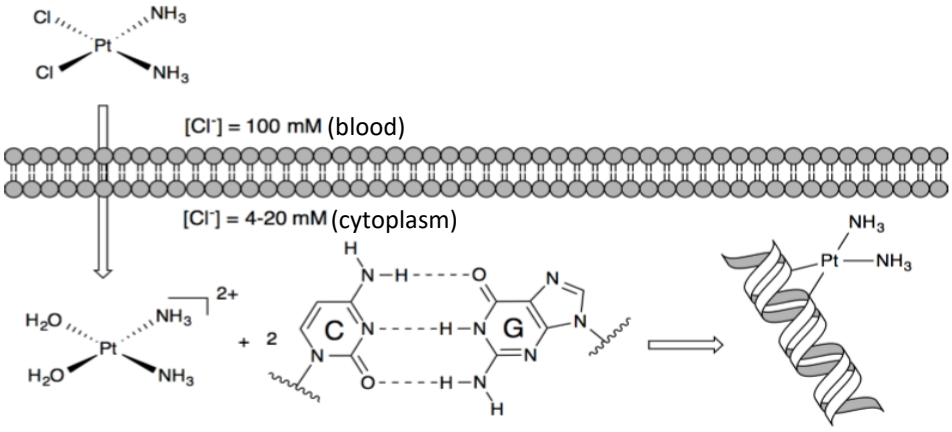

Figure 1 Scheme of action of cisplatin.

Unfortunately, cisplatin and its derivatives (carboplatin and oxaliplatin) are not devoid of unpleasant side effects due by their toxicity, specially to kidneys (nephrotoxicity) and to the nervous system (neurotoxicity). Another problem connected with cisplatin and its derivatives is the presence of intrinsic or acquired resistance phenomena when used for repetitive treatments [12]. These drawbacks have encouraged the research of new metallodrugs that combine a good activity against the tumor cells with a low toxicity and less side effects. In this prospective new cisplatin-like compounds (nedaplatin, heptaplatin, lobaplatin and satraplatin) have been obtained and currently are under clinical trials in the USA (figure 2).

The effort to obtain new non-toxic metallodrugs doesn't end with the synthesis of new cisplatin-like compounds. In fact, all the metal elements of the d-block are involved in this research. One of the most studied metal for the synthesis of new metallodrugs is ruthenium, that is the main character of a succeeding chapter of this thesis.

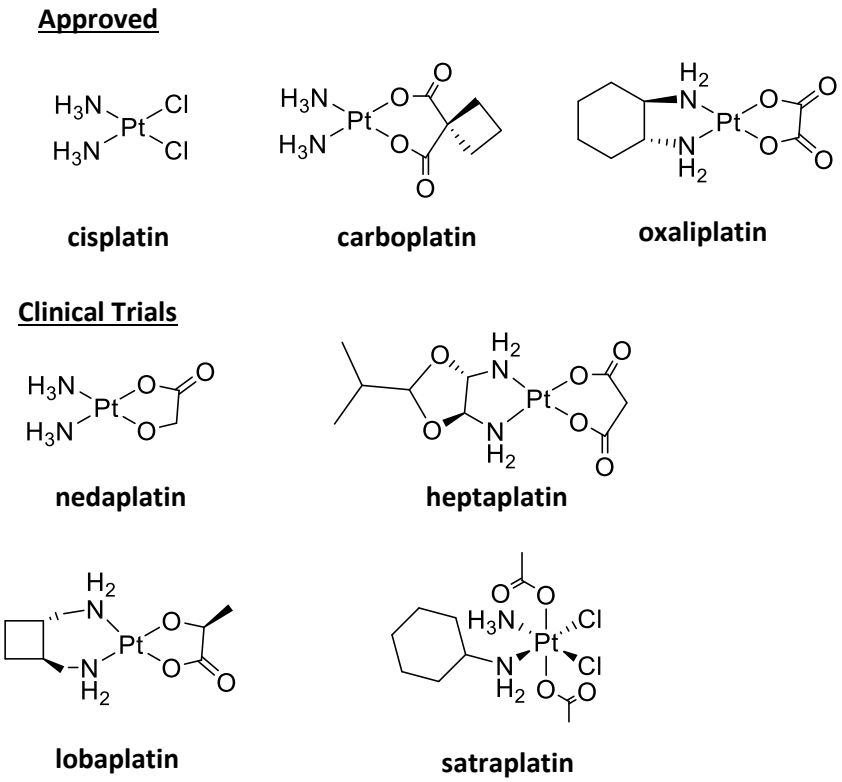

Figure 2 Structure of cisplatin and its derivatives.

In biology, the most used metal ions of the d-block belong to the first row of the periodic table. More precisely, four of these elements (iron, nickel, copper, and zinc) are involved in several biological pathways in all the life forms, from the simplest to the most complex [13]. The fact that they are micronutrients for most living beings make them less toxic than platinum compounds with the consequence to decrease the unpleasant side-effects. The speciation of these metals and the use of an adequate class of ligands is crucial to obtain a good biological activity with a low toxicity. In this context thiosemicarbazones [14], a well-known class of organic molecules, can play a useful role.

1.2 Thiosemicarbazones

Thiosemicarbazones (TSs) are a class of compounds with a peculiar structure in which a thione group coexists with a hydrazine part. The singularity of this structure leads to an extensive electronic delocalization with the presence of a thione-thiol tautomerism (figure 3). The R substituent can be both aliphatic and aromatic.

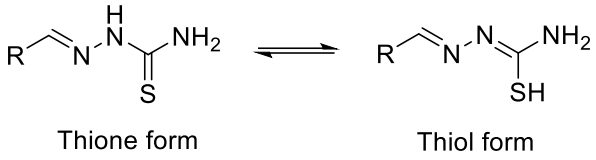

Figure 3 Thione-thiol tautomerism of the TSs.

TSs are obtained by the simple condensation between the hydrazinic part of thiosemicarbazide with the carbonyl group of an aldehyde or a ketone (figure 4) usually in solvents like methanol or ethanol. The key feature of TSs is the ease of their structure modification using different kinds of aldehydes or ketones.

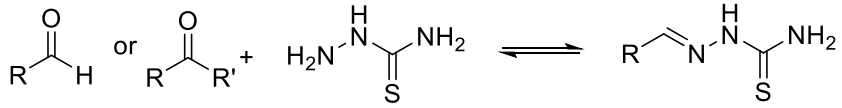

Figure 4 General synthetic way to obtain a TS.

The main feature that makes TSs an interesting class of compounds is the ability to interact through their donor atoms with metals. More precisely, TSs are able to chelate metal ions with sulfur and nitrogen atom of the imine, N^1, with the formation of a five-term coordination ring. This type of donor atoms gives a good mixing of hard-soft behavior enhancing TSs affinity to many different metals. TSs are also able to deprotonate the hydrazinic nitrogen, N^2, with the formation of a negative charge. This negative charge is not located on the N^2 during the complexation but, thanks to the extensive electronic delocalization, is placed on the sulfur atom. Figure 5 depicts the typical metal complex scheme of a bidentate TS.

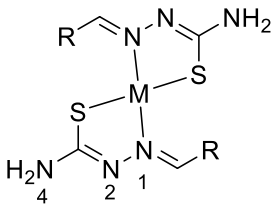

Figure 5 General structure of a metal complex with two TSs and a bivalent metal.

The ease with which TSs structure can be modified and their ability to chelate different metal ions make them very useful in different biological fields. In the next chapters of this thesis, I will show different interesting results obtained with this class of molecules.

1.2.1 Anticancer properties of thiosemicarbazones

The anticancer activity of TSs is the most studied topic and the most promising field of this class of compounds. Their antitumor activity is extremely various and depend on many factors: structure of TSs, metal used in the complexation and the typology of tumor cells. This great amount of information makes difficult to extract from the literature general informations valid for the whole class of compounds since their activity is certainly due to more than one target in the cell machinery. The only information obtainable from the literature is that with the presence of a metal ion TSs systematically increase their activity with the reduction of the side effects of the organic compounds [15]. Nowadays, the main effects related to their anticancer activity are, in order of discovery, ribonucleotide reductase (RR) inhibition [16], reactive oxygen species (ROS) production [17], topoisomerase II inhibition [18], mitochondria disruption [19], and, more recently, a direct interaction with DNA [20].

1.2.2 Ribonucleotide reductase inhibition

Ribonucleotide reductase (RR) is an iron-dependent enzyme that induces the reduction of ribose to deoxyribose through a free radical mechanism. This enzyme is composed by two large alpha and two small beta subunits associated to form a heterodimeric tetramer. In the beta subunits there are the Fe(III) atoms responsible of the formation of the tyrosyl radical. This radical migrates along the enzyme, through different residues, coming in the alpha subunits, where the substrates (ADP, GDP, CDP or UDP) are located. In the last step three residues of cysteine are involved in the reduction, one transfers the radical to the ribose and two oxidize their ligand during the reduction.

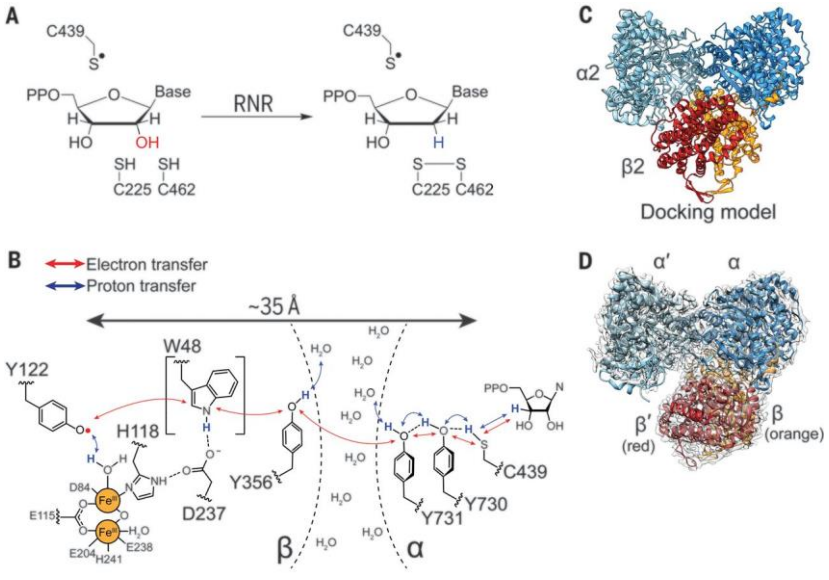

Figure 6 (A) Reaction catalyzed by RR (B) Pathway of the radical through the RR (C) and (D) Structure of the protein [21].

Deoxyribose is necessary for the synthesis of DNA and the inhibition of the RR brings to a block in the synthesis phase of the cell cycle and eventually to cell death by apoptosis. TSs, acting like a radical scavenger

[22, 23] on the tyrosyl free radical, block the synthesis of deoxyribose. Iron and copper complexes of TSs are more active respect to the free ligands [24].

1.2.3 ROS generators

The regulation of redox equilibrium is essential for the life of the cell. Cancer cells have a higher level of ROS compared to healthy cells. This misregulation of the ROS level in cancer cells is due by the Warburg effect (aerobic glycolysis) and to the loss of proper antioxidant control systems [25]. The high level of ROS and a reduced ability of control of the oxidative stress make the cancer cells more responsive to drugs that induce oxidative stress. Some TSs are able to produce ROS and deregulate the antioxidative potential of a cell [26]. The production of ROS can be increased using redox metals (iron, copper, or nickel) to obtain metal complexes of TSs [27].

1.2.4 Topoisomerase inhibition

Topoisomerase II is a ubiquitous eukaryotic enzyme fundamental in the DNA replication. The DNA in the cells is not unwind but is compacted in the cell nucleus in supercoiled structures, in which the DNA strands are over- or under-winding. Herein, topoisomerase II decatenates and disentangles DNA coils allowing the replication [28]. Topoisomerase II is essential for DNA synthesis and proliferating cells, like tumor cells, overexpress this enzyme, making this protein a good target.

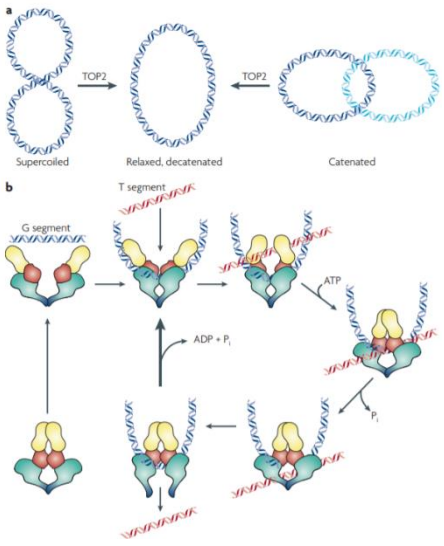

Figure 7 Mechanism of action of topoisomerase II [28].

TSs and their metal complexes are known in literature [29] to be inhibitors of topoisomerase II. Specifically, the metal complexes of the 1,2-naphthoquinone-2-thiosemicarbazone can stabilize the cleavable products formed by topoisomerase-II and DNA. The stabilization of topoisomerase II– DNA complexes is a prerogative of the metal complexes that TSs themselves don't have.

1.2.5 Mitochondria disruption

The ability to target and damage mitochondria is related to the ability to produce ROS. Mitochondria are the center of the cellular respiration and the chance to generate ROS inside this organelle is greater than in other parts of the cell. TSs that act against mitochondria are usually characterized by a great lipophilicity, obtained with a correct functionalization in the carbazone moiety [30]. A damaged mitochondrion can induce apoptosis in two ways. The first is related with the block of the cellular respiration, that for the cancer cells is not a great injury because they can obtain the ATP in hypoxia conditions, with the Warburg effect. The second is related with the release of cytochrome c. The presence of cytochrome c in the cytoplasm promotes the formation of the apoptosomes inducing apoptosis [31].

1.2.6 Direct interaction with the DNA

In the first part of this chapter, I explained how cisplatin attacks DNA and exerts its biological activity. For this complex, a lot of biological studies are performed to confirm the specific way of action in the cells. Instead, for the newest metal complexes, the activity against the DNA structure and the DNA metabolism can arise from direct or indirect actions. The direct action against DNA is the direct interaction of the metal complexes with nucleobases, causing a distortion of the DNA morphology, like cisplatin does. Another type of direct interaction is the intercalation of the complexes in the DNA grooves, typical of the aromatic species. The indirect actions are injuries that don't involve the DNA itself but are related to other biological molecules necessary for the DNA metabolism. An example is the topoisomerase II inhibition previously described. Another example is the targeting of the histones, the chief protein component of the chromatin [32-36]. The chromatin is a complex of DNA and proteins whose primary function is condensing long DNA molecules into a more compact structure (figure 8).

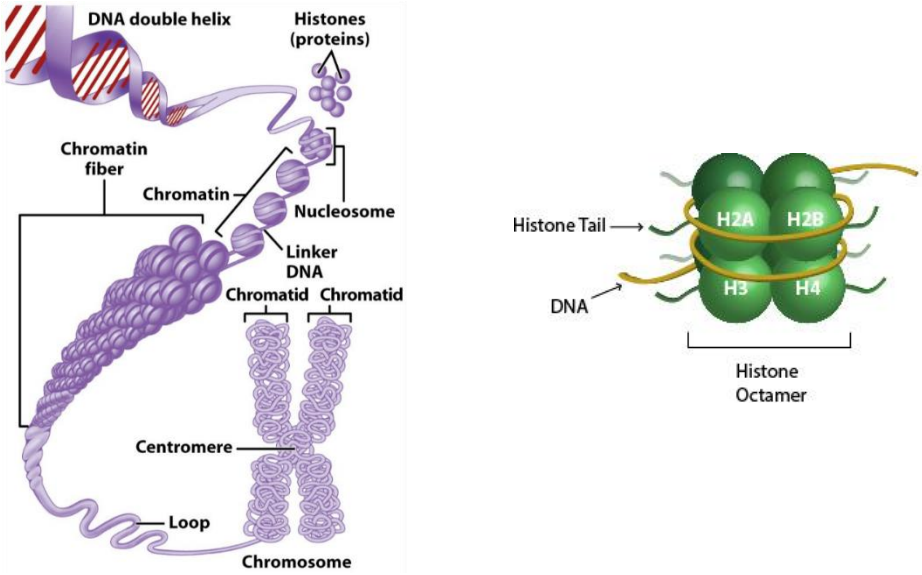

Figure 8 Structure of chromatin and the role of the histones in the DNA packing.

In the laboratories where I carried out my PhD, have been previously synthesized new metal complexes with long chain aliphatic thiosemicarbazone ligands [37-44]. In particular, the nickel and copper derivatives of S-citronellal-thiosemicarbazone (Htcitr) show a high activity on histiocytic lymphoma cell line U937. The preliminary information [42-44] about these complexes make them appealing for a further investigation on their biological mechanism of action. In the next chapter I will describe the synthesis and characterization of Pt(II) of S-citronellal-thiosemicarbazone [Pt(tcitr)$_2$] (figure 9 b) together with a deep study to investigate if the biological activity found versus the nucleic acid can be ascribed to a direct or an indirect interaction. We compared the biological action of the Ni(II) [Ni(tcitr)$_2$] (figure 9 a) and Cu(II) [Cu(tcitr)$_2$] (figure 9 c) analogue compounds with the activity exerted by the Pt(II) complex. We investigated the direct interaction towards DNA by means of AFM and spectroscopic techniques (CD, UV-Vis), and the indirect interaction studying the perturbation of a peptide modeling the potential metal binding site in the "C-Tail" Region of Histone H2A by means of NMR, CD and UV-Vis.

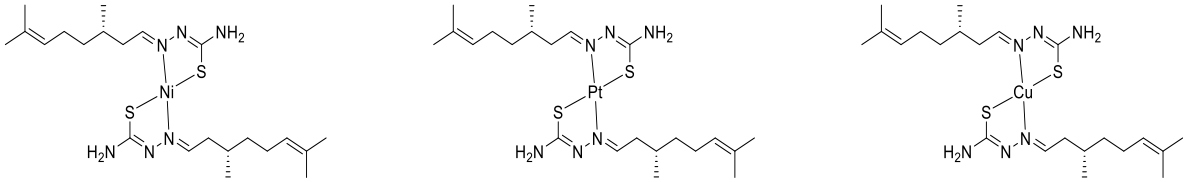

a) b) c)

Figure 9 Structure of the complexes: a) [Ni(tcitr)$_2$], b) [Pt(tcitr)$_2$] and c) [Cu(tcitr)$_2$]

2 DNA as a direct and indirect target: the Htcitr's metal complexes case

2.1 DNA as a direct target: interaction among metal complexes and CT-DNA

To evaluate the ability and the mechanism with which the three metal complexes interact with DNA, we performed several experiments. First of all, we have compared the thermal denaturation profiles and the melting temperature of CT-DNA in the presence and in the absence of the metal complexes (figure 10). The biological activity of these compounds, against DNA, is performed by dissolving the target complex in DMSO, forming a stock solution, subsequently diluted in an aqueous solution of PBS (phosphate-buffered saline). The total amount of DMSO is maintained lower than 2%. The cycles heating-cooling are repeated three times. The presence of the compounds modifies the thermal denaturation profiles of CT-DNA reducing its absorbance. This behavior is associated to a further DNA compaction induced by the metal complexes.

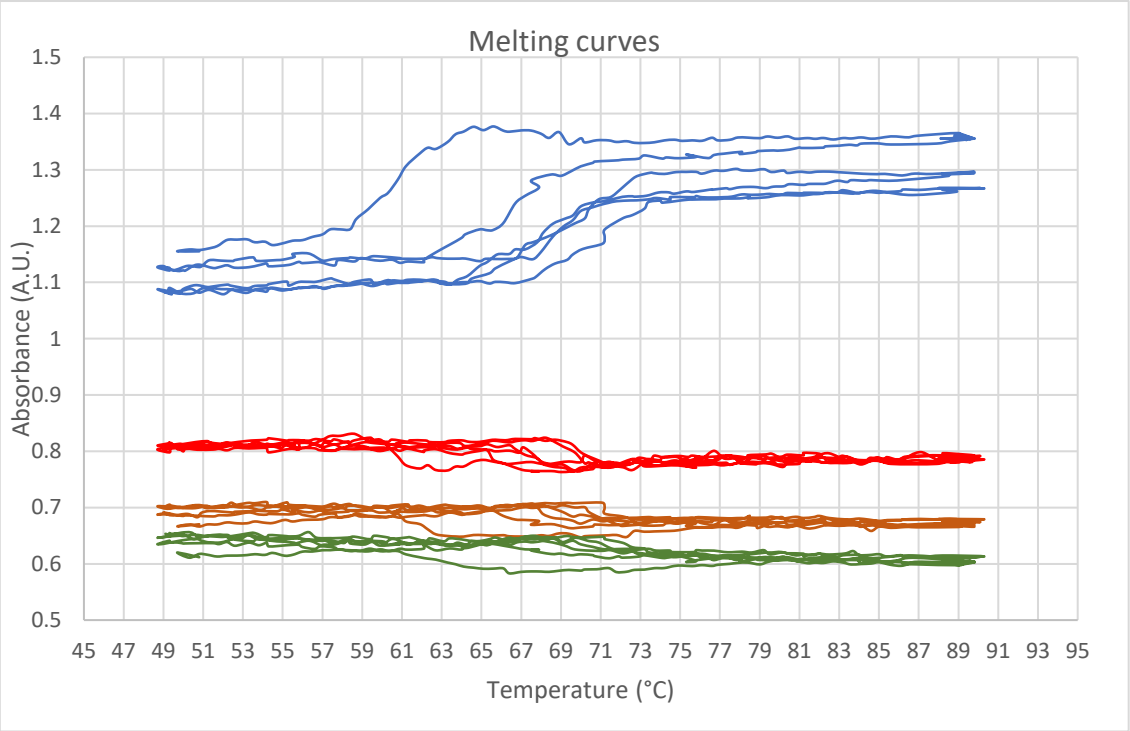

Figure 10 Thermal denaturation profiles of CT-DNA before (above) and after (below) addition of metal complexes; [CT-DNA] = 45 µM; ratio [metal complex]/[CT-DNA] = 0.25. [Pt(tcitr)$_2$] (red line), [Ni(tcitr)$_2$] (orange line), [Cu(tcitr)$_2$] (green line).

To better understand the conformational change induced by the metal complexes on DNA double helix, CD spectra of the DNA with these compounds were recorded (figure 11).

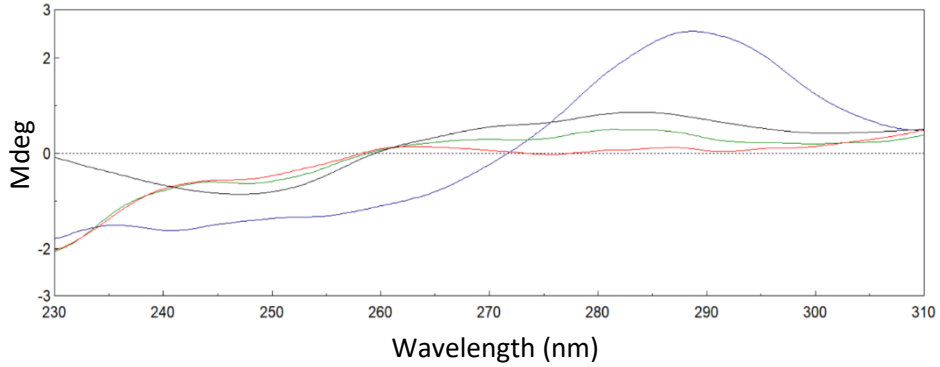

Figure 11 CD spectra of DNA (black line), DNA + [Pt(tcitr)$_2$] (red line), DNA + [Ni(tcitr)$_2$] (blueline), DNA + [Cu(tcitr)$_2$] (green line).

The observed CD spectrum of natural calf thymus DNA consists of a positive band at 280 nm due to base stacking and a negative band at 250 nm due to helicity, features characteristic of DNA in right-handed B form, with the intersection point at the absorption maximum (UV: λ max, 260 nm) [45]. The effect of the complexes on the conformation of the secondary structure of DNA was studied using the same concentration of CT-DNA (45 µM) and the same r ([complex]/[DNA] = 0.25) used in the previous experiment. Observing Figure 10 it is possible to notice that [Cu(tcitr)$_2$] and [Pt(tcitr)$_2$] induce a decrease of both band intensities, compatible with a B → C transition. For what [Ni(tcitr)$_2$] is concerned, the CD spectrum of DNA has great differences respect to the other three spectra. The intersection point is shifted to 270 nm while both bands' intensities are

increased. It is clear that [Ni(tcitr)$_2$] exerts a strong effect on the nucleic acid, but it's not possible to define a specific transition.

Another step ahead to better understand the action mechanism of these metal complexes, in particular their interactions with DNA, has been taken with the advantage of the Atomic Force Microscopy (AFM) technique, in collaboration with the group of professor Rivetti at Unipr. Initially, DNA was monitored in the absence of the compounds. Under these conditions, the double helix presents a homogeneous thickness of about 1nm all along the fragment and no structural complexities. Besides a topographical analysis, we also measured the average length of the single fragments and it resulted to be 308.8 ± 11.9 nm (figure 12).

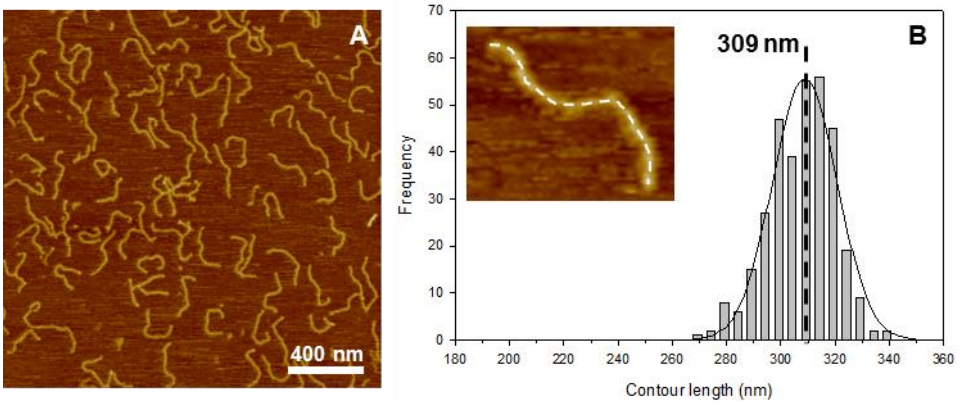

Figure 12 A) AFM image of 965 bp long DNA fragments deposited on mica. B) Length distribution of the DNA molecules used in the experiment.

The addition of the compounds in a concentration range of the order of the µM induces in the double helix the formation of knot-like structures and hairpins. This structural alteration of DNA was observed in all experiments, independently from the compound (figure 13 and 14). Nevertheless, the number of such structures found in each experiment is proportional to the concentration of the compound incubated with DNA, in particular for [Pt(tcitr)$_2$] and [Cu(tcitr)$_2$] (Table 1). These structures are preferentially formed near the ends of the DNA fragments and present a thickness of about 2 – 3 nm. The morphology of knots and hairpins observed on the double helix and the shortening of the DNA fragments up to about 50 nm (Table 1) suggests a local overlapping or condensation of the double strand assignable to the interaction with the metal compounds. A shortening can also be observed in those DNA fragments that do not present knots or hairpins, in which we noticed a decrease in fragment length of about 10-15 nm with respect to non-treated DNA (table 1). Such phenomenon has been observed particularly in DNA molecules incubated with the platinum and nickel derivatives, while for the copper complex no appreciable shortening or only very small ones (1-4 nm) have been recorded (table 1).

Based on the length reduction observed in DNA molecules, it is possible to hypothesize compound-DNA interactions different from a classical intercalation mechanism which would produce the opposite effect. The shortening observed in DNA molecules without knots or hairpins suggests that these compounds can induce DNA structural modifications that lead to a more compact helical structure. Interesting to note is that the shortening of about 10 nm that we observe is compatible with a B → C transition of DNA.

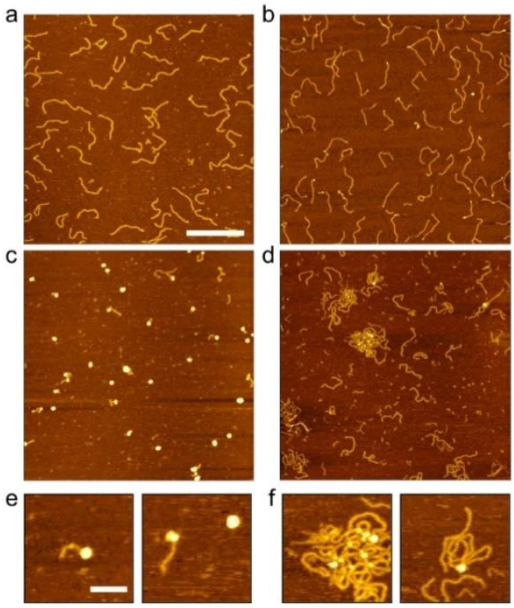

Figure 13 Comparison of the DNA in presence and in absence of 1 mM metal compounds. (a) DNA fragments deposited into mica alone. (b) DNA fragments in the presence of 1 mM [Cu(tcitr)$_2$]. (c) DNA fragments in the presence of 1 mM [Pt(tcitr)$_2$]. (d) DNA fragments in the presence of 1 mM [Ni(tcitr)$_2$]. (e) Closed-up views of [Pt(tcitr)$_2$] induced DNA condensation. (f) Closed-up views of [Ni(tcitr)$_2$] induced DNA aggregation. (a-d) Scale bar 500 nm. (e-f) Scale bar 100 nm.

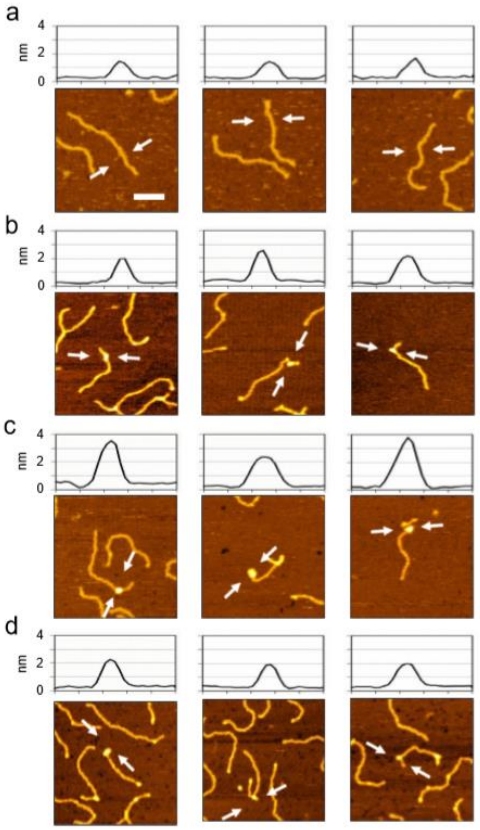

Figure 14 Closed-up views DNA deposited into mica and imaged by AFM in the absence and in the presence of the metal compounds. The image profile taken along the direction indicated by white arrows is shown on top of each panel and spans a distance of 100 nm. (a) DNA fragments in the absence of compounds. (b) DNA fragments in the presence of 100 µM [Cu(tcitr)$_2$]. (c) DNA fragments in the presence of 100 µM [Pt(tcitr)$_2$]. (d) DNA fragments in the presence of 100 µM [Ni(tcitr)$_2$]. Knot-like structures and hairpins are shown as white globular features along the DNA double helix. Scale bar 100 nm.

Experiment	Length of the DNA molecules without knots (nm)	Length of the DNA molecules with knots (nm)	DNA molecules with knots (%)
DNA	309 ± 12 (334)	-	-
DNA + 1 mM $PtCl_2$	313 ± 10 (163)	-	-
DNA + 100 µM $Ni(CH_3COO)_2$	314 ± 11 (207)	-	-
DNA + 1 mM $Cu(CH_3COO)_2$	311 ± 9 (94)	-	-
DNA + 1 µM $[Pt(tcitr)_2]$	300 ± 13 (256)	270 ± 18 (99)	27.8
DNA + 10 µM $[Pt(tcitr)_2]$	302 ± 13 (259)	274 ± 27 (89)	25.5
DNA + 100µM $[Pt(tcitr)_2]$	293 ± 16 (220)	258 ± 21 (139)	38.7
DNA + 1 µM $[Cu(tcitr)_2]$	307 ± 12 (247)	277 ± 20 (48)	16.2
DNA + 10 µM $[Cu(tcitr)_2]$	307 ± 11 (223)	278 ± 29 (67)	23.1
DNA + 100 µM $[Cu(tcitr)_2]$	307 ± 11 (199)	278 ± 17 (100)	33.2
DNA + 1 µM $[Ni(tcitr)_2]$	311 ± 22 (283)	292 ± 17 (61)	17.7
DNA + 10 µM $[Ni(tcitr)_2]$	310 ± 17 (255)	285 ± 21 (84)	24.8
DNA + 100 µM $[Ni(tcitr)_2]$	311 ± 17 (238)	281 ± 17 (102)	30.0
DNA + [Htcitr] 100 µM	319 ± 12 (170)	-	-

Table 1 Average DNA length, average DNA length after treatment with $PtCl_2$, $Ni(CH_3COO)_2$, $Cu(CH_3COO)_2$ and length after treatment with increasing concentrations of the compounds. The values reported correspond to the average ± standard deviation. In parenthesis is the number of DNA molecules analysed. In the right-hand side column are reported the the percentage of molecules with knots/hairpins with respect to the total number of molecules appearing in the AFM images for each experiment.

In conclusion, for the study of the interaction among DNA and the metal complexes we can assume that no intercalative behaviors are observed. A shortening of DNA is postulated by the exam of UV and CD spectra, inducing to think to a DNA conformational change from B to C. If for the Cu complex a unique way of action can be imagined, it is not the same for Ni and Pt ones. For the Ni derivative it is supposed also that a DNA condensation can occur. Finally, topological effects are more evident for $[Ni(tcitr)_2]$ and $[Pt(tcitr)_2]$ than for $[Cu(tcitr)_2]$.

2.2 DNA as an indirect target: interaction among metal complexes and Histone

In this second part of the chapter, I examine the ability of the metal complexes [Ni(tcitr)$_2$], [Pt(tcitr)$_2$] and [Cu(tcitr)$_2$] to interact with an hexapeptide, AmTESHHKac (threonine, aspartate, serine, histidine, histidine, lysine). This peptide is a model that represents the C-tail region of the Histone H2A, the part of the protein exposed to the solvent [34]. Several techniques are used to understand the ability of these complexes to interact with the peptide, like ^{1}H-NMR, UV-visible and circular dichroism (CD). For [Ni(tcitr)$_2$] and [Pt(tcitr)$_2$] I measured a series of mono- and bi-dimensional ^{1}H-NMR spectra recorded in DMSO-D_6 at 7 mM concentration with a preliminary incubation of 24h in solution at 37.5°C.

^{1}H-NMR, ^{1}H-^{1}H COSY and ^{1}H-^{1}H TOCSY experiments have been used for the total characterization of the peptide and subsequently the same experiments were performed in the presence of the complex (complex: peptide ratio = 1:1). In table 2 are presented the chemical shifts of free and bound hexapeptide. This type of experiments has not been performed for [Cu(tcitr)$_2$] because its paramagnetic nature. Methanolic solutions with a concentration of 50 µM were used for the determination of UV-visible and CD spectra. For these experiments, methanol is more useful than DMSO because of its lower cutoff. Also, in this case the peptide and the complexes were incubated for 24h at 37.5°C.

Fragment	**Free**	**in the presence of [Ni(tcitr)$_2$]**	**in the presence of [Pt(tcitr)$_2$]**	**Fragment**	**Free**	**in the presence of [Ni(tcitr)$_2$]**	**in the presence of [Pt(tcitr)$_2$]**
Thr α	4.14	4.18	4.12	**His^3 α**	4.55	4.41	4.56
β	3.98	3.99	3.95	ß	3.01	3.44	2.95
γ	1.07	1.07	1.06	NH_{back}	8.10	/	8.14
$NH_{back.}$	7.93	/	7.93	C_2	7.58	/	7.58
OH	4.99	?	?	C_5	7.29	/	7.34
Glu α	4.30	4.37	4.26	**His^4 α**	4.51	4.32	4.53
β	1.73	1.73	1.72	ß	3.09	3.52	2.91
γ	2.26	2.26	2.22	$NH_{back.}$	8.24	/	8.27
$NH_{back.}$	7.97	/	7.99	C_2	7.33	/	7.38
COOH	14.07	/	14.12	C_5	7.23	/	?
Ser α	4.18	4.11	4.18	**Lys α**	4.23	4.26	4.21
ß	3.55	3.53	?	ß	1.68	1.64	1.68
$NH_{back.}$	7.86	/	7.87	γ	1.31	1.38	1.31
OH	5.16	?	?	δ	1.56	1.57	1.50
				ε	2.75	2.80	2.75
				$NH_{back.}$	8.16	/	8.17
				NH_2	7.68	7.68	7.72

Table 2 Chemical shifts of the free peptide and in the presence of [Ni(tcitr)$_2$] and [Pt(tcitr)$_2$].

2.2.1 NMR studies: [Ni(tcitr)2] and AmTESHHKac

The nickel complex [Ni(tcitr)$_2$] induces a substantial alteration of the peptide spectrum (figure 15). This alteration is evident in the low-fields region, particularly in the zone between 7.0 and 8.5 ppm. Herein, there are the signals of the amide groups of the peptide backbone with the amine group of the lysine and the imidazole groups of the histidines. The nickel complex induces the total disappearance of these signals, except for the lysine side chain (figure 15 b, green point). Surprisingly, together with the nickel complex and the peptide signals, it is present a third set of signals associable with the free ligand, Htcitr (figure 15 b, red points).

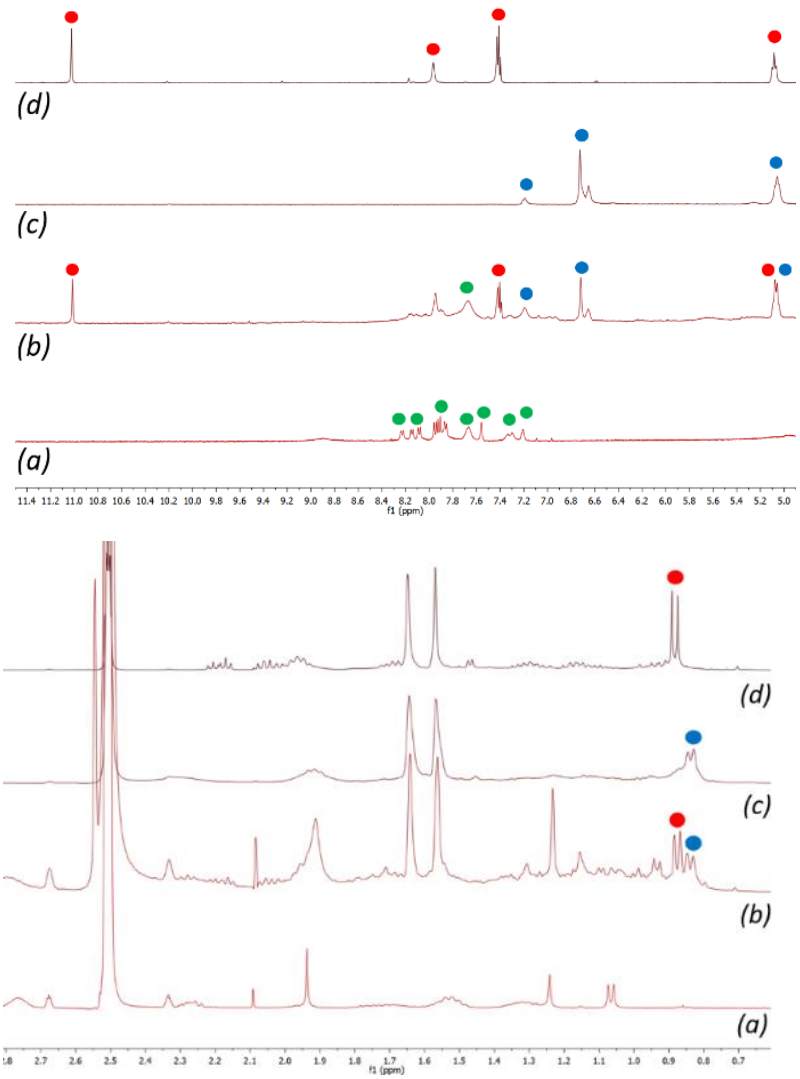

Figure 15 Proton spectra in DMSO-D$_6$ of (a) histone tail, (b) histone tail + [Ni(tcitr)$_2$], (c) [Ni(tcitr)$_2$] and (d) Htcitr. Above low fields, below high fields. ^{1}H-NMR experiments are performed in DMSO-D$_6$ with a concentration of 7 mM.

These spectra suggest that [Ni(tcitr)$_2$] interacts with the peptide dissociating a ligand and interacting with the metal center on the peptide. This interaction involves the amide groups of the backbone and the imidazole rings of the histidines, with a different coordination geometry. In the first case, the probable structure is a

diamagnetic complex with a square planar geometry (scheme 1). This geometry is suggested by the small variations of chemical shift of the α protons, that are very close to the amide groups.

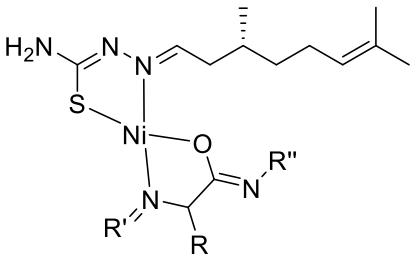

Scheme 1 Proposed adduct between [Ni(tcitr)$_2$] and TESHHK, in which the metal center interacts with the amide groups of the backbone.

In the second case, the complexation through the imidazole rings of the histidines induce a change of geometry of the metal center to an octahedral environment, with the formation of a paramagnetic adduct. This could explain the fact that C_2 and C_5 signals of imidazole rings disappear with the addition of [Ni(tcitr)$_2$] (scheme 2).

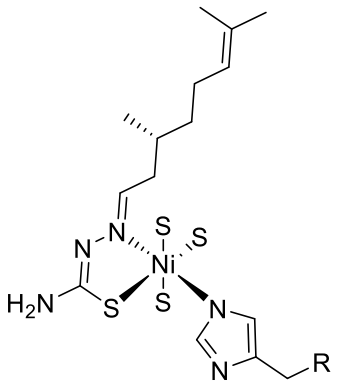

Scheme 2 Proposed adduct between [Ni(tcitr)$_2$] and TESHHK, in which the metal center interacts with the imidazole rings. "S" stands for "solvent".

2.2.2 NMR studies: [Pt(tcitr)$_2$] and AmTESHHKac

The complex [Pt(tcitr)$_2$] induces an alteration of the peptide spectrum (figure 16) that differs from the one observed for the nickel complex. The differences are mainly three: the presence of the amide groups of the backbone and the side chains of the histidines and the lysine, the absence of signals related to the ligand, Htcitr, and the presence of new signals not associable with the single species.

To understand if this interaction is due by the citronellal moiety or by the platinum complex, I observed how the NMR spectrum of the hexapeptide in presence of 2 equivalents of the ligand, Htcitr, changed. The results are reported in figure 17. Herein, we can observe that the presence of the ligand doesn't change the peptide NMR spectrum.

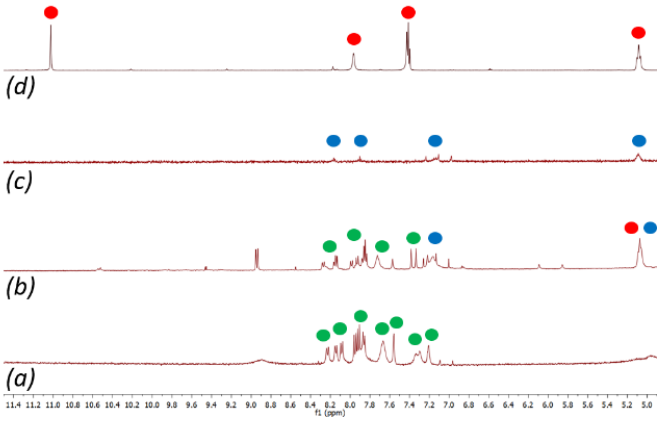

Figure 16 Proton spectra in DMSO-D_6 at low field of (a) peptide, (b) peptide + [Pt(tcitr)$_2$], (c) [Pt(tcitr)$_2$] and (d) Htcitr. ^{1}H-NMR experiments are performed in DMSO-D_6 with a concentration of 7 mM.

The NMR experiments suggest that the platinum complex interacts with the peptide without the dissociation of a ligand and without the involvement of the metal center. At the same time, this interaction is not due by the role exerted by the ligand. [Pt(tcitr)$_2$] interacts with the hexapeptide like a single and not dissociated entity. The inability of the platinum complex to dissociate the Htcitr, respect to the nickel complex, might be explained by the reduced kinetics in the ligand exchange, typical of the heavy metals, and for the greater affinity of platinum to the S-donor atoms of the Htcitr ligands.

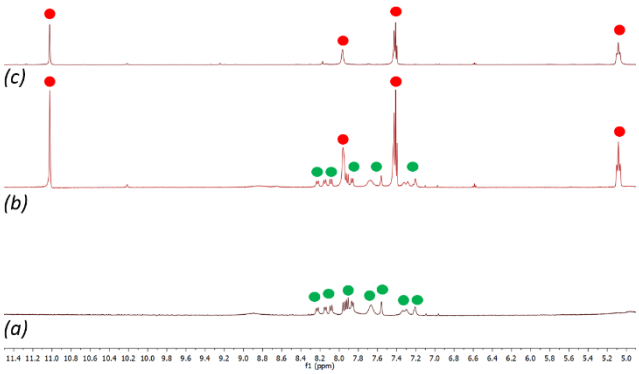

Figure 17 Proton spectra in DMSO-D_6 at low field of (a) peptide, (b) peptide + Htcitr, (c) Htcitr. ^{1}H-NMR experiments are performed in DMSO-D_6 with a concentration of 7 mM.

2.2.3 Metal complexes and AmTESHHKac interaction studies: UV-visible and CD spectra

To corroborate the results obtained with the NMR technique, and to study the interaction between the peptide and the paramagnetic complex [Cu(tcitr)$_2$], I performed other experiments using UV-visible spectroscopy and circular dichroism (CD). The setup of these experiments differs by the NMR for the solvent used and for the concentration of the sample. In this case the solvent used was methanol because its cutoff is lower than the DMSO one.

In figure 18 are presented the nickel complex and the peptide spectra. In the UV-visible spectra (figure 18 a) the interaction is confirmed because the spectrum of the species incubated is remarkable different if compared to the spectra of the single species.

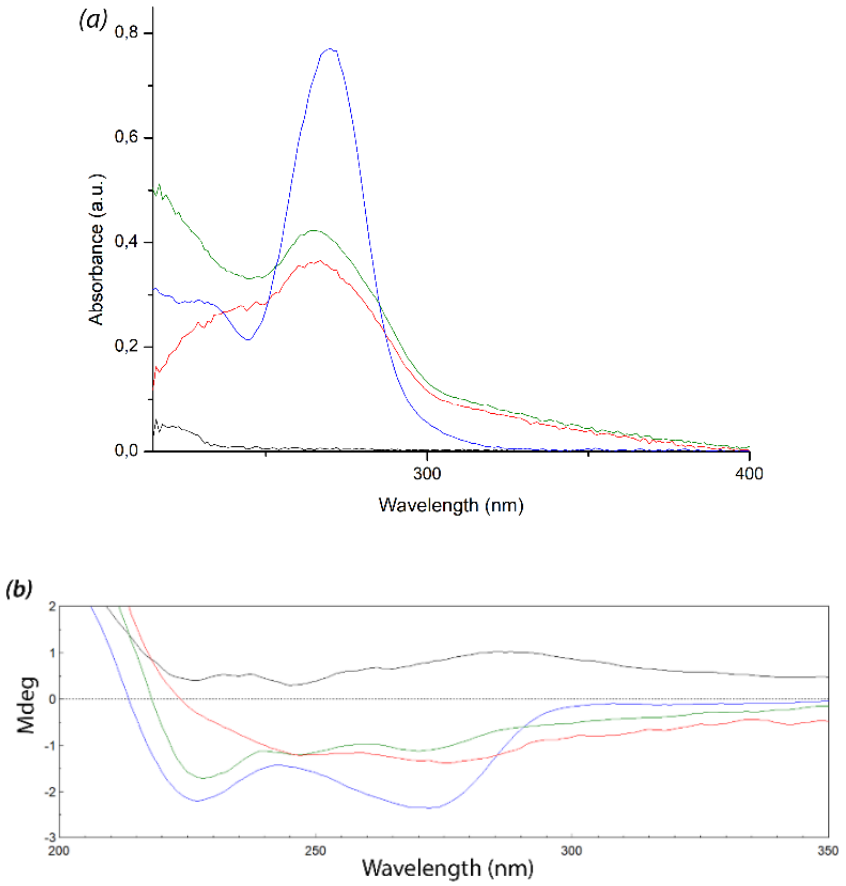

Figure 18 (a) UV-visible spectra and (b) circular dichroism (CD) spectra of peptide (black line), [Ni(tcitr)$_2$] (red line), Htcitr (blue line), peptide + [Ni(tcitr)$_2$] (green line). UV-visible and CD spectra are obtained in methanol with a concentration of 50 µM.

More information is obtained from CD spectra. The circular dichroism is a useful technique in this study because both the peptide and the citronellal contain a chiral center. As in the case of UV-visible, the CD spectra (figure 18 b) of the species incubated is remarkable different if compared to the spectra of the single species. The further information is that the spectrum of the two species interacting (figure 18 b, green line) is characterized by one band, at 217 nm, absent in the two single species, [Ni(tcitr)$_2$] and the peptide, but present in the ligand alone. This confirms the suppositions made studying the NMR spectra.

In table 3 are presented the spectroscopic parameters.

Species	UV/vis λ_{max} nm (Absorbance)	CD λ_{max} nm (mdeg)
peptide	219 (0,048)	286 (1,01)
$[Ni(tcitr)_2]$	265 (0,36)	275 (-1,39)
Htcitr	217 (0,31), 270 (0,77)	226 (-2,20) 271 (-2,36)
Histone + $[Ni(tcitr)_2]$	217 (0,51), 265 (0,42)	226 (-1,71) 275 (-1,11)

Table 3 Spectroscopic parameters of peptide, $[Ni(tcitr)_2]$, Htcitr and the adduct among peptide and $[Ni(tcitr)_2]$.

In figure 19 are presented the spectra of platinum complex and the peptide. As in the previous case, the UV-visible spectra (figure 19 a) confirm the interaction between the species.

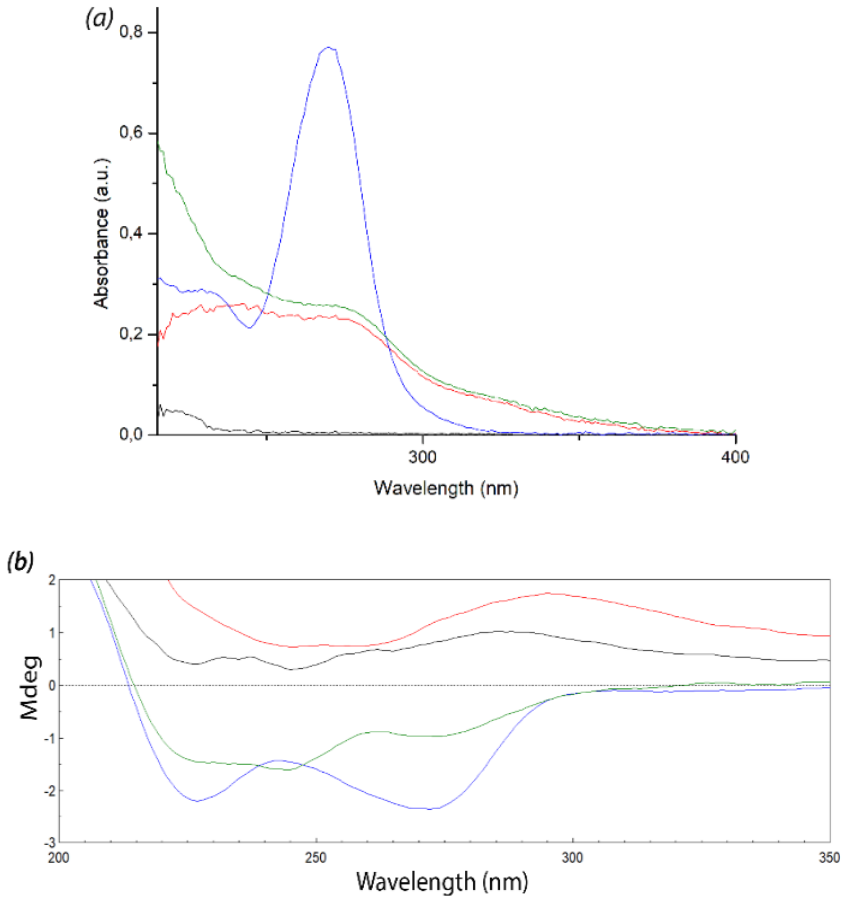

Figure 19 (a) UV-visible spectra and (b) circular dichroism (CD) spectra of peptide (black line), $[Pt(tcitr)_2]$ (red line), Htcitr (blue line), peptide + $[Pt(tcitr)_2]$ (green line). UV-visible and CD spectra are obtained in methanol with a concentration of 50 µM.

In the CD spectra (figure 19 b, green line) is absent the band at 217 nm. This information is consistent with the results observed in the NMR spectra. The $[Pt(tcitr)_2]$ interacts with the peptide like a single entity, i.e. without the dissociation and the release of a ligand.

In table 4 are presented the spectroscopic parameters.

Species	UV/vis λ_{max} nm (Absorbance)	CD λ_{max} nm (mdeg)
peptide	219 (0,048)	286 (1,01)
$[Pt(tcitr)_2]$	240 (0,26)	296 (1,70)
Htcitr	217 (0,31), 270 (0,77)	226 (-2,20) 271 (-2,36)
Histone + $[Pt(tcitr)_2]$	215 (0,58)	243 (-1,66) 275 (-0,99)

Table 4 Spectroscopic parameters of peptide, $[Pt(tcitr)_2]$, Htcitr and the adduct among peptide and $[Pt(tcitr)_2]$.

Herein, are presented the spectra of $[Cu(tcitr)_2]$. This complex is paramagnetic and the UV-visible and CD spectra are crucial to study the possible interaction between the complex and the peptide.

The coordinative behavior of $[Cu(tcitr)_2]$ complex towards the peptide is extremely different if compared with the previous complexes. In fact, the incubation of the two species generates spectra (figure 20 a and figure 20 b, green lines) very similar to the spectrum of the copper complex, without the formation of new bands. With this information we can conclude that $[Cu(tcitr)_2]$ complex interacts only in a negligible way with the peptide TESHHK.

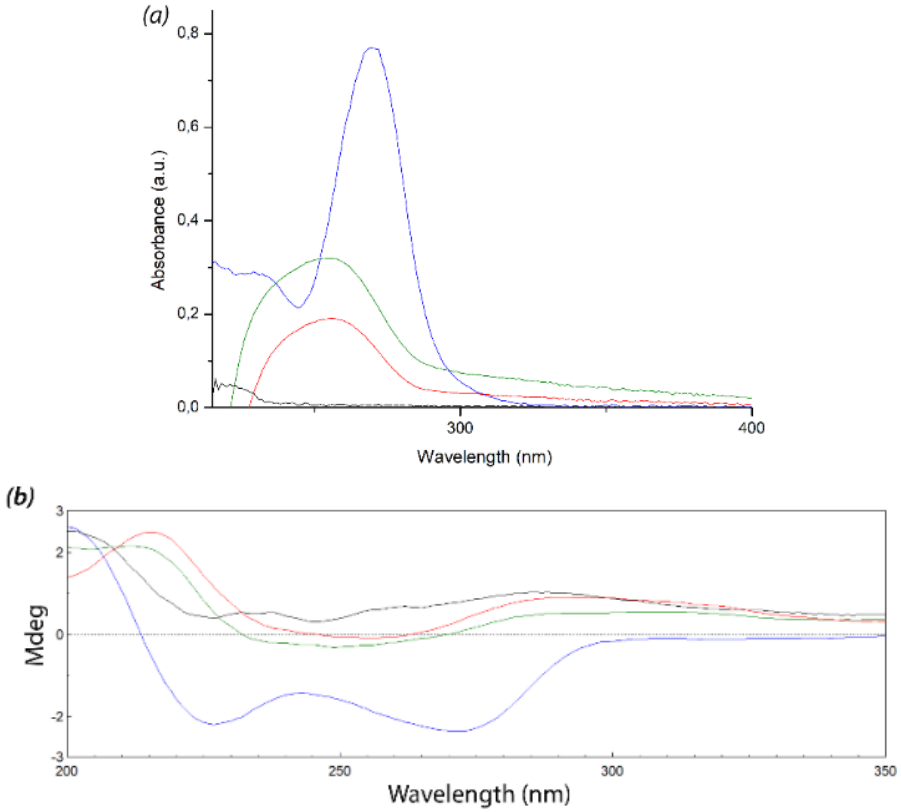

Figure 20 (a) UV-visible spectra and (b) circular dichroism (CD) spectra of peptide (black line), $[Cu(tcitr)_2]$ (red line), Htcitr (blue line), peptide + $[Cu(tcitr)_2]$ (green line). UV-visible and CD spectra are obtained in methanol with a concentration of 50 µM.

In table 5 are presented the spectroscopic parameters.

Species	UV/vis λ_{max} nm (Absorbance)	CD λ_{max} nm (mdeg)
peptide	219 (0,048)	286 (1,01)
$[Cu(tcitr)_2]$	256 (0,19)	216 (2,49) 290 (0,90)
Htcitr	217 (0,31), 270 (0,77)	226 (-2,20) 271 (-2,36)
Histone + $[Cu(tcitr)_2]$	253 (0,32)	212 (2,15) 309 (0,55)

Table 5 Spectroscopic parameters of peptide, $[Cu(tcitr)_2]$, Htcitr and the adduct among peptide and $[Cu(tcitr)_2]$.

3 Conclusions

In conclusion, in this chapter I established that the metal complexes of S-citronellal thiosemicarbazone are able to interact with biological molecules. The chosen targets are DNA and a model hexapeptide with the sequence AmTESHHKac (threonine, aspartate, serine, histidine, histidine, lysine). This peptide represents the C-tail of the histone H2A, that is exposed to the solvent.

The Htcitr metal complexes can interact directly with DNA with the compaction of the double strands and the formation of knots and hairpins. This behaviour is glaring for the complexes $[Pt(tcitr)_2]$ and $[Ni(tcitr)_2]$ while is less evident for $[Cu(tcitr)_2]$.

For what the studies with the peptide is concerned, the trend is the same observed with DNA. The nickel and platinum complexes are the most active respect to the copper one. At the same time, the NMR experiments allow us to understand the possible mechanism of action of these complexes. The $[Ni(tcitr)_2]$ is able to set a ligand free and can interact with the peptide through the metal center, instead $[Pt(tcitr)_2]$ acts like a single and not dissociated entity on the hexapeptide because the platinum has an increased affinity for the sulfur atoms of Htcitr and it has a reduced kinetics for the ligand exchange.

Finally, in this work I demonstrated that the three metal complexes of the S-citronellal thiosemicarbazone ($[Ni(tcitr)_2]$, $[Pt(tcitr)_2]$ and $[Cu(tcitr)_2]$) are able to interact with the DNA in direct and indirect ways, working directly on the double helix or destabilizing the chromatin through the interaction with histones.

Chapter two:

in silico docking studies:

thiosemicarbazones as inhibitors of the mitochondrial complex III

4 Introduction

In the previous chapter I described the structure and the anticancer activity of a thiosemicarbazone, Htcitr, and its metal complexes. As mentioned above, the ease to functionalize the TSs structure and their ability to chelate different metal ions, make them very useful in different biological fields. For example, TSs can be successfully applied like antifungal agents. The first case of TS created and used as antifungal agents dates to 1960 [46]. Herein, Benns et al. evaluated the antifungal activity of a panel of fourty TSs and their copper complexes on *A. niger* and *Chaetomium globosum* cultures. The activity of these compounds was compared with two commercial fungicides: the 2,2'dihydroxy-5,5'-dichlorodiphenylmethane and the copper/8-hydroxyquinolinolate mixture. The most interesting compound was the 9-undecenal thiosemicarbazone which showed an antifungal activity comparable with the commercial fungicides.

Their mechanism of action is not clear for all the species of fungi. Some studies indicate that TSs can influence the regulation and biosynthesis of ergosterol, an essential vitamin for fungal cells strictly connected with the metabolism of lipids and membrane synthesis [47], for the species *Candida* sp. and *Cryptococcus neoformans*.

4.1 Aflatoxins: an overview

The aflatoxins are polyketide-derived difuranocumarins produced by filamentous fungi of the generus *Aspergillus*. These filamentous fungi are ubiquitous and infesting organisms that can contaminate agricultural crops [48]. The term aflatoxin refers to a family of mycotoxins, all characterized by a common structure. In figure 21 are represented the six most dangerous mycotoxins of this family, due to their toxicity and diffusion, that count fourteen different species. The classification is based on the color of emission when irradiated by a 365 nm light (B = blue and G = green). Instead, the number 1 or 2 depends on their mobility in TLC. The M class is for the aflatoxins that contaminate the milk. M_1 and M_2 are, respectively, the metabolites of aflatoxins B_1 and B_2, found in milk.

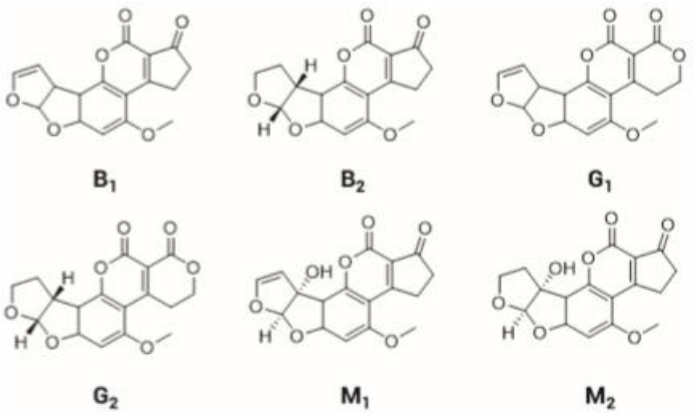

Figure 21 Structures of the most dangerous and harmful aflatoxins.

The toxicity of these aflatoxins is double: acute and chronic. The acute toxicity is expressed through tissue injuries, mainly in the liver, and immune system suppression [49]. The chronic toxicity is due by mutagenicity, carcinogenicity, and teratogenicity. The most dangerous aflatoxin is the aflatoxin B_1, that is considered one of the most carcinogenic natural products. This aflatoxin is metabolized by the cytochrome P450, a ubiquitous enzyme cluster, mainly present in liver, lungs and intestine, whose function is the mono-oxidation of drugs and other lipophilic xenobiotics. Cytochrome P450 induces the oxidation of the furan double bond of the aflatoxin B_1, with the formation of the B_1-exo-8,9-epoxide. This epoxide is extremely reactive and can interact with nucleophiles of nucleic acids. In fact, it can interact with the N^7 of the guanine. This adduct can induce the break of the N^7-C^8 double bond with the formation of the B1-FAPY. The damage induced by the aflatoxin B_1 causing the G→T mutation, with the possible outbreak of cancer [50] (figure 22).

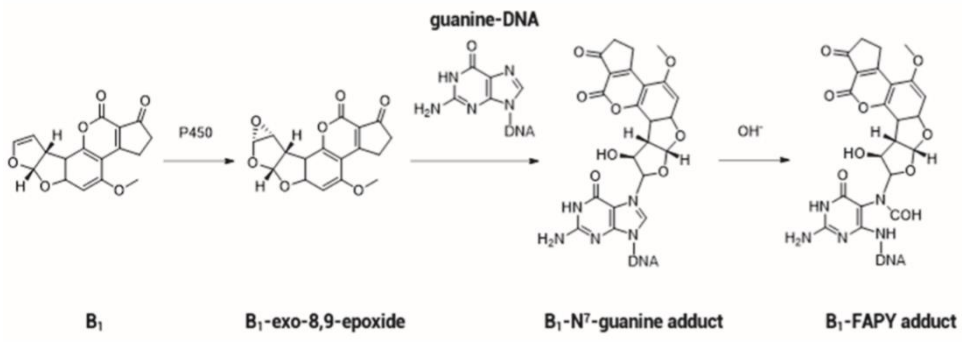

Figure 22 Mechanism of the DNA damage induced by the aflatoxin B_1 [51].

4.2 Aflatoxins: biosynthetic pathway and physiological triggers

The aflatoxins are secondary metabolite of the *Aspergilli*, i.e., a chemical species not directly involved in the growth, development, or reproduction of the organism. In figure 23 is presented the biosynthetic pathway of the aflatoxins. The synthesis of the aflatoxins is regulated by a series of enzymes and genes. These enzymes belong, principally, to the family of monooxygenase, whose function is the selective oxidation of substrates. The plenty of the monooxygenases in the synthetic pathway of the aflatoxins, suggests the possible

connection between the oxidation stress and the production of this second metabolite. In literature [52], is reported that in *A. parasiticus* the aflatoxin production is triggered by increased oxidative stress. *A. flavus* has the genes of the aflatoxin biosynthetic pathway downregulated when it is treated with the caffeic acid, a well-known antioxidant [53]. In other papers [54, 55] it is proposed that the synthesis of the aflatoxins is a secondary antioxidant defense system used together with the primary antioxidant mechanism that involves catalases, superoxide dismutases, peroxidases, and the thioredoxin system. This series of evidence show the connection between the oxidation stress and the production of aflatoxins, however, the specific molecular mechanism that underlies these two phenomena is not completely clear [56].

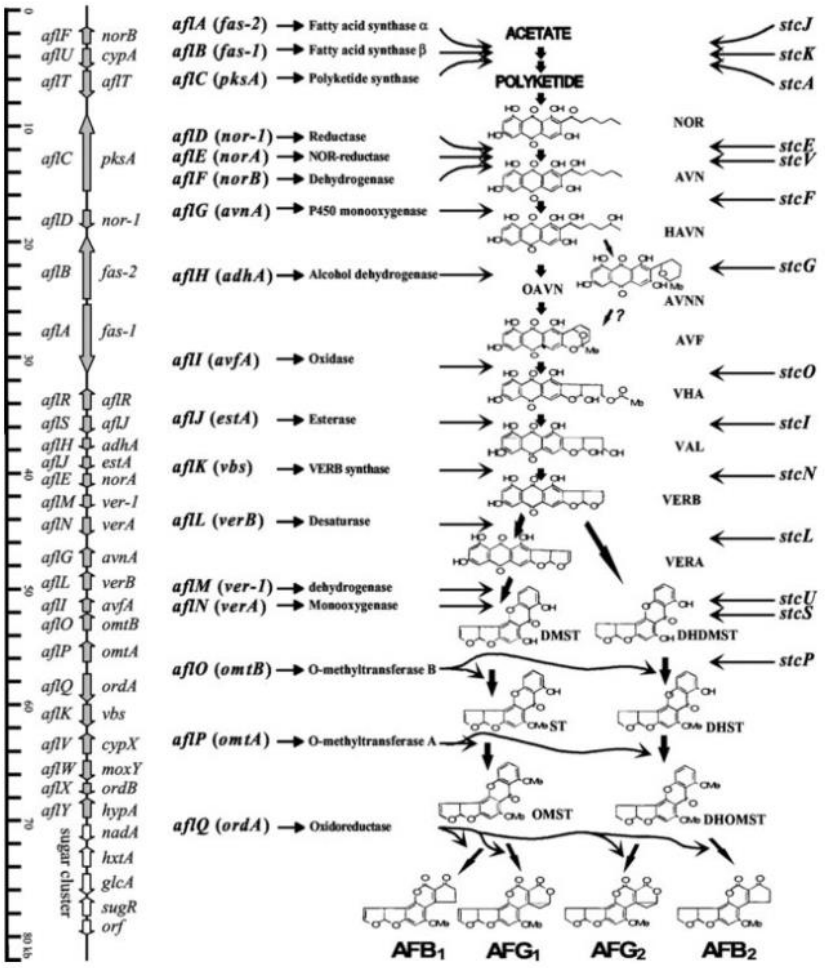

Figure 23 Aflatoxins' synthetic pathway [57].

4.3 Thiosemicarbazones as inhibitors of the aflatoxin biosynthesis

In 2015, CARIPLO foundation founded a new project, called aflatox project, whose aim was the develop of new antimycotic and antiaflatoxigenic compounds. Our laboratory was chosen for this project to synthesize a set of molecules belonging to the class of thiosemicarbazones (TSs). As described above, the pros of this class of molecules is the ease of modification of the molecular structure and the coordination versatility. The TSs synthesized for this purpose are obtained using natural aldehydes contained in spices [58-61] or derivatives

of the jasmonic acid, a plant hormone [62]. These natural aldehydes are chosen because the spices have been used for many centuries by humans to protect foods by molds and other contaminants.

Generally, if we want to block the aflatoxins production, we may proceed through two ways: the inhibition of the growth of the fungus, introducing a fungistatic compound that is able to block the primary metabolism of the organism, or the specific inhibition of the aflatoxin production, with a more specific antiaflatoxigenic compound. The second is the eligible way, because a fungistatic compound can alter the biological environment necessary for the optimal growth of the crops.

The most promising and interesting TSs discovered in our laboratory for the antiaflatoxigenic application are the isomers of the cuminaldehydethiosemicarbazone (Htcum).

4.4 Cuminaldehydethiosemicarbazone and its isomers: how the structural modifications play a crucial role in the inhibition of the aflatoxin production

In a previous work [59], it has been demonstrated that a little modification in the isopropylbenzaldehyde moiety, precisely changing the position of the isopropyl group respect to the thiosemicarbazone moiety, induces great differences in the biological activity against the *Aspergillus flavus*.

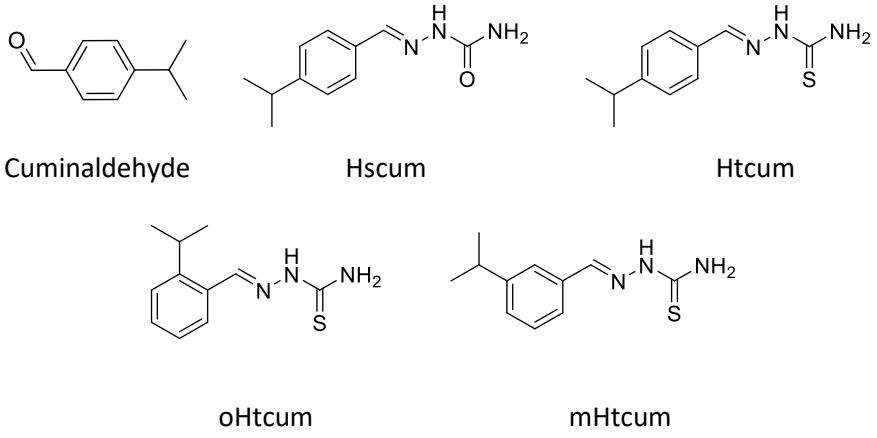

Figure 24 Structure of the molecules tested [59].

The structures of Htcum and its isomers are represented in figure 24; in figure 25 are reported the biological data of the compounds respect to the mycelium growth and the aflatoxin inhibition. The cuminaldehyde and Hscum, the semicarbazone analogue of Htcum, are slightly active in both the cases, demonstrating that the presence of the thiosemicarbazone moiety is *condicio sine qua non* for the biological activity. Instead, the thiosemicarbazones isomers, Htcum, mHtcum and oHtcum, have a different behavior. The oHtcum has an activity that is similar to Htscum. The Htcum is extremely active against the fungus and the aflatoxin. The activity against the aflatoxin is usually a reflex of the growth inhibition. In fact, when a molecule harms the primary metabolism, all the metabolic pathways are interested.

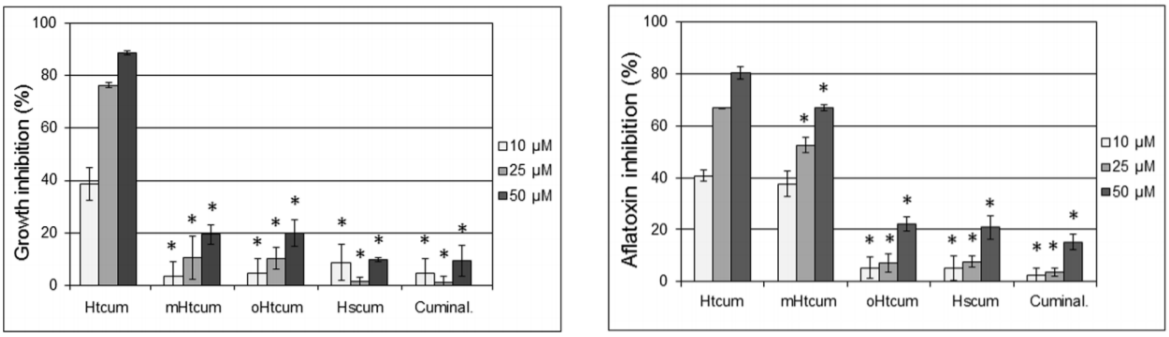

Figure 25 Activity of the Htcum's isomers respect to the mycelium growth (left) and toxin accumulation (right) of the *Aspergillus flavus*. The data are presented as percentage of inhibition as compared to the control, i.e., treated with only DMSO.

mHtcum, instead, is the best candidate in this panel of molecules. In fact, it can block selectively the aflatoxin synthesis, while the fungal growth is not significantly affected. Therefore, Htcum is a specific inhibitor of the aflatoxin production and investigated in depth to better understand how this molecule acts inside the fungal cell.

In the same paper [59], a series of genetic, proteomic, and biochemical experiments are performed showing that the molecular target of Htcum is involved in the energy generation and the redox homeostasis control of the cell, specifically at the mitochondrial level. The mitochondrial respiratory chain is a well-known molecular target to prevent the formation of mycotoxins [63]. In figure 26 is reported the effect of four natural inhibitors of the respiration cell on the aflatoxin production and the mycelium growth. These four compounds inhibit the aflatoxin production in a dose-dependent manner, while the mycelium growth is not reduced.

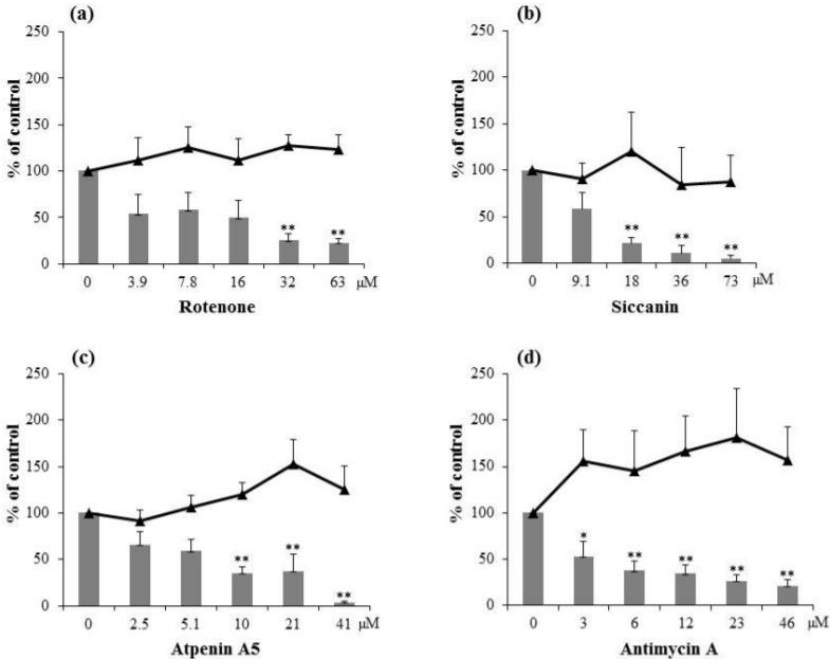

Figure 26 Effect of the respiratory chain inhibitors on the aflatoxin production (grey bars) and mycelium growth (black triangles) [64].

To understand in which part of the mitochondrial respiratory chain mHtcum acts, we use *Saccharomyces cerevisiae*, a well-known in literature [65, 66] model organism for the study of antioxidant compounds.

In another work [67] has been studied the specific activity of mHtcum respect to the complexes of the respiratory chain. In figure 27 are presented the specific inhibition of the complexes by mHtcum, at different concentrations. Here, the only complex whose activity is affected by mHtcum is the complex III, with a reduction of the activity close to the 30% at the higher concentration of the molecule.

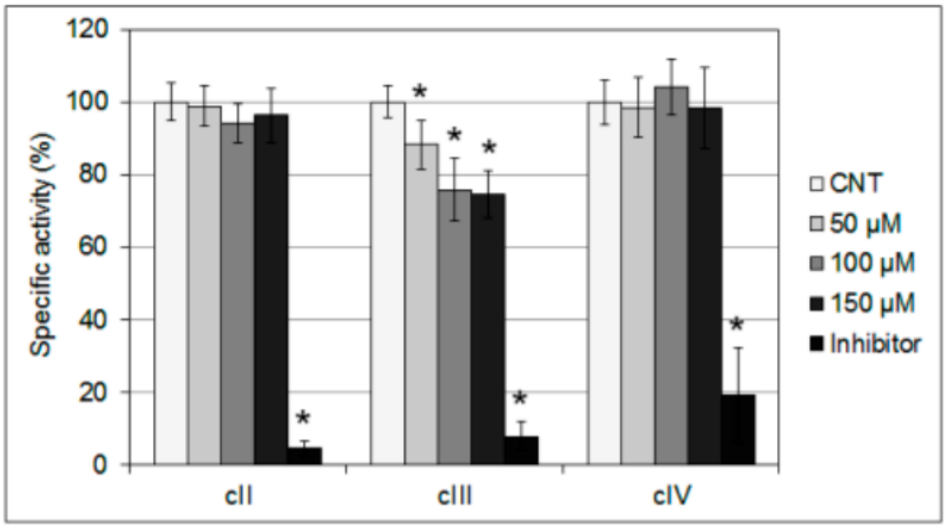

Figure 27 Activity of the respiratory chain complexes: succinate quinone DCPIP reductase (cII), NADH-cytochrome c oxidoreductase (cIII) and cytochrome c oxidase (cIV). Their activity is measured with an increasing concentration of mHtcum and compared respect to the DMSO treated cell, CNT, and the specific inhibitor of the complex. These inhibitors are malonate (cII), antimycin A (cIII) and Na-azide (cIV) [67].

This result corroborates the hypothesis that mHtcum induces a deficiency in the electron flow along the respiratory chain, with a specific inhibition of the complex III.

To better understand how mHtcum acts in the complex III some structure-based docking studies were performed. For this type of measurements is necessary to define a binding site on the enzyme, in which is reasonably foreseeable the interaction of the inhibitor. The guess of our *in silico* experiment was the competition between mHtcum and the most studied inhibitor of the complex III, the Antimycin A. Its activity is due by the interaction with Q_i/Q_n site of the cytochrome reductase [68], causing a collapse of the proton gradient.

The characteristics of these *in silico* experiments and the results obtained are better explained in a subsequent paragraph, because are the core experiments of this chapter.

5 Small structural variations, large biological deviations: an antiaflatoxigenic and *in silico* study

5.1 How the functionalization of the thiosemicarbazone moiety influence the antiaflatoxigenic activity

As described above, the position of the isopropyl in the thiosemicarbazones play a crucial role for the activity and the selectivity of the biological action. Hence, I studied how the functionalization of the thiosemicarbazone moiety influences the biological activity.

The functionalizations chosen are presented in figure 28. On the left, the functionalization of the N^2 of the thiosemicarbazone with a methyl, whose effect is the suppression of the tautomerism thione-thiol described in the introduction. On the right, the dimethylation of the N^4, that induces an increase of the hydrophobicity of the entire molecule.

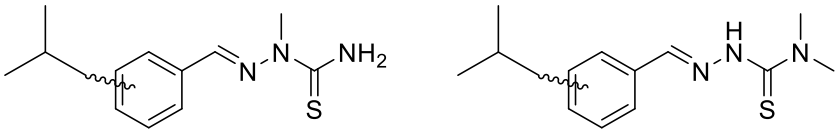

2-methyl functionalization

4,4'-dimethyl functionalization

Figure 28 Structure of the functionalized thiosemicarbazones.

In the next figures (figures 29, 30 and 31) are presented the results of the growth inhibition and antiaflatoxigenic activity. The functionalization of the N^2 with the methyl has a slightly effect on the fungus, with a damping effect on the aflatoxin inhibition of the Htcum and mHtcum, the two most active compounds.

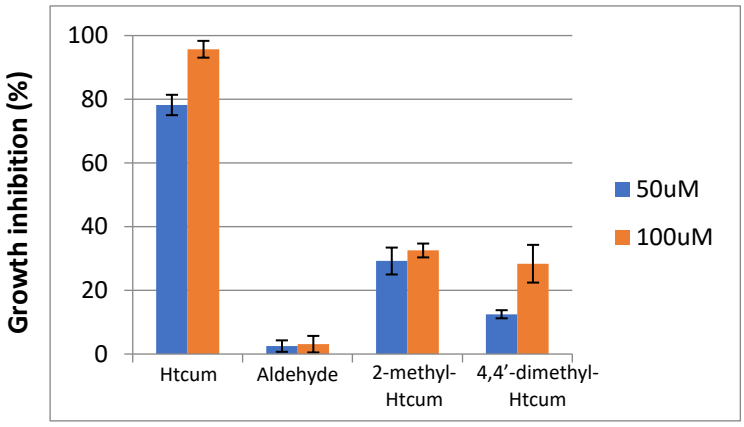

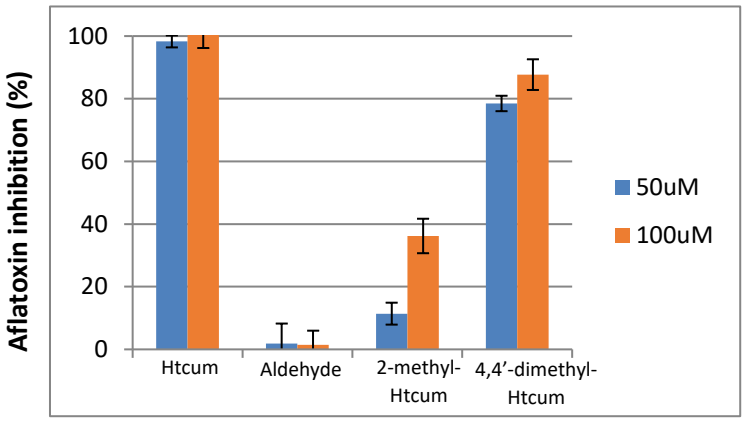

Figure 29 Activity of the Htcum and its thiosemicarbazones derivatives respect to the mycelium growth (above) and toxin accumulation (below) of the *Aspergillus flavus*. The data are presented as percentage of inhibition as compared to the control, i.e., treated with only DMSO.

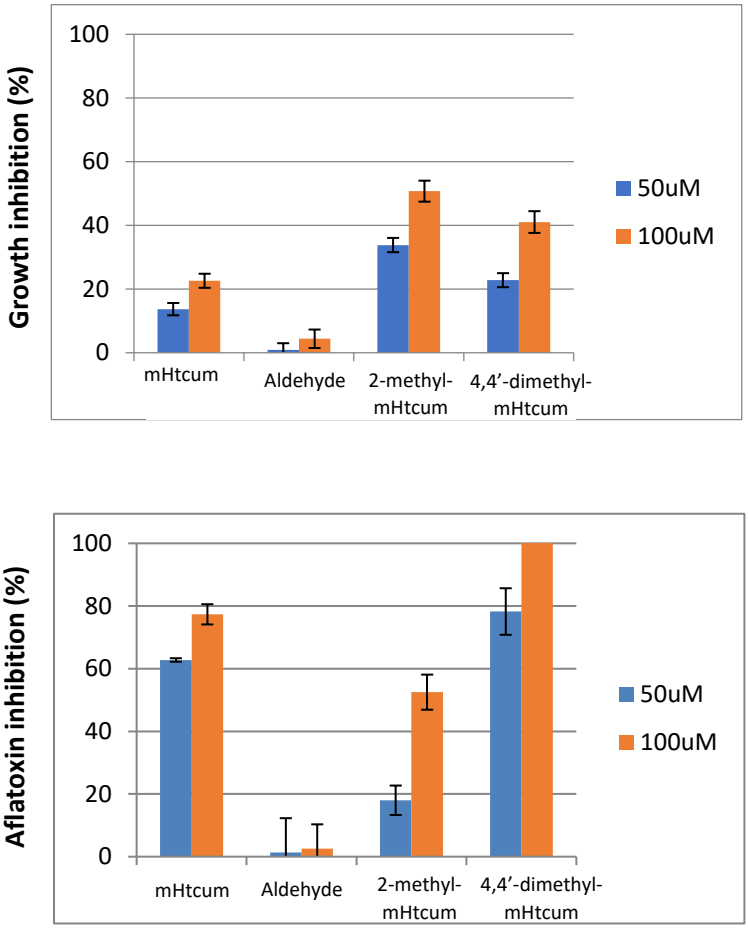

Figure 30 Activity of the mHtcum and its thiosemicarbazones derivatives respect to the mycelium growth (above) and toxin accumulation (below) of the *Aspergillus flavus*. The data are presented as percentage of inhibition as compared to the control, i.e., treated with only DMSO.

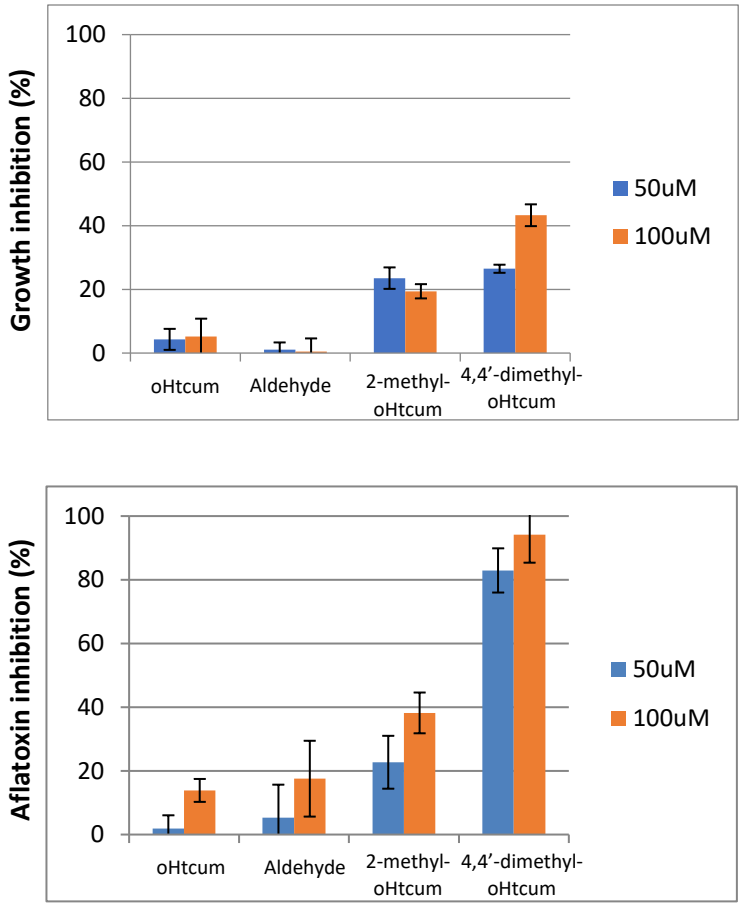

Figure 31 Activity of the oHtcum and its thiosemicarbazones derivatives respect to the mycelium growth (above) and toxin accumulation (below) of the *Aspergillus flavus*. The data are presented as percentage of inhibition as compared to the control, i.e., treated with only DMSO.

On the contrary, the dimethylation of the N^4 nitrogen is extremely interesting. All the three isomers of the cuminaldehydethiosemicarbazone have enhanced their selectivity respect the aflatoxin. The reduction of the fungus growth that does not exceed the 40% also for the Htcum compound, the most active thiosemicarbazone against the fungus. On the other hand, the antiaflatoxigenic activity is static, for Htcum and mHtcum, or extremely enhanced, for oHtcum.

In conclusion, the functionalization of the N^4 with two methyl groups, for the cuminaldehydethiosemicarbazone family, bears to the increase of the selectivity of this molecules respect to the aflatoxin.

5.2 *In silico* evaluation of the best inhibitor of the complex III: a docking study

5.2.1 Molecular docking: an overview

The molecular docking [69] is a useful tool for the medicinal chemists to design new compounds that specifically inhibit target biomolecules. The core principle of the docking is the prediction, through computational calculations, if a specific molecular scaffold is able to interact with a specific protein, evaluating the geometry and the possible interactions between the "host" and the "guest". The molecular docking can be used to perform a wide virtual screening of libraries of compounds to define the most promising candidates for the inhibition of a specific biomolecule. In a typical docking study, the putative inhibitor is placed, by the algorithm, in different conformations in the active binding site, until the best pose, i.e., the best position respect to the shape selectivity of the binding site and the best binding affinity from the energetical point of view. The affinity of the inhibitor for a specific binding site is the sum of different contributes: hydrogen bonds, ionic interactions, Van der Waals interactions and lipophilic interactions.

Obviously, the software used for molecular docking cannot use accurate methods based on quantum-mechanics, because the biomolecules are extremely complex and the computational cost would become unsustainable. For this reason, the molecular docking uses easier concepts and approximations, like the utilization of proteins in blocked conformation, whose structure is defined by crystallography. In that way, the protein used is devoid of any dynamism and possible structural changes induced by the inhibitor. Obviously, these approximations and simplifications are source of errors and uncertainty, which constitute the major limit of the docking technique.

The software that I used for the docking experiments is GOLD (Genetic Optimization for Ligand Docking) in version 5.8.1, a software of the Cambridge Crystallographic Data Center, CCDC. This software is characterized by several type of algorithms, called scoring functions, that can be extremely simple, like the GoldScore and ASP functions, able only to classify conformations of the ligands, or more complex, like the ChemScore function, that is able to estimate the binding energy of each conformation.

5.2.2 Molecular docking: setup of the experiment

As described in the previous pages, mHtcum is able to interact specifically with the complex III of the respiratory chain and docking studies are performed [67] to confirm this interaction. Herein, all the cuminaldehydethiosemicarbazone derivatives are studied as inhibitors of the complex III, and the binding energies are compared.

The protein used for the molecular docking is obtained from the Protein Data Bank (PDB) with the code 3BCC. This protein is crystallized with the inhibitor antimycin (AMY) bounded to the cytochrome bc1. The first step to validate the docking is the approach of the self-docking, in which the inhibitor present in the crystallographic protein structure, in this case AMY, is deleted and its position is recalculated with GOLD. If the root-mean-square deviation (RMSD) between the inhibitor present in the crystal and the inhibitor calculated is low than 2 Å, the docking method is considered valid [70, 71]. In this case, with a 50-run docking

using the chemscore_kinase as template, the ChemScore function for the scoring and the ChemPLP function for the rescoring the RMSD obtained for AMY is 1.572 Å, confirming the method.

5.2.3 Molecular docking: results of the *in silico* study

In table 6 are presented the binding energies of AMY and the cuminaldehydethiosemicarbazone derivatives, obtained with the ChemScore function.

The results obtained for some thiosemicarbazones are at odds over the antiaflatoxigenic activity showed above. For example, 2-methyl-oHtcum has the best activity against this enzyme, according to the docking, but its aflatoxin inhibition is lower than other thiosemicarbazones. These discrepancies can have different origins, for example some molecules can have uptake problems and they cannot interact with the target enzyme because they cannot reach that enzyme.

In the next pages I will focus my attention on the 4,4'-dimethyl derivatives, because their very high antiaflatoxigenic activity, as demonstrated above.

Molecules	Binding energy
AMY	ΔG_{bind} = -6.05 kcal/mol
oHtcum 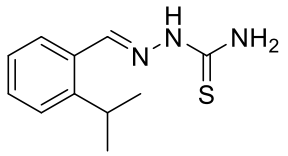	ΔG_{bind} = -6.45 kcal/mol
mHtcum 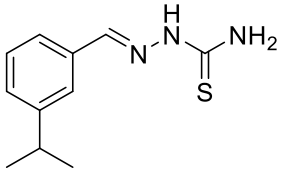	ΔG_{bind} = -5.96 kcal/mol
Htcum 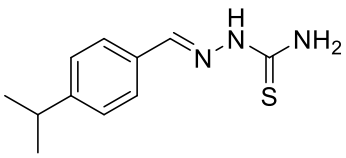	ΔG_{bind} = -6.00 kcal/mol
2-methyl-oHtcum 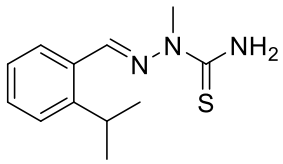	ΔG_{bind} = -6.82 kcal/mol

2-methyl-mHtcum 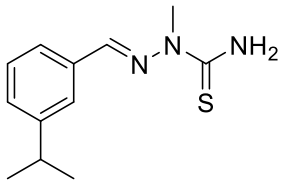	ΔG_{bind} = -6.21 kcal/mol
2-methyl-Htcum 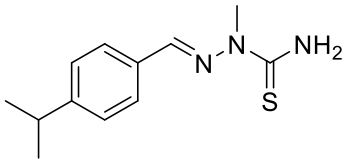	ΔG_{bind} = -6.33 kcal/mol
4,4'-dimethyl-oHtcum 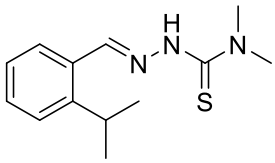	ΔG_{bind} = -6.32 kcal/mol
4,4'-dimethyl-mHtcum 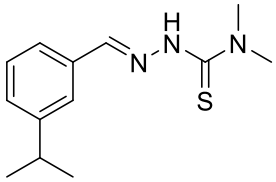	ΔG_{bind} = -6.33 kcal/mol
4,4'-dimethyl-Htcum 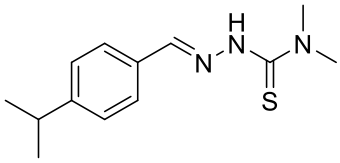	ΔG_{bind} = -6.43 kcal/mol

Table 6 Binding energies of AMY and the cuminaldehydethiosemicarbazone derivatives.

The complex III of the respiratory chain is involved in the oxidation of ubiquinol to ubiquinone. The actual moiety of this enzyme involved in the oxidation is a heme b_H. In this enzyme, the heme b_H is close to a pocket exposed to the solvent, called Qi site, and characterized by a hydrophobic environment, in which the quinone substrate can enter easily in the complex III.

The Qi site is the point in which AMY block the activity of the complex III, interacting with the heme b_H. The theoretical positioning of the thiosemicarbazones is compared respect to AMY.

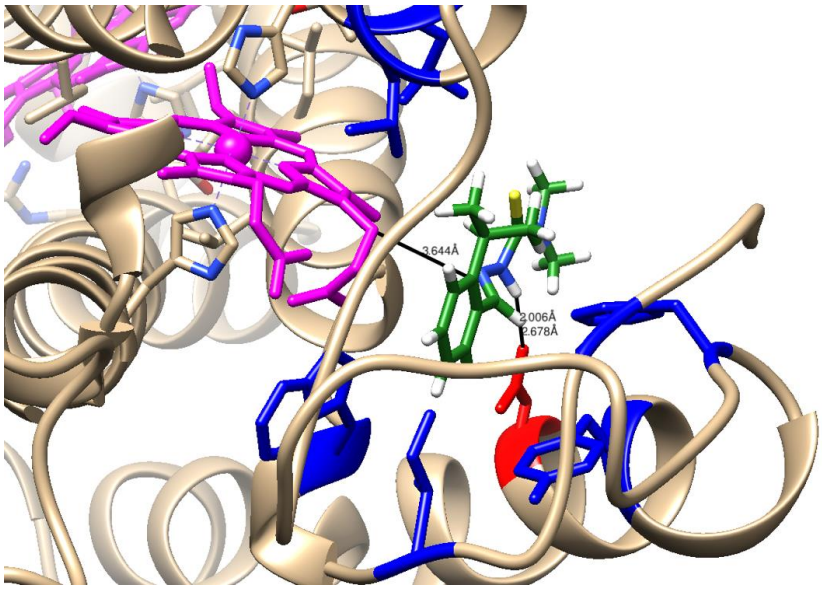

Figure 32 Theoretical positioning of 4,4'-dimethyl-oHtcum (green) in the Qi site. In the image are also colored the heme group (magenta), the residue Asp229 (red) and the hydrophobic residues (blue) involved in the formation of the hydrophobic pocket.

In figure 32 is showed the best pose obtained with GOLD for the thiosemicarbazone 4,4'-dimethyl-oHtcum into the Qi site. The hydrophobic pocket is formed by Phe221, Ile28, Tyr225, Ala24, Trp32, Leu201 and Leu198 (the blue residues). This pocket stabilizes the aromatic moiety of 4,4'-dimethyl-oHtcum. Additionally, the N^2 and the carbon of the imine bond of the thiosemicarbazone are involved in a hydrogen bond with the carboxyl group of Asp229, whose lengths are 2.006 Å for N^2- Asp229 bond and 2.678 Å for the imine carbon and Asp229. These hydrogen bonds may be responsible for the maintaining of the thiosemicarbazone into the Qi site, placing the aromatic moiety in the hydrophobic pocket of the protein. Another interesting result is the proximity of the 4,4'-dimethyl-oHtcum to heme group (3.644 Å), like AMY. This proximity is considered crucial for the inhibition mechanism of AMY.

In figure 33 is showed the best pose obtained with GOLD for the thiosemicarbazone 4,4'-dimethyl-mHtcum into the Qi site. Here, the considerations explained above are still viable. The aromatic moiety is positioned in the same hydrophobic pocket and two hydrogen bonds are responsible for the positioning of the thiosemicarbazone. The differences are the shorter lengths of the hydrogen bonds, 1.946 Å for N^2- Asp229 bond and 2.535 Å for the imine carbon and Asp229, and the increase of the proximity (3.320 Å) between the heme group and 4,4'-dimethyl-mHtcum.

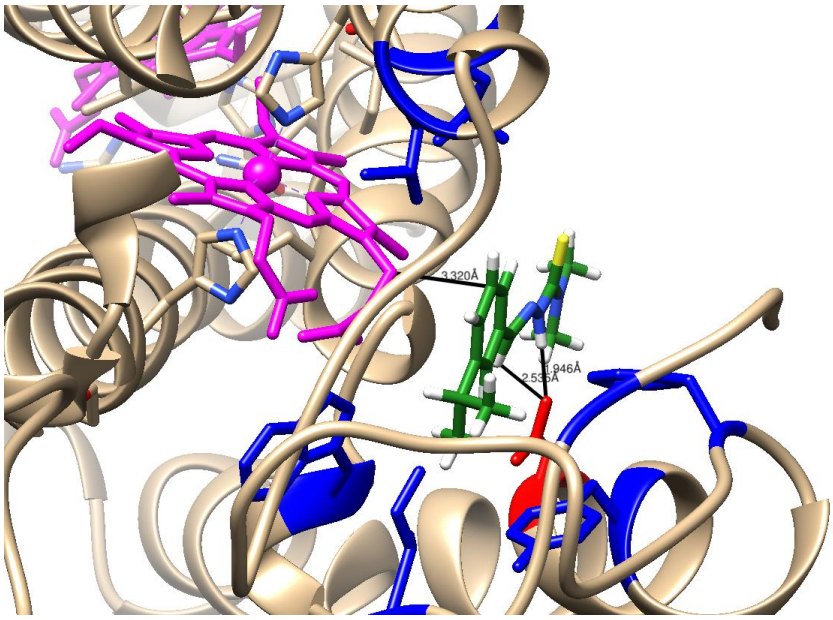

Figure 33 Theoretical positioning of 4,4'-dimethyl-mHtcum (green) in the Qi site. In the image are also colored the heme group (magenta), the residue Asp229 (red) and the hydrophobic residues (blue) involved in the formation of the hydrophobic pocket.

The theoretical positioning of 4,4'-dimethyl-Htcum, showed in figure 34, is different respect to the previous two thiosemicarbazones. In fact, the isopropyl in para respect to the thiosemicarbazone moiety hinders the formation of the hydrogen bonds with Asp229. According to this theoretical positioning, the 4,4'-dimethyl-Htcum prefers maximize the hydrophobic interactions to the detriment of the hydrogen bonds. Another effect of this different positioning is the minor proximity between the thiosemicarbazone and the heme group.

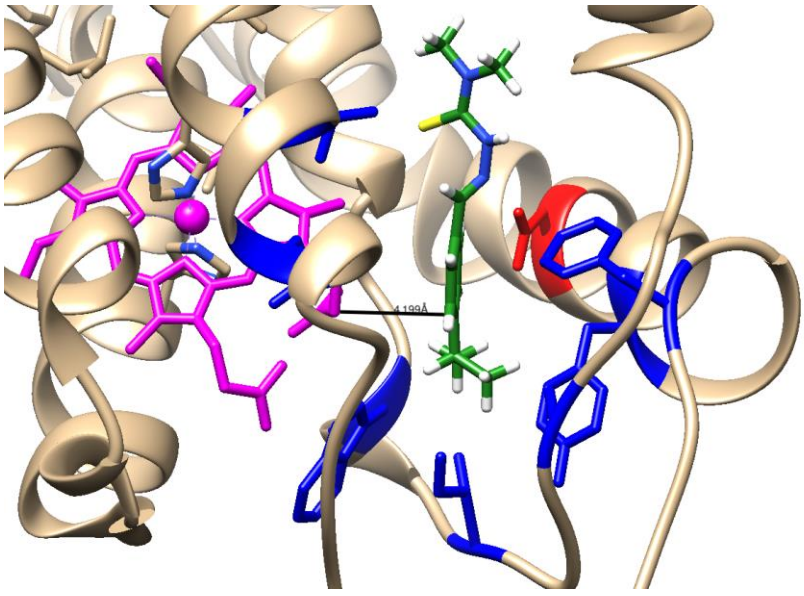

Figure 34 Theoretical positioning of 4,4'-dimethyl-Htcum (green) in the Qi site. In the image are also colored the heme group (magenta), the residue Asp229 (red) and the hydrophobic residues (blue) involved in the formation of the hydrophobic pocket.

6 Conclusions

In conclusion, in this chapter I explored how small variations in the molecular scaffold of thiosemicarbazones change dramatically their biological activity against *Aspergillus flavus*. More precisely, the introduction of a methyl group in the N^2 induces a general reduction of the antiaflatoxigenic activity while the dimethylation of the N^4 increases the inhibition of the aflatoxin production and the selectivity.

In previous experiments, a specific molecular target for mHtcum has been found in the complex III of the mitochondrial respiratory chain. For this reason, I wondered if this enzyme is still the target of this new thiosemicarbazones, and, using the molecular docking, I evaluated the theoretical positioning of these molecules comparing their position with the natural inhibitor AMY. Through the ChemScore function it was possible to define the binding energies. In the Qi site, the theoretical positioning of the dimethylated thiosemicarbazones shows that these molecules are able to interact with the hydrophobic pocket, through their aromatic moiety, while 4,4'-dimethyl-oHtcum and 4,4'-dimethyl-mHtcum form two hydrogen bonds with the Asp229. Furthermore, these molecules are very close to the heme group, like the inhibitor AMY.

7 Experimental section

7.1 Synthesis and characterization of the S-citronellal-thiosemicarbazone and its metal complexes

S-citronellal-thiosemicarbazone (Htcitr)

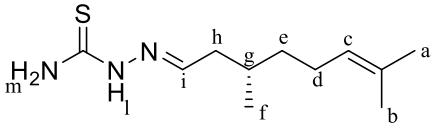

To a stirred solution of thiosemicarbazide (177 mg, 1.94 mmol, 1 eq.) in 30 ml of ethanol 350 µL of S-citronellal (1.94 mmol, 1 eq.) were added. The solution was heated to reflux for six hours. The mixture was then evaporated under reduced pressure and dried under vacuum. Light brown oil. **Yield**: 95% **^{1}H-NMR** (δ, ppm, 400MHz, DMSO-D_6): 0.87 (d, J = 8 Hz, 3H, H_f); 1.16 (m, 1H, H_{e1}); 1.29 (m, 1H, H_{e2}); 1.57 (s, 3H, H_a); 1.65 (s, 3H, H_b); 1.69 (m, 1H, H_g); 1.96 (m, 2H, H_d); 2.04 (m, 1H, H_{h1}); 2.17 (m, 1H,H_{h2}); 5.08 (s, 1H, H_c); 7.41 (t, J = 8 Hz, 1H, H_i); 7.44 (s, 1H, H_{m2}); 7.98 (s, 1H, H_{m1}); 11.02 (s, 1H, H_l) **ATR-FTIR** (cm^{-1}) 3410 (s) and 3265 (s, br) ν (NH_2); 3164 (s) ν (NH); 3024 (m) ν (CH_3); 2965 (s) and 2917 (s) ν (CH_2); 1596 (s) ν (CN) + ν (C═C); 925 (w) and 824 (m) ν (CS) **ESI-MS (+)** m/z calc. 226.36 found 226.39.

bis(S-citronellal-thiosemicarbazonate)nickel(II) [Ni(tcitr)$_2$]

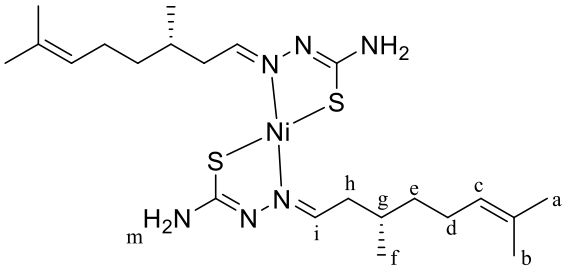

A solution of $Ni(CH_3COO)_2{\cdot}4H_2O$ (26 mg, 0.154 mmol, 1 eq.) was prepared in 5 mL of ethanol and added dropwise to a solution of S-citronellalthiosemicarbazone (Htcitr) (70 mg, 0.308 mmol, 2 eq.) in 10 mL of ethanol, at room temperature with stirring. Dark green powder. **Yield**: 87%. **^{1}H-NMR** (δ, ppm, 400MHz, DMSO-D_6): 0.83 (d, J = 8 Hz, 3H, H_f); 1.13 (m, 1H, H_{e1}); 1.23 (m, 1H, H_{e2}); 1.45 (m, 1H, H_g); 1.57 (s, 3H, H_a); 1.64 (s, 3H,H_b); 1.92 (m, 2H, H_d); 2.31 (m, 2H, H_h); 5.06 (s, 1H, H_c); 6.65 (s, 1H, H_i); 6.73 (s, 1H, H_{m2}); 7.19 (s, 1H, H_{m1}). **ATR-FTIR** (cm^{-1}) 3464 (m), 3328 (s) and 3150 (s) ν (NH_2); 2960 (m) ν (CH_3); 2911 (m) ν (CH_2); 1614 (m) ν (C═C); 1523 (vs) ν (CN); 871 (w) ν (CS). **ESI-MS (+)** m/z calc. 511.42 found 511.21.

bis(S-citronellal-thiosemicarbazonate)platinum(II) [Pt(tcitr)$_2$]

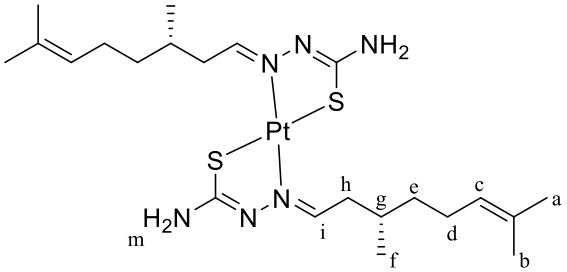

$PtCl_2$ (41 mg, 0.154 mmol, 1 eq.) was dissolved in 25 mL of acetonitrile at 80°C. This solution was added dropwise to a solution of S-citronellalthiosemicarbazone (Htcitr) (70 mg, 0.308 mmol, 2 eq.) in 10 mL of ethanol, at room temperature with stirring. Yellow powder. **Yield:** 84%. **^{1}H-NMR** (δ, ppm 400MHz, DMSO-D_6): 0.89 (d, J = 8 Hz, 3H, H_f); 1.24 (m, 2H, H_e); 1.57 (s, 3H, H_a); 1.65 (s, 3H, H_b); 1.73 (m, 1H, H_g); 1.95 (s, 2H, H_d); 2.42 (m, 2H, H_h); 5.08 (s, 1H, H_c); 7.11 (bs, 1H, H_i); 7.90 (s, 1H, H_{m2}); 8.17 (s, 1H, H_{m1}) **ATR-FTIR** (cm^{-1}) 3249 (m) and 3138 (m) ν (NH_2); 2955 (s) ν (CH_3); 2920 (s) ν (CH_2); 1618 (s) ν (C═C); 1565 (s) ν (CN); 824 (w) ν (CS) **ESI-MS** m/z $[M+H]^+$ calc. 648.81 found 648.47.

bis(S-citronellal-thiosemicarbazonate)copper(II) [Cu(tcitr)$_2$]

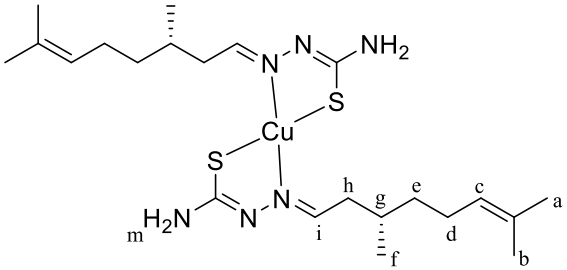

A solution of $CuCl_2{\cdot}2H_2O$ (26 mg, 0.154 mmol, 1 eq.) was prepared in 5 mL of ethanol and added dropwise to a solution of S-citronellalthiosemicarbazone (Htcitr) (70 mg, 0.308 mmol, 2 eq.) in 10 mL of ethanol, at room temperature under magnetic stirring. Black powder. **Yield:** 78%. **ATR-FTIR** (cm^{-1}) 3243 (s) and 3103 (s) ν (NH_2);

2964 (s) ν (CH_3); 2917 (s) ν (CH_2); 1615 (s) ν (C═C); 1511 (vs) ν (CN); 716 (w) ν (CS) **ESI-MS** m/z calc. 516.27 found 516.35.

7.2 Synthesis of the cuminaldehydethiosemicarbazone and its derivatives

For the synthesis of these molecules I used a single procedure. The desired thiosemicarbazide was mixed with an equimolar amount of an appropriate aldehyde in ethanol. The solution was then refluxed under stirring for 8 hours and left overnight at 0°C. The precipitate was filtered out, washed with cold ethanol, and dried under vacuum.

Cuminaldehydethiosemicarbazone (Htcum)

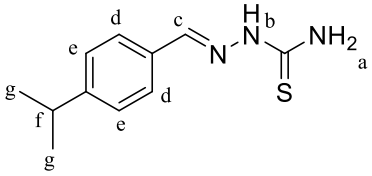

Thiosemicarbazide (0.30 g, 3.3 mmol), cuminaldehyde (4-isopropylbenzaldehyde) (0.49 g, 3.3 mmol). Pale yellow powder. **Yield**: 86% **^{1}H-NMR** (δ, ppm, DMSO-D_6): 1.21 (d, J = 6.7 Hz, 6H, H_g), 2.91 (m, 1H, H_f), 7.28 (d, J = 7.7 Hz, 2H, H_e), 7.71 (d, J = 7.7 Hz, 2H, H_d), 7.93 (s, 1H, H_c), 8.02 (s, 1H, H_a), 8.17 (s, 1H, H_a), 11.34 (s, 1H, H_b) **ATR-FTIR** (cm^{-1}): 3411 (m) and 3280 (m) ν (NH); 3013 (m) ν ($CH_{aromatic}$); 2957 (m) ν ($CH_{aliphatic}$); 1586 (s) ν (CN); 820 (m) ν (CS) **ESI-MS** m/z $[M+H]^+$ calc. 222.32 found 222.49.

3-isopropylbenzaldehydethiosemicarbazone (mHtcum)

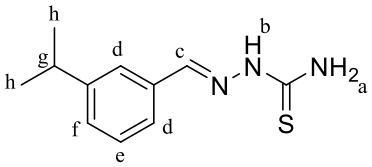

Thiosemicarbazide (0.30 g, 3.3 mmol), 3-isopropylbenzaldehyde (0.49 g, 3.3 mmol). White powder. **Yield**: 79% **^{1}H-NMR** (δ, ppm, DMSO-D_6): 1.23 (d, J = 6.8 Hz, 6H, H_h), 2.91 (m, 1H, H_g), 7.30 (m, 2H, H_d), 7.57 (d, J = 7.7 Hz, 1H, H_e), 7.69 (s, 1H, H_f); 8.00 (s, 1H, H_c), 8.03 (s, 1H, H_a), 8.20 (s, 1H, H_a), 11.41 (s, 1H, H_b) **ATR-FTIR** (cm^{-1}): 3382 (m) and 3230 (m) ν (NH); 3031 (m) ν ($CH_{aromatic}$); 2952 (mw) ν ($CH_{aliphatic}$); 1597 (s) ν (CN); 839 (m) ν (CS) **ESI-MS** m/z $[M+H]^+$ calc. 222.32 found 222.12.

2-isopropylbenzaldehydethiosemicarbazone (oHtcum)

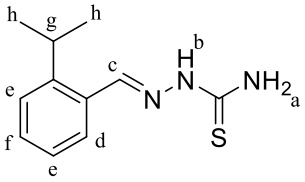

Thiosemicarbazide (0.30 g, 3.3 mmol), 2-isopropylbenzaldehyde (0.49 g, 3.3 mmol). White powder. **Yield**: 75% **^{1}H-NMR** (δ, ppm, DMSO-D_6): 1.22 (d, J = 6.8 Hz, 6H, H_h), 3.26 (m, 1H, H_g); 7.21 (t, J = 6.8 Hz, 1H, H_e), 7.37

(m, 2H, H_e, H_f), 7.91 (s, 1H, H_c), 8.08 (d, J = 7.6 Hz, 1H, H_d), 8.19 (s, 1H, H_a), 8.56 (s, 1H, H_a), 11.32 (s, 1H, H_b) **ATR-FTIR** (cm^{-1}): 3430 (m) and 3256 (m) ν (NH); 3031 (w) ν ($CH_{aromatic}$); 2955 (mw) ν ($CH_{aliphatic}$); 1594 (s) ν (CN); 848 (m) ν (CS) **ESI-MS** m/z $[M+H]^+$ calc. 222.32 found 222.25.

Cuminaldehyde-2-methyl-thiosemicarbazone (2-methyl-Htcum)

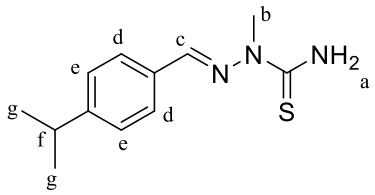

2-methyl-thiosemicarbazide (0.14 g, 1.4 mmol), 4-isopropylbenzaldehyde (0.20 g, 1.4 mmol). White powder. **Yield**: 73% **^{1}H-NMR** (δ, ppm, DMSO-D_6): 1.22 (d, J = 6.7 Hz, 6H, H_g), 2.94 (m, 1H, H_f), 3.77 (s, 3H, H_b), 7.30 (d, J = 8.0 Hz, 2H, H_e), 7.84 (d, J = 8.0 Hz, 2H, H_d), 7.87 (s, 1H, H_c), 8.25 (s, 1H, H_a), 8.37 (s, 1H, H_a) **ATR-FTIR** (cm^{-1}): 3415 (s) and 3235 (m) ν (NH_2); 3116 (m) ν ($CH_{aromatic}$); 2958 (m) and 2868 (m) ν ($CH_{aliphatic}$); 1582 (s) ν (CN); 828 (s) ν (CS) **ESI-MS** m/z calc. 235.35 found 235.59.

3-isopropylbenzaldehyde-2-methyl-thiosemicarbazone (2-methyl-mHtcum)

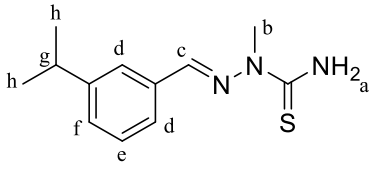

2-methyl-thiosemicarbazide (0.07 g, 0.7 mmol), 3-isopropylbenzaldehyde (0.10 g, 0.7 mmol). White powder. **Yield**: 81% **^{1}H-NMR** (δ, ppm, DMSO-D_6): 1.25 (d, J = 6.6 Hz, 6H, H_h), 3.54 (m, 1H, H_g), 3.83 (s, 3H, H_b), 7.25 (m, 2H, H_e, H_f), 7.79 (m, 2H, H_d), 8.11 (s, 1H, H_c), 8.25 (s, 1H, H_a), 8.42 (s, 1H, H_a) **ATR-FTIR** (cm^{-1}): 3398(s) and 3257 (m) ν (NH_2); 3145 (m) ν ($CH_{aromatic}$); 2862 (m) and 2954 (s) ν ($CH_{aliphatic}$); 1585 (m) ν (CN); 786 (m) ν (CS) **ESI-MS** m/z calc. 235.35 found 235.41.

2-isopropylbenzaldehyde-2-methyl-thiosemicarbazone (2-methyl-oHtcum)

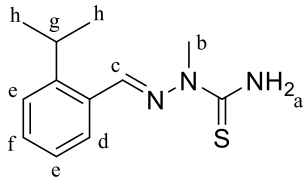

2-methyl-thiosemicarbazide (0.07 g, 0.7 mmol), 2-isopropylbenzaldehyde (0.10 g, 0.7 mmol). White powder. **Yield**: 81% **^{1}H-NMR** (δ, ppm, DMSO-D_6): 1.25 (d, J = 6.7 Hz, 6H, H_h), 3.54 (m, 1H, H_g), 3.83 (s, 3H, H_b), 7.25 (m, 3H, H_e, H_f), 7.81 (m, 1H, H_d), 8.11 (s, 1H, H_c), 8.18 (s, 1H, H_a), 8.42 (s, 1H, H_a) **ATR-FTIR** (cm^{-1}): 3398(s) and 3257 (m)) ν (NH_2); 3145 (m) ν ($CH_{aromatic}$); 2862 (m) and 2954 (s) ν ($CH_{aliphatic}$); 1585 (m) ν (CN); 786 (m) ν (CS) **ESI-MS** m/z calc. 235.35 found 235.25.

Cuminaldehyde-4,4'-dimethyl-thiosemicarbazone (4,4'-dimethyl-Htcum)

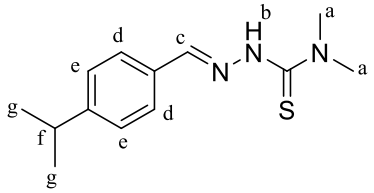

4,4-dimethyl-thiosemicarbazide (0.10 g, 0.8 mmol), 4-isopropylbenzaldehyde (0.12 g, 0.8 mmol). White powder. **Yield**: 73% **^{1}H-NMR** (δ, ppm, DMSO-D_6): 1.23 (d, J = 6.7 Hz, 6H, H_g), 2.93 (m, 1H, H_f), 3.30 (s, 6H, H_a), 7.38 (d, J = 8.0 Hz, 1H, H_e), 7.87 (d, J = 8.0 Hz, 2H, H_d), 8.17 (s, 1H, H_c), 10.93 (s, 1H, H_b) **ATR-FTIR** (cm^{-1}): 3354 (m) ν (NH); 3358 (m) ν ($CH_{aromatic}$); 2957 (m) ν ($CH_{aliphatic}$); 1565 (m) ν (CN); 783 (m) ν (CS) **ESI-MS** m/z calc. 249.38 found 249.41.

3-isopropylbenzaldehyde-4,4'-dimethyl-thiosemicarbazone (4,4'-dimethyl-mHtcum)

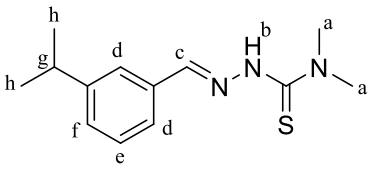

4,4-dimethyl-thiosemicarbazide (0.10 g, 0.8 mmol), 3-isopropylbenzaldehyde (0.12 g, 0.8 mmol). White powder. **Yield**: 79% **^{1}H-NMR** (δ, ppm, DMSO-D_6): 1.25 (d, J = 6.7 Hz, 6H, H_h), 2.99 (m, 1H, H_g), 3.33 (s, 6H, H_a), 7.31 (m, 2H, H_e, H_f), 7.82 (m, 2H, H_d), 8.23 (s, 1H, H_c), 10.93 (s, 1H, H_b) **ATR-FTIR** (cm^{-1}): 3412 (m) ν (NH); 3245 (m) ν ($CH_{aromatic}$); 2896 (m) ν ($CH_{aliphatic}$); 1532 (m) ν (CN); 802 (m) ν (CS) **ESI-MS** m/z calc. 249.38 found 249.59.

2-isopropylbenzaldehyde-4,4'-dimethyl-thiosemicarbazone (4,4'-dimethyl-oHtcum)

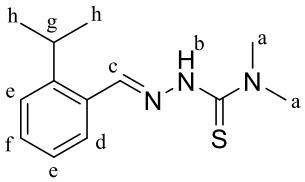

4,4-dimethyl-thiosemicarbazide (0.10 g, 0.8 mmol), 2-isopropylbenzaldehyde (0.12 g, 0.8 mmol). White powder. **Yield**: 80% **^{1}H-NMR** (δ, ppm, DMSO-D_6): 1.22 (d, J = 6.7 Hz, 6H, H_h), 3.01 (m, 1H, H_g), 3.29 (s, 6H, H_a), 7.27 (m, 3H, H_e, H_f), 7.85 (m, 1H, H_d), 8.14 (s, 1H, H_c), 10.94 (s, 1H, H_b) **ATR-FTIR** (cm^{-1}): 3395 (m) ν (NH); 3307 (m) ν ($CH_{aromatic}$); 2921 (m) ν ($CH_{aliphatic}$); 1592 (m) ν (CN); 829 (m) ν (CS) **ESI-MS** m/z calc. 249.38 found 249.44.

PART TWO

Ruthenium(II) photoactivatable half-sandwich complexes: a flexible molecular scaffold for photoactivated chemotherapy (PACT)

8 Introduction

In the first part of this thesis, I explained the way of action of cisplatin and its derivatives with the drawbacks associated with these platinum complexes. Subsequently, I explained how thiosemicarbazones and their metal complexes are compounds of interest for the treatment of cancer. Herein, I will present the synthesis and the biological activity of new ruthenium(II) photoactivable metal complexes.

8.1 Ruthenium: an overview

Ruthenium [72] is the element with 44 atomic number and $[Kr]4d^7 5s^1$ electronic configuration. It is a rare transition metal belonging to the platinum-group metals and like the other elements of this group is a hard and white metal. In nature it has seven stable isotopes ^{96}Ru, ^{98}Ru, ^{99}Ru, ^{100}Ru, ^{101}Ru, ^{102}Ru and ^{104}Ru, with a relative abundance of 5.54, 1.87, 12.76, 12.60, 17.06, 31.55, and 18.62%, respectively. Two of these isotopes, ^{99}Ru and ^{101}Ru, are NMR active with a nuclear spin of 5/2. The quadrupolar behavior of these nucleus, associated with a low resonance frequency, has prevented a general study of the NMR spectroscopy of these nuclei, though there are some examples [73,74]. Ruthenium has a wide range of oxidation states, of whom the most common are +2, +3 and +4. The higher oxidation states, like +6 and +8, requires the most electronegative elements, fluorine, and oxygen, for stability.

Ruthenium is one of the most relevant elements in the field of catalysis. The coordination and organometallic chemistry of this element is well known thanks to the large number of ruthenium complexes synthesized, provided several oxidation states, coordination numbers, and geometries. Two of the main features that make this element the preferred choice for many catalytic processes is the low price, if compared with the other platinum-group metals, and the low toxicity of the ruthenium compounds.

Ruthenium is not strictly used in the catalysis field. In fact, since at the 1990s the organometallic complexes of ruthenium have moved into medicinal inorganic chemistry like anticancer compounds.

8.2 Ruthenium anticancer compounds

In the last years, a wide range of metals, like palladium, iridium, rhodium, ruthenium, tin, copper, and gold, [75] are studied to overcome cisplatin and its derivatives and to obtain new anticancer metal complexes that combine a good activity against the tumor cells with a low toxicity and less side effects. With this try and error approach, ruthenium compounds turned out to be the most promising ones [76]. The first characteristic that makes ruthenium(II) complexes an interesting class of compounds is the kinetic of the exchange of ligand in aqueous solution. In fact, for platinum(II) and ruthenium(II) complexes the ligand exchange processes are slow, in the range of hours (rates 10^{-3} to 10^{-2} s^{-1}) [77]. For many ruthenium compounds this slow kinetic is associated with a low toxicity and a good selectivity for cancer cells [78, 79]. This selectivity, according to the literature, [80, 81] is due by the similarity of ruthenium with iron. The cancer cells overexpress transferrin receptors because they need a great amount of iron for their metabolism and ruthenium anticancer

compounds (remembering that ruthenium is in the group of iron) may use this receptor to interact selectively with the cancer cells.

The first isolated ruthenium complexes with an interesting biological activity are the chloro-ammine complexes [82]: in 1976 Durig observed that the ruthenium(III) complex fac-$Ru(NH_3)_3Cl_3$ caused the same effects on E. coli cells seen for cisplatin. Subsequently, this complex and its related ruthenium(II) complex cis-$Ru(NH_3)_4Cl_2$ were studied for their anticancer activities. They show a good activity but a low solubility, that avoid their application like a drug [83, 84]. It has been demonstrated [84] that Ru(II) complexes are coordinated more rapidly by biomolecules. This is due by the inaction of the oxidation state +3 respect to the ligand exchange reaction. In fact, the aquation of the ruthenium complexes is accelerated with the reduction of Ru(III) into Ru(II), leading to an increased biological activity. This series of information brought Clarke [84] to propose the "activation-by-reduction" hypothesis. In this hypothesis, the Ru(III) complexes work like prodrugs that are activated preferentially in the less oxygenated environment of solid tumors [85]. Herein, the presence of reducing agents, like glutathione, and the hypoxia conditions (low concentrations of O_2) promote the reduction of the ruthenium.

The first step ahead in the field of the ruthenium anticancer compounds is due by the introduction of the imidazole and the indazole ligands. Keppler and coworkers [86] synthesized two isoelectronic ruthenium(III) complexes: [imiH]trans-$[Ru(N\text{-}imi)_2Cl_4]$ and [indH]trans-$[Ru(N\text{-}ind)_2Cl_4]$ (imi = imidazole, ind = indazole). The major advantage of those complexes is the activity against platinum-resistant colorectal autochthonous tumors.

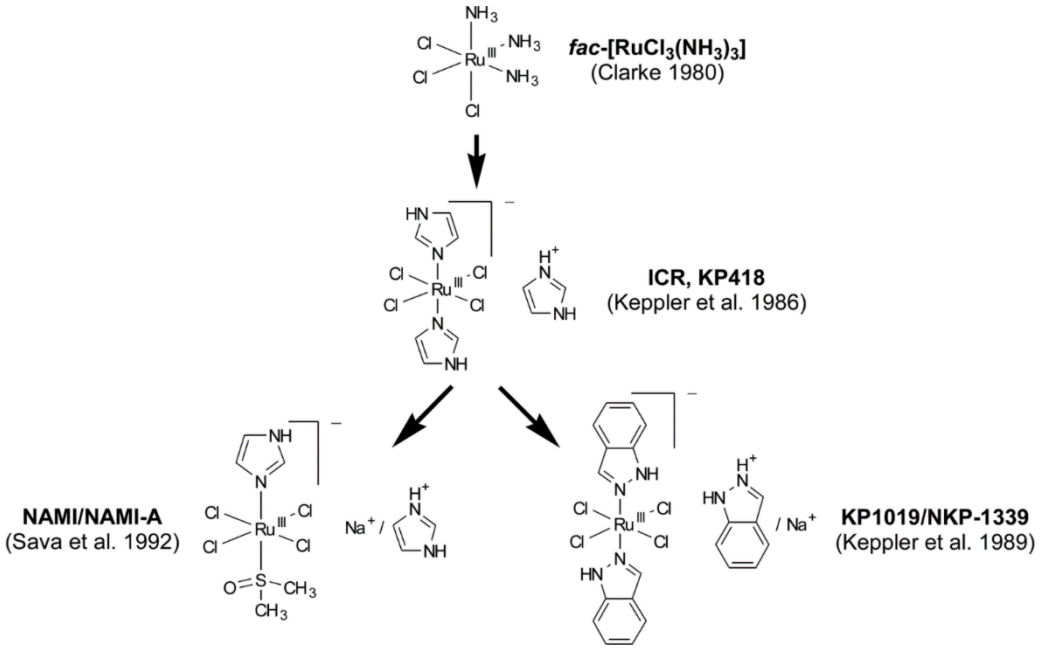

Figure 35 Genealogy of tumor-inhibiting ruthenium complexes [87].

Another type of ruthenium(III) complex with a good biological activity is trans-$[Ru(N\text{-}imi)(S\text{-}dmso)Cl_4]^-$ synthesized by Alessio and Sava [88]. This complex is specifically active against solid metastasizing tumors in mice. In figure 35 are presented the ruthenium(III) complexes and their structural similarity.

A second generation of antitumoral and antimetastatic ruthenium complexes are represented by the organometallic ruthenium(II) arene. The structure of these complexes is characterized by a η^6-coordinated arene ligand, directly connected with ruthenium and able to stabilize the +2 oxidation of the metal. The pioneers of this type of complexes are Dyson [89] and Sadler [90] (figure 36).

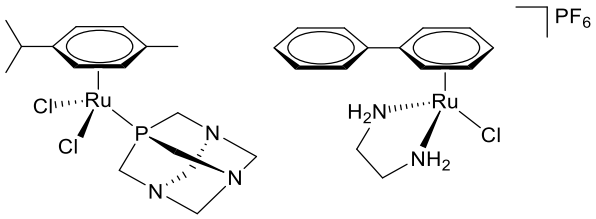

RAPTA-C **RAED**

Figure 36 Structure of the ruthenium arene complexes synthesized by Dyson and Sadler.

The biological activity of these two ruthenium complexes is exerted through the release of one or more chloride ligands [91]. The target of RAED is the DNA: in fact it can coordinate it through the N7 of guanine residues [92]. Instead, RAPTA can interact with multiple biological targets, like DNA and histone proteins [92].

8.3 Photochemistry of the ruthenium complexes: an overview

The low selectivity of the metal-based drugs is the principal hindrance for an extensive use in medicine. A way to overcome this problem is the drug delivery, i.e., the use of carriers (generally biomolecules or biomimetic molecules) able to transport the drug to the cancer cells, exploiting specific receptors [93]. Another mechanism is the introduction of a prodrug, showing no biological activity until the activation into the corresponding toxic compound, i.e., the drug [94]. The activation of a prodrug can be achieved by a stimulus of two different origins: an internal one (reducing environment within the cells, enzymatic reactions, hypoxia, etc.) or an external one (temperature, magnetic field, light, etc.). The main drawback of an internal stimulus mediated activation is the reliance on intracellular parameters, i.e., when injected inside the body there is no possible control over the fate of the compound [95]. This unpredictable behavior can lead to undesired side effects. On the other hand, an external stimulus mediated activation provides complete spatial and temporal control over the generation of the actual toxic pharmaceutical. One of these external impulses is the use of light for the prodrug activation. To date, two light-dependent medical techniques have been developed in the field of anticancer research: the photodynamic therapy (PDT) and the photoactivated chemotherapy (PACT).

8.4 Photochemistry of the ruthenium complexes: a short quanto-mechanic guide

The light irradiation of a ruthenium complex can induce different transitions, with the formation of different excited states. To understand the photochemical transitions and transformations it's necessary represent which MOs of the complex are involved. For ease, I represent the well-known photoactivable ruthenium(II) complex $[Ru(bpy)_3]^{2+}$ (figure 37).

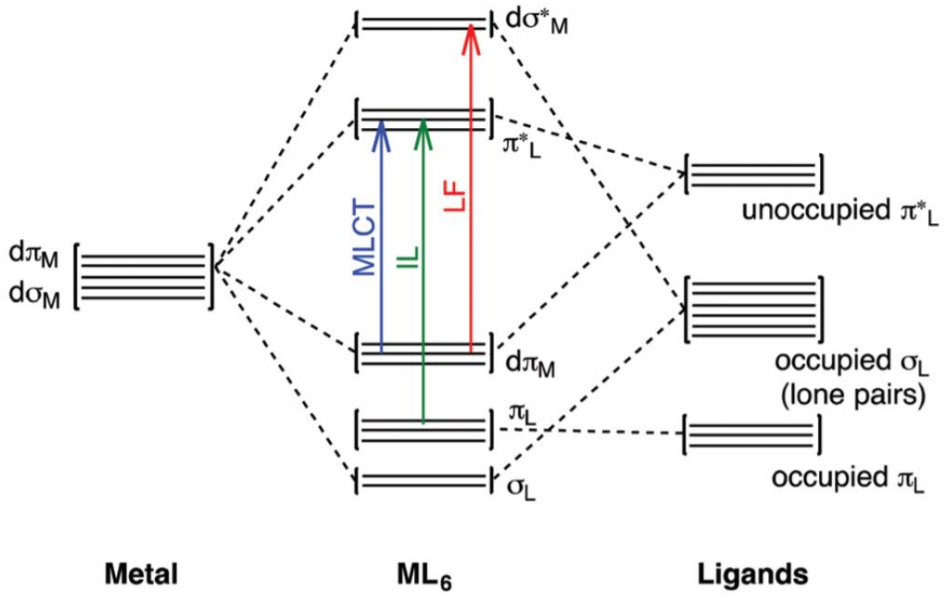

Figure 37 Simplified molecular orbital diagram for an octahedral Ru(II)compound with polypyridyl ligand [96].

Herein, the metal complex can befall to several transitions:

- **Metal-centered (MC) transitions (d-d or ligand-field (LF) transitions).** These transitions involve electronic promotion between orbitals that are predominantly metal d-orbital in character, leading to the population of metal-centered ligand field (LF) excited states.
- **Charge-transfer (CT) transitions (metal-to-ligand (MLCT), ligand-to-metal (LMCT).** These transitions involve redistribution of charge which can be characterized by the promotion of an electron from an orbital prevalently of the ligand to one largely metal in character (LMCT), or by the opposite process (MLCT).
- **Ligand-centered (LC) transitions (or interligand (IL) transitions).** These transitions involve electronic promotion between ligand-centered orbitals (i.e. π to π*).

Once these excited states are generated, deactivation can happen by means of different pathways:

- **Radiationless processes:** intersystem crossing (ISC), internal conversion (IC) vibrational relaxation.
- **Radiative processes:** fluorescence (singlet–singlet) and phosphorescence (triplet– singlet).
- **Photochemical reactions:** ligand dissociation, redox processes etc.

The most interesting deexcitation process, for the aim of this chapter, is the ligand dissociation.

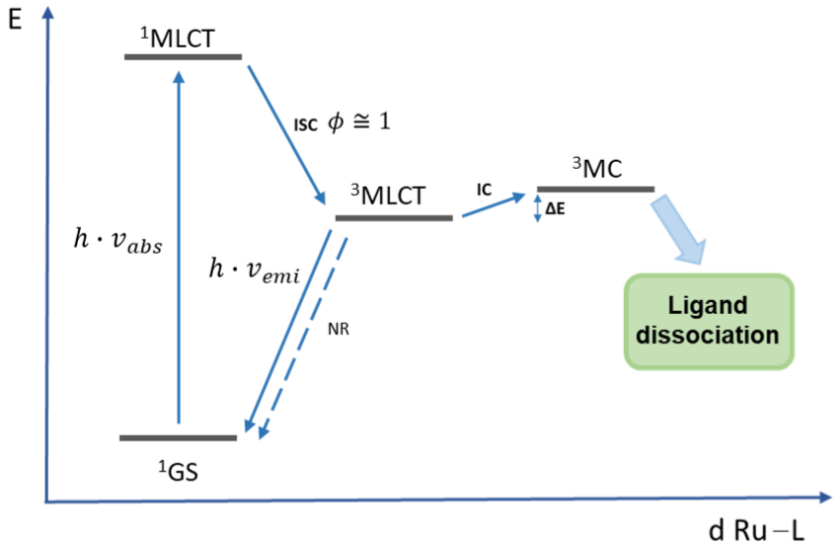

Figure 38 Energy level diagram for a photoactivable Ru(II) complex. After the absorption of a photon, an electron can be promoted from the ground state to the ^{1}MLCT state. ISC=intersystem crossing, IC= internal conversion, NR=non radiative, ΔE= energy gap between ^{3}MLCT and ^{3}MC state [97].

The photoexcitation results in the population of the singlet metal-to-ligand charge-transfer (^{1}MLCT) state, followed by efficient intersystem crossing (ISC) to the long-lived triplet ^{3}MLCT state. From the ^{3}MLCT state a triplet metal-centered state (^{3}MC) is thermally accessible depending on the energy separation of the two states and the temperature [98, 99]. In particular, these excited states are obtained when an electron from a t_{2g} orbital is promoted into a metal-ligand antibonding e_g orbital. These states have a strong dissociative character, causing the weakening of one or two coordination bonds and leading to the substitution of ligands by solvent molecules, typically water.

8.5 Photodynamic therapy (PDT)

With the name of photodynamic therapy (PDT) is defined a process where the light is in synergic action with a chemical compound (called photosensitizer, PS) and the oxygen naturally present in the cell [100].

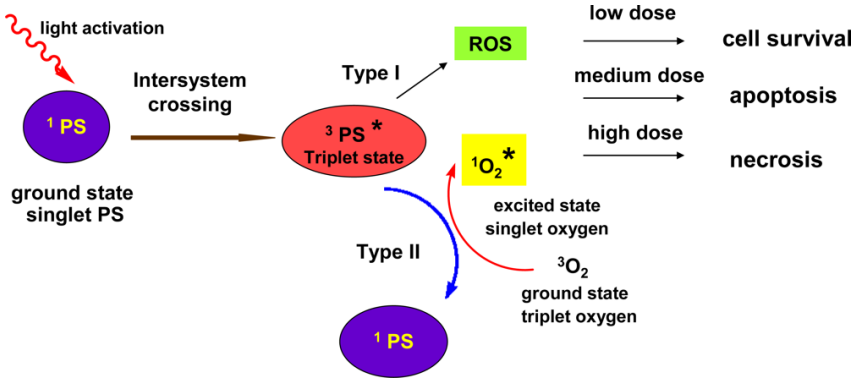

Figure 39 Mechanism of action of the PDT [101].

The activation of the PS induces the formation of ROS and the singlet oxygen, the actual biological active species. In PDT, the PS acts like a photocatalyst and may be photostable to keep the activity during the time.

These characteristics make PDT dependent on the oxygen concentration. In fact, in well-oxygenated tissues, which typically have 5–7% O_2, the PDT works very well. Instead, a lot of tumors are characterized by a suboptimal vascularization, with the formation of hypoxia regions, where O_2 concentration is very low, typically 0.1–1% [102-104]. This handicap makes PDT less appealing for a future therapeutic application of the light in medicine.

8.6 Photoactivated chemotherapy (PACT)

The term photoactivated chemotherapy (PACT) [105] is associated to a compound that is able to change its molecular structure through the light. Theoretically, the non-irradiated form of this PACT compounds is in a "caged" form and unable to have biological activity. Subsequently, with the irradiation, the structure of compound may change in the "uncaged" form with the increasing of the biological activity. The change of structure of a PACT compound can be due by the presence of a bond light-cleavable that, with the irradiation, releases new species with a strong biological activity, for example species specifically active against biological molecules, like DNA or proteins (figure 40). In principle, both the photoreleased products, i.e., the ligand and the metal-based photoproduct, may be the source of the biological activity. However, this biological activity is generally due by the metal-containing photoproduct [106, 107].

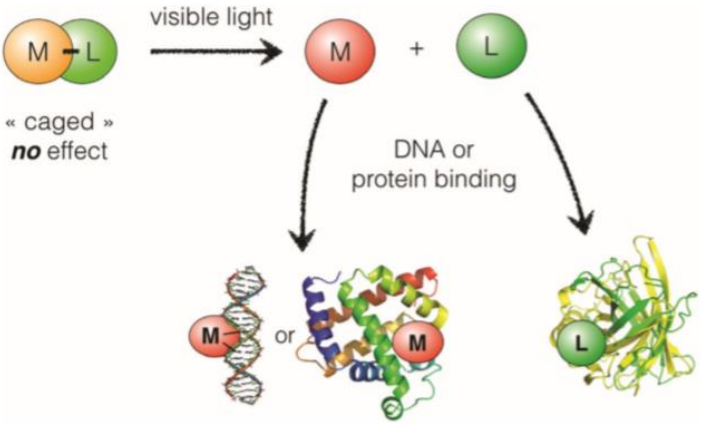

Figure 40 General principle of PACT [105].

In that way, the photoactivation of a prodrug is completely untied respect to the concentration of O_2, allowing the treatment of hypoxia regions of a tumor with a photoactivable compound.

8.6.1 Examples of PACT Ru(II) complexes: polypyridyl derivatives

The polypyridyl ruthenium(II) complexes are a well-known class of compounds able to produce singlet oxygen and other ROS, usable in the PDT. However, ruthenium complexes don't have a prominent position in PDT. The reactivity that make Ru(II) complexes unique and different from other metal-containing compounds is the ability to photo substitute ligands. This reactivity was initially discovered like a decomposition pathway of the $[Ru(bpy)_3]^{2+}$ (bpy = 2,2'-bipyridine) [108] and subsequently used in supramolecular chemistry and for biological application.

For the ruthenium(II) polypyridyl complexes the transition ^{3}MLCT $\longrightarrow$ ^{3}MC is possible only if there is a steric hindered ligand that induces a distortion in the octahedral geometry of the complex [109]. In other hand, in the unstrained ruthenium(II) polypyridyl complexes the population of the ^{3}MC state is inefficient due to the large energy gap between the ^{3}MLCT and ^{3}MC, resulting mainly in emission from the ^{3}MLCT state and a minimal dissociation. The geometric distortion can be achieved if the polypyridyl complex bears a ligand methylate in the position close to the N-N chelate center. The methyl groups are directed towards the other coordinating ligands, causing steric clashes. Complexes with general formula $[Ru(bpy)_2(NN)]^{2+}$, where NN= Me_2bpy, Me_2dpq, or Me_2dppz undergo to the substitution of the hindered methylate bidentate ligand upon illumination (figure 41).

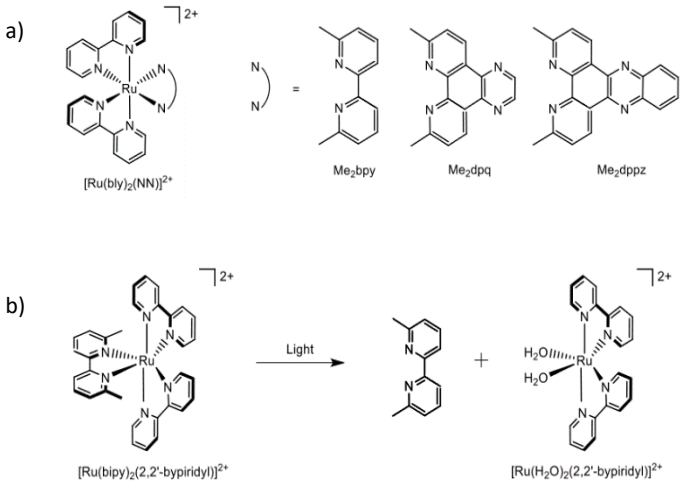

Figure 41 a) examples of ruthenium(II) polypyridyl complexes sterically hindered b) photodissociation process [110].

8.6.2 Examples of PACT Ru(II) complexes: organometallic arene derivatives

A second class of ruthenium complexes useful in the PACT are the organometallic arene complexes. As described above, in these complexes there is a direct bond carbon-ruthenium in which the carbon is represented by an arene coordinated with an hapticity η^6.

The photochemistry of this class of complexes is well-known in literature [111-113], in fact the half-sandwich complex $[(CH_3CN)_3Ru(\eta^5\text{-}C_5H_5)]^+$ is obtained through the irradiation of the sandwich complex $[(\eta^6\text{-}C_6H_6)Ru(\eta^5\text{-}C_5H_5)]^+$ in acetonitrile.

The typical half-sandwich complexes applied in bioinorganic chemistry are characterized by the general formula $[(\eta^6\text{-arene})Ru(XY)(Z)]^{n+}$ where X and Y are generally two monodentate ligands or two donor atoms of a chelate ligand and Z is a leaving group, typically an halogen. How explained in the case of RAED [91], the activity of this class of complexes is associated with the aquation of the Ru-Z bond, generating more reactive aqua species [114, 115]. Moreover, the presence of a bidentate chelating ligand through the linking of the ligands X and Y, provides additional stability to the whole structure and seems to be advantageous for anticancer activity [116].

Sadler and co-workers [116, 117] have developed a different strategy to increase the biological activity of the half-sandwich organometallic ruthenium(II). They have developed a new class of photoactivatable

compounds able to release the monodentate ligand Z by irradiation, with the consequent formation of the aqua adduct. The general formula of this class of compounds is $[(\eta^6\text{-arene})Ru\text{-}(N,N')(L)][PF_6]_2$, where N,N' is a bidentate chelating ligand and L is a pyridine or a pyridine-like ligand that can be selectively dissociated upon photoirradiation.

The progenitor of this class of compounds is the complex $[(p\text{-cym})Ru(bpm)(py)][PF_6]_2$, where the bidentate is a 2,2'-bipyrimidine, the arene is a para-cymene and the monodentate is a pyridine. In figure 42 is presented the mechanism of action of this complex, in which the blue light induces the photodissociation of the pyridine, the monodentate ligand, with the subsequently formation of the aqua complex. This complex is able to interact with the DNA through a guanine residue [117].

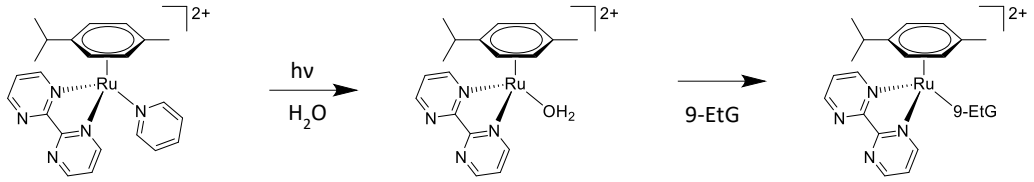

Figure 42 Structure, photodissociation mechanism and binding of the 9-EtG [117].

These results have promoted the synthesis of a panel of molecules [118] with the same structure of the previous complex but characterized by different arenes, chelates and monodentate ligands. All the complexes obtained are characterized by a good stability in aqueous solution, in dark, and the ability to release the monodentate ligand under a white lamp. These information suggest that the general structure $[(\eta^6\text{-arene})Ru\text{-}(N,N')(L)]^{2+}$ can be a useful scaffold to build new photoactivatable complexes with different and more elaborate ligands.

The mechanism proposed with whom these complexes get in the cells is present in literature [91]. These ruthenium(II) complexes have the interesting feature to be amphiphilic, because they combine the hydrophobic behavior of the arene moiety with the hydrophilicity of the metal center. This characteristic makes these complexes more able to pass the cell membrane with passive diffusion.

9 New photoactivatable Ru(II) complexes with naphthalenimides and pyridine derivatives as ligands

9.1 Naphthalenimides: an overview

Naphthalenimides (NIs) are a class of organic molecules well known in literature characterized by a planar structure with a high electronic delocalization among the naphthalene moiety and the imide. This feature makes NIs very useful in different fields of chemistry, like anticancer drugs [119], in labeling and sensing [120] and smart materials [121].

The planarity of NIs makes them strong DNA intercalators and, for this reason, extensively studied in medicinal chemistry. The most promising candidates in the cure of cancer are Amonafide and Mitonafide (figure 43) that obtained the FDA approval for the treatment of Secondary Acute Myeloid Leukemia.

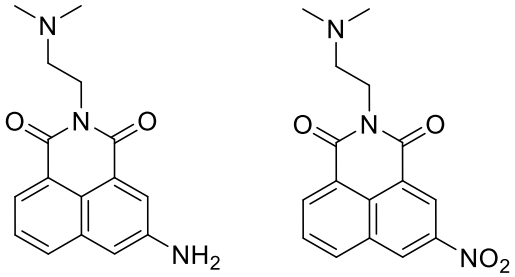

Amonafide Mitonafide

Figure 43 Structures of Amonafide and Mitonafide.

9.2 Naphtalenimides: a different synthetic approach for their insertion in Ru(II) complexes

A key characteristic that makes NIs very appealing is the simplicity of functionalization and the possibility, with the right functionalization, to bind metal ions. In literature [122] are present several ruthenium(II) arene complexes with NIs, functionalized with a pyridine, like monodentate ligands. In that case the complexes are not completely caged, as in the case of the Sadler's complexes [118], but with two chlorides instead of a chelate ligand.

In our laboratory, it was developed a new synthetic way to introduce more elaborate ligands to expand and explore the photochemistry and the photobiology of the ruthenium complexes. This synthetic route is reported in figure 44 and is characterized by the insertion of the monodentate ligand before the bidentate ligand. This means that the order of insertion of the ligands is inverted respect to the Sadler's strategy. This inversion is necessary when ligands more complex than pyridines are used, because the Sadler's strategy requires very large excess of the monodentate ligand (10-20 equivalents) with serious problems in the purification of the products and in the recovery of the non-reacted ligand. Instead, with our strategy, the reagents are used in stoichiometric quantities.

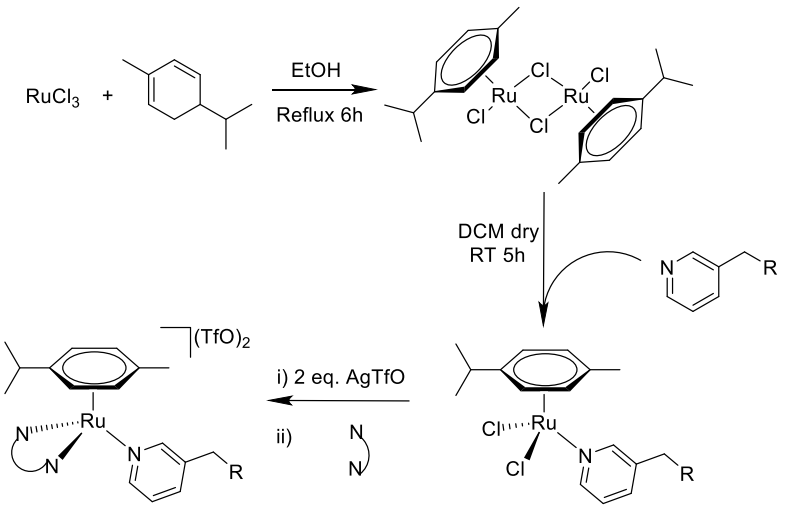

Figure 44 Synthetic route used for all the complexes presented in this chapter.

This multistep synthesis is divided in three parts:

Synthesis of the ruthenium dimer $[(\eta^6\text{-p-Cym})RuCl_2]_2$.

The ruthenium p-cymene dimer is synthesized in degassed ethanol reacting $RuCl_3 \cdot nH_2O$ with an excess of α-phellandrene for 6 hours. The pentane is added to precipitate the product which was collected by filtration.

Insertion of the monodentate ligand.

In this step, two equivalents of monodentate ligand are mixed with one equivalent of ruthenium dimer in dry dichloromethane under nitrogen. The intermediate complex formed is neutral.

Insertion of the bidentate ligand.

The final step can be divided in two sections: the halogen scavenging and the insertion of the bidentate ligand.

Firstly, the intermediate complex obtained in the previous step is mixed with two equivalents of silver triflate. The aim is the scavenging of the chlorides, with the formation of AgCl, and their substitution with the triflates, non-coordinating anions.

Secondly, there is the effective insertion of the bidentate, exploiting the chelate effect. The final complex is bi-cationic in which two triflate anions neutralizes the positive charges of ruthenium without interfering with the metal coordination.

All the complexes present in this chapter are obtained following this synthetic route.

9.3 Photochemistry and photobiology of Ru(II) complexes with naphthalenimides like monodentate ligands: C1, C2 and C3

The first three ligands used are naphtalenimides with a pyridine in the amide moiety (Figure 45). This functionalization is obtained with the reaction of the respective naphthalene anhydride with 3-picolylamine (the different synthetic conditions are presented in the experimental section for L1, L2, L3 and L4). The structural differences are in the naphthalene moiety: L1 is devoid of functionalization, L2 has a strong electron withdrawing group in the position 3 of the naphthalene and L4 has a strong electron donating group in the position 4 of the naphthalene.

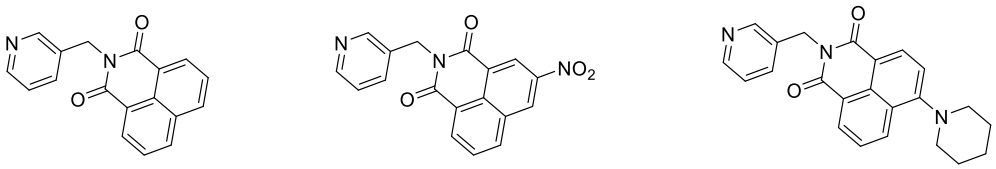

L1 L2 L4

Figure 45 Structures of the ligands L1, L2 and L4.

The functional groups, in the naphthalene moiety, of the ligands L2 and L4 are not casual. In fact, the type of substituents and their position respect to the amide, are responsible of the different photophysical properties of the naphthalenimides [123].

The presence of a strong electronic withdrawing group like the nitro group, as well as the imides, leads to an increase of the energy of the excited states. On the other hand, the positioning of an electron donating group in para position respect to the amide, brings to a shift of the maximum of absorption in the blue region, with the formation of a large band between 400 nm and 500 nm. This shift is due by a "push-pull" effect due by an internal charge transfer (ICT). The piperidine, like substituent, has been chosen because the molecule L4 is present in literature [124] and used like a conformer for fluorescent cocrystals.

The ligands L1, L2 and L4 are used for the synthesis of the complexes C1, C2 and C3, presented in figure 46. The bidentate ligand used is a bipyridine.

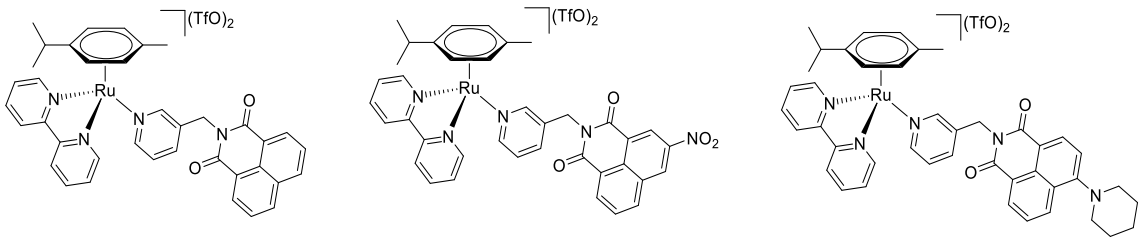

C1 C2 C3

Figure 46 Structures of the complexes C1, C2 and C3.

9.3.1 Absorption and emission spectra: C1, C2 and C3 and related ligands

The different functionalization of the naphthalene moiety bears to a shift of the maximum of absorption. In figure 47, the absorption spectra of the three ligands are compared. L1 and L2 are characterized by a maximum of absorption in the UV region. Instead, L4, thanks to the "push-pull" effect, has a maximum in the blue region, specifically at 418 nm.

In the same conditions, the absorption spectra of the three complexes are obtained and compared in figure 48. Herein, the maximum of absorption of the complex spectra is the same of their monodentate ligands. C1 and C2 have the maximum of absorption in the UV region, like L1 and L2, while C3 absorbs in the blue region, with the maximum still at 418 nm, like L4.

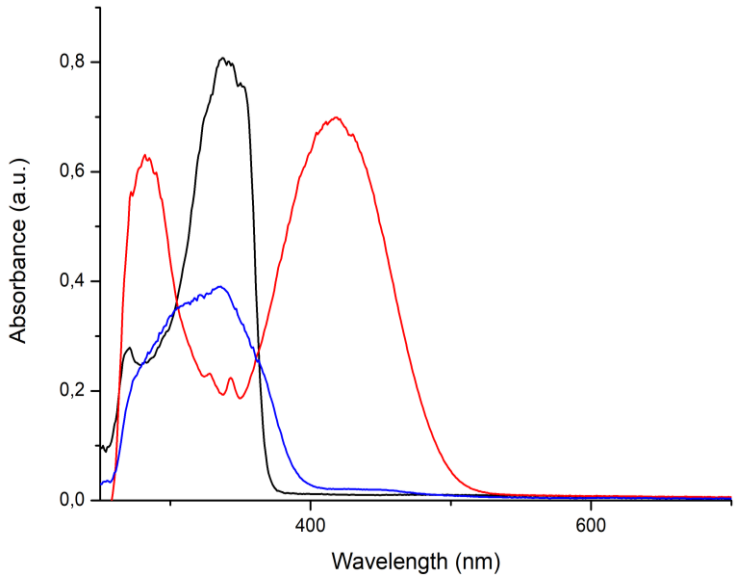

Figure 47 Absorption spectra of L1 (black line), L2 (blue line) and L4 (red line). The spectra are performed in DMSO at 100 µM.

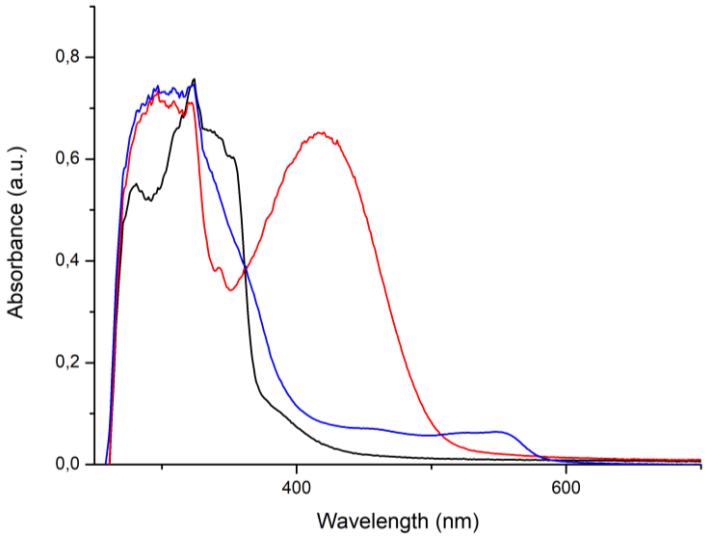

Figure 48 Absorption spectra of C1 (black line), C2 (blue line) and C3 (red line). The spectra are performed in DMSO at 100 µM.

The next step, once obtained the UV-visible spectra, is the measurement of the emission spectra. In that case the two complexes C1 and C2, as well as their ligands L1 and L2, are excited with the same wavelength, at 370 nm, in the UV region. Instead, for the complex C3 and its ligand L4 I explored how to change the emission using an excitation wavelength of 418 nm. I focused my attention only in this excitation wavelength, for the couple L4/C3, because is the unique maximum located in the blue region and the most interesting.

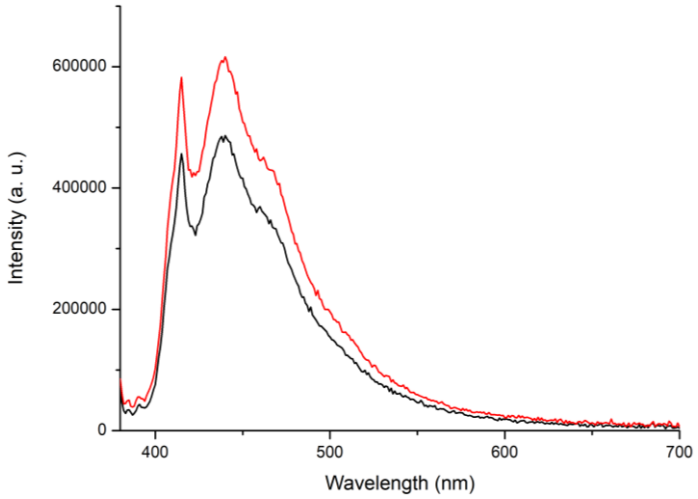

Figure 49 Emission spectra of L1 (black line) and C1 (red line). The spectra are performed in DMSO at 10 µM with a λ_{ex} = 370 nm.

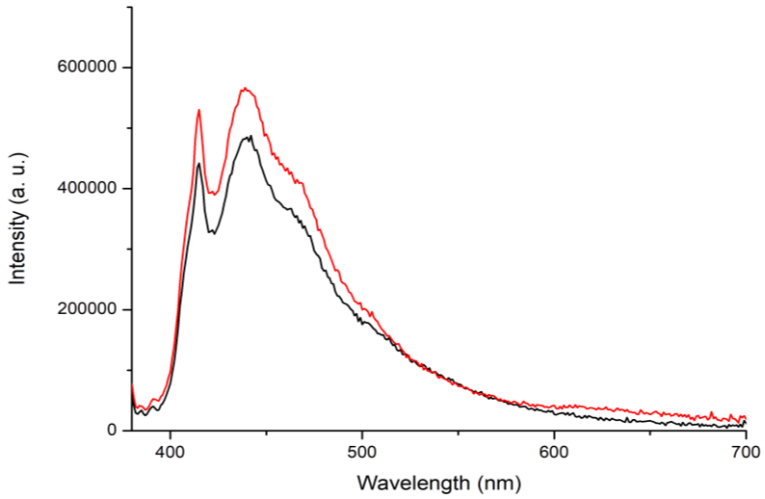

Figure 50 Emission spectra of L2 (black line) and C2 (red line). The spectra are performed in DMSO at 10 µM with a λ_{ex} = 370 nm.

In figures 49 and 50 are compared the emission spectra of the two couples L1/C1 and L2/C2, in the same conditions. In both the cases the complexes have an emission band that is slightly more intense respect to the ligand alone. For the couple L4/C3, instead, the emission of the complex is significantly less intense than the ligand (figure 51).

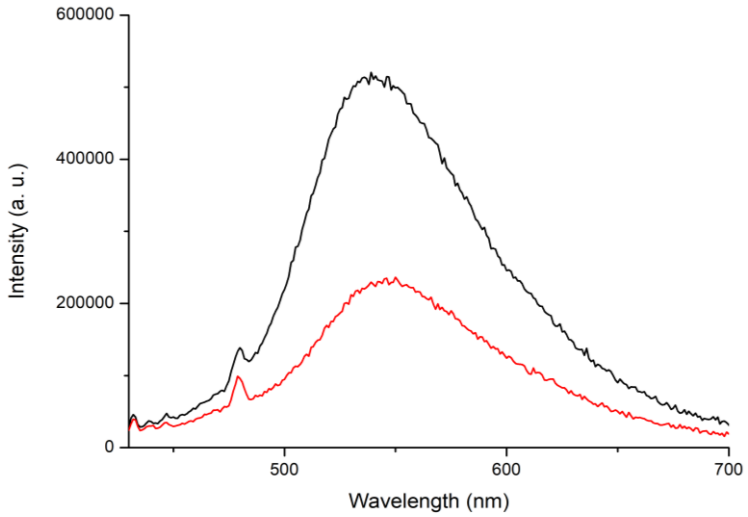

Figure 51 Emission spectra of L4 (black line) and C3 (red line). The spectra are performed in DMSO at 10 µM with a λ_{ex} = 418 nm.

This behavior can be ascribed by a radiationless mechanism of deactivation of the excited state, that is preferred respect to the emission of photons. How described above, the radiationless pathways can be various: intersystem crossing (ISC), internal conversion (IC), vibrational relaxation and the ligand dissociation.

In table 7 are resumed the spectroscopic properties.

Compounds	λ_{abs} (nm)	λ_{em} (nm)	[b]ε (M^{-1} cm^{-1})	[c]Φf
L1	337	[a]440	7685	0,046
C1	324	[a]440	6392	0,030
L2	336	[a]440	3517	0,051
C2	323	[a]440	7121	0,225
L4	418	550	7020	0,060
C3	418	550	6543	0,027

Table 7 (a) the emission wavelength is referred to an excitation wavelength of 370 nm (b) molar extinction coefficient is calculated on the maximum of absorption (c) quantum yield is obtained using quinine sulfate like reference. The excitation wavelength is still 370 nm.

9.3.2 Stability in the dark: C1, C2 and C3

The key aspect that makes the PACT compounds interesting is their ability to release a ligand only when the complex is irradiated. For this reason, the stability, in the dark and in physiological conditions, is a crucial preliminary step that must precede the photoactivation experiments to prove that the drug is activated only by light and not by other components in the environment.

The biological activity of these compounds is performed by dissolving the target complex in DMSO, forming a stock solution subsequently diluted in the cell medium. The DMSO concentration must be lower than 2% because it has a harmful effect on the cell [125]. Hence, the stability has been performed using a mixture of an aqueous solution, 98%, and DMSO, 2%, in which the complex is dissolved. The aqueous solution used is not the cell medium because is an extremely complex water mixture and problematic to use outside of biological laboratory. For this reason, I used an aqueous solution of PBS (phosphate-buffered saline) that maintain a

constant pH, similar to the cell's environment, with the presence of salts. The stability is evaluated by means of UV-visible spectroscopy comparing the absorption spectra along the 24 hours. The solution is maintained at 37°C in the dark. In figures 52, 53 and 54 are presented the results of this stability studies.

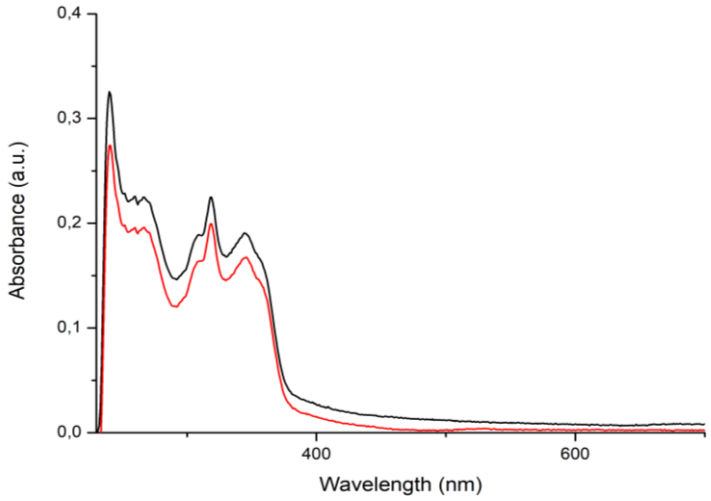

Figure 52 Stability of the complex C1. Comparison between time zero solution (black line) with the same solution after 24 hours of incubation at 37°C in the dark (red line). Concentration of the complex is 20 µM, concentration of PBS buffer is 10 mM and the pH is 7.4. The solution is a mixture of an aqueous solution of PBS, 98%, and DMSO, 2%.

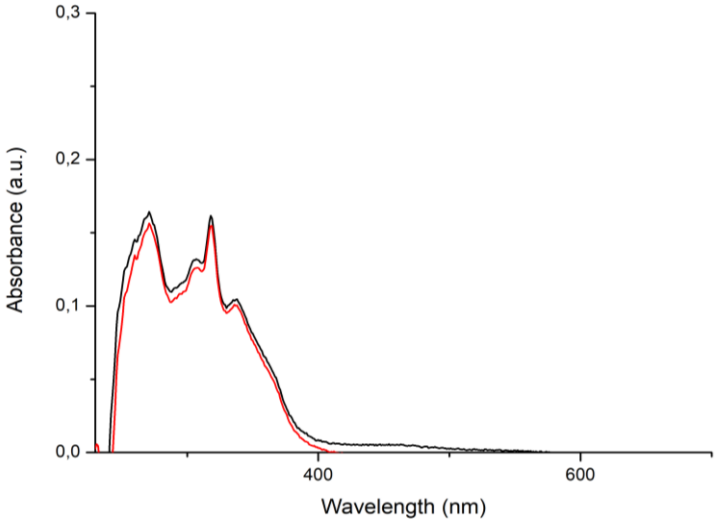

Figure 53 Stability of the complex C2. Comparison between time zero solution (black line) with the same solution after 24 hours of incubation at 37°C in the dark (red line). Concentration of the complex is 20 µM, concentration of PBS buffer is 10 mM and the pH is 7.4. The solution is a mixture of an aqueous solution of PBS, 98%, and DMSO, 2%.

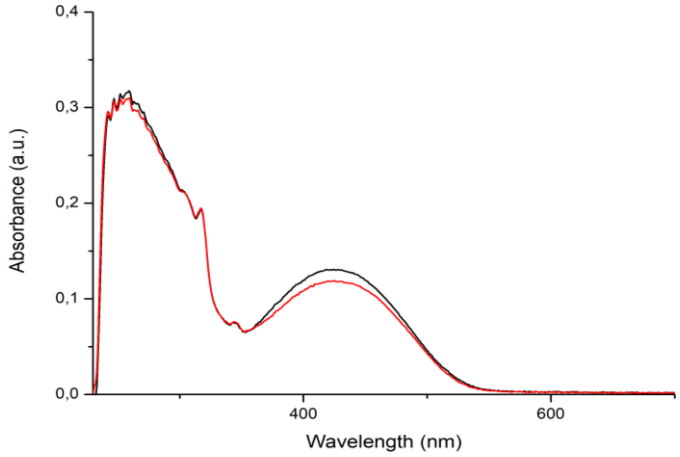

Figure 54 Stability of the complex C3. Comparison between time zero solution (black line) with the same solution after 24 hours of incubation at 37°C in the dark (red line). Concentration of the complex is 20 µM, concentration of PBS buffer is 10 mM and the pH is 7.4. The solution is a mixture of an aqueous solution of PBS, 98%, and DMSO, 2%.

The three complexes are stable in the physiological conditions, with no considerable change during the 24 hours.

9.3.3 Photoactivation experiments: an overview on the setup

The last step before the application in cell of the Ru(II) complexes is the study of the photoactivation with NMR, to better understand the molecular modification induced by the light. The problem of which type of light can be used and how apply this light in the target tissue is not simple. In figure 55 is represented the position of the phototherapeutic window. In this range of wavelengths, between 650 nm and 850 nm, the absorption of the components of human tissues and cells is minimum. The wavelengths of the phototherapeutic window are also slightly energetic, with a low toxicity on the cells. The principal problem is the development of complexes able to absorb in this range. In fact, they usually absorb in the UV or blue region. A strategy to overcome this problem can be the application of the light inside the body of the patient through devices like optical fibers [126]. Obviously, the application of light in the visible window is better, for its lower energy, respect to the light in the UV region.

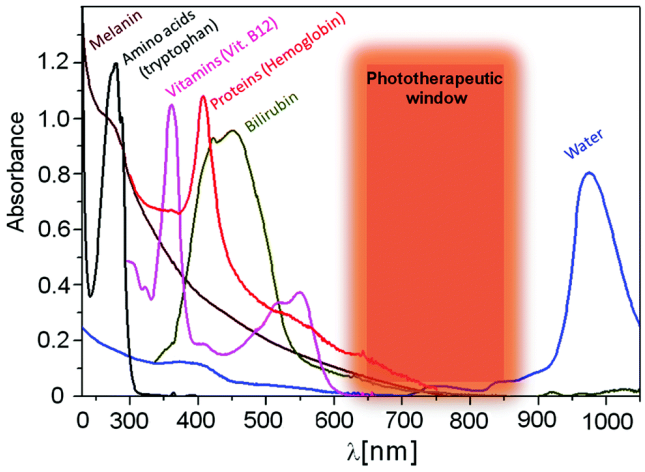

Figure 55 Absorption spectra of the typical components of the human tissues and cells [127].

The ligands and the complexes here described are not enough delocalized to have an absorption band in the phototherapeutic window. For these complexes, I used for the photoactivation experiments a LED blue light centered at 420 nm, with a light intensity of 405 $\mu W/cm^2$. The same lamp was then used for the photoactivation in cell.

The photoactivation experiments are performed in a "photo-oven" built in the lab, illustrated in figure 56. The "photo-oven" consists in a plastic box with a light source inside which can be regulated from the outside through a switch. A lid ensures that the box is completely dark when the light inside is switched off. The sample can be placed from 0 up to 25 cm from the light source and the temperature inside is controlled by a thermometer. No temperature modifications induced by the light source were registered during the experiments.

The complexes are dissolved in DMSO-D_6 during the photoactivation. This solvent was chosen because combines the coordinating behavior, necessary for the solvation of the Ru(II) complex during the photorelease of the monodentate ligand, with a good ability to dissolve the complexes in the range of concentration of the NMR experiments.

All the samples were prepared with the same concentration of 3 mM in 500 µL of DMSO-D_6. The effects of the light irradiation were analyzed by collecting five different spectra of the same sample. The "dark" spectrum was collected immediately after the sample preparation. The following spectra were collected after 1, 3, 5 and 8 hours of irradiation.

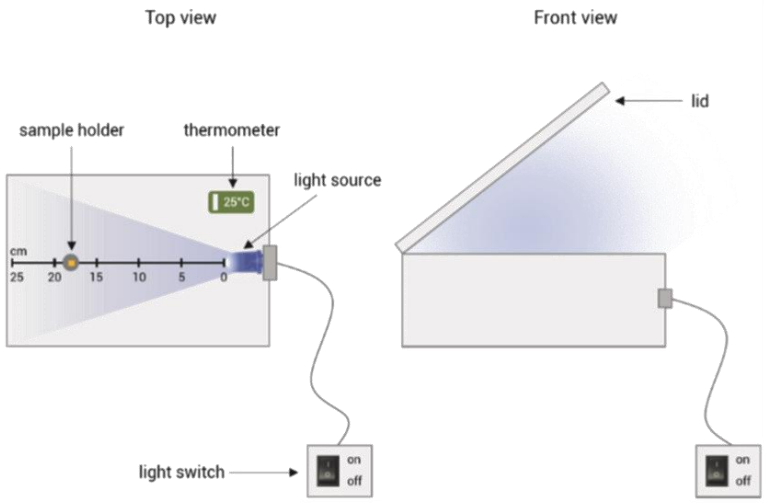

Figure 56 Illustration of the photo-oven used in the photoactivation experiments.

9.3.4 Photoactivation experiments: C1, C2 and C3

The effects of the light irradiation were analyzed by collecting five different spectra of the same sample. The "dark" spectrum was collected immediately after the sample preparation. The following spectra were collected after 1, 3, 5 and 8 hours of irradiation. The results are reported stacking the spectra in ascending order of time, in the figures 57, 58 and 59.

In the scheme 3 is presented the mechanism of photolysis and the color code used in the next figures to describe the NMR.

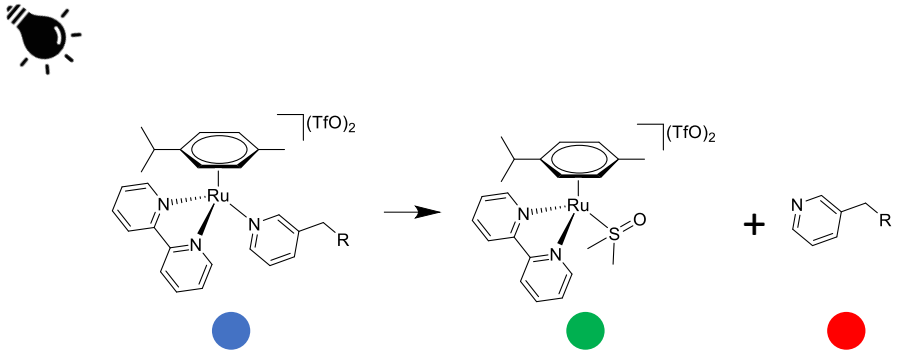

Scheme 3 Mechanism of photolysis of the complexes.

All the three complexes here reported are able to photoactivate thanks to the blue LED light. In fact, during the irradiation, the signals of the starting complex (blue spots, Figures 57, 58 and 59) are reducing their intensity and simultaneously new sets of signals are increasing their intensity. These signals are associated with the two products of the photolysis: the free naphthalenimide ligand (red spots, Figures 57, 58 and 59) and the $[(\eta^6\text{-p-cym})Ru(N,N\text{-bipy})(DMSO)]^{2+}$ (green spots, Figures 57, 58 and 59).

The free ligands are easy to recognize because their signals coincide with the signals of the naphthalenimides not involved with the complexation while the solvate ruthenium complex is detectable by the doublet at 9.43 ppm, the quadruplet at 7.10 ppm and the couple of signals close to 6.50 ppm.

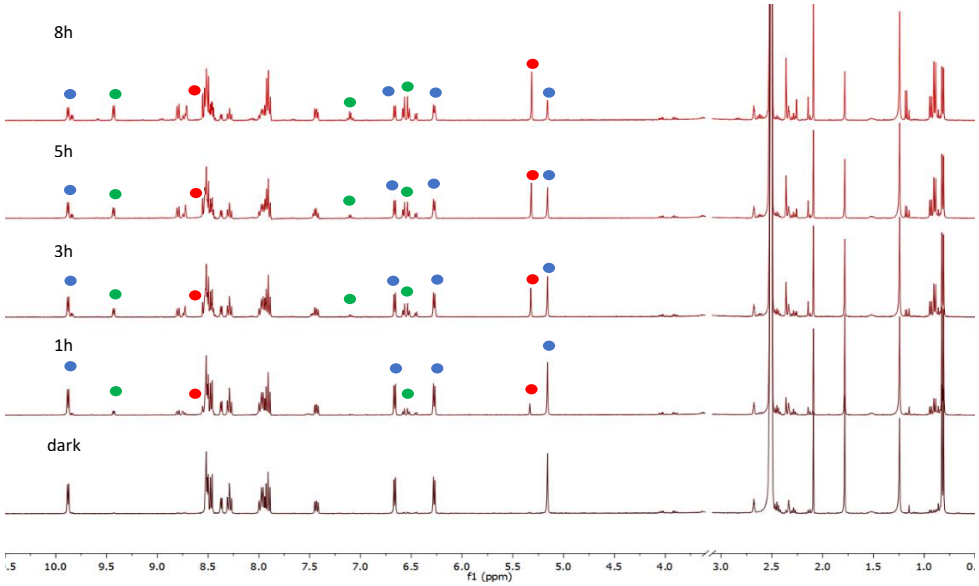

Figure 57 Photoactivation of the complex C1.

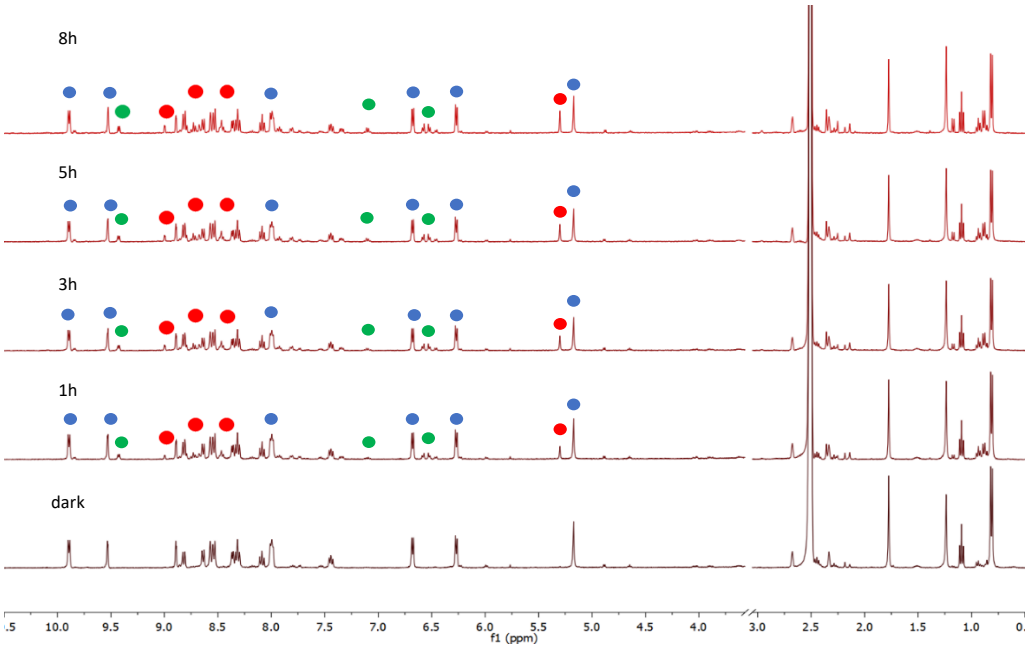

Figure 58 Photoactivation of the complex C2.

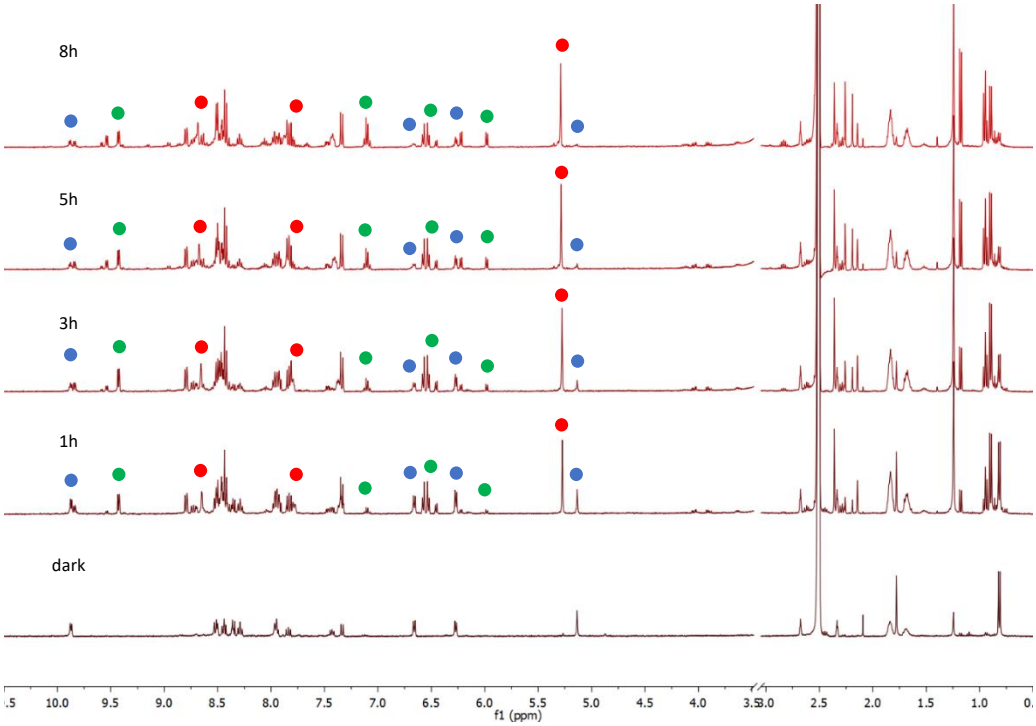

Figure 59 Photoactivation of the complex C3.

The signal that is diagnostic to understand the photolysis is the singlet of the methylene group of the naphthalimides (table 8). This signal is a singlet that shifts notably when the naphthalenimide is released by the light and for this reason is used to study the kinetics of the photolysis.

	C	L
C1/L1	5.16 ppm	5.32 ppm
C2/L2	5.17 ppm	5.30 ppm
C3/L4	5.13 ppm	5.27 ppm

Table 8 Chemical shift of the methylene group in the complexes and their ligands.

All the three complexes are able to release the monodentate ligand with the light, as explained above. The principal difference between the complexes is the rate with which the naphthalenimide is released. In fact, focusing our attention on the singlet of the methylene group of the naphthalimides (figure 60) we can observe that the difference of the rate is remarkable. After 3 hours of irradiation the complex C3 disappears while more than 50% of the complexes C1 and C2 are still present.

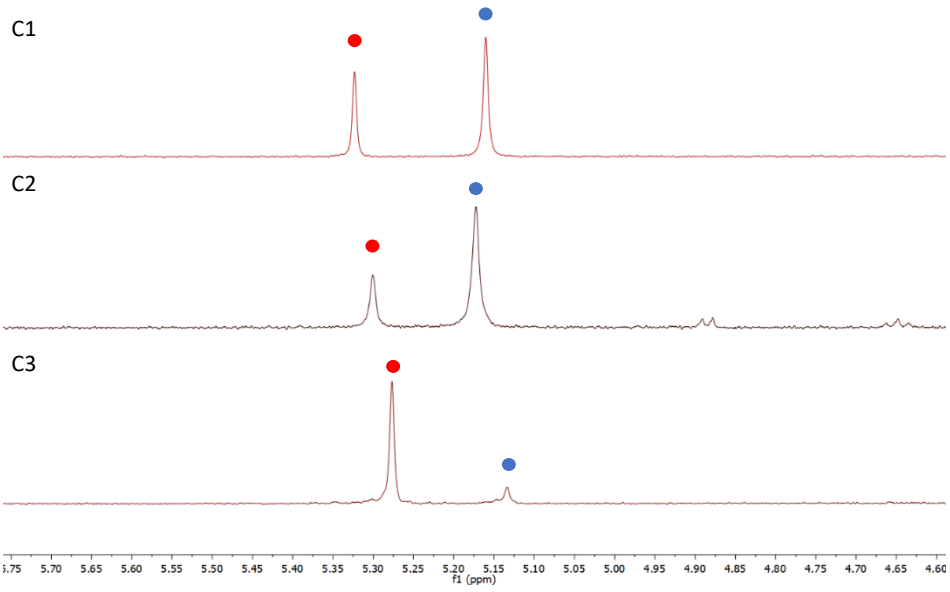

Figure 60 Comparison of the release of the naphthalenimide in C1, C2 and C3 after 3 hours of irradiation.

The next step is quantifying the amount of ligand released during the irradiation to study the kinetics and to define the order of the reaction of photolysis. First of all, I have defined a reference signal of the monodentate ligand, away to the metal center, that doesn't change during the irradiation. This reference signal is not the same for the three complexes, because the molecular structure of the three ligands is different. For the complexes C1 and C2 I used a signal related to the naphthalene moiety of the monodentate ligands (the signal at 7.43 ppm for C1 and the signal at 9.53 ppm for C2). Instead, for C3 I used one of the signals of the piperidine group at 1.84 ppm. In this way I obtained the concentration of the complexes during the time of irradiation. All the calculations are presented in the tables at the end of the thesis.

The order of a kinetics reaction can belong to three integer orders: the zero order, the first order and the second order. The order can be defined plotting the concentration of the complex in function of time, for the zero order; the natural logarithm of the concentration of the complex in function of time, for the first order; or the reciprocal of the concentration of the complex in function of time, for the second order. A dissociation process induced by the light could belong to the first order. To confirm this guess, in figure 61 are presented the evolution of the natural logarithms of the complexes in function of time. In table 9 are presented the data of the lines.

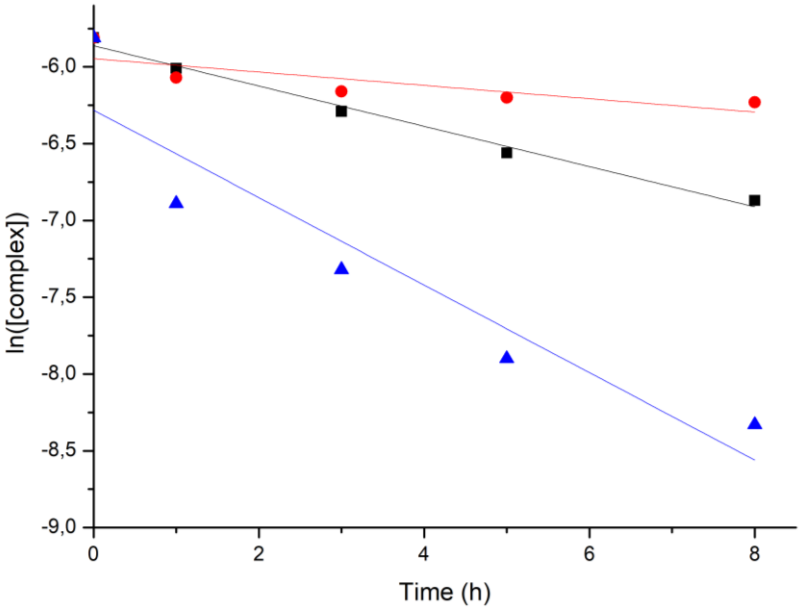

Figure 61 Linear fitting of the photolysis reactions. Black line C1, red line C2, blue line C3.

C1		C2		C3	
R^2_{adj}		R^2_{adj}		R^2_{adj}	
0.986		0.568		0.841	
Intercept	Slope	Intercept	Slope	Intercept	Slope
-5.862	-0.131	-5.946	-0.043	-6.281	-0.285

Table 9 Parameters of the linear fitting in figure 61.

In figure 62 and table 10 are presented the lines and their data obtained plotting the reciprocal of the complex concentration in function of time. Observing the R squared of the complexes the best fitting is obtained with the second order kinetics, but as explained above, a dissociation process is usually a reaction belonging to the first order kinetics.

C1		C2		C3	
R^2_{adj}		R^2_{adj}		R^2_{adj}	
0.989		0.638		0.987	
Intercept	Slope	Intercept	Slope	Intercept	Slope
0.321	0.077	0.385	0.019	0.339	0.471

Table 10 Parameters of the linear fitting in figure 62.

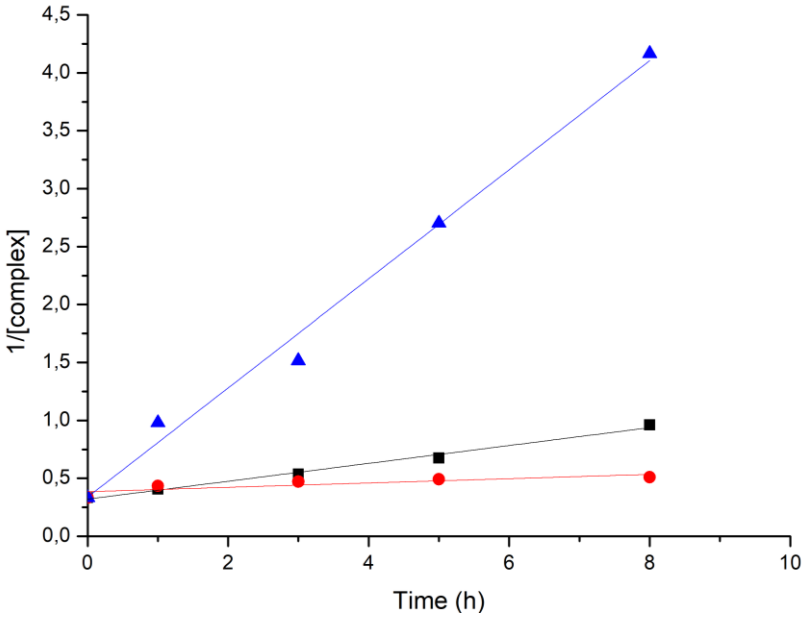

Figure 62 Linear fitting of the photolysis reactions. Black line C1, red line C2, blue line C3.

Observing the percentage of complexes in function of time (figure 63) the complex C1 disappeared linearly with time while the photolysis of complexes C2 and C3 occurs principally in the first hour reducing during the hours, reaching a plateau.

In conclusion, complex C3 absorbs the photons in the blue region, thanks to the monodentate ligand L4, and for this reason its rate of photodissociation is greater than the other two complexes. In the next paragraph, we will see if this difference in the rate of photodissociation play a role in the biological activity.

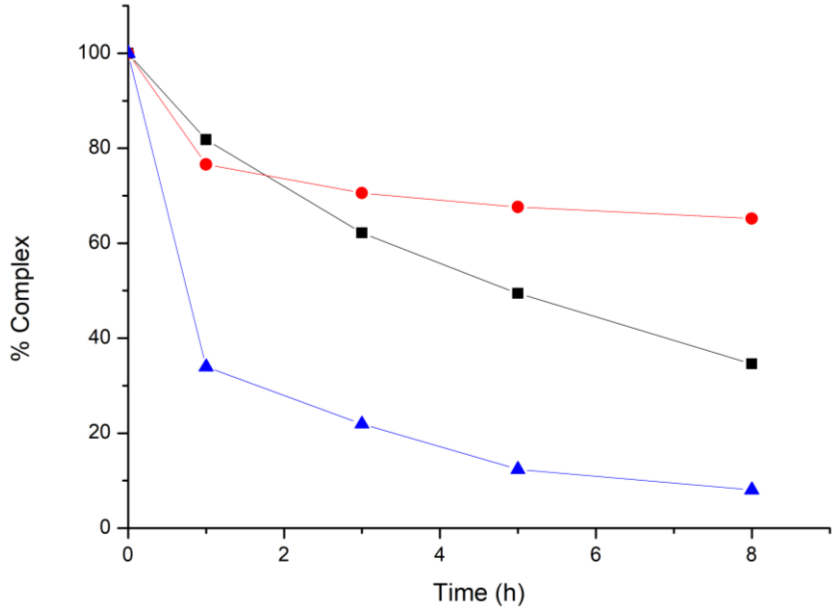

Figure 63 Percentage of complex in function of time. Black line C1, red line C2, blue line C3.

9.3.5 Photobiology of the complexes C1, C2 and C3

Once confirmed the ability of these complexes to release the monodentate ligand only under the irradiation of blue light, I decided to verify their activity in cells. The cell line chosen for the evaluation of these complexes, and for all the ruthenium complexes presented in this thesis, is the A549, a solid lung tumor without effective cure. This class of cells are suitable for the light treatment because are simple to treat with the light, thanks to their ability to adhere to the walls of the well plates. The test used to evaluate the cytotoxicity of the complexes here described, with and without irradiation, is the MTT colorimetric assay. Here, a brief description of this test.

The cells are seeded into 96-well plates overnight, and then exposed to compounds at indicated concentrations. At the end of the treatment, MTT was added for 3 hours at 37°C. The MTT is the abbreviation of 3-(4,5-dimethylthiazol-2-yl)-2,5-diphenyltetrazolium bromide, a compound characterized by a strong purple color. The cells, thanks to the action of mitochondrial dehydrogenases naturally present during their metabolic activity, reduce MTT into formazan, a colorless compound. So, greater is the activity of the tested compound, greater is the reduction of viability of the cells and greater is the color of the cell plate. The concentration of the MTT, after the treatment, is evaluated with a spectrophotometer, observing the absorbance at 550 nm. For every compound, at least three independent experiments were performed. The half maximal inhibitory concentration (IC_{50}) was determined as the concentration resulting in 50% cell growth reduction compared with untreated control cells.

For the irradiation of the cells, I used the same light of the photoactivation experiments described above. During the irradiation, some of the cells were used as control, i.e., without the complex but irradiated. A further level of control is necessary during this type of experiments to study the possible harmful effect of the light.

The time of irradiation chosen to evaluate the biological activity of the ruthenium complexes is 3 hours. This threshold has been selected because is a good compromise between the activation of the compounds, that within the 3 hours reaches a good point, and the harmful effect of the blue light, that after the 3 hours starts to be considerable.

In table 11 are presented the biological activity results of the ligands and complexes, previous described, before and after the photoactivation. The ligands are completely inactive respect to the cell and the DNA, and completely unable to intercalate it. This fact can be ascribed by the chain length of the imide moiety, that in literature [118] is considered fundamental for a good intercalation. The monodentate ligands, despite their biological inactivity, play a key role in the biological activity of the complexes, because acting like antennas. C3 is the unique complex with a biological activity because, as explained above, is the unique compound able to absorb in the blue region and the unique complex that, once irradiated, releases the two photoproducts in a discrete amount. The two photoproducts are the monodentate ligand and the solvate ruthenium complex, the source of the biological activity.

In conclusion, the biological activity of these photoactivatable ruthenium complexes is directly associated with the photodissociation rate, in turn connected with the ability of the monodentate ligand to absorb the photons in the blue region.

	IC_{50} (μM) A549 24h	
	Non irradiated	**3 hours of irradiation**
L1	>100	>100
C1	>100	>100
L2	>100	>100
C2	>100	>100
L4	98 ± 6	>100
C3	76,74 ± 1,32	10,55 ± 0,30

Table 11 IC_{50} in micromolar of the ligands, L1, L2 and L4, and the complexes, C1, C2 and C3, before and after the irradiation.

9.4 Photochemistry and photobiology of Ru(II) complex with a functionalized rhodamine like monodentate ligand

Previously, I demonstrated that the half sandwich ruthenium(II) complexes are useful for the development of new PACT compounds, in which the pyridine, used like monodentate ligand, can be functionalized in different ways. In the previous three complexes I have focused my attention on the naphtahlenimides ligands that act like antennas for their complexes.

Here, I explored the possibility to obtain a new photoactivable metal complex using a monodentate ligand with a maximum of absorption at larger wavelength. The aim is obtaining a photoactivatable ruthenium complex that absorbs less energetic light. The molecule choose is the Rhodamine 6G.

9.4.1 Rhodamine: an overview

The term rhodamine is associated to a family of molecules widely used like dyes. These molecules are well-known fluorophores [128] with a lot of application like, for example, laser dyes [129, 130], in the biological field to

study the fluidity of lipid membranes [131], the dynamics of micelles [132] or for imaging in living cells [133-135]. This class of molecules is characterized by a strong absorption band at 540 nm.

In literature [136] it is presented a photoactive Ru(II)-bipyridine complex with a rhodamine 6G functionalized with a pyridine. Through the coordination of this fluorescent ligands to the Ru centre, it was possible to establish an energy transfer pathway that allows these kinds of complexes to extend the range of photoactivation up to higher wavelengths. A peculiarity of the synthetized rhodamine amide is that it can exist in two main forms: a fluorescent, open form and a nonabsorptive, nonfluorescent closed spirolactam. These species are in equilibrium and the switching between these two forms depends on the pH of the medium (figure 64). In aqueous solution the spirolactam is the prevalent species at pH > 5 and the conversion from this form to the open one takes several minutes after acid addition, while the reversion to the nonfluorescent form by adding a base appears as instantaneous in the UV−vis measurement time scale.

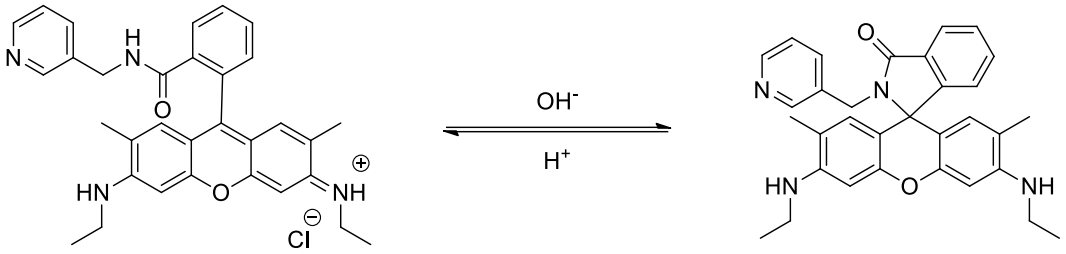

Figure 64 The two forms, open (left) and close (right), of the functionalized rhodamine 6G.

9.4.2 Absorption and emission spectra: C4 and L8

In figure 65 are presented the structure of the monodentate ligand, the rhodamine 6G functionalized with a pyridine, and the corresponding complex, in which the bidentate is still a bipyridine. The complex has been obtained with the synthetic pathway described above.

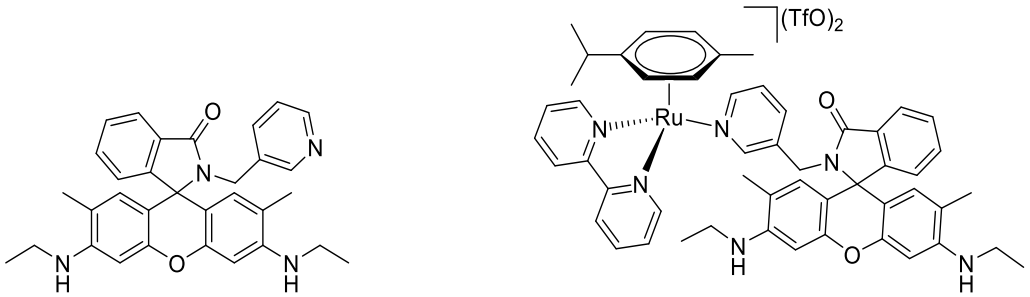

L8 C4

Figure 65 Structure of the functionalized rhodamine 6G and its ruthenium complex.

Both the rhodamines, the ligand and the complex, are described in figure 65 in the spirolactam closed form. This conformation is confirmed by the absorption spectra presented in figure 66, in which the band at 540 nm, typical of the open conformation, is absent. This must be considered during the setup of the photoactivation experiment for complex C4.

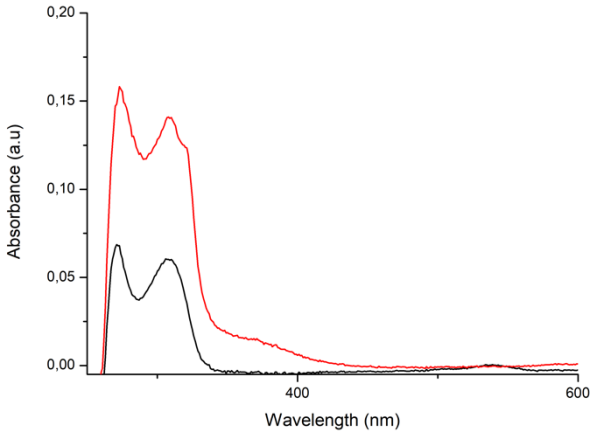

Figure 66 Absorption spectra of L8 (black line) and C4 (red line). The spectra are performed in DMSO at 10 µM.

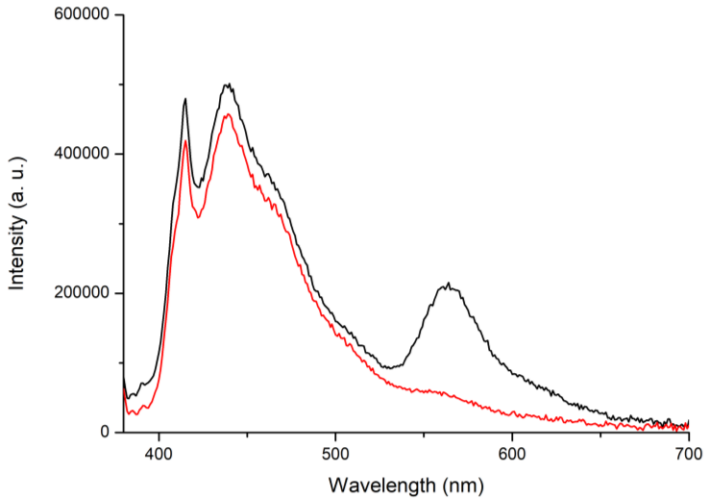

Figure 67 Emission spectra of L8 (black line) and C4 (red line). The spectra are performed in DMSO at 10 µM with a λ_{ex} = 370 nm.

In figure 67 are represented the emission spectra of L8 and C4. The principal difference is the presence, in the ligand spectrum, of a second band at 564 nm, completely absent in the complex.

In table 12 are resumed the spectroscopic properties.

Compounds	λ_{abs} (nm)	[a]λ_{em} (nm)	[b]ε (M^{-1} cm^{-1})	[c]Φ_f
L8	310	440/564	4203	0,713
C4	310	440	5143	0,351

Table 12 (a) the emission wavelength is referred to an excitation wavelength of 370 nm (b) molar extinction coefficient is calculated on the maximum of absorption (c) quantum yield is obtained using quinine sulfate like reference. The excitation wavelength is still 370 nm.

9.4.3 Stability in the dark: C4

The preliminary step that must precede the photoactivation studies is the evaluation of the stability of the complex in the dark, in physiological conditions. The stability is evaluated using the same type of mixture explained above, composed by a 98% of aqueous PBS solution and 2% of DMSO, in which the complex is

dissolved. The stability is still evaluated in the 24 hours maintaining the solution in the dark. The stability, in the dark, is confirmed in figure 68.

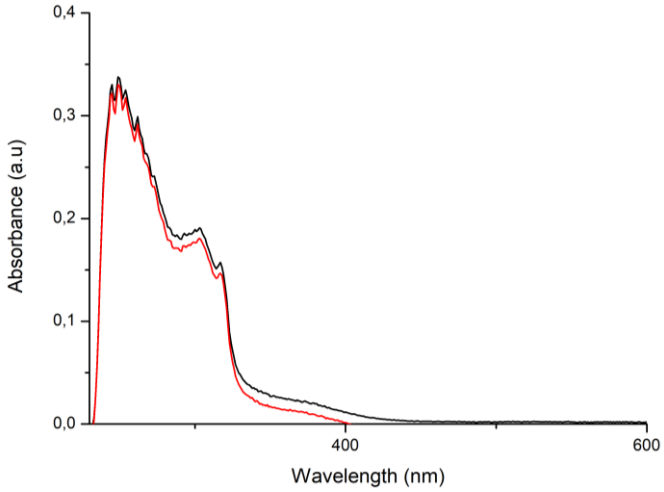

Figure 68 Stability of the complex C4. Comparison between the time zero solution (black line) with the same solution after 24 hours of incubation at 37°C in the dark (red line). Concentration of the complex is 20 µM, concentration of PBS buffer is 10 mM and the pH is 7.4. The solution is a mixture of an aqueous solution of PBS, 98%, and DMSO, 2%.

9.4.4 Photoactivation experiments: C4 in open and close conformation

The photoactivation experiments are performed with the same setup explained above, using the same solvent, DMSO-D_6, the same concentration of the sample, 3 mM, and the same "photo-oven". In that case I used a different type of light source using a LED green light centered at 540 nm, with the same energy of 64 mW/cm^2. For the photoactivation in cell was used this LED green light. The photoactivation of the complex C4 is evaluated in the two conformation, open and close. As observed above, the functionalized rhodamine 6G in the complex C4 is in the close conformation. To induce the opening of the spirolactam ring is necessary the presence of an acidic environment. In this case, two different samples were prepared for the experiment, using only DMSO-D_6 (530 µL) as solvent for C4 in the first NMR tube and DMSO-D_6 (500 µL) plus a small addition of deuterated TFA (30 µL) for the second one, in order to obtain an enough acid pH to open the cyclized structure of rhodamine. The opening could be checked also from the colorimetric point of view looking to the NMR samples. As could be seen from Figure 69, since the open form possess an absorption band in the UV-vis region, it turned into a much more intense colour than the closed one, which, in contrast, resulted colourless.

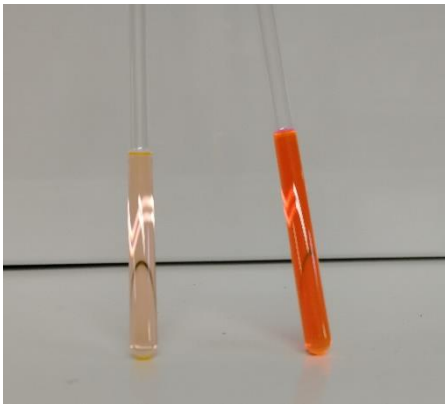

Figure 69 Color difference between complex C4 in the closed form (left tube) and in the open form (right tube).

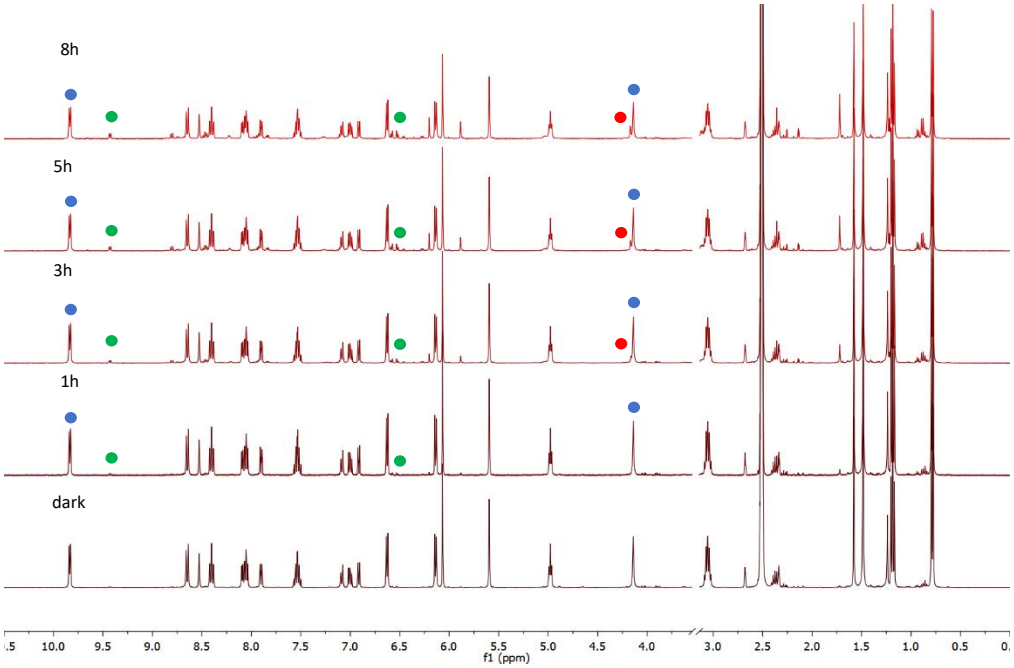

Figure 70 Photoactivation of the complex C4 close conformation.

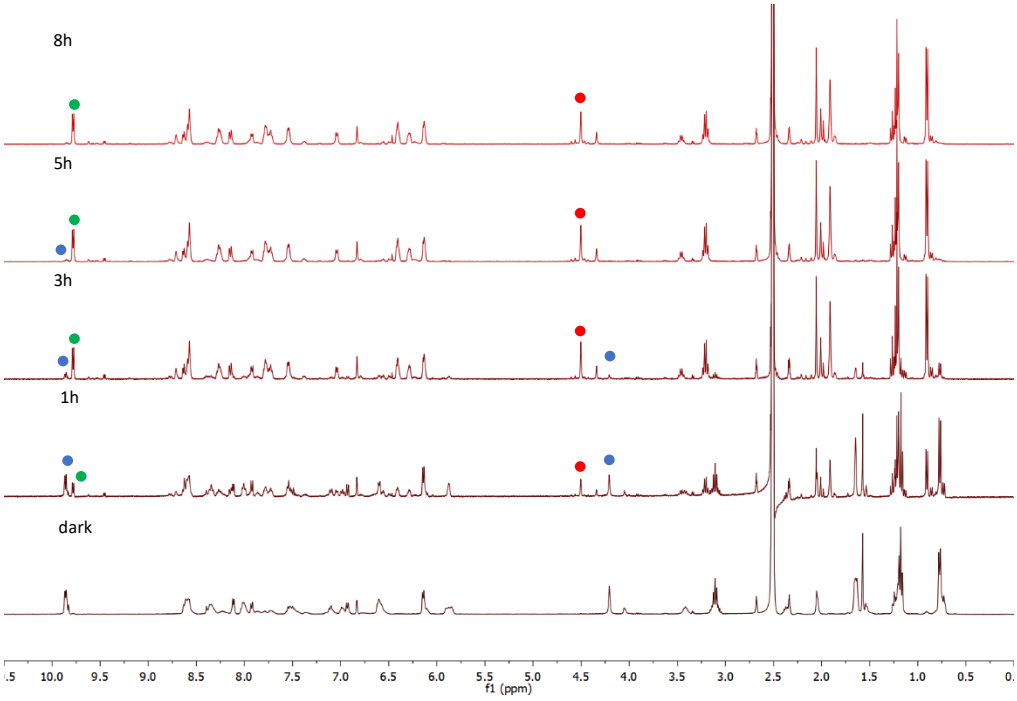

Figure 71 Photoactivation of the complex C4 open conformation.

In figures 70 and 71 are presented the photoactivation of C4 in the two conformations. The species present during the photoactivation are three: the starting complex (blue spots), the free ligand (red spots) and the solvate complex $[(\eta^6\text{-p-cym})\text{Ru(N,N-bipy)(DMSO)}]^{2+}$ (green spots). The behavior of the two conformations was quite the opposite. The close form of the complex C4 is unable to absorb the green light and its rate of photoactivation is extremely slow. On the contrary, the structural change for the open form allowed a much faster photoactivation rate. In fact, the original complex disappeared already after 3 hours only. The

methylene group of the methyl-pyridine moiety remains the most diagnostic signal to observe the photoactivation of the complex (table 13).

	C	L
C4 closed/L8	4.14 ppm	4.27 ppm
C4 open/L8	4.21 ppm	4.50 ppm

Table 13 Chemical shift of the methylene group in the complex C4 and the ligand L8. The variation in chemical shift is due by the different conformation of the functionalized rhodamine 6G and the different type of solvents used in the two experiments.

For the complex C4 the kinetic order cannot be defined in both the conformation. The closed one has the rate of photoactivation extremely low, and the concentration of the undissociated complex remains constant. On the other hand, complex C4 with the open conformation has a NMR spectrum with a low resolution, due by the presence of two type of deuterated solvents, in which there is no signals that don't change during the photoactivation.

9.4.5 Photobiology of complex C4

The biology activity of the ligand L8 and complex C4 is evaluated in the same conditions described above, with the MTT test, using the A549 cell line, and with the same light source used for the photoactivation experiments, in that case, the green LED light.

The results are resumed in table 14. Unfortunately, the ligand L8 and the complex C4 are completely inactive in cell, before and after the photoirradiation. The total absence of the biological activity for complex C4 can be explained considering that the pH within the cells is not sufficiently acidic to induce the opening of the structure of the rhodamine ligand, which led to the non-availability of absorption by the complex in the green region.

	IC_{50} (μM) A549 24h	
	Non irradiated	**3 hours of irradiation**
L8	>100	>100
C4	>100	>100

Table 14 IC_{50} in micromolar of the ligand L8 and the complex C4, before and after the irradiation.

To conclude this paragraph, the half sandwich ruthenium(II) complex here proposed is a valid molecular scaffold to obtain PACT compounds using different type of antennas, i.e., the monodentate ligand. The complex C4, with the rhodamine in the open form, is photoactivatable, as described above. Unfortunately, the close form of rhodamine is predominant in the tumor cells. A future prospective, for this PACT ruthenium(II) complex with a rhodamine like ligand, can be the use of a tertiary amide in the methyl-pyridine moiety. In that way, the structure of the rhodamine is open independently by the pH level.

9.5 Photochemistry and photobiology of Ru(II) complexes with different type of bidentate ligands: C5, C6 and C7

Once demonstrated that ruthenium(II) half-sandwich scaffold is available to obtain new photoactivatable compounds with different type of monodentate ligands, I focused my attention on the behavior of this class of complexes with different kind of bidentate ligands. In figure 72 are presented the complexes described in this chapter.

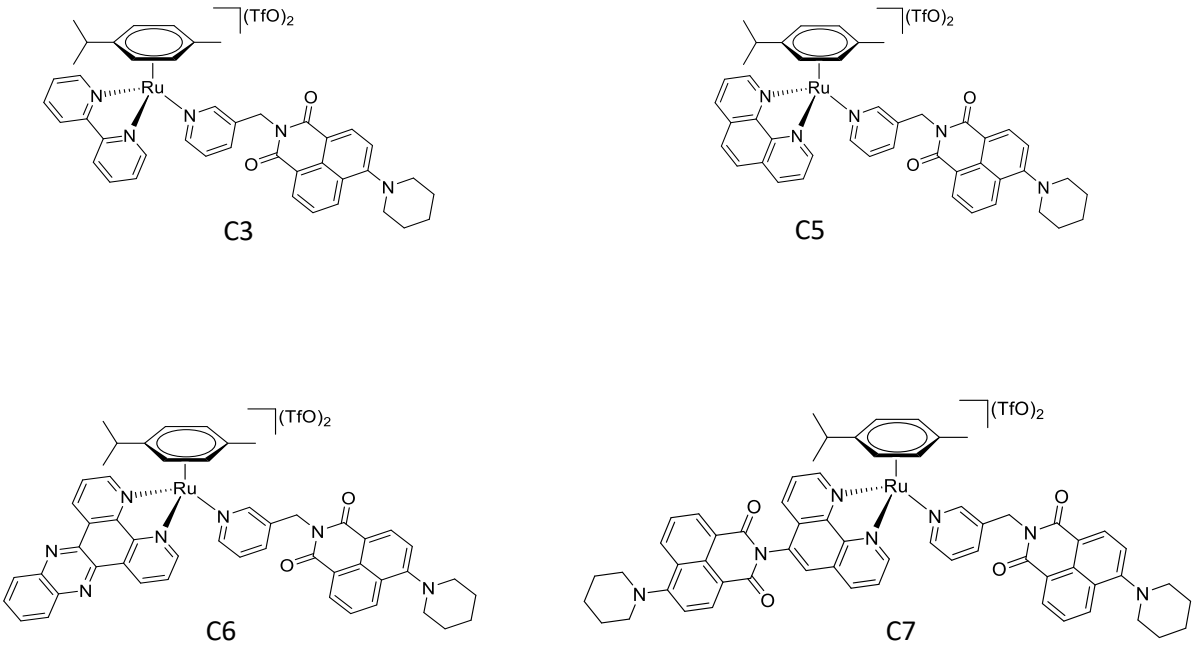

Figure 72 Structure of the complexes C3, C5, C6 and C7.

The ligand chosen as monodentate is L4, the best antenna used above. The bidentate ligands used for these compounds are characterized by an increasing molecular complexity. In the complex C5 there is a simple phenanthroline, a dipyridophenazine (dppz) is used as bidentate ligand in the complex C6 and in C7 I introduced a phenanthroline functionalized with the piperidine naphthalenimide moiety, already present in the ligand L4.

For complex C6 the aim is to obtain a photoactivatable complex generating as photoproduct a ruthenium solvate complex with a greater biological activity. In fact, dppz is well-known in literature [137-138] as DNA intercalator.

Instead, in C7 I introduced a second antenna in the bidentate ligand. The aim is to observe if the photoactivation rate can increase with the presence of a double chromophore.

Here, the complex C3 described in the previous chapter has been used like a standard to compare the photoactivation rate and the biologic activity of these new complexes.

9.5.1 Absorption and emission spectra: C3, C5, C6 and C7

Firstly, in figure 73 are compared the monodentate piperidine naphthalenimide, L4, the bidentate piperidine naphthalenimide, L6, and the complex C7. The three molecules have the characteristic absorption band at 418 nm, thanks to the "push-pull" effect between the piperidine and the amide, but with a different intensity. In fact, the complex C7 has the band with the higher absorbance.

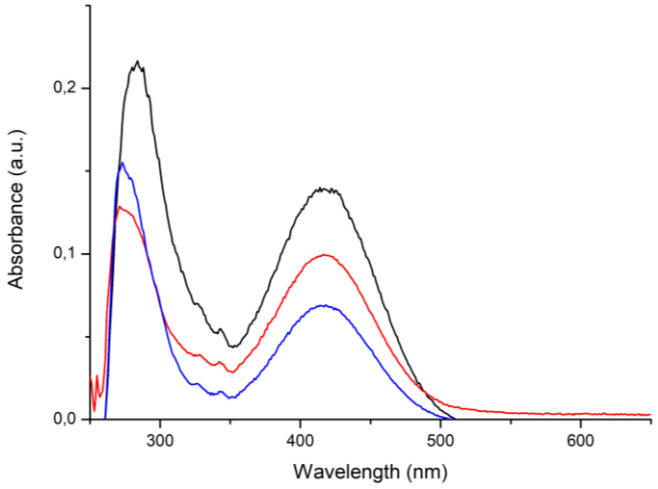

Figure 73 Absorption spectra of C7 (black line), L4 (red line) and L6 (blue line). The spectra are performed in DMSO at 10 µM.

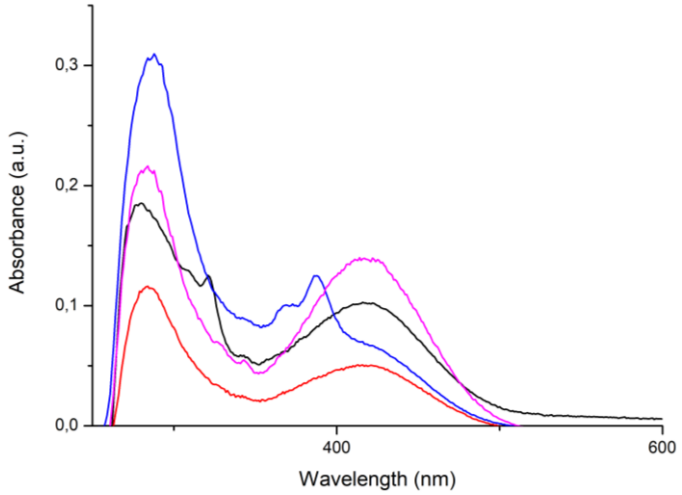

Figure 74 Absorption spectra of C3 (black line), C5 (red line), C6 (blue line) and C7 (magenta line). The spectra are performed in DMSO at 10 µM.

In figure 74 are compared the absorption spectra of the four complexes. In these spectra is possible to observe that the presence of the same antenna, the monodentate ligand L4, with different bidentate ligands

lead to different intensity of absorbance in the blue region. This information suggests that the ligands, monodentate and bidentate, influence each other when they form this type of complex.

The emission spectra of the same compounds are compared in the next figures. In figure 75 the emission spectra of L4, L6 and C7 are presented. We can observe that the ligand L6 has the greater intensity, thanks to its structural rigidity that promotes the radiative processes. Instead, the complex C7 has an intensity of emission that is lower than the two ligands, suggesting that the radiationless mechanisms are preferred.

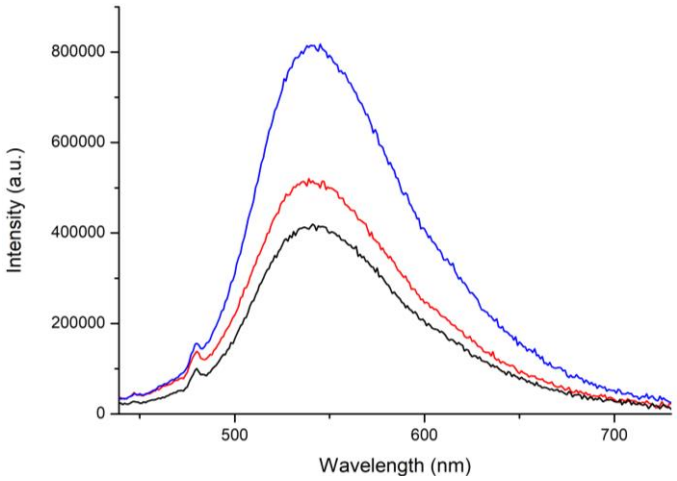

Figure 75 Emission spectra of C7 (black line), L4 (red line) and L6 (blue line). The spectra are performed in DMSO at 10 µM with a λ_{ex} = 418 nm.

In figure 76 are compared the emission spectra of the complexes with their monodentate ligand, L4. These complexes have an intensity of emission extremely variable. In fact, C6 has an intensity of emission that is greater of L4, while the other three complexes have reduced their emission. Hence, different kind of ligands can change the electronic and spectroscopic behavior of their complexes in unexpected ways.

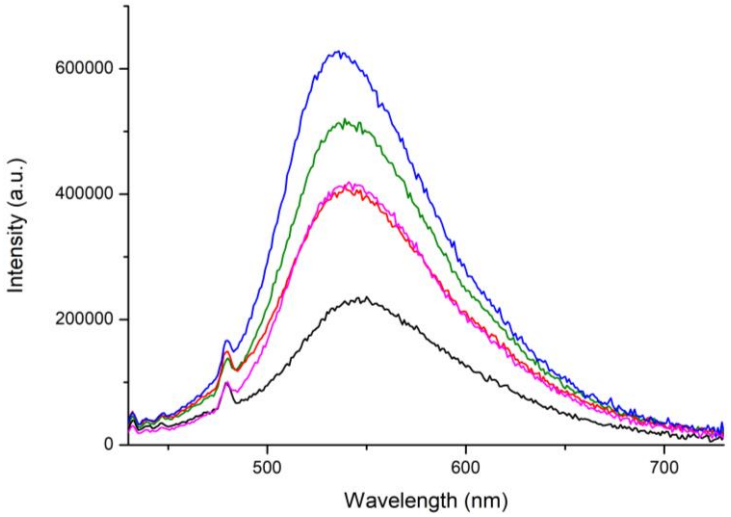

Figure 76 Emission spectra of C3 (black line), C5 (red line), C6 (blue line), C7 (magenta line) and L4 (green line). The spectra are performed in DMSO at 10 µM with a λ_{ex} = 418 nm.

In table 15 are resumed the spectroscopic properties.

Compounds	λ_{abs} (nm)	λ_{em} (nm)	[a]ε (M^{-1} cm^{-1})	[b]Φ_f
L6	418	550	4695	0,624
C5	418	550	2679	0,149
C6	418	550	4566	0,137
C7	418	550	4409	0,369

Table 15 (a) molar extinction coefficient is calculated on the maximum of absorption (b) quantum yield is obtained using quinine sulfate like reference. The excitation wavelength is still 370 nm.

9.5.2 Stability in the dark: C5, C6 and C7

In the figures 77, 78 and 79 is confirmed the stability of the complexes in the dark in physiological conditions. The series of stability in the dark until now proposed proves that the ruthenium half sandwich molecular scaffold is extremely sturdy. In fact, all the complexes result stable, independently by the type and complexity of the ligands.

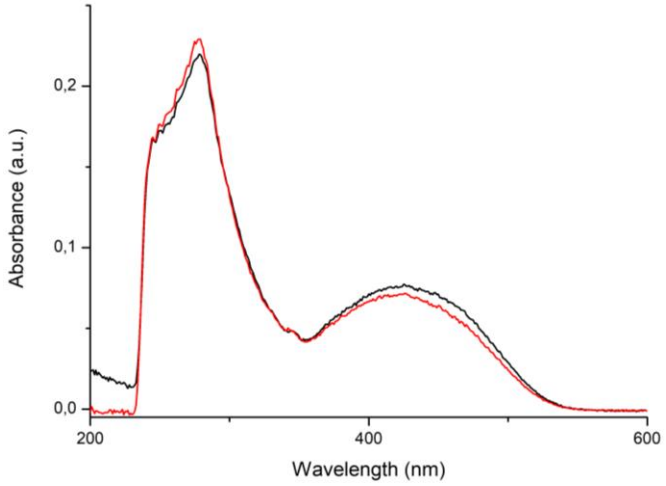

Figure 77 Stability of the complex C5. Comparison between the time zero solution (black line) with the same solution after 24 hours of incubation at 37°C in the dark (red line). Concentration of the complex is 20 µM, concentration of PBS buffer is 10 mM and the pH is 7.4. The solution is a mixture of an aqueous solution of PBS, 98%, and DMSO, 2%.

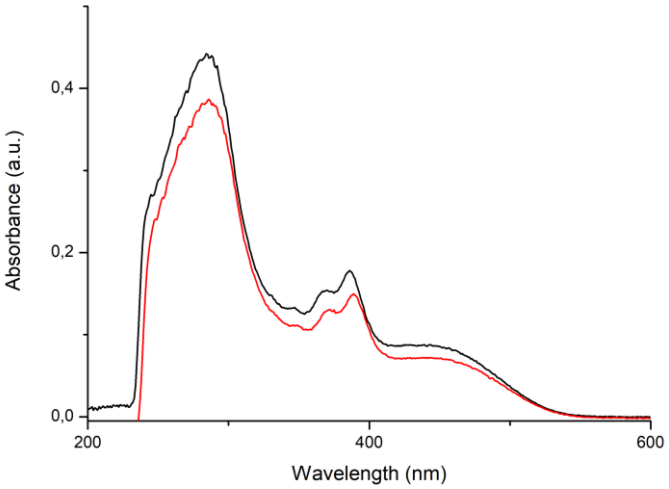

Figure 78 Stability of the complex C6. Comparison between the time zero solution (black line) with the same solution after 24 hours of incubation at 37°C in the dark (red line). Concentration of the complex is 20 µM, concentration of PBS buffer is 10 mM and the pH is 7.4. The solution is a mixture of an aqueous solution of PBS, 98%, and DMSO, 2%.

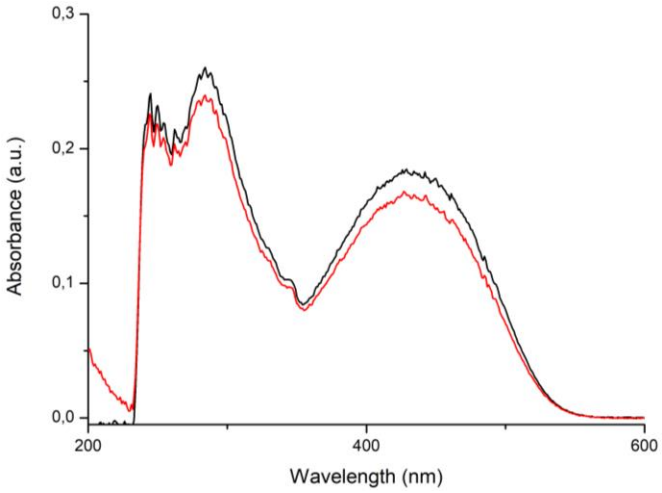

Figure 79 Stability of the complex C7. Comparison between the time zero solution (black line) with the same solution after 24 hours of incubation at 37°C in the dark (red line). Concentration of the complex is 20 µM, concentration of PBS buffer is 10 mM and the pH is 7.4. The solution is a mixture of an aqueous solution of PBS, 98%, and DMSO, 2%.

9.5.3 Photoactivation experiments: C5, C6 and C7

The photoactivation experiments are performed in the same conditions of the previous experiments. For these complexes, I used the LED blue light, as in the case of C1, C2 and C3. Scheme 4 summarizes the mechanism of photolysis and the generated photoproducts, with the color code used in the NMR spectra.

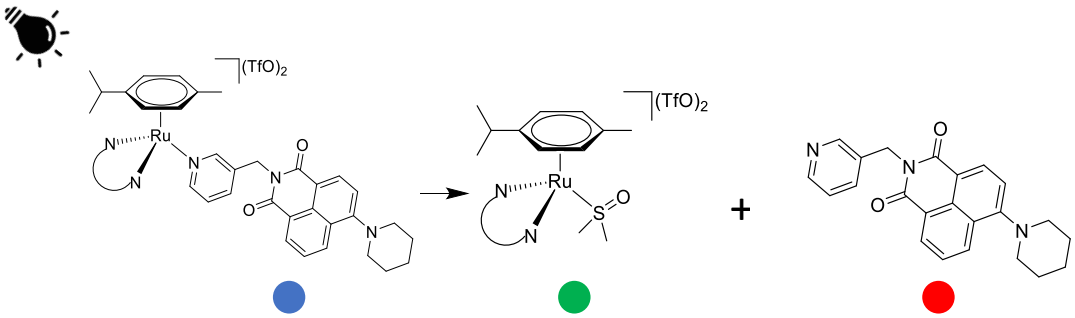

Scheme 4 Mechanism of photolysis of the complexes.

In figures 80, 81 and 82 are presented the NMR spectra of the photoactivation experiments. The three complexes change their structure when irradiated with the light. This is confirmed by the formation of typical signals, like the one close to 10 ppm, (green spots), and associated to the aromatic protons of the bidentate ligand close to the nitrogen atoms involved in the complexation of ruthenium, or like the signals close to 6.5 ppm, still indicated with the green spots, and associated to the aromatic protons of the para-cymene. The most diagnostic signal is still the singlet of the methylene group of the naphthalimides.

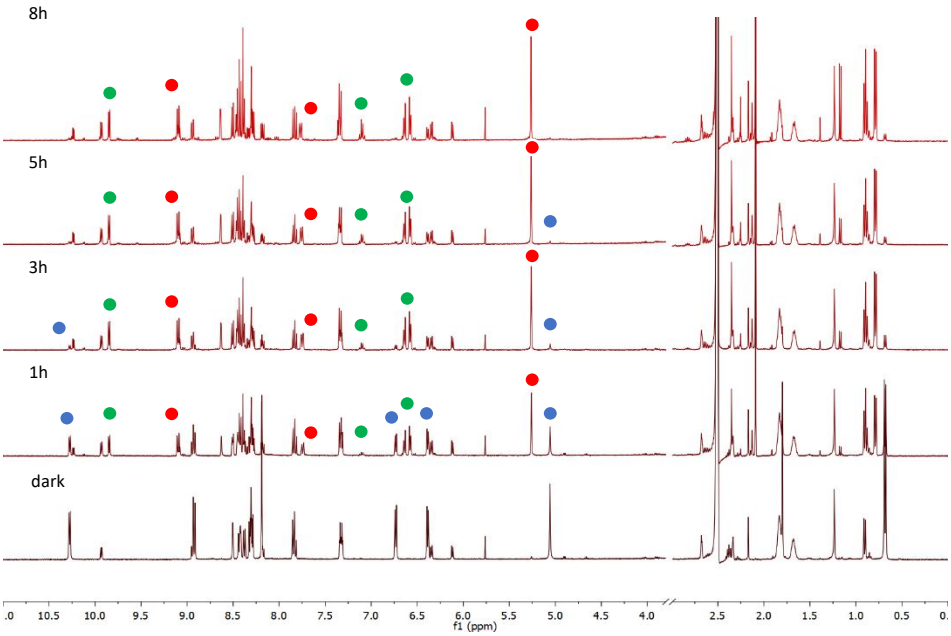

Figure 80 Photoactivation of the complex C5.

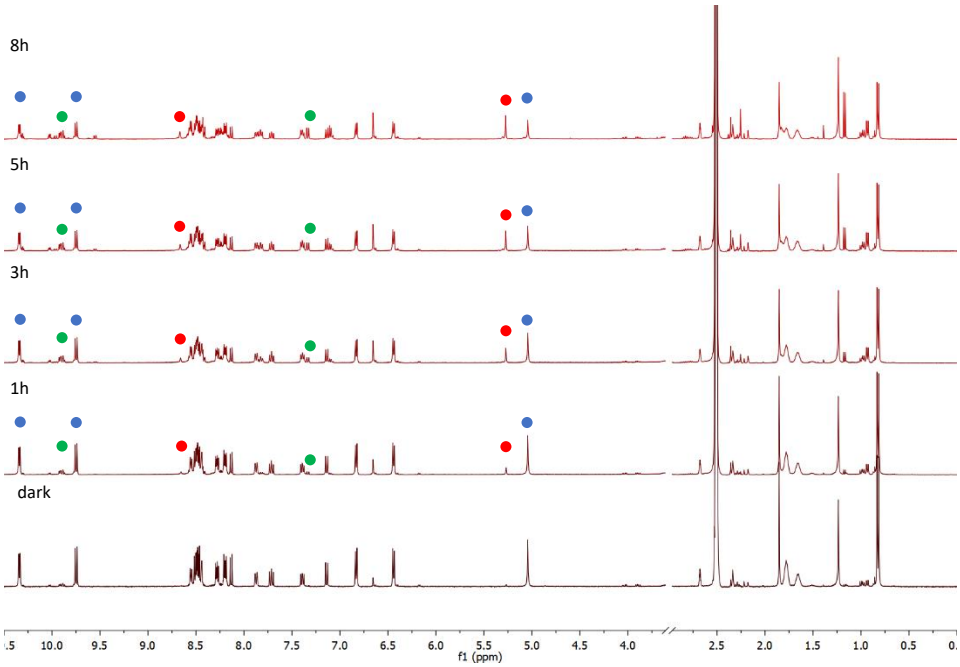

Figure 81 Photoactivation of the complex C6.

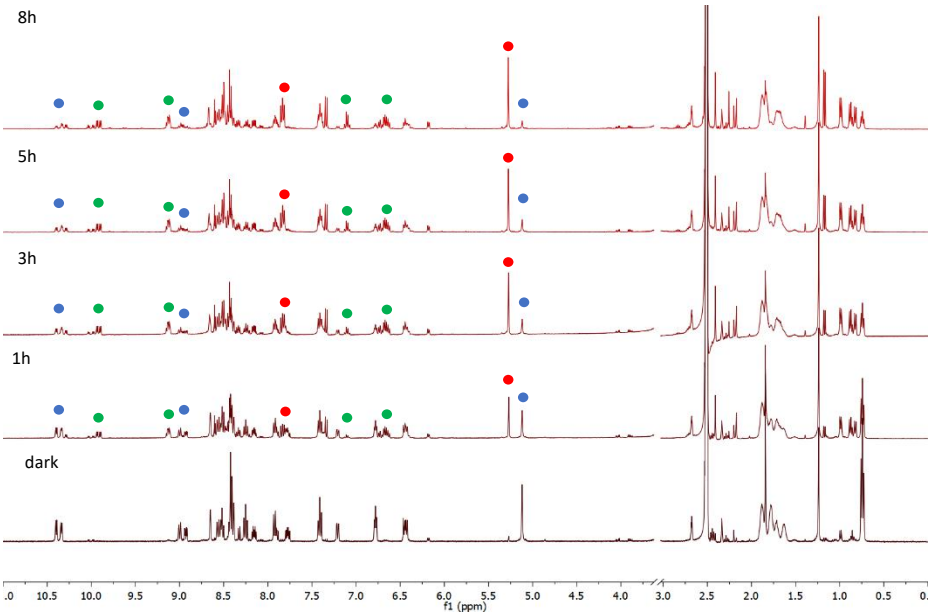

Figure 82 Photoactivation of the complex C7.

We can observe that the complexes C5 and C7 (figures 80 and 82) have a rate of photoactivation very similar while the complex C6 (figure 81), surprisingly, has a rate of photoactivation that is very slow respect to the other two. This difference can be appreciated in figure 83, comparing the release of the monodentate ligands, during the 3 hours, and observing the variation of the signal of the methylene group. The complex C6 is the unique that after 3 hours is predominantly associated, while the other three complexes are completely dissociated. In table 16 are resumed the chemical shifts of the methylene groups.

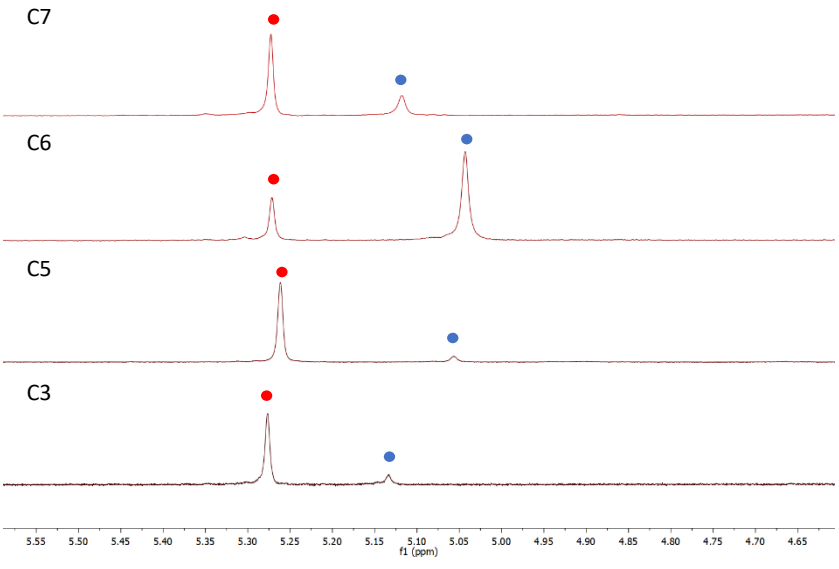

Figure 83 Comparison of the release of the naphthalenimide in C3, C5, C6 and C7 after 3 hours of irradiation.

	C	L
C3/L4	5.13 ppm	5.27 ppm
C5/L4	5.06 ppm	5.27 ppm
C6/L4	5.04 ppm	5.27 ppm
C7/L4	5.12 ppm	5.27 ppm

Table 16 Chemical shift of the methylene group in the complexes compared to the ligands.

For these complexes I evaluated the amount of the ligand released and the kinetics of these photolysis reactions using the same method described above. The reference signals chosen for these complexes belong to the piperidine group. At the end of the thesis are showed the tables of the calculations.

As in the case of the complexes C1, C2 and C3, the complexes here presented have a good fitting with the first order kinetics (figure 84, table 17) despite the best fitting is obtained with the second order kinetics (figure 85, table 18). Nevertheless, as explained above, a dissociation process is usually a reaction belonging to the first order kinetics.

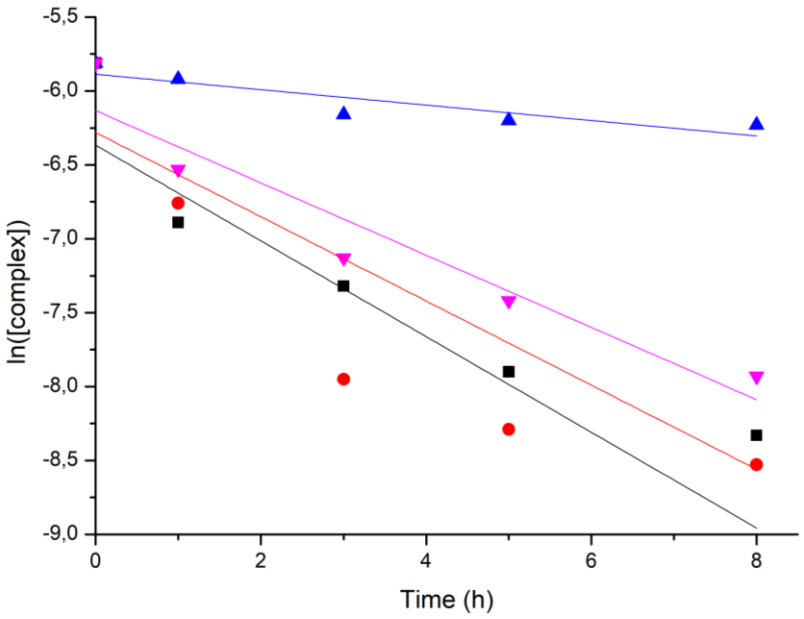

Figure 84 Linear fitting of the photolysis reactions. Black line C3, red line C5, blue line C6, magenta line C7.

C3		C5		C6		C7	
R^2_{adj}		R^2_{adj}		R^2_{adj}		R^2_{adj}	
0.841		0.757		0.777		0.888	
Intercept	Slope	Intercept	Slope	Intercept	Slope	Intercept	Slope
-6.281	-0.285	-6.367	-0.324	-5.886	-0.052	-6.133	-0.244

Table 18 Parameters of the linear fitting in figure 84.

We have a further corroboration of the uniqueness of the complex C6 plotting the percentage of complexes in function of time (figure 86). C3, C5 and C7 have the same trend while C6 is isolated.

In conclusion, the ligands, monodentate and bidentate, influence each other when they form this type of complexes. Hence, the properties of the final ruthenium complex are not the sum of the properties of the single ligands. Observing the experimental data, the complex C6 is the only bearing ligand L4 that has a slow rate of photoactivation and is the same complex with an intensity of emission that is greater than the monodentate ligand (figure 76). This information suggests that the rate of photoactivation is directly connected with the fluorescence spectrum.

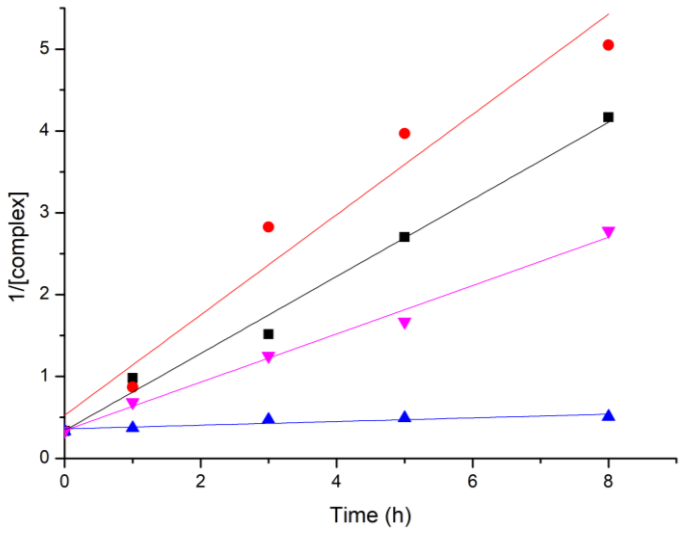

Figure 85 Linear fitting of the photolysis reactions. Black line C3, red line C5, blue line C6, magenta line C7.

C3		C5		C6		C6	
R^2_{adj}		R^2_{adj}		R^2_{adj}		R^2_{adj}	
0.987		0.949		0.777		0.988	
Intercept	Slope	Intercept	Slope	Intercept	Slope	Intercept	Slope
0.339	0.471	0.527	0.612	0.360	0.022	0.338	0.295

Table 19 Parameters of the linear fitting in figure 85.

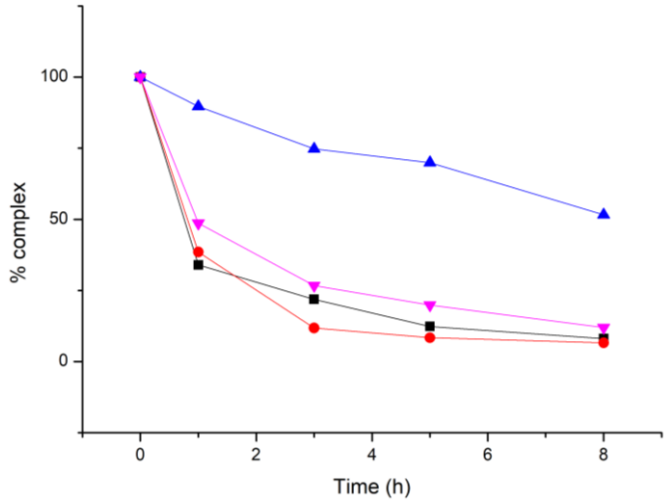

Figure 86 Percentage of complex in function of time. Black line C3, red line C5, blue line C6, magenta line C7.

9.5.4 Evaluation of the interactions between CT-DNA and the Ru(II) complexes

In the previous pages, I explained how the source of the biological activity in this type of complexes is the solvate Ru(II) complex, characterized by a solvent molecule that replaces the monodentate ligand. This type of piano-stool complexes are able to interact directly with the DNA [118].

The four complexes here presented have different chelate ligands, and possibly different biological activity. Therefore, a step to evaluate the ability of the solvate Ru(II) complexes to interact with the DNA is necessary in order to deepen the study of the biological activity against the A549 cells. The four complexes here studied are not the C3, C5, C6 C7 presented above, but their intermediate analogues with a chloride instead of L4 (figure 87). In water the chloride is easily exchanged with a molecule of solvent, generating the active aqua species.

The first experiment enforced is the UV-visible titration of the CT-DNA with the four intermediate complexes. The CT-DNA is dissolved in an aqueous solution of PBS (10 mM) and its concentration is expressed in base pairs. The intermediate complexes are dissolved in a stock solution of DMSO and added to the DNA solution, avoiding that the amount of DMSO exceed the 2%. In that way, I monitored the evolution of the DNA band at 260 nm in function of the complexes' concentration, expressed as the ratio r = [complex]/[DNA]. In figure 87 is presented the variation of the absorbance at 260 nm with different r of the intermediate complexes.

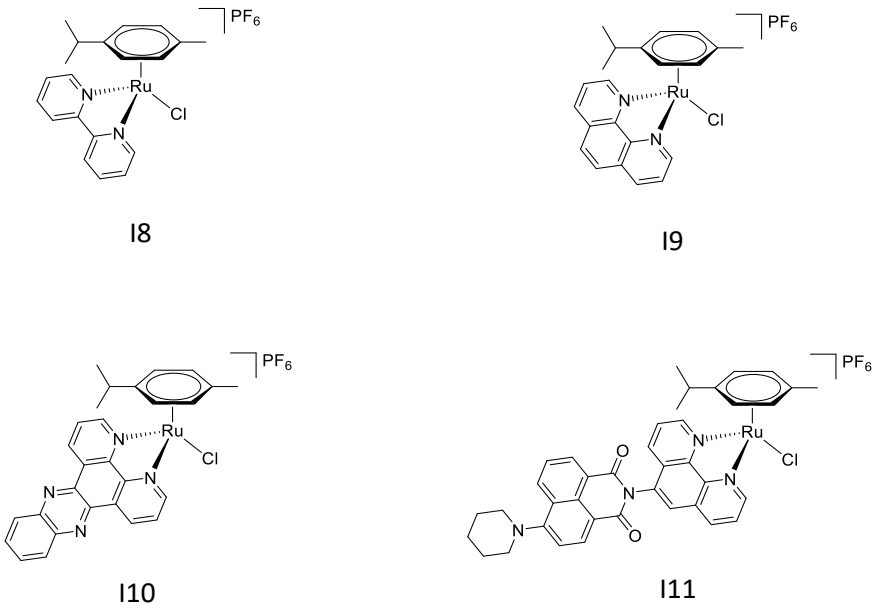

Figure 87 Structure of the complexes I8, I9, I10 and I11.

The four complexes tested here induce the decrease of the absorbance at 260 nm, but they can be divided in two categories: two of them (I8 and I9) reach a plateau when the ratio r exceeds 0.5, while I10 and I11 reduce the absorbance even if the r exceeds 0.5. Hence, I8 and I9 reach the optimum interaction when a molecule of the complex interacts with two base pairs (DNA/complex 2:1), instead I10 and I11 have the optimal interaction when a molecule of the complex interacts with one base pairs (DNA/complex 1:1).

Once confirmed the ability of these complexes to interact with the DNA, I studied the morphological and conformational transformation through the circular dichroism (CD) technique. As previously explained, the CD spectrum of CT-DNA is composed by a negative band at 250 nm due to helicity and a positive band at 280 nm due to base stacking, with the intersection point at the absorption maximum at 260 nm [44]. The ratio DNA/complex 2:1, i.e., r equal to 0.5, is used for the CD experiments, despite is the suboptimal ratio for the complexes I10 and I11, in order to have a single r to better compare the DNA transformation induced by the complexes.

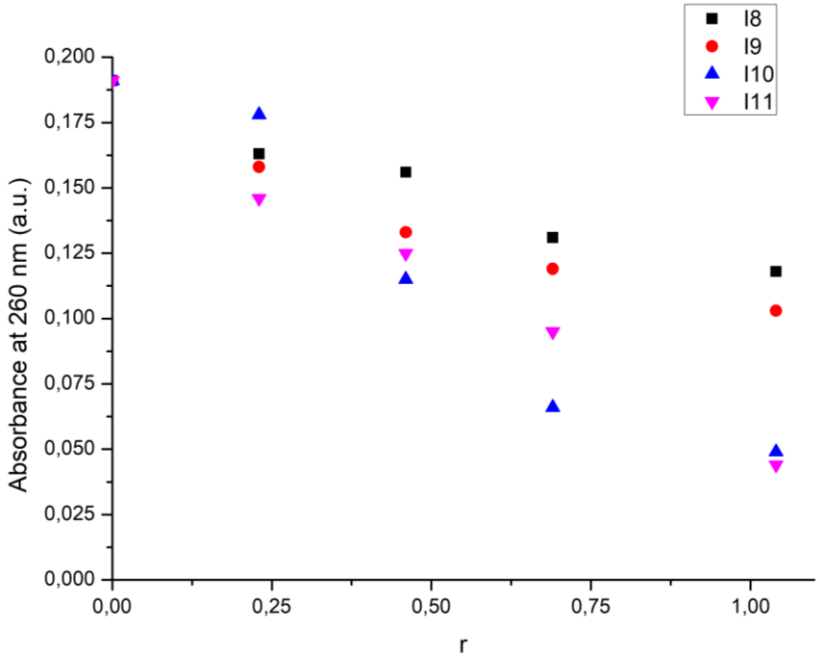

Figure 88 DNA's absorbance at 260 nm in function of the concentration of the complexes, expressed with the ratio r. The r values here presented correspond to r = 0; r = 0.23; r = 0.46; r = 0.69; r = 1.04.

All the four complexes induce the decrease of the band intensity, associated with the B → C transition.

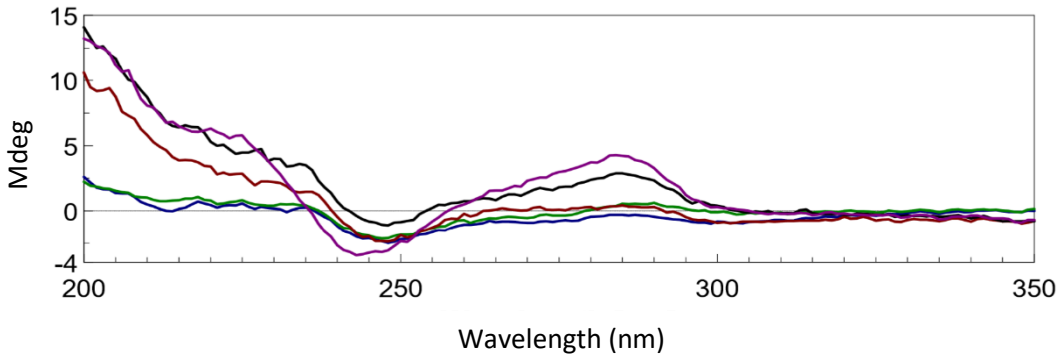

Figure 89 CD spectra of DNA (purple line), DNA + I8 (blue line), DNA + I9 (green line), DNA + I10 (red line), DNA + I11 (black line).

Finally, I studied the variation of the thermal denaturation behavior of the CT-DNA with and without the intermediate complexes (figure 89). Even in this experiment I used the ratio r equal to 0.5. All the four complexes induce a decrease of the melting temperature (T_m) of the DNA (table 20). This information

suggests that the intercalation is not the favored way of action of these complexes against the DNA, because the intercalation induce a stabilization of the double stranded DNA, inducing an increase of the T_m. Hence, it can be assumed that these complexes interact with the DNA through a monofunctional coordination.

Compound	T_m
CT-DNA	83°C
CT-DNA + I8	82°C
CT-DNA + I9	82°C
CT-DNA + I10	81°C
CT-DNA + I11	81°C

Table 20 Meting temperature of CT-DNA alone and in presence of the complexes.

9.5.5 Photobiology of complexes C5, C6 and C7

In table 21 are showed the IC_{50} values of the complexes C3, C5, C6 and C7. All these complexes are extremely active after the irradiation, while are inactive without the irradiation. The less active compound is C6 because, as demonstrated above, is the less photoactivatable compound. C3 and C7 have the same activity while C5 is the compound with the best activity amongst the ones tested until now.

At the same time, the IC_{50} of the intermediate complexes is obtained without the irradiation. These complexes do not show any biological activity against the tumor cells. This inactivity might be due by the reduced uptake of the aquo complexes.

	IC_{50} (µM) A549 24h	
	Non irradiated	**3 hours of irradiation**
C3	76,74 ± 1,32	10,95 ± 0,30
C5	>100	1,72 ± 0,24
C6	> 100	21,03 ± 0,93
C7	77,20 ± 2,05	8,57 ± 0,19
I8	>100	/
I9	>100	/

I10	>100	/
I11	>100	/

Table 21 IC_{50} in micromolar of the complexes C3, C5, C6 and C7 before and after the irradiation.

In conclusion, this panel of ruthenium complexes have demonstrated that the presence of the ligands involved in the complexation influence each other, generating complexes with different properties. Another interesting feature is the connection between the photoactivation rate and the emission spectrum, as suggested for the case of C6. The high intensity of emission is due by the preference of radiative mechanism for the de-excitation, respect to radiationless mechanisms, in which the ligand dissociation is included.

10 New photoactivatable Ru(II) complexes with N-heterocyclic carbenes as ligands

10.1 N-heterocyclic carbene: an overview

The term carbene [139] defines a molecule in which a carbon atom bears a lone pair of electrons. N-Heterocyclic carbenes (NHCs) are a family of the carbene compounds in which the carbene is included in an N-heterocyclic molecule. Today, NHCs is a family of ligands widely used in different fields of chemistry, like organocatalysis [140] and organometallic chemistry [141]. For example, the ruthenium-NHCs complexes are well known in literature [142-145] as efficient and sturdy catalysts for the olefin metathesis.

Recently [146-148], the ruthenium-NHCs complexes have been applied against cancer cells with good results. Instead, the photoactivation properties of ruthenium-NHCs complexes are still unexplored. For this reason, I decided to synthesize new all-caged ruthenium complexes with NCHs like monodentate ligands.

10.2 Synthesis of photoactivatable Ru(II) complexes with N-heterocyclic carbenes as ligands

The synthetic approach to obtain the desired photoactivatable ruthenium-NHCs complexes differs from the synthetic pathway presented in figure 44 in the second step, i.e., the insertion of the monodentate ligand. Preliminarily, we have the formation of a linear silver complex through the reaction of the imidazolium salt analogue with the silver(I) oxide. This linear silver complex is not isolated and its formation is monitored through NMR. Once confirmed the formation of the carbene and its silver complex we can introduce the $[(\eta^6$-p-Cym$)RuCl_2]_2$, promoting the transmetallation and the formation of the intermediate ruthenium complex.

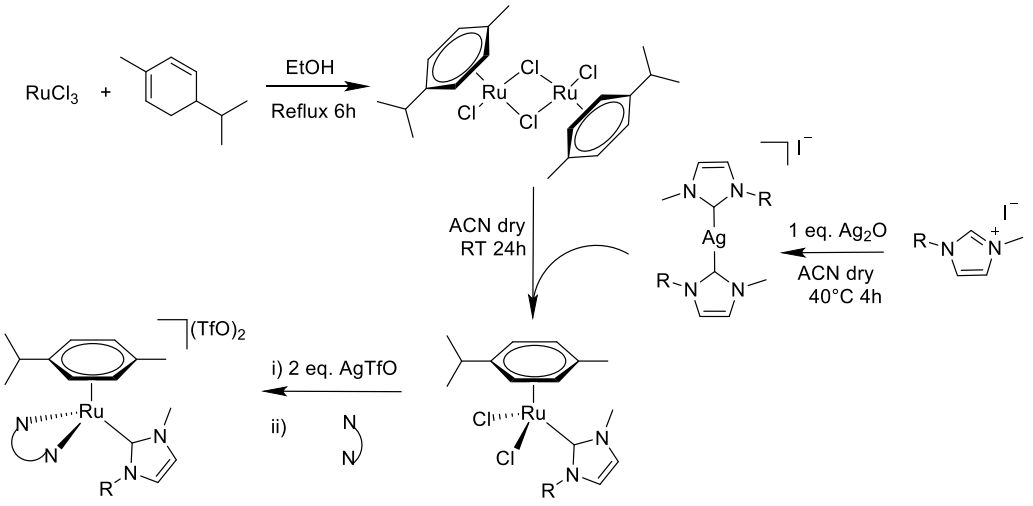

Figure 90 Synthetic route used to obtain photoactivatable ruthenium-NHCs complexes.

In figure 91 are showed the photoactivatable ruthenium-NHCs complexes here described. Complex C8 has, like monodentate ligand, a simple N-heterocyclic carbene obtained from the dimethyl-imidazolium salt. Instead, in C9 I used a more complex carbene functionalized with the piperidine naphthalenimide moiety. The aim is to observe the photoactivation properties of these ruthenium-NHCs complexes in presence and absence of an antenna with a phenanthroline as bidentate ligand.

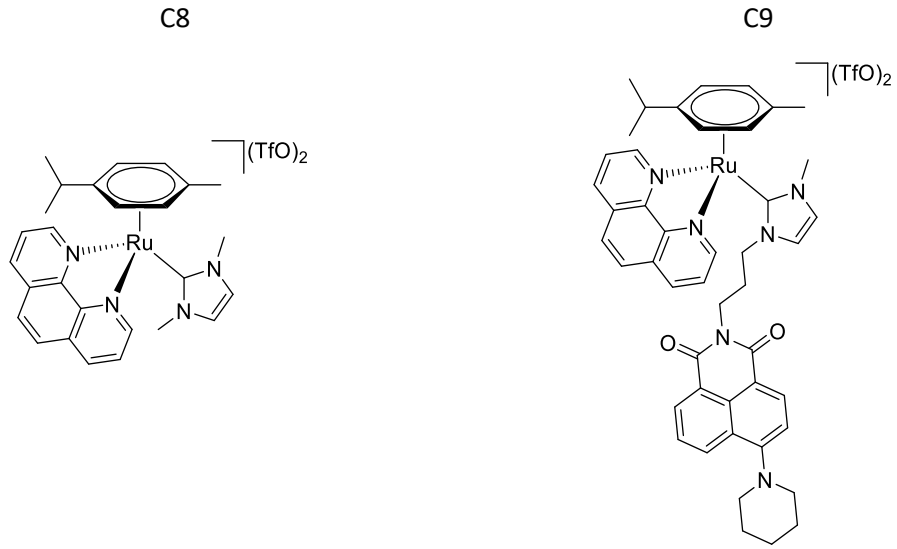

Figure 91 Structure of the complexes C8 and C9.

10.3 Absorption and emission spectra: C8 and C9

In figure 92 are compared the absorption spectra of the two ruthenium-NHCs complexes.

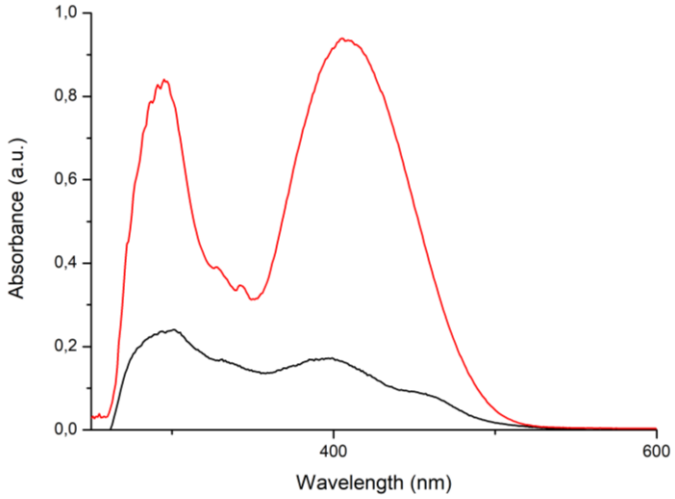

Figure 92 Absorption spectra of C8 (black line) and C9 (red line). The spectra are performed in DMSO at 100 µM.

As expected, the presence of the piperidine naphthalenimide moiety increases the intensity of the absorbance band in the blue region.

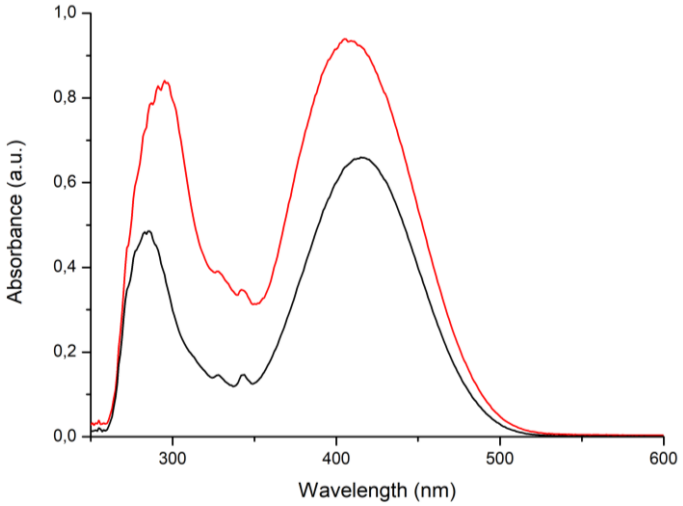

Figure 93 Absorption spectra of L12 (black line) and C9 (red line). The spectra are performed in DMSO at 100 µM.

The ligand L12, the imidazolium salt, and complex C9 have very similar absorption spectra, that differ by the intensity of the bands.

The emission spectra (figure 94) of the ligand L12 and the complex C9 confirmed that the complex prefers a radiationless mechanism for the de-excitation.

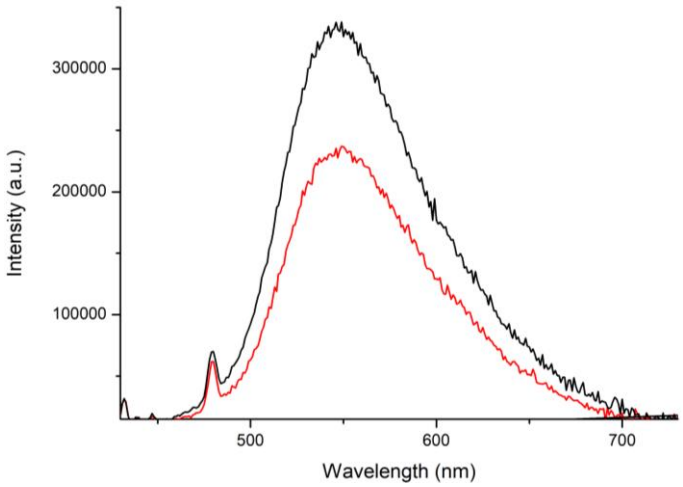

Figure 94 Emission spectra of L12 (black line) and C9 (red line). The spectra are performed in DMSO at 10 µM with a λ_{ex} = 418 nm.

In table 22 are summarized the spectroscopic properties.

Compounds	λ_{abs} (nm)	λ_{em} (nm)	$^{a}\varepsilon$ (M^{-1} cm^{-1})	$^{b}\Phi_f$
L12	418	550	5998	0,067
C9	418	550	9455	0,035

Table 22 (a) molar extinction coefficient is calculated on the maximum of absorption (b) quantum yield is obtained using quinine sulfate like reference. The excitation wavelength is still 370 nm.

10.4 Stability in the dark: C8 and C9

In figures 95 and 96 are showed the stability in the dark of the ruthenium-NHCs complexes. Also this type of complexes, with a carbene like the monodentate ligand instead of a pyridine, are stable in the dark in physiological conditions.

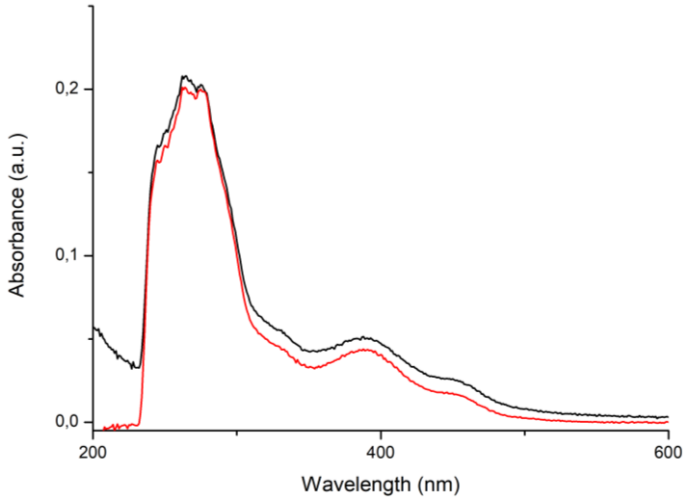

Figure 95 Stability of the complex C8. Comparison between the time zero solution (black line) with the same solution after 24 hours of incubation at 37°C in the dark (red line). Concentration of the complex is 20 µM, concentration of PBS buffer is 10 mM and the pH is 7.4. The solution is a mixture of an aqueous solution of PBS, 98%, and DMSO, 2%.

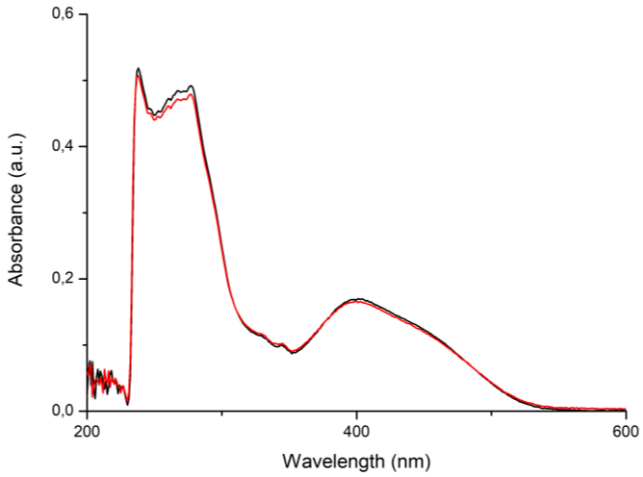

Figure 96 Stability of the complex C9. Comparison between the time zero solution (black line) with the same solution after 24 hours of incubation at 37°C in the dark (red line). Concentration of the complex is 20 µM, concentration of PBS buffer is 10 mM and the pH is 7.4. The solution is a mixture of an aqueous solution of PBS, 98%, and DMSO, 2%.

10.5 Photoactivation experiments: C8 and C9

Once evaluated the stability in the dark, I studied the photoactivation of the complexes with NMR, using the same conditions of the previous experiments. The LED blue light is the light source used for these complexes.

In figures 97 and 98, we can observe that these ruthenium-NHCs complexes are stable during the photoirradiation. For simplicity, I indicated with green spots those signals associated with the solvate ruthenium complex, that remain extremely small. All the other signals are completely stable. These complexes are extremely inert under the light irradiation if compared with the previous compounds. In fact, other complexes like C1 and C2, that are unable to absorb in the blue region, have a moderate photoactivation rate, while the complex C8 is totally stable. Surprisingly, also C9 is completely inert during the photoactivation, despite the presence of the piperidine naphthalenimide moiety.

This photostability can be ascribed by the fact that the carbene bond seems to be more resistant than the coordination bond of pyridine to the photoactivation.

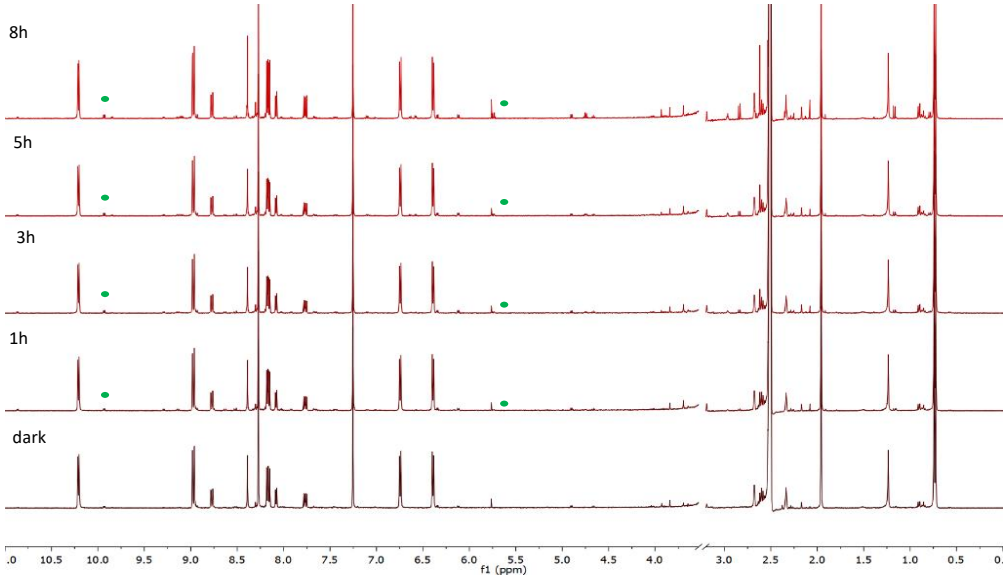

Figure 97 Photoactivation of the complex C8.

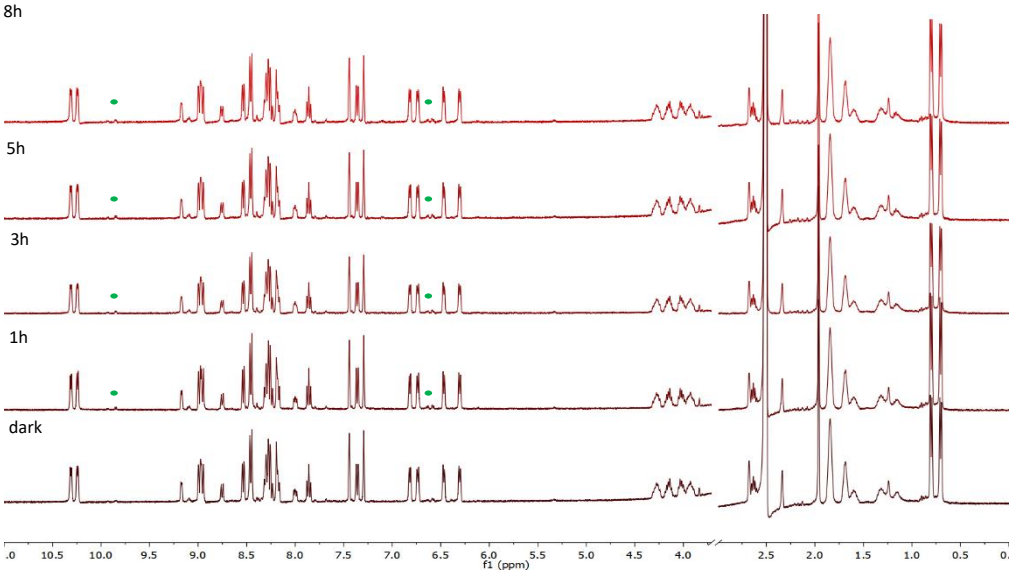

Figure 98 Photoactivation of the complex C9.

10.6 Photobiology of the complexes C8 and C9

In table 23 are presented the biological data of C8 and C9 respect the cell line A549. Despite the photostability described above, the biological activity of these complexes increases after the photoactivation like C8, that improves its biological activity of one order of magnitude. The peculiar biological activity of C8 can be due by the monodentate ligand, the dimethyl imidazolium. In fact, in literature [149-151] are present some papers that prove the biologic activity of ionic liquids, in particular imidazolium salts, respect the lung cancer cells A549.

	IC_{50} (µM) A549 24h	
	Non irradiated	**3 hours of irradiation**
C8	>100	11,68 ± 3,95
C9	63,33 ± 8,4	32,59 ± 7,11

Table 23 IC_{50} in micromolar of the complexes C8 and C9 before and after the irradiation.

In conclusion, this class of photoactivatable ruthenium-NHCs complexes show the most peculiar and interesting behavior during the photoactivation and the biological activity. The next necessary step will be the evaluation of the biological activity of the monodentate ligand alone.

11 New photoactivatable Ru(II) complexes with functionalized riboflavin as ligands

11.1 Riboflavin: an overview

The riboflavin (Rf), known as vitamin B_2, is an organic molecule naturally present in food and an essential nutrient for living beings, precursor of all biologically important flavins. Flavins are a class of yellow-colored molecules with the common structure of 7,8-dimethyl-10-alkylisoalloxazine [152] moiety. This molecular structure is characterized by three conjugated rings: a homocycle ring (benzene) and two heterocycle piperazine and pyrimidine. At the N^{10} of the piperazine ring an alcoholic sugar, ribityl, is additionally connected. The name riboflavin derives from the two components of the molecule: the ribityl side chain and the isoalloxazine unit responsible for the bright yellow color called in Latin flavus [153].

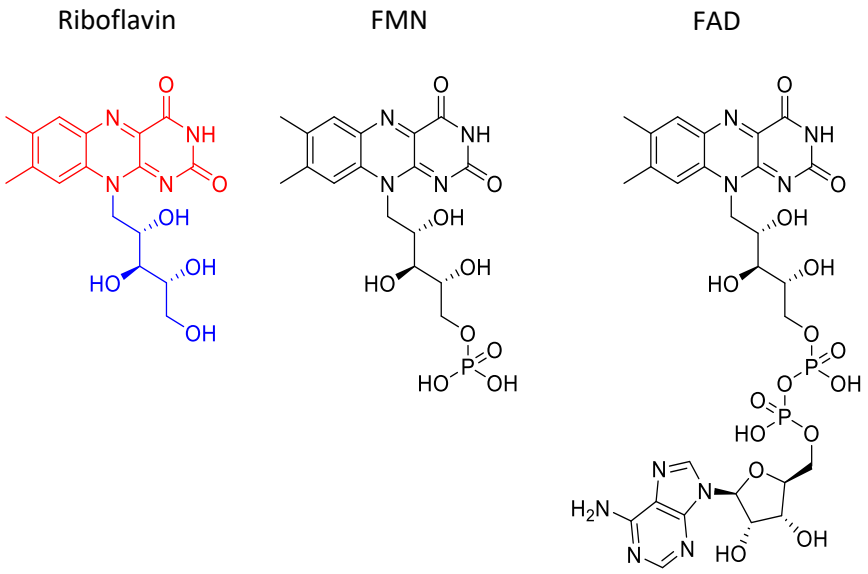

Figure 99 Structures of riboflavin and the most important flavin derivatives in biochemistry: FMN and FAD. In the riboflavin are indicated the two components of this molecule: the ribityl side chain, in blue, and the isoalloxazine unit, in red.

Rf is well-known for its redox properties and its central role in different one-electron and two-electron transfer processes. RFs can exist in three different redox states: oxidized, one-electron reduced (semiquinone), and two-electron reduced. Figure 100 shows that each of these three different redox states are in a pH-dependent equilibrium between a neutral, protonated and deprotonated state.

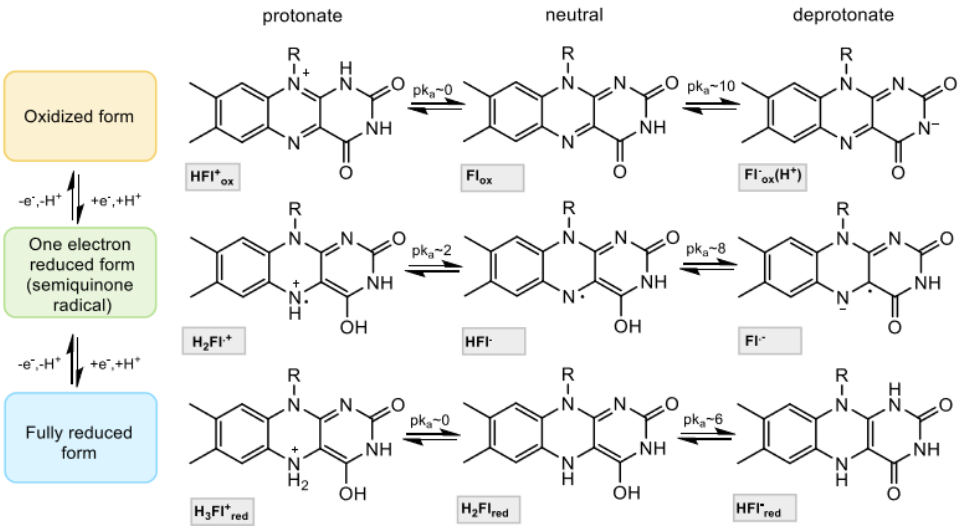

Figure 100 Redox states at different pH levels of Rf.

When Rf in the oxidized form is irradiated with blue light, it reaches the excited singlet state (^{1}Rf*) and then, through intersystem crossing, the triplet exited state (^{3}Rf*) is populated. Different pathways become possible when the ^{3}Rf* excited state is reached. It is important to highlight that passing from the ground state to the triplet excited state induces the variation of the reduction potential from -200 mV to +170 mV, redox potential referred for the two-electron reduction ($E_{ox/hq}$). Hence, the photoexcitation of Rf to the triplet exited state makes it a strong oxidation agent. In the absence of an external reductant, the ribityl side chain acts as

an electron donor towards the isoalloxazine ring system, leading to an intramolecular photoreduction. This results in the formation of multiple photoproducts. When instead an external electron donor substrate is present, an efficient intermolecular photoreduction happens. This allows to prevent the photodegradation, thanks to an electron-transfer process that can occur because of the high reduction potential of the ^{3}Rf* state. In presence of oxygen, riboflavin can also show photosensitizing properties: the ^{3}Rf* state is involved in the reaction with oxygen via Type I (electron transfer) or Type II (energy transfer) mechanism.

11.1.1 Riboflavin as catalyst for transition metal complex

Salassa and co-workers [154-157] have discovered a new way to take advantage of this Rf's property using this molecule like photocatalyst for the reduction and activation of Pt(IV) prodrugs. This approach subverted the typical catalyst approach, in which a coordination or organometallic complex is used to transform an organic substrate into added-value products, using an organic molecule in particular conditions, like Rf under light excitation, to transform metallic prodrugs in active metal complexes.

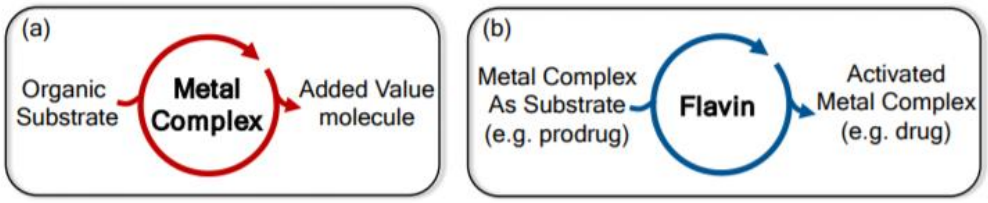

Figure 101 (a) Metal-based catalysis and (b) catalysis toward metal substrates [156].

Hence, Rf can be used like catalyst to achieve the spatial and temporal control of action of Pt(IV) prodrugs. In figure 102 is showed the proposed mechanism of action of this molecule. Rf absorbs 460 nm photons to reach the triplet excited state, ^{3}Rf*, taking two electrons from two MES molecules, in experiments outside the cell, or form NADH in cell, forming the reduced species RfH_2/RfH^-. The Pt(IV) prodrug, in this case a succinate derivative of cisplatin, interacts with the reduced Rf and it is subject to photoreduction and elimination reactions with a further absorption of photons, generating the cisplatin and the initially Rf catalyst.

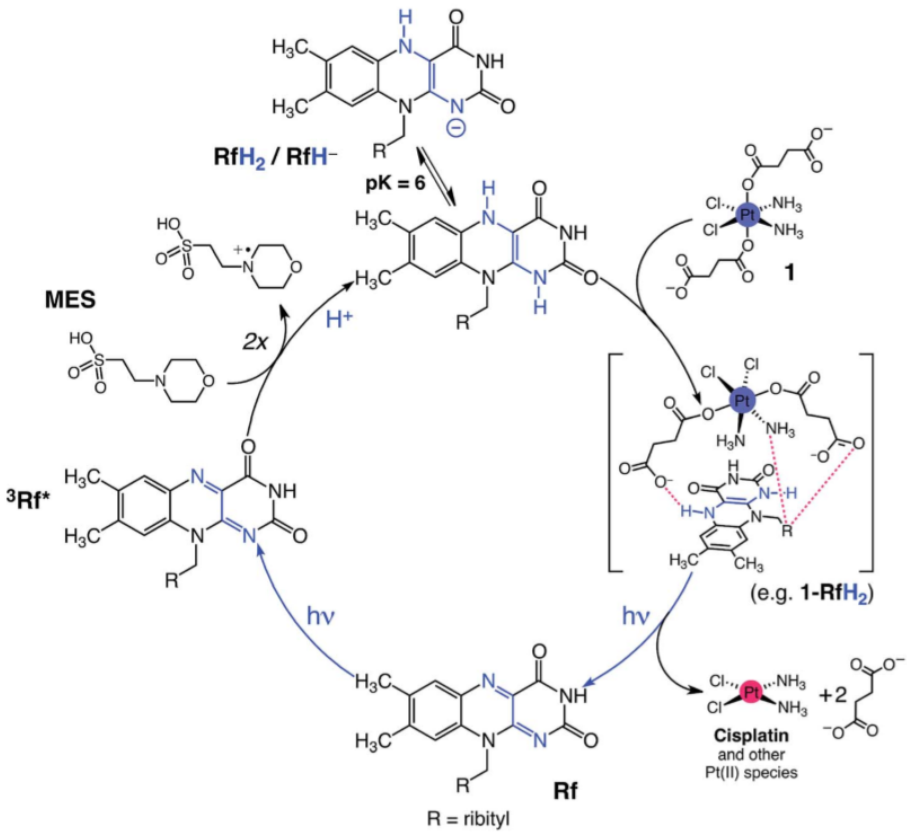

Figure 102 Proposed mechanism for the photocatalytic activation of a Pt(IV) prodrug [155].

11.1.2 New functionalized riboflavins as ligands for Ru(II) complexes

My PhD visiting period has been exploited in the laboratories of professor Salassa in San Sebastian, Spain, at Donostia International Physics Center (DIPC). The aim of my project was the synthesis of new functionalized Rfs to make them usable as ligands for ruthenium. These complexes can be studied for a "tandem" application, exploiting the photodissociation of the monodentate ligand of the ruthenium complexes with the ability to reduce a Pt(IV) prodrug by the Rfs. I investigated three new RFs, functionalized with an imidazolium moiety (L20), with a pyridine (L18) and a bipyridine (L24) respectively. The functionalized Rfs are obtained through a multistep synthetic pathway presented in the next figures 103, 104 and 105.

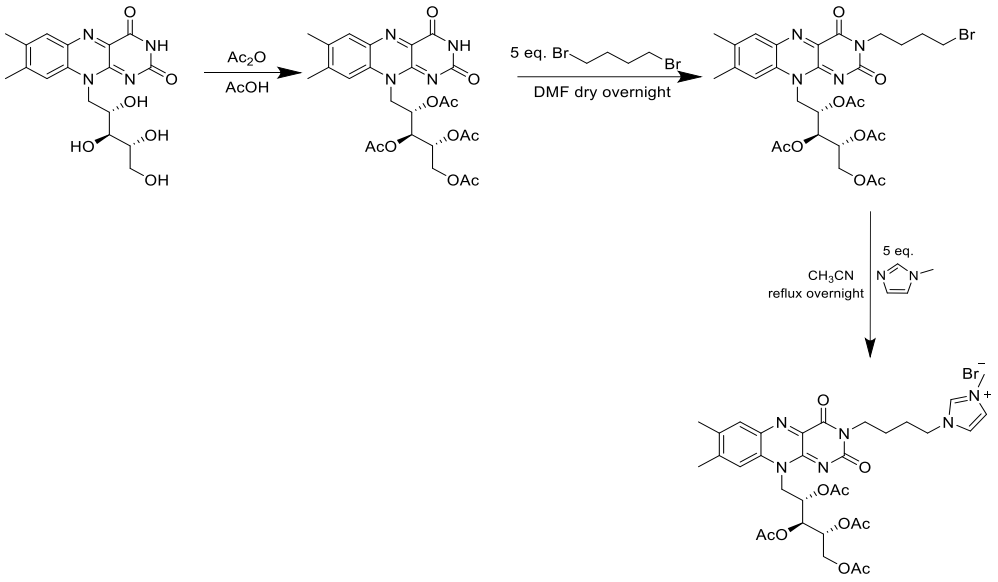

Figure 103 Synthetic pathway to obtain L20.

The first common step for all the Rfs described is the acetylation of the ribityl chain. It is necessary for two reasons: to prevent the photodecomposition of Rf, reducing intramolecular photoreduction of the isoalloxazine core by the ribityl side chain, and to increase the solubility of Rf in organic solvents.

In the synthesis of L20 (figure 103), the second step is the insertion of 1,4-dibromobutane in the NH group through a nucleophilic substitution. For the insertion of the methyl imidazole moiety is exploited the free bromo atom, with the formation of an imidazolium salt. This ligand is designed to form a ruthenium-NHC complex.

For the synthesis of L18 (figure 104) I introduced a bromo propyl amine protected with BOC. This protecting group is then eliminated with TFA to form the free amine. Thus, the pyridine moiety is inserted with the formation of an amide between the free amine and the isonicotinic active ester. The aim is to use this molecule like monodentate ligand in the ruthenium(II) complex.

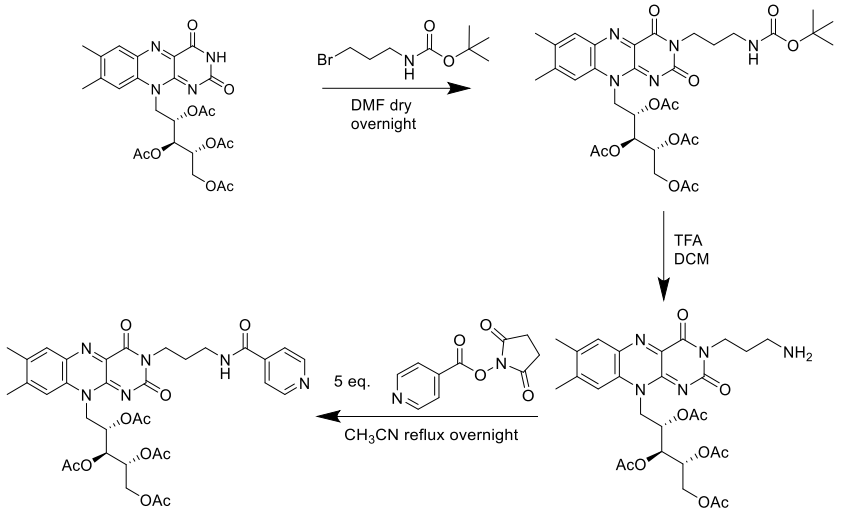

Figure 104 Synthetic pathway to obtain L18.

Finally, in figure 105 is presented the synthesis of L24. The synthetic pathway is the same of L18. In that case I used a bipyridine with two different ester moieties, a methyl-ester and the active ester. The L24 is synthesized to obtain a bidentate ligand for the ruthenium(II) complex.

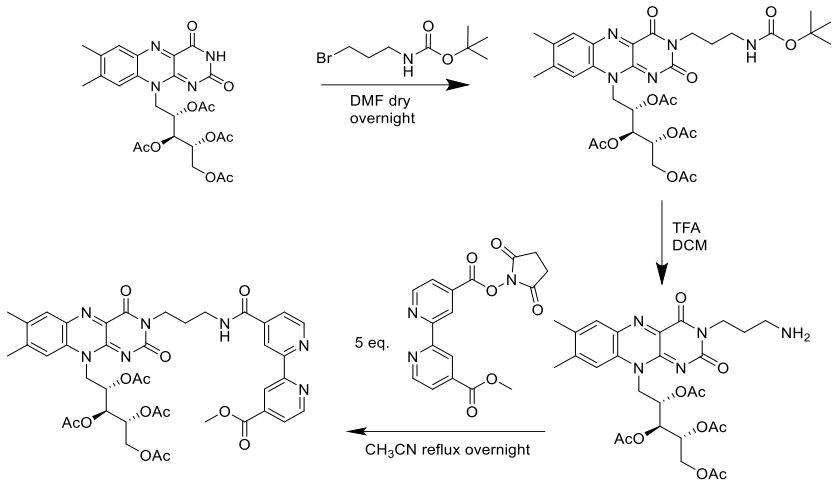

Figure 105 Synthetic pathway to obtain L24.

Once obtained the ligands I used them to synthesize new ruthenium(II) complexes with the RF moiety. As already observed, Rfs L20 and L18 are monodentate ligands while L24 is a bidentate ligand.

As described in the previous chapters, silver compounds are fundamental during the synthesis of the ruthenium(II) complexes. The silver(I) oxide is necessary for the formation of the carbene while silver(I) triflate is used for the halogen scavenging of the chlorides before the insertion of the bidentate ligand. In literature [158], is described the formation of complex between riboflavin and both silver(I) and copper(I) ions. In particular, this molecule interacts with the metal ion trough the nitrogen atom in 10 position and the carbonyl group in 4 position, as shown in figure 106. The concomitant presence of silver(I) and Rfs is a serious problem for the ability of Rf to interact with the metal ion Ag^+, seizing it from the reaction environment.

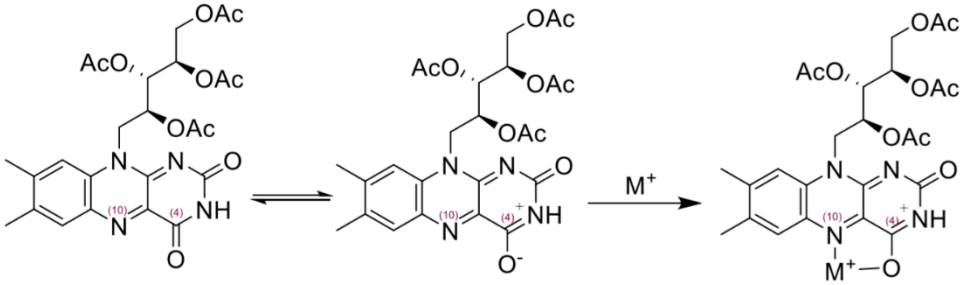

Figure 106 Rf complexation of Ag(I) and Cu(I).

This unexpected behavior of the Rf respect to the silver(I) ion, hindered the isolation of the ruthenium-NHC complex with L20. Instead, the other two complexes C10 and C11 were obtained with L18 and L20 ligands respectively (figure 107).

Complex C10 is characterized by the Rf L18 monodentate ligand while the 1,10-phenanthroline is the bidentate ligand. Instead, C11 has Rf L20 like the bidentate ligand, while the monodentate ligand chosen is L4, the naphthalenimide with the best performance in term of photoactivation.

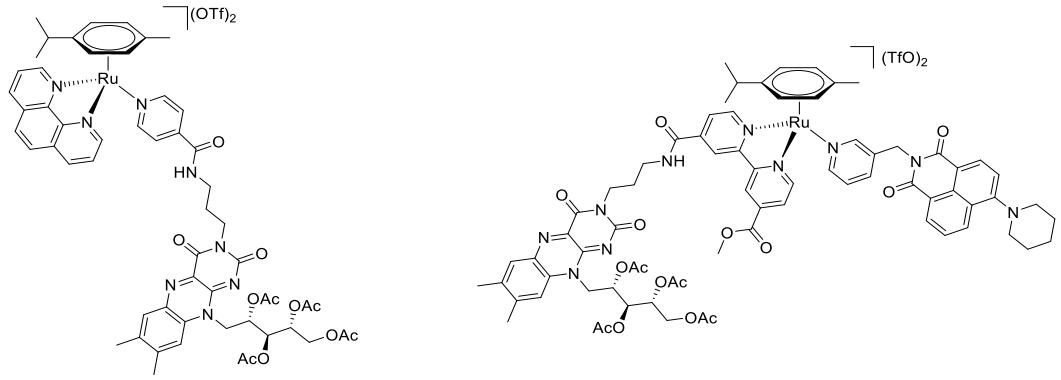

C10 C11

Figure 107 Structure of the complexes C10 and C11.

11.2 Absorption spectra: C10 and C11

In figure 108 are compared the absorption spectra of the three functionalized Rfs. L18 and L24 have the same absorbance and their spectra are superimposed. The absorption spectra of this Rfs doesn't change with the functionalization, keeping the absorption band in the blue region, *conditio sine qua non* for the photocatalysis of prodrugs.

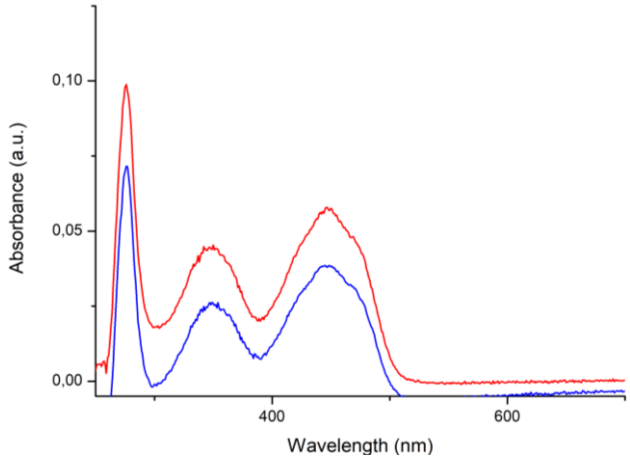

Figure 108 Absorption spectra of L18 (black line), L20 (red line) and L24 (blue line). L18 and L24 have the same absorbance and their spectra are superimposed. The spectra are performed in DMSO at 10 µM.

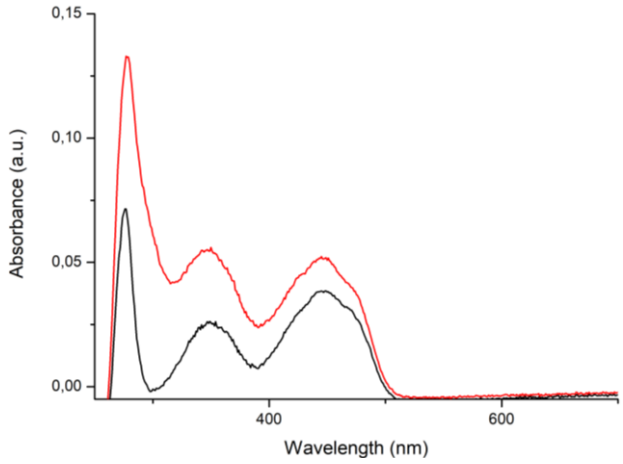

Figure 109 Absorption spectra of L18 (black line) and C10 (red line). The spectra are performed in DMSO at 10 µM.

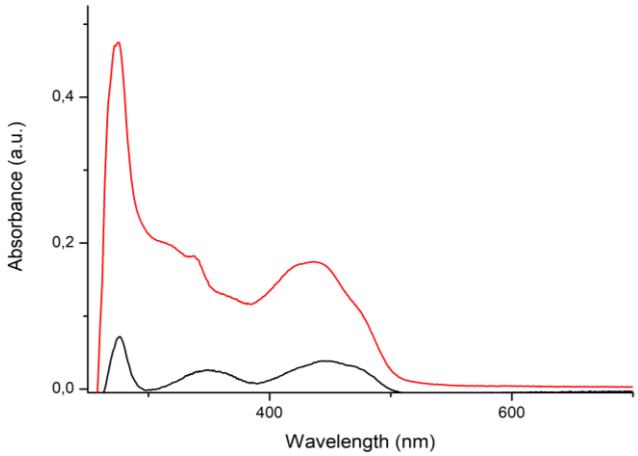

Figure 110 Absorption spectra of L24 (black line) and C11 (red line). The spectra are performed in DMSO at 10 µM.

In figures 109 and 110 are showed the absorption spectra of C10 and C11 compared with their ligands. In both cases, the complexes are able to interact in the blue region with a major intensity respect to their ligands.

11.3 Stability in the dark: C10 and C11

The stability in the dark and in physiological conditions for complexes C10 and C11 are showed in figures 111 and 112 respectively. Also for this type of complexes, characterized by ligands with a great structural complexity, the stability in the dark is confirmed.

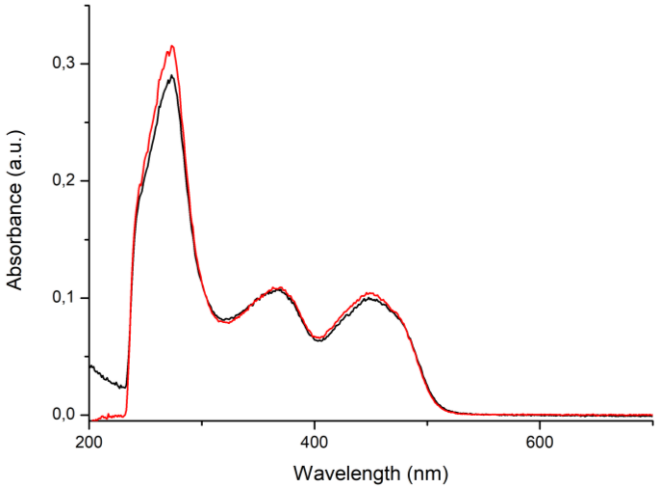

Figure 111 Stability of the complex C10. Comparison between the time zero solution (black line) with the same solution after 24 hours of incubation at 37°C in the dark (red line). Concentration of the complex is 20 µM, concentration of PBS buffer is 10 mM and the pH is 7.4. The solution is a mixture of an aqueous solution of PBS, 98%, and DMSO, 2%.

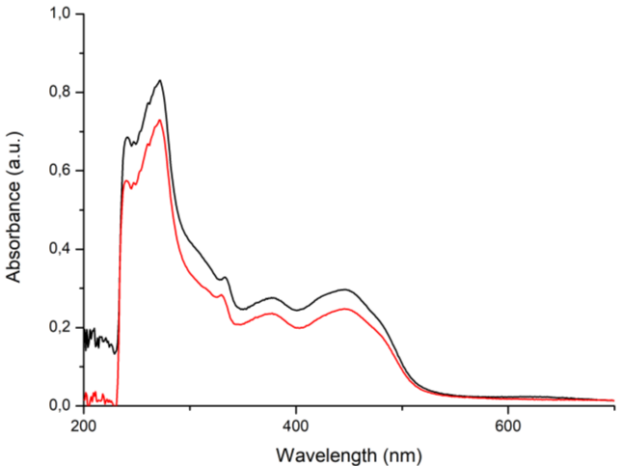

Figure 112 Stability of the complex C11. Comparison between the time zero solution (black line) with the same solution after 24 hours of incubation at 37°C in the dark (red line). Concentration of the complex is 20 µM, concentration of PBS buffer is 10 mM and the pH is 7.4. The solution is a mixture of an aqueous solution of PBS, 98%, and DMSO, 2%.

11.4 Photoactivation experiments: C10 and C11

The photoactivation of these complexes is evaluated with the blue LED light. The characteristic of these complexes is the great complexity of the NMR spectra, that makes them difficult to understand.

In figure 113 is presented the photoactivation experiments of the complex C9. Here, the spectra are described using the same color code of the previous experiments. The signals between 5.5 ppm and 4.0 ppm are associated with the ribityl chain and during the photoactivation don't change. This information suggests the ligand doesn't photodegrade, and the unique change induced by the light is the photodissociation of the complex.

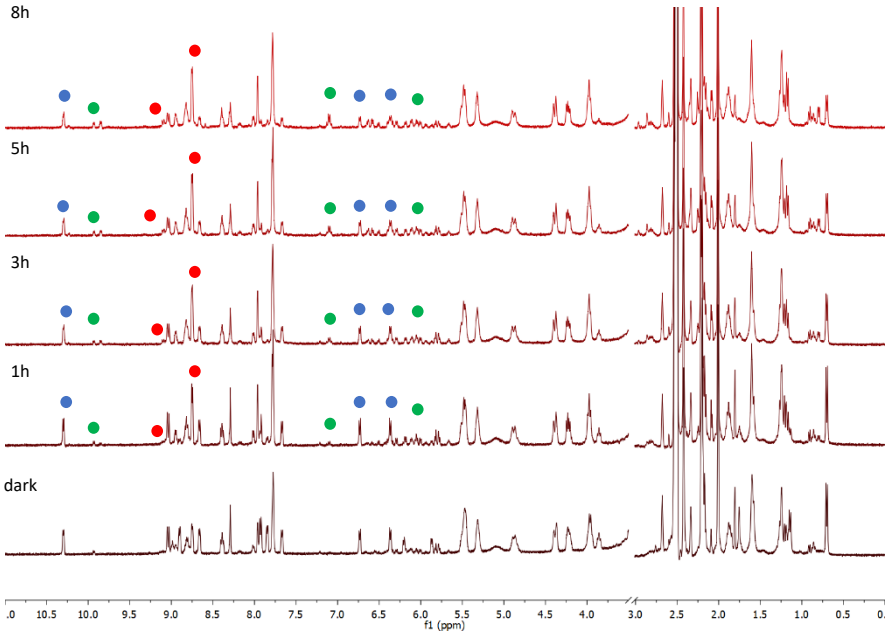

Figure 113 Photoactivation of the complex C10.

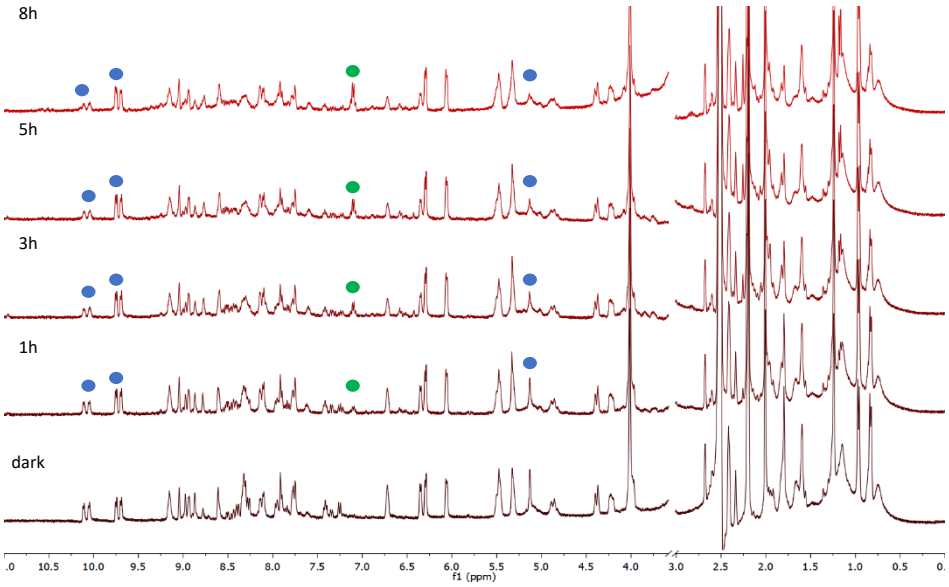

Figure 114 Photoactivation of the complex C11.

The photoactivation experiments for C11 are presented in figure 114. The spectra of this complex are more chaotic of the previous one and is not possible an extensive description of all the signals. It is noteworthy that also in that case the signals of the ribityl chain don't change during the photoactivation. The only signal that varies during the irradiation time is the signal at 5.17 ppm, indicated with a blue spot. This signal is associated with the methylene group of L4, also present in the complex C11.

Both these Rf-complexes are able of change their structure with the light without the degradation of the Rfs. These spectra are extremely chaotic and tough to describe extensively, so the kinetics rate cannot be defined like in the previous cases.

11.5 Photobiology of the complexes C10 and C11

Finally, the biological activity of these complexes is evaluated against the tumor cell line A549 in table 24. Both these complexes increase their antiproliferative activity after the irradiation. C10 increases its biological activity of one order of magnitude after the photoirradiation. In conclusion, these new Rf-ruthenium complexes are able to release the monodentate ligand under light without the degradation of the Rfs. Unfortunately, both the ligands, L18 and L24, are more active after the irradiation, than the respective complexes.

	IC_{50} (µM) A549 24h	
	Non irradiated	**3 hours of irradiation**
C10	>100	1,51 ± 0,19
C11	>100	13,65 ± 2,83
L18	>100	<1
L24	>100	5,96 ± 1,32

Table 24 IC_{50} in micromolar of the complexes C10 and C11 before and after the irradiation.

12 Conclusion

To conclude, in this chapter I described a new class of photoactivatable piano-stool Ru(II) arene complexes with different class of monodentate and bidentate ligands. The piano-stool Ru(II) complex is a useful and flexible scaffold to develop new photoactivated chemotherapeutic complexes. All the complexes here presented are stable in physiological conditions in the dark. They can be divided, according to the kind of ligands, in three different classes: ruthenium complexes with pyridine-like ligands, ruthenium complexes with carbene ligands and ruthenium complexes with Rf ligands.

The first class is the most studied and the richest of examples. Here, I used different type of naphtahlenimides like monodentate ligands, and different bidentate ligands. The data collected for this class of molecules

suggest that the rate of photoactivation is inversely proportional respect to the intensity of the emission. The complex C5 has the best biological activity in this class.

The second class, the ruthenium-NHC complexes, is characterized by a great photostability, due by the carbene bond. Despite this photostability, the biological activity of the two ruthenium-NHC complexes here presented increase a lot after the irradiation. This fact can be due by the great biological activity of the ionic liquid, like imidazolium salts, making this class of complexes extremely interesting for future studies.

Finally, the third class is the Rf-ruthenium complexes. Also these complexes are photoactivatable with a biological activity that increases after the irradiation, but they are less effective than their Rf ligands, L18 and L24. In the future can be interesting evaluate the ability of these functionalized Rfs to reduce Pt(IV) prodrugs in cells.

13 Experimental section

13.1 Ligands

N-(3-methylenepyridyl)-1,8-naphthalimide (L1)

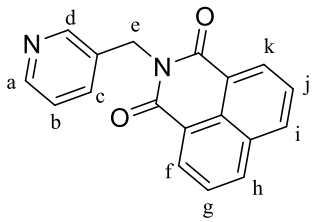

L1 was synthesized according to the procedure reported in literature [122]: 1,8-naphthalenic anhydride (0.30 g, 1.51 mmol) and 3-picolylamine (0.196 g, 1.81 mmol) were dissolved in 10 mL of DMF. The mixture was heated at 130°C for 24 hours. The mixture was cooled to room temperature obtaining a solid which was separated by filtration and dried under vacuum. Pale yellow microcrystalline solid. **Yield**: 87%. **^{1}H-NMR** (δ, ppm, 400 MHz, DMSO-D_6): 8.66 (dd, J = 2.3 Hz, J' = 0.9 Hz, 1H, H_d), 8.51 (m, 4H, H_f, H_h, H_i, H_k), 8.46 (dd, J = 4.8 Hz, J' = 1.7 Hz, 1H, H_a), 7.89 (dd, J = 8.3 Hz, J' = 7.3 Hz, 2H, H_b, H_c), 7.78 (ddd, J = 7.9 Hz, J' = 2.4 Hz, J'' = 1.7 Hz, 1H, H_g), 7.33 (ddd, J = 7.9 Hz, J' = 4.8 Hz, J'' = 0.9 Hz, 1H, H_j), 5.32 (s, 2H, H_e). **^{1}H-NMR** (δ, ppm, 400 MHz, $CDCl_3$): 8.89 (d, J = 2.1 Hz, 1H, H_d), 8.62 (dd, J = 8.5 Hz, J = 1.0 Hz, 2H, H_f, H_k), 8.54 (dd, J = 5.2 Hz, J = 2.1 Hz, 1H, H_a), 8.24 (dd, J = 8.5 Hz, J = 1.0 Hz, 2H, H_h, H_i), 8.02 (dt, J = 8.0 Hz, J' = 2.1 Hz, 1H, H_b), 7.76 (t, J = 8.5 Hz, 2H, H_g, H_j), 7.34 (ddd, J = 8.0 Hz, J' = 5.2 Hz, J'' = 2.1 Hz, 1H, H_c), 5.43 (s, 2H, H_e) **^{13}C-NMR** (δ, ppm, 100 MHz, DMSO-D_6): 164.08 (C=O imides), 149.75 (C-H pyridine close to N), 148.83 (C-H pyridine close to N), 135.97 (C-H naphthalene), 135.12 (C-H naphthalene), 133.54 (C-H pyridine), 131.84 (C quaternary pyridine), 131.52 (C-H naphthalene), 128.01 (C quaternary naphthalene), 127.78 (C quaternary naphthalene), 124.05 (C quaternary naphthalene), 122.43 (C-H pyridine), 41.27 (CH_2 bridge) **ESI-MS (+)** m/z calc. 289.3 found 288.8 **CHNS analysis**: $C_{18}H_{12}N_2O_2$: calculated: C: 74.99, H: 4.20, N: 9.72. Found: C: 74.93, H: 4.14, N: 9.80.

3-nitro-N-(3-methylenepyridyl)-1,8-naphthalimide (L2)

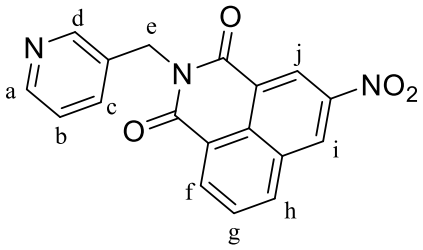

3-nitro-1,8-naphthalenic anhydride (0.5 g, 2.06 mmol) and 3-picolylamine (0.267 g, 2.47 mmol) were dissolved in 25 ml of ethanol at 80°C and heated for 24 hours. After 1 hour of reaction there was the formation of a solid precipitate. The mixture was cooled to room temperature and the solid was separated by filtration and dried under vacuum. Pale brown solid. **Yield**: 89%. **^{1}H-NMR** (δ, ppm, 400 MHz, DMSO-D_6): 9.50 (d, J = 2.3 Hz, 1H, H_j), 8.99 (d, J = 2.3 Hz, 1H, H_i), 8.80 (dd, J = 8.4 Hz, J' = 1.2 Hz, 1H, H_h), 8.71 (dd, J = 7.3 Hz, J' = 1.1 Hz, 1H, H_a), 8.67 (d, J = 2.3 Hz, 1H, H_d), 8.47 (dd, J = 4.9 Hz, J' = 1.6 Hz, 1H, H_f), 8.07 (dd, J = 8.3 Hz, J' = 7.3 Hz, 1H, H_g), 7.81 (dt, J = 7.9 Hz, J' = 2.1 Hz, 1H, H_b), 7.34 (m, 1H, H_c), 5.30 (s, 2H, H_e). **^{1}H-NMR** (δ, ppm, 400 MHz, $CDCl_3$): 9.37 (d, J = 2.2 Hz, 1H, H_j), 9.17 (d, J = 2.3 Hz, 1H, H_i), 8.87 (d, J = 2.3 Hz, 1H, H_d), 8.83 (dd, J = 7.3 Hz, J' = 1.2 Hz, 1H, H_a), 8.55 (dd, J = 4.8 Hz, J' = 1.7 Hz, 1H, H_f), 8.47 (ddd, J = 8.2 Hz, J' = 1.2 Hz, J'' = 0.5 Hz, 1H, H_h), 7.98 (dd, J = 8.3 Hz, J' = 7.3 Hz, 1H, H_g), 7.93 (m, 1H, H_b), 7.28 (m, 1H, H_c), 5.43 (s, 2H, H_e) **^{13}C-NMR** (δ, ppm, 100 MHz, $CDCl_3$): 163.06 (C=O imides), 162.52 (C=O imides), 149.49 (C-H pyridine close to N), 147.91 (C quaternary naphthalene close to NO_2), 146.36 (C-H pyridine close to N), 138.45 (C-H naphthalene), 136.02 (C-H naphthalene), 134.89 (C-H naphthalene), 133.11 (C-H pyridine), 131.09 (C quaternary pyridine), 130.12 (C quaternary naphthalene), 129.36 (C-H naphthalene), 129.23 (C-H naphthalene), 124.70 (C quaternary naphthalene), 124.43 (C quaternary naphthalene), 123.94 (C quaternary naphthalene), 122.92 (C-H pyridine), 41.41 (CH_2 bridge) **ESI-MS (+)** m/z calc. 334.30 found 334.15 **CHNS analysis**: $C_{18}H_{11}N_3O_4$: calculated: C: 64.87, H: 3.33, N: 12.61. Found: C: 65.68, H: 3.29, N: 12.46.

4-bromo-N-(3-methylenepyridyl)-1,8-naphthalimide (L3)

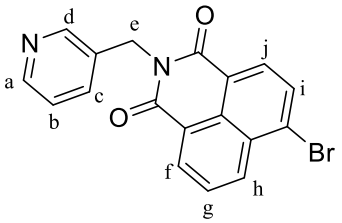

4-bromo-1,8-naphthalenic anhydride (0.2 g, 0.73 mmol) and 3-picolylamine (0.093 g, 0.86 mmol) were dissolved in 15 ml of ethanol at 80°C and heated for 24 hours. After 1 hour of reaction there was the formation of a solid precipitate. The mixture was cooled to room temperature and the solid was separated by filtration and dried under vacuum. White solid. **Yield**: 91%. **^{1}H-NMR** (δ, ppm, 400 MHz, $CDCl_3$): 8.87 (d, J = 2.4 Hz, 1H, H_d), 8.70 (dd, J = 7.3 Hz, J' = 1.2 Hz, 1H, H_i), 8.62 (dd, J = 8.5 Hz, J' = 1.2 Hz, 1H, H_j), 8.55 (dd, J = 5.0 Hz, J' = 1.6 Hz, 1H, H_a), 8.46 (d, J = 7.9 Hz, 1H, H_h), 8.09 (d, J = 7.8 Hz, 1H, H_f), 7.99 (dt, J = 8.0 Hz, J' = 2.0 Hz, 1H, H_g), 7.89 (dd, J = 8.5 Hz, J' = 7.3 Hz, 1H, H_b), 7.33 (dd, J = 8.0 Hz, J' = 4.9 Hz, 1H, H_c), 5.41 Hz (s, 2H, H_e) **^{13}C-NMR** (δ, ppm, 100 MHz, $CDCl_3$): 163.56 (C=O imides), 150.25 (C-H pyridine close to N), 148.56 (C-H pyridine close to N), 137.39 (C-H naphthalene), 133.70 (C-H naphthalene), 132.94 (C-Br naphthalene), 132.44 (C-H pyridine), 131.59 (C-H naphthalene), 131.22 (C-H naphthalene), 130.78 (C quaternary pyridine), 130.71 (C quaternary naphthalene), 129.02 (C quaternary naphthalene), 128.18 (C-H pyridine), 123.57 (C-H naphthalene), 122.79 (C quaternary naphthalene), 121.91 (C quaternary naphthalene), 41.24 (CH_2 bridge) **ESI-MS (+)** m/z calc. 368.20 found 368.97 **CHNS analysis**: $C_{18}H_{11}N_2O_2Br$: calculated: C: 58.88, H: 3.03, N: 7.63. Found: C: 58.84, H: 3.00, N: 7.88.

4-piperidinyl-N-(3-methylenepyridyl)-1,8-naphthalimide (L4)

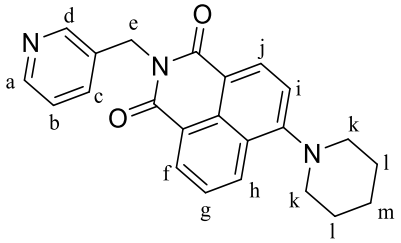

This ligand was synthesized according to the procedure reported in literature [159]: **L3** (0.459 g, 1.25 mmol) was dissolved in 3 mL of piperidine and the mixture was heated to 110°C for 2 hours. After cooling to room temperature, the excess of piperidine was removed under vacuum. The solid was dissolved in hot ethanol and recrystallized at -4°C. The product was then collected by filtration, washed whit ethanol, and finally dried under vacuum. Bright orange solid. **Yield**: 89%. **^{1}H-NMR** (δ, ppm, 400 MHz, DMSO-D_6): 8.63 (d, J = 2.3 Hz, 1H, H_d), 8.50 (dd, J = 7.3 Hz, J' = 1.1 Hz, 1H, H_f), 8.44 (m, 3H, H_a, H_i, H_j), 7.83 (dd, J = 8.5 Hz, J' = 7.3 Hz, 1H, H_b), 7.74 (dt, J = 8.0 Hz, J' = 2.0 Hz, 1H, H_g), 7.33 (dd, J = 8.2 Hz, J' = 5.4 Hz, 2H, H_h, H_c), 5.27 (s,2H, H_e), 3.23 (d, J = 10.6 Hz, 4H, H_k), 1.83 (bs, 4H, H_l), 1.68 (bs, 2H, H_m). **^{1}H-NMR** (δ, ppm, 400 MHz, $CDCl_3$): 8.86 (d, J = 2 Hz, 1H, H_d), 8.60 (dd, J = 8.4 Hz, J' = 1.2 Hz, 1H, H_f), 8.53 (dd, J = 8.4 Hz, J' = 1.6 Hz, 2H, superimposed signals H_a e H_j), 8.42 (d, J = 9.6 Hz, J' = 1.2 Hz, 1H, H_h), 7.99 (dt, J = 8 Hz, 1H, H_b), 7.70 (dd, J = 16 Hz, J' = 7.6 Hz, 1H, H_g), 7.32 (dd, J = 12.8 Hz, J' = 3,2 Hz, 1H, H_c), 7.20 (d, J = 8.2 Hz, 1H, H_i), 5.41 (s, 2H, H_e), 3.26 (bs, 4H, H_k),1.91 (bs, 4H, H_l), 1.75 (bs, 2H, H_m) **^{13}C-NMR** (δ, ppm, 100 MHz, $CDCl_3$): present in literature [160] **ESI-MS (+)** m/z calc. 372.44 found 372.78 **CHNS analysis**: $C_{23}H_{21}N_3O_2$: calculated: C: 74.37, H: 5.70, N: 11.31. Found: C: 74.15, H: 5.82, N: 11.24.

4-bromo-N-(5-phenantrolin)-1,8-naphthalimide (L5)

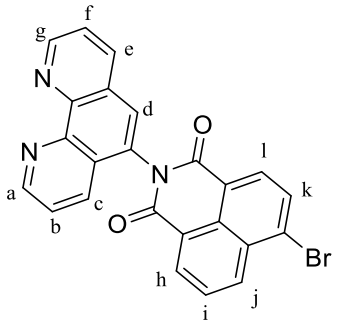

4-Bromo-1,8-naphthalenic anhydride (0.400 g, 1.44 mmol, 1 eq.) and 1,10-phenantrolin-5-amine (0.282 g, 1.44 mmol, 1 eq.) were dissolved in 20 mL of glacial acetic acid and the mixture was heated to 100°C for 24 hours. After a few hours, the solution turned from bright orange to dark red. The reaction was monitored by TLC (eluent DCM – methanol ratio 9:1). The solution was cooled to room temperature and 10 mL of ethyl acetate was added to proceed with extraction. The solution was extracted with water and $NaHCO_{3\,(aq)}$ and dried under vacuum. The dark solid was then purified with the chromatographic column (eluent DCM - methanol 98:2, 95:5 and finally 90:10). White solid. **Yield**: 64%. **^{1}H-NMR** (δ, ppm, 400 MHz, $CDCl_3$): δ 7.65 (dd, 1H, J=12.8 Hz, ^{1}J=4.4 Hz, H_f), 7.77 (dd, 1H, J=12.4 Hz, ^{1}J=4.4 Hz, H_b), 7.94 (s, 1H, H_d), 7.99 (dd, 1H, J=16 Hz, ^{1}J=7.2 Hz, H_i), 8.08 (d, 1H, J=7.2 Hz, H_e), 8.19 (d, 1H, J=4.4 Hz, H_k), 8.37 (d, 1H, J=8 Hz, H_c), 8.54 (d, 1H, J=7.6 Hz, H_l), 8.77 (m, 2H, superimposed signals H_h e H_j), 9.31 (d, 1H, J=3.6 Hz, H_a), 9.36 (d, 1H, J=4.4 Hz, H_g) **^{13}C-NMR** (δ, ppm, 100 MHz, $CDCl_3$): 162.57 (C=O imides), 159.83 (C=O imides), 156.65 (C quaternary phenantroline), 148.73 (C-H phenantroline close to N), 143.02 (C quaternary phenatroline), 136.25 (C-H naphthalene), 132.48 (C-H naphthalene), 132.30 (C-Br naphthalene), 131.01 (C-H phenantroline), 130.98 (C-H naphthalene), 130.77 (C-H phenantroline), 130.49 (C-H naphthalene), 130.71 (C quaternary naphthalene), 128.79 (C quaternary naphthalene), 127.59 (C quaternary phenantroline), 126.12 (C-H phenantroline), 124.37 (C-H phenantroline), 123.32 (C-H naphthalene), 122.92 (C quaternary naphthalene), 122.19 (C

quaternary phenantroline), 121.46 (C quaternary naphthalene) **ESI-MS (+)** m/z calc. 453.01 found 453.42 **CHNS analysis**: $C_{24}H_{12}N_3O_3Br$: calculated: C: 63.45, H: 2.66, N: 9.25 Found: C: 62.78, H: 2.84, N: 9.03.

4-piperidinyl-N-(5-phenantrolin)-1,8-naphthalimide (L6)

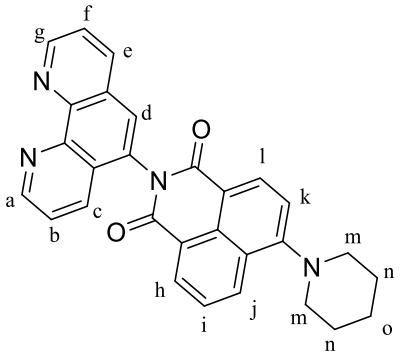

The same procedure used for compound **L4** was applied by reacting compound **L5** (0.407 g, 0.896 mmol) in 10 mL of piperidine. Orange solid. **Yield**: 95%. **^{1}H-NMR** (δ, ppm, 400 MHz, DMSO-D_6): 8.63 (d, J = 2.3 Hz, 1H), 8.50 (dd, J = 7.3 Hz, J' = 1.1 Hz, 1H), 8.44 (m, 3H), 7.83 (dd, J = 8.5 Hz, J' = 7.3 Hz, 1H), 7.74 (dt, J = 8.0 Hz, J' = 2.0 Hz, 1H), 7.33 (dd, J = 8.2 Hz, J' = 5.4 Hz, 2H), 5.27 (s,2H), 3.23 (d, J = 10.6 Hz, 2H), 1.83 (s, 5H), 1.68 (d, J = 6.4 Hz, 3H). **^{1}H-NMR** (δ, ppm, 400 MHz, $CDCl_3$): 8.85 (m, 1H), 8.61 (dd, J = 7.3 Hz, J' = 1.2 Hz, 1H), 8.53 (d, J = 8.1 Hz, 1H), 8.51 (dd, J = 4.8 Hz, J' = 1.7 Hz, 1H), 8.42 (dd, J = 8.4 Hz, J' = 1.2 Hz, 1H), 7.89 (m, 1H), 7.70 (dd, J = 8.5 Hz, J' = 7.3 Hz, 1H), 7.24 (ddd, J = 7.8 Hz, J' = 4.8 Hz, J'' = 0.9 Hz, 1H), 7.20 (d, J = 8.2 Hz, 1H), 5.39 (s,2H), 3.26 (t, J = 5.1 Hz, 4H), 1.91 (p, J = 5.7 Hz, 4H), 1.75 (d, J = 5.6 Hz, 2H) **^{13}C-NMR** (δ, ppm, 100 MHz, $CDCl_3$): 164.69 (C=O imides), 164.13 (C=O imides), 158.20 (C-N piperidine quaternary), 157.55 (C quaternary phenantroline), 149.60 (C-H phenantroline close to N), 141.79 (C quaternary phenatroline), 133.74 (C-H naphthalene), 133.20 (C quaternary naphthalene), 132.13 (C-H phenantroline), 131.88 (C-H phenantroline), 128.59 (C quaternary naphthalene), 127.62 (C-H naphthalene), 127.01 (C quaternary phenantroline), 126.50 (C quaternary naphthalene), 125.68 (C-H phenantroline), 124.95 (C quaternary naphthalene), 124.28 (C quaternary naphthalene), 124.11 (C-H phenantroline), 122.56 (C quaternary phenantroline), 114.88 (C-H naphthalene), 54.56 (CH_2 piperidine close to N), 26.21 (CH_2 piperidine), 24.32 (CH_2 piperidine) **ESI-MS (+)** m/z calc. 372.44 found 372.78. **CHNS analysis**: $C_{29}H_{22}N_4O_2$: calculated C: 75.97, H: 4.84, N: 12.22. Found: C: 75.82, H: 4.02, N: 12.57.

Dipyridophenazine (L7)

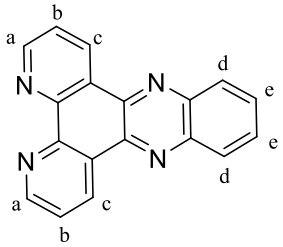

1,2-Phenylendiamine (0.200 g, 1.85 mmol, 1 eq.) and 1,10-phenantrolin-5,6-dione (0.389 g, 1.85 mmol, 1 eq.) were dissolved in 25 mL of methanol. A clear yellow solution was obtained, and it was heated to 70°C for 2 hours. While cooling to room temperature, the pure product precipitated and then it was collected by filtration, washed with methanol, and dried under vacuum. White crystalline solid. **Yield**: 90%. **^{1}H-NMR** (δ, ppm, 400 MHz, $CDCl_3$): 7.82 (dd, J = 12.8 Hz, J' = 4.4 Hz, 2H, H_b), 7.95 (dd, J = 10 Hz, J' = 3.2 Hz, 2H, H_e), 8.39 (dd, J = 9.6 Hz, J' = 3.2 Hz, 2H, H_d), 9.30 (dd, J = 4.4 Hz, J' = 1.6 Hz, 2H, H_c), 9.67 (dd, J = 8.2 Hz, J' = 2 Hz, 2H, H_a) **^{13}C-NMR** (δ, ppm, 100 MHz, $CDCl_3$): present in literature [161] **ESI-MS (+)** m/z calc. 282.31 found 282.68 **CHNS analysis**: $C_{18}H_{10}N_4$: calculated C: 76.58, H: 6.39, N: 19.85. Found: C: 77.12, H: 3.86, N: 18.64.

N-(3-Methylenpyridyl)-rhodamine 6G (L8)

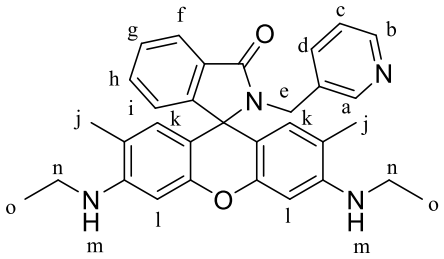

Rhodamine 6G (0.200 g, 0.418 mmol, 1 eq.) was dissolved in 5 mL of DMF. Then, 3-picolylamine (0.090 g, 0.836 mmol, 2 eq.) was added and the purple mixture was heated and stirred to 50°C for 72 hours. The solution was cooled to room temperature and then distilled water was slowly dropped at 0°C to induce precipitation of the product. The white solid was centrifuged, washed with water, and dried under vacuum. Bright purple solid. **Yield**: 55% **^{1}H-NMR** (δ, ppm, 400 MHz, $CDCl_3$): 8.25 (dd, J = 6.4 Hz, J' = 1.6 Hz, 1H, H_b), 8.04 (d, J = 2 Hz, 1H, H_a), 7.99 (m, 1H, H_i), 7.49 (m, 3H, superimposed signals H_c, H_g, H_h), 7.08 (m, 1H, H_f), 6.97 (dd, J = 12.8 Hz, J' = 4.8 Hz, 1H, H_d), 6.31 (s, 2H, H_l), 6.02 (s, 2H, H_k), 4.32 (s, 2H, H_e), 3.22 (m, 4H, H_n), 1.78 (s, 6H, H_j), 1.34 (t, J = 14 Hz, 6H, H_o) **^{13}C-NMR** (δ, ppm, 100 MHz, $CDCl_3$): 168.05 (C quaternary amide), 153.36 (C quaternary rhodamine close to O), 151.72 (C-H pyridine close to N), 148.99 (C quaternary rhodamine close to NH), 147.46 (C-H pyridine close to N), 146.77 (C quaternary rhodamine close to NH), 137.14 (C quaternary rhodamine), 133.82 (C quaternary rhodamine), 132.72 (C-H pyridine), 130.89 (C quaternary pyridine), 128.63 (C-H rhodamine), 128.16 (C-H pyridine), 123.87 (C-H rhodamine), 122.97 (C-H rhodamine), 122.58 (C quaternary rhodamine), 117.90 (C-H rhodamine), 105.41 (C-H rhodamine), 96.40 (C-H rhodamine), 65.13 (C quaternary rhodamine), 41.13 (CH_2 bridge), 38.35 (CH_2 NH ethyl rhodamine), 16.53 (CH_3 NH ethyl rhodamine), 14.74 (CH_3 rhodamine) **ESI-MS (+)** m/z $[M+H^+]^+$ calc. 504.25 found 504.85 m/z $[M+Na^+]^+$ calc. 527.24 found 527.40 **CHNS analysis**: $C_{32}H_{32}N_4O_2$: calculated C: 76.16, H: 6.39, N: 11.10. Found: C: 76.45, H: 6.09, N: 10.97.

1,3-dimethyl-imidazolium iodide (L9)

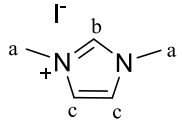

Methyl iodide (0.414 g, 2.92 mmol, 1.2 eq.) was added to a solution (5M) of 1-methylimidazole (0.200 g, 2.43 mmol. 1 eq.) dissolved in dichloromethane. The reaction was stirred at room temperature for 90 minutes. The solution was concentrated under reduced pressure and dried under vacuum. Yellow liquid. **Yield**: 91% **^{1}H-NMR** (δ, ppm, 400 MHz, $CDCl_3$): 10.03 (s, 1H, H_b), 7.43 (s, 2H, H_c), 4.12 (s, 6H, H_a) **^{13}C-NMR** (δ, ppm, 100 MHz, $CDCl_3$): present in literature [162] **ESI-MS (+)** m/z $[M-I^-]^+$ calc. 97.14 found 96.72.

4-bromo-N-(3-propylimidazole)-1,8-naphthalimide (L10)

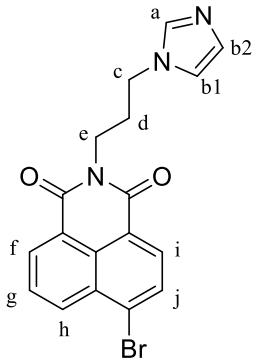

4-bromo-1,8-naphthalenic anhydride (0.2 g, 0.73 mmol) and 1-(3-aminopropyl)imidazole (0.108 g, 0.86 mmol) were dissolved in 10 ml of ethanol at 80°C and heated for 24 hours. During the reaction there is not the formation of a precipitate. The solution was concentrated under reduced pressure, 5 ml of diethyl ether were added, and the solution was left al -4°C overnight. The precipitate was collected by filtration, washed with cold diethyl ether and dried under vacuum. Brown solid. **Yield**: 65% **^{1}H-NMR** (δ, ppm, 400 MHz, $CDCl_3$): 8.69 (dd, J = 7.2 Hz, J' = 0.8 Hz, 1H, H_f), 8.64 (dd, J = 7.2 Hz, J' = 0.8 Hz, 1H, H_h), 8.45 (d, J = 8 Hz, 1H, H_j), 8.10 (d, J = 8 Hz, 1H, H_i), 7.90 (t, J = 7.2 Hz, H_g), 7.80 (s, 1H, H_a), 7.13 (s, 1H, H_{b2}), 7.09 (s, 1H, H_{b1}), 4.26 (t, J = 6.8 Hz, 2H, H_e), 4.26 (t, J = 6.8 Hz, 2H, H_e), 4.14 (t, J = 6.8 Hz, 2H, H_c), 2.31 (q, J = 6 Hz, 2H, H_d) **^{13}C-NMR** (δ, ppm, 100 MHz, $CDCl_3$): 163.41 (C=O imides), 137.16 (C-H imidazole), 133.37 (C-H naphthalene), 132.04 (C-H naphthalene), 131.18 (C-H naphthalene), 131.06 (C-H imidazole), 130.50 (C-Br naphthalene), 130.39 (C quaternary naphthalene), 129.52 (C-H naphthalene), 128.66 (C quaternary naphthalene), 128.05 (C-H imidazole), 122.54 (C quaternary naphthalene), 121.66 (C quaternary naphthalene), 118.68 (C-H naphthalene), 44.90 (CH_2 close to N), 37.80 (CH_2 close to N), 29.47 (CH_2 propyl) **ESI-MS (+)** m/z $[M+H^+]^+$ calc. 384.23 found 384.13 $[M-C_4H_6N_2]^+$ calc. 316.00 found 316.11 **CHNS analysis**: $C_{18}H_{14}N_3O_2Br$: calculated C: 56.27, H: 3.67, N: 10.94. Found: C: 55.43, H: 3.70, N: 12.20.

4-bromo-N-(3-propyl-1-methyl-imidazolium iodide)-1,8-naphthalimide (L11)

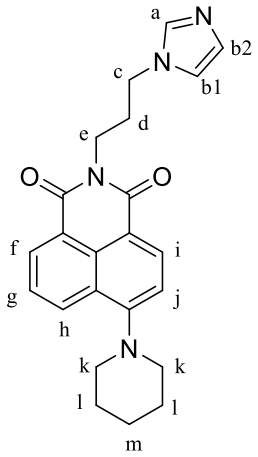

The same procedure used for compound **L4** was applied by reacting compound **L10** (0.2 g, 0.052 mmol) in 10 mL of piperidine. Orange sticky solid. **Yield**: 71% **^{1}H-NMR** (δ, ppm, 400 MHz, $CDCl_3$): 8.52 (d, J = 8 Hz, 1H, H_f), 8.44 (d, J = 8 Hz, 1H, H_i), 8.36 (d, J = 8 Hz, 1H, H_h), 7.64 (t, J = 8 Hz, 1H, H_g), 7.57 (s, 1H, H_a), 7.14 (d, J = 8 Hz, 1H, H_j), 7.02 (d, J = 8 Hz, 2H, H_{b1}, H_{b2}) 4.20 (t, J = 6.8 Hz, 2H, H_e), 4.06 (t, J = 6.8 Hz, 2H, H_c), 3.21 (s, 4H, H_k), 2.24 (q, J = 6 Hz, 2H, H_d), 1.87 (s, 4H, H_l), 1.71 (s, 2H, H_m) **^{13}C-NMR** (δ, ppm, 100 MHz, $CDCl_3$): 164.55 (C=O imide), 164.02 (C=O imide), 157.54 (C-N piperidine quaternary), 137.16 (C-H imidazole), 132.83 (C-H naphthalene), 131.11 (C-H naphthalene), 130.91 (C quaternary naphthalene), 129.87 (C-H naphthalene), 128.88 (C-H imidazole), 126.10 (C quaternary naphthalene), 125.32 (C-H naphthalene), 122.64 (C quaternary naphthalene), 118.95 (C-H imidazole), 115.24 (C quaternary naphthalene), 114.68 (C-H naphthalene), 54.47 (CH_2 piperidine close to N), 44.48 (CH_2 close to N), 37.35 (CH_2 close to N), 29.68 (CH_2 propyl), 26.15 (CH_2 piperidine), 24.26 (CH_2 piperidine) **ESI-MS (+)** m/z $[M+H^+]^+$ calc. 389.47 found 389.28

4-piperidinyl-N-(3-propyl-1-methyl-imidazolium iodide)-1,8-naphthalimide (L12)

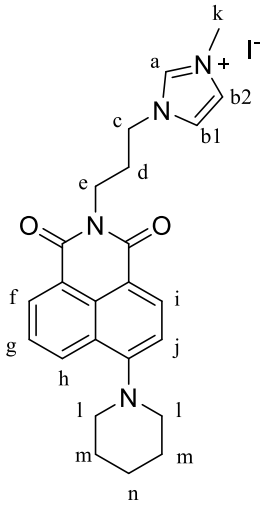

L11 (0.2 g, 0.515 mmol) was dissolved in 10 ml of DCM. A large excess of methyl iodide was added to the solution. The reaction was stirred at room temperature overnight. The solution was concentrated under reduced pressure and dried under vacuum. Orange sticky solid. **Yield**: 94% **^{1}H-NMR** (δ, ppm, 400 MHz, DMSO-D_6): 9.10 (s, 1H, H_a), 8.49 (d, J = 8 Hz, 1H, H_f), 8.44 (d, J = 8 Hz, 1H, H_i), 8.41 (d, J = 8 Hz, 1H, H_h), 7.84 (t, J = 7.2 Hz, 1H, H_g), 7.80 (s, 1H, H_{b2}), 7.68 (s, 1H, H_{b1}), 7.34 (d, J = 8.4 Hz, H_j), 4.26 (t, J = 6.8 Hz, 2H, H_e), 4.10 (t, J = 6.8 Hz, 2H, H_c), 3.84 (s, 3H, H_k), 3.22 (bs, 4H, H_l), 2.21 (q, J = 6 Hz, 2H, H_d), 1.84 (bs, 4H, H_m), 1.67 (bs, 2H, H_n) **^{1}H-NMR** (δ, ppm, 400 MHz, $CDCl_3$): 9.80 (s, 1H, H_a), 8.32 (d, J = 8 Hz, 1H, H_f), 8.25 (d, J = 8 Hz, 1H, H_i), 8.17 (d, J = 8 Hz, 1H, H_h), 7.76 (s, 1H, H_{b2}), 7.71 (s, 1H, H_{b1}), 7.50 (t, J = 7.2 Hz, 1H, H_g), 7.01 (d, J = 8.4 Hz, H_j), 4.41 (t, J = 6.8 Hz, 2H, H_e), 4.12 (s, 3H, H_k), 4.08 (t, J = 6.8 Hz, 2H, H_c), 3.11 (bs, 4H, H_l), 2.34 (q, J = 6 Hz, 2H, H_d), 1.80 (bs, 4H, H_m), 1.66 (bs, 2H, H_n) **^{13}C-NMR** (δ, ppm, 100 MHz, $CDCl_3$): 164.57 (C=O imide), 164.03 (C=O imide), 157.52 (C-N piperidine quaternary), 136.92 (C-H imidazole), 132.89 (C-H naphthalene), 131.11 (C-H naphthalene), 130.92 (C quaternary naphthalene), 129.69 (C quaternary naphthalene), 125.83 (C-H naphthalene), 125.27 (C quaternary naphthalene), 123.98 (C-H imidazole), 122.65 (C quaternary naphthalene), 122.25 (C-H imidazole), 114.74 (C quaternary naphthalene), 114.65 (C-H naphthalene), 54.42 (CH_2 piperidine close to N), 53.61 (CH_3 methyl imidazole), 47.97 (CH_2 close to N), 37.32 (CH_2 close to N), 29.12 (CH_2 propyl), 26.14 (CH_2 piperidine), 24.24 (CH_2 piperidine) **ESI-MS (+)** m/z $[M\text{-}I^-]^+$ calc. 403.51 found 403.28.

Riboflavin tetra-acetylated (L13)

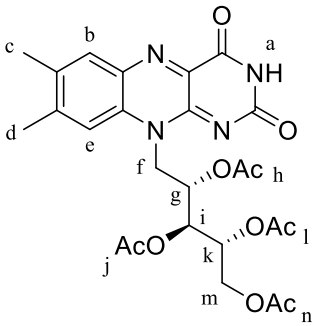

Dissolve the riboflavin (5.00 g, 13.28 mmol) in 100 mL of acetic anhydride and 100 mL of acetic acid, then add drop by drop 1 mL of perchloric acid. The reaction was stirred at 40 °C for forty minutes and was monitored by TLC (eluent ethyl acetate). The solution was cooled to room temperature and 200 mL of ethyl acetate was added to proceed with extraction. The solution was extracted with NaHCO3 (aq), concentrated under pressure and dried under vacuum. Bright yellow solid. **Yield**: 70% **^{1}H-NMR** (δ, ppm, 400 MHz, $CDCl_3$): 8.58 (s, 1H, H_a), 8.05 (s, 1H, H_b), 7.59 (s, 1H, H_e), 5.68 (s, 1H, H_g), 5.49 (m, 1H, H_i), 5.44 (m, 1H, H_k), 4.93 (bs,

2H, H_f), 4.46 (dd, J = 12.4 Hz, J' = 2.8 Hz, 1H, H_m), 4.27 (dd, J = 12.4 Hz, J' = 5.6 Hz, 1H, H_m), 2.59 (s, 3H, H_d), 2.47 (s, 3H, H_c), 2.31 (s, 3H, H_h), 2.24 (s, 3H, H_j), 2.10 (s, 3H, H_l), 1.78 (s, 3H, H_n) **^{13}C-NMR** (δ, ppm, 100 MHz, $CDCl_3$): present in literature [163] **ESI-MS (+)** $[M+Na^+]^+$ calc. 567.51 found 567.27 **CHNS analysis**: $C_{25}H_{28}N_4O_{10}$: calculated C: 55.15, H: 5.18, N: 10.29. Found: C: 54.85, H: 5.20, N: 9.82.

tert-butyl (3-bromopropylamine)carbamate (L14)

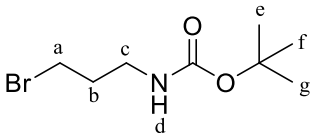

3-bromopropylamine hydrobromide (2 g, 9.14 mmol, 1 eq.) and triethylamine (5.09 ml, 36.56 mmol, 4 eq.) were dissolved in 30 ml of dichloromethane and stirred at room temperature for 30 minutes. Di-tert-butyl-dicarbonate (2.39 g, 10.97 mmol, 1.2 eq.) was added at the mixture and stirred overnight. The mixture was extracted with brine (3x50 ml) and the product was purified with the chtomatographic column (eluent hexane – ethyl acetate 5:1, 4:1 and 3:1). Colorless liquid. **Yield**: 55%. **^{1}H-NMR** (δ, ppm, 400 MHz, $CDCl_3$): 4.78 (bs, 1H, H_d), 3.43 (t, J = 6.4 Hz, 2H, H_a), 3.26 (s, 2H, H_c), 2.04 (q, J = 6.4 Hz, 2H, H_b), 1.43 (s, 9H, H_e, H_f, H_g) **^{13}C-NMR** (δ, ppm, 100 MHz, $CDCl_3$): present in literature [164] **ESI-MS (+)** m/z $[M+Na^+]^+$ calc. 260.03 found 260.15 m/z.

Riboflavin tetra-acetylated N-(tert-butyl (3-propylamine)carbamate) (L15)

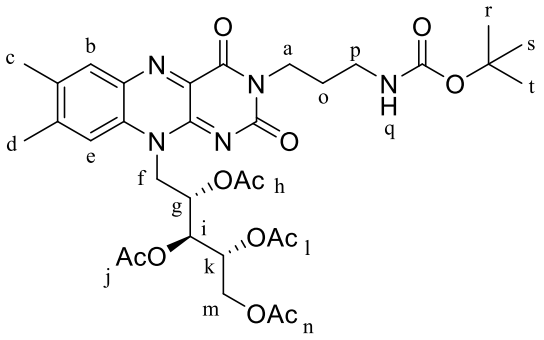

L14 (1.15 g, 4.83 mmol, 5 eq.), **L13** (0.526 g, 0.96 mmol, 1 eq.) and the cesium carbonate (0.472 g, 1.45 mmol, 1.5 eq.) were dissolved in 10 mL of DMF dry in a Schlenk flask with nitrogen atmosphere. The mixture was stirred in the dark, overnight at room temperature. After 10 mL of ethyl acetate was added to proceed with extraction. The solution was extracted with a supersaturate solution of lithium chloride, concentrate under pressure. The dark solid was then purified with the chromatographic column (eluent ethyl acetate: hexane 2:1, 3:1, 4:1 and finally only ethyl acetate). Orange solid. **Yield**: 66% **^{1}H-NMR** (δ, ppm, 400 MHz, $CDCl_3$): 7.99 (s, 1H, H_b), 7.54 (s, 1H, H_e), 5.64 (s, 1H, H_g), 5.43 (m, 1H, H_i), 5.39 (m, 1H, H_k), 4.93 (bs, 2H, H_f), 4.40 (dd, J = 12.4 Hz, J' = 2.8 Hz, 1H, H_m), 4.22 (dd, J = 12.4 Hz, J' = 5.6 Hz, 1H, H_m), 4.12 (t, J = 8.4 Hz, 2H, H_a), 3.10 (s, 2H, H_p), 2.54 (s, 3H, H_d), 2.42 (s, 3H, H_c), 2.25 (s, 3H, H_h), 2.19 (s, 3H, H_j), 2.04 (s, 3H, H_l), 1.86 (m, 2H, H_o), 1.71 (s, 3H, H_n), 1.41 (s, 9H, H_r, H_s, H_t) **^{13}C-NMR** (δ, ppm, 100 MHz, $CDCl_3$): 170.71 (C=O ribityl acetate), 170.35 (C=O ribityl acetate), 169.90 (C=O ribityl acetate), 169.78 (C=O ribityl acetate), 160.30 (C=O flavin core), 156.12 (HN-C=O Boc), 155.08 (C=O flavin core), 149.07 (N-C=N flavin core), 147.78 (C-CH_3 flavin core), 136.77 (C-CH_3 flavin core), 135.55 (N=C-C=O flavin core), 134.74 (N-C=C aromatic flavin core), 132.95 (C-H aromatic flavin core), 131.35 (N-C=C aromatic flavin core), 115.30 (C-H aromatic flavin core), 70.48 (C-H ribityl), 69.53 (C-H ribityl), 69.02 (C-H ribityl), 61.87 (C-H ribityl), 53.56 (CH_2-NH amide), 44.74 (CH_2 ribityl), 39.18 (CH_2-N propyl), 37.16 (O-C tert-butyl Boc), 28.48 (CH_3 tert-butyl Boc), 28.18 (CH_2 propyl), 21.52 (CH_3 aromatic flavin core), 21.10 (CH_3 acetate ribityl), 20.85 (CH_3 acetate ribityl), 20.75 (CH_3 acetate ribityl), 20.39 (CH_3 acetate ribityl), 19.52 (CH_3 aromatic flavin core) **ESI-MS (+)** m/z $[M+Na^+]^+$ calc. 724.28 found 724.31 m/z **CHNS analysis**: $C_{33}H_{43}N_5O_{12}$: calculated C: 56.48, H: 6.18, N: 9.98. Found: C: 55.41, H: 6.20, N: 9.82.

Riboflavin tetra-acetylated N-(3-propylamine) (L16)

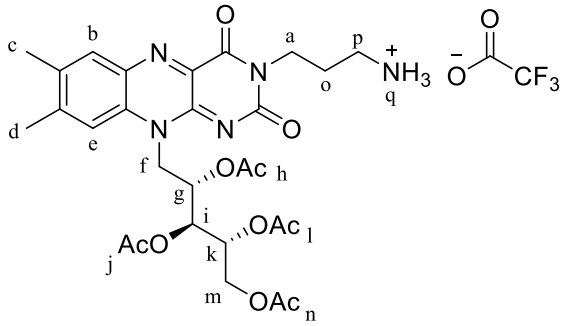

Dissolve **L15** in 15 mL of dichloromethane, after 5 mL of TFA were added drop by drop. The reaction was stirred at 0°C for forty minutes and monitored with TLC (eluent Ethyl acetate). The solution was extracted with $NaHCO_{3\ (aq)}$, concentrate under pressure, and dried under vacuum. Orange sticky solid. **Yield**: 92% **^{1}H-NMR** (δ, ppm, 400 MHz, $CDCl_3$): 12.28 (bs, 1H, H_q), 8.08 (s, 1H, H_b), 8.40 (bs, 2H, H_q), 7.61 (s, 1H, H_e), 5.67 (s, 1H, H_g), 5.47 (m, 2H, H_i, H_k), 5.07 (bs, 2H, H_f), 4.48 (dd, J = 12.4 Hz, J' = 2.8 Hz, 1H, H_m), 4.25 (m, 3H, H_m, H_a), 3.15 (m, 2H, H_p), 2.59 (s, 3H, H_d), 2.48 (s, 3H, H_c), 2.26 (m, 5H, H_h, H_o), 2.22 (s, 3H, H_j), 2.09 (s, 3H, H_l), 1.75 (s, 3H, H_n) **^{13}C-NMR** (δ, ppm, 100 MHz, $CDCl_3$): 170.77 (C=O ribityl acetate), 170.43 (C=O ribityl acetate), 169.93 (C=O ribityl acetate), 169.62 (C=O ribityl acetate), 160.49 (C=O flavin core), 155.86 (C=O flavin core), 149.21 (N-C=N flavin core), 148.28 (C-CH_3 flavin core), 137.26 (C-CH_3 flavin core), 135.11 (N=C-C=O flavin core), 135.01 (N-C=C aromatic flavin core), 132.75 (C-H aromatic flavin core), 131.22 (N-C=C aromatic flavin core), 115.54 (C-H aromatic flavin core), 70.23 (C-H ribityl), 69.34 (C-H ribityl), 68.93 (C-H ribityl), 61.75 (C-H ribityl), 45.61 (CH_2-NH_2 amine), 44.62 (CH_2 ribityl), 38.56 (CH_2-N propyl), 25.65 (CH_2 propyl), 21.54 (CH_3 aromatic flavin core), 21.04 (CH_3 acetate ribityl), 20.78 (CH_3 acetate ribityl), 20.71 (CH_3 acetate ribityl), 20.33 (CH_3 acetate ribityl), 19.43 (CH_3 aromatic flavin core) **ESI-MS (+)** m/z $[M\text{-}C_2F_3O_2]^+$ calc. 602.24 found 602.21.

2,5-dioxopyrrolidin-1-yl isonicotinate (L17)

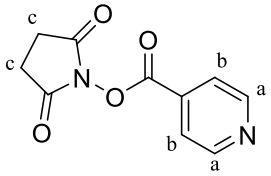

EDC (0.310 g, 1.62 mmol, 1 eq.), isonicotinic acid (0.2 g, 1.62 mmol, 1 eq.) and N-hydroxysuccinimide (0.186 g, 1.62 mmol, 1 eq.) were dissolved in 10 ml of dry dichloromethane in a Schlenk flask with nitrogen atmosphere and stirred overnight. The mixture was extracted with $NaHCO_{3\ (aq)}$ (3x10 ml) and dried under vacuum. The pure product was obtained without any further purification. White solid. **Yield**: 73% **^{1}H-NMR** (δ, ppm, 400 MHz, $CDCl_3$): 8.91 (dd, J = 8 Hz, J' = 2 Hz, 2H, H_a), 7.98 (dd, J = 8 Hz, J' = 2 Hz, 2H, H_b), 2.96 (s, 4H, H_c) **^{13}C-NMR** (δ, ppm, 100 MHz, $CDCl_3$): present in literature [165] **ESI-MS (+)** m/z $[M+H^+]^+$ calc. 221.05 found 221.06 m/z $[M\text{-}C_4H_4NO_2]^+$ calc. 123.02 found 123.99 **CHNS analysis**: $C_{25}H_{28}N_4O_{10}$: calculated C: 54.55, H: 3.66, N: 17.22. Found: C: 53.20, H: 4.37, N: 16.34.

Riboflavin tetra-acetylated N-(3-propylisonicotinic amide) (L18)

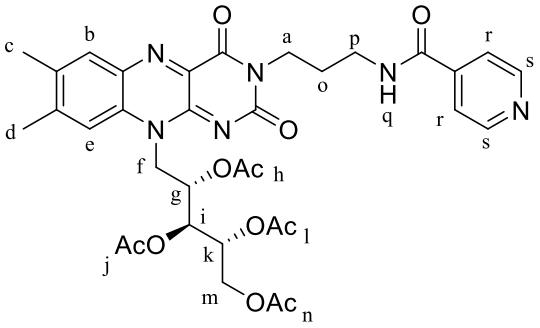

Dissolve **L16** (0.139 g, 0.23 mmol, 1.0 eq.) and **L17** (0.254 g 1.15 mmol, 5.0 eq) in 10 mL of acetonitrile dry, the reaction was stirred and heated at 70°C overnight. The solution was cooled to room temperature and then was extracted with brine (2x50 mL). The organic phase was reduced under pression. The dark solid was then purified with the chromatographic column (eluent DCM:MeOH 99:1, 98:2; 97:3; 96:4; 95:5). Orange solid. **Yield**: 54% **^{1}H-NMR** (δ, ppm, 400 MHz, DMSO-D_6): 8.80 (t, J = 6.4 Hz, 1H, H_q), 8.73 (d, J = 6 Hz, 2H, H_r), 7.97 (s, 1H, H_b), 7.78 (s, 1H, H_e), 7.75 (d, J = 6 Hz, 2H, H_s), 5.48 (m, 2H, H_g, H_i), 5.32 (m, 1H, H_k), 5.09 (bs, 2H, H_f), 4.90 (m, 1H, H_f), 4.38 (m, 1H, H_m), 4.23 (m, 1H, H_m), 3.97 (t, J = 8.4 Hz, 2H, H_a), 2.60 (s, 3H, H_d), 2.42 (s, 3H, H_c), 2.22 (s, 3H, H_h), 2.20 (s, 3H, H_j), 2.01 (s, 3H, H_l), 1.86 (m, 2H, H_o), 1.61 (bs, 5H, H_n) **^{1}H-NMR** (δ, ppm, 400 MHz, $CDCl_3$): 8.77 (d, J = 6 Hz, 2H, H_r), 8.08 (s, 1H, H_b), 7.91 (t, J = 6.4 Hz, 1H, H_q), 7.85 (d, J = 6 Hz, 2H, H_s), 7.61 (s, 1H, H_e), 5.64 (s, 1H, H_g), 5.43 (m, 1H, H_i), 5.39 (m, 1H, H_k), 4.93 (bs, 2H, H_f), 4.40 (dd, J = 12.4 Hz, J' = 2.8 Hz, 1H, H_m), 4.22 (dd, J = 12.4 Hz, J' = 5.6 Hz, 1H, H_m), 4.12 (t, J = 8.4 Hz, 2H, H_a), 3.42 (s, 2H, H_p) 2.54 (s, 3H, H_d), 2.42 (s, 3H, H_c), 2.25 (s, 3H, H_h), 2.19 (s, 3H, H_j), 2.04 (s, 5H, H_l, H_o), 1.71 (s, 3H, H_n) **^{13}C-NMR** (δ, ppm, 100 MHz, $CDCl_3$): 170.67 (C=O ribityl acetate), 170.24 (C=O ribityl acetate), 169.75 (C=O ribityl acetate), 169.68 (C=O ribityl acetate), 163.98 (HN-C=O pyridine), 160.57 (C=O flavin core), 155.62 (C=O flavin core), 149.20 (N-C=N flavin core), 148.48 (C-CH_3 flavin core), 148.17 (C-H pyridine close to amide), 143.78 (C quaternary pyridine close to carbonyl), 137.28 (C-CH_3 flavin core), 135.18 (N=C-C=O flavin core), 135.01 (N-C=C aromatic flavin core), 132.97 (C-H aromatic flavin core), 131.29 (N-C=C aromatic flavin core), 122.21 (C-H pyridine close to nitrogen), 115.53 (C-H aromatic flavin core), 70.43 (C-H ribityl), 69.38 (C-H ribityl), 69.13 (C-H ribityl), 61.86 (C-H ribityl), 44.75 (CH_2 ribityl), 39.12 (CH_2-N propyl), 36.24 (CH_2-NH amide), 27.23 (CH_2 propyl), 21.57 (CH_3 aromatic flavin core), 21.05 (CH_3 acetate ribityl), 20.80 (CH_3 acetate ribityl), 20.72 (CH_3 acetate ribityl), 20.36 (CH_3 acetate ribityl), 19.52 (CH_3 aromatic flavin core) **ESI-MS (+)** m/z $[M+Na^+]^+$ calc. 729.70 found 729.36 m/z **CHNS analysis**: $C_{34}H_{38}N_6O_{11}$: calculated C: 57.79, H: 5.42, N: 11.89. Found: C: 57.27, H: 5.37, N: 12.20.

Riboflavin tetra-acetylated N-(4-bromobutyl) (L19)

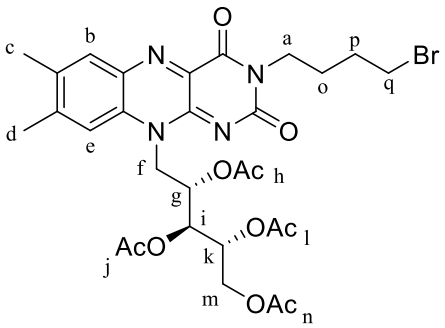

L13 (0.504 g, 0.93 mmol, 1 eq.) was dissolved in 10 mL of DMF dry in a Schlenk flask with nitrogen atmosphere, after was added the 1,4 dibromo butane (1.000 g, 4.63 mmol, 5 eq.). The mixture was transfer in another Schlenk flask with nitrogen atmosphere, containing the cesium carbonate (0.452,4 g, 1.39 mmol,

1.5 eq.). The mixture was stirred in the dark, overnight at room temperature. After 10 mL of ethyl acetate was added to proceed with extraction. The solution was extracted with a supersaturate solution of lithium chloride, concentrated under pressure, and dried under vacuum. The dark solid was then purified with the chromatographic column (eluent ethyl acetate:hexane ratio 2:1, 3:1 and finally 4:1). Orange solid. **Yield**: 68% **^{1}H-NMR** (δ, ppm, 400 MHz, $CDCl_3$): 8.02 (s, 1H, H_b), 7.55 (s, 1H, H_e), 5.67 (s, 1H, H_g), 5.47 (m, 1H, H_i), 5.41 (m, 1H, H_k), 4.92 (bs, 2H, H_f), 4.43 (dd, J = 12.4 Hz, J' = 2.8 Hz, 1H, H_m), 4.25 (dd, J = 12.4 Hz, J' = 5.6 Hz, 1H, H_m), 4.10 (m, 2H, H_a), 3.46 (m, 2H, H_q), 2.56 (s, 3H, H_d), 2.44 (s, 3H, H_c), 2.29 (s, 3H, H_h), 2.22 (s, 3H, H_j), 2.08 (s, 3H, H_l), 1.94 (m, 2H, H_o), 1.87 (m, 2H, H_p), 1.73 (s, 3H, H_n) **^{13}C-NMR** (δ, ppm, 100 MHz, $CDCl_3$): 170.71 (C=O ribityl acetate), 170.37 (C=O ribityl acetate), 169.92 (C=O ribityl acetate), 169.76 (C=O ribityl acetate), 159.75 (C=O flavin core), 154.90 (C=O flavin core), 149.16 (N-C=N flavin core), 147.74 (C-CH_3 flavin core), 136.53 (C-CH_3 flavin core), 135.52 (N=C-C=O flavin core), 134.65 (N-C=C aromatic flavin core), 132.95 (C-H aromatic flavin core), 131.11 (N-C=C aromatic flavin core), 115.47 (C-H aromatic flavin core), 70.45 (C-H ribityl), 69.47 (C-H ribityl), 68.99 (C-H ribityl), 61.88 (C-H ribityl), 44.45 (CH_2 ribityl), 40.96 (CH_2-N bromo butyl), 33.23 (CH_2-Br bromo butyl), 30.11 (CH_2-CH_2 bromo butyl), 26.57 (CH_2-CH_2 bromo butyl), 21.50 (CH_3 aromatic flavin core), 21.11 (CH_3 acetate ribityl), 20.86 (CH_3 acetate ribityl), 20.76 (CH_3 acetate ribityl), 20.39 (CH_3 acetate ribityl), 19.50 (CH_3 aromatic flavin core) **ESI-MS (+)** m/z $[M+Na^+]^+$ calc. 701.14 found 701.20 m/z **CHNS analysis**: $C_{29}H_{35}N_4O_{10}Br$: calculated C: 51.26, H: 5.19, N: 8.25. Found: C: 50.70, H: 5.18, N: 7.84.

Riboflavin tetra-acetylated N-(4-butyl imidazolium bromide) (L20)

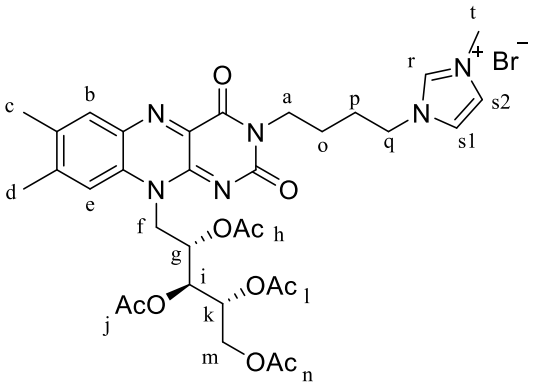

L19 (0.242 g, 0.356 mmol, 1 eq.) and 1-methylimidazole (0.146 g, 1.78 mmol, 5 eq.) were dissolved in 10 ml of CH_3CN at 70°C and heated for 18 hours. The solvent was removed under reduced pressure and the solid was washed several time with diethyl ether until the solvent became colorless. Brown sticky solid. **Yield**: 77% **^{1}H-NMR** (δ, ppm, 400 MHz, DMSO-D_6): 9.12 (s, 1H, H_r), 7.96 (s, 1H, H_b), 7.79 (s, 2H, H_{s1}, H_{s2}), 7.71 (s, 1H, H_e), 5.48 (m, 2H, H_g, H_i), 5.32 (m, 1H, H_k), 5.08 (bs, 2H, H_f), 4.90 (m, 1H, H_f), 4.38 (m, 1H, H_m), 4.23 (m, 3H, H_m, H_q), 3.92 (t, J = 8.4 Hz, 2H, H_a), 3.85 (s, 3H, H_t), 2.54 (s, 3H, H_d), 2.43 (s, 3H, H_c), 2.22 (s, 3H, H_h), 2.21 (s, 3H, H_j), 2.01 (s, 3H, H_l), 1.85 (m, 2H, H_o), 1.59 (bs, 5H, H_p, H_n) **^{1}H-NMR** (δ, ppm, 400 MHz, $CDCl_3$): 10.48 (s, 1H, H_r), 8.04 (s, 1H, H_b), 7.59 (s, 1H, H_e), 7.53 (t, J = 1.6 Hz, 1H, H_{s2}), 7.33 (t, J = 1.6 Hz, 1H, H_{s1}), 5.72 (s, 1H, H_g), 5.50 (m, 1H, H_i), 5.43 (m, 1H, H_k), 5.01 (bs, 2H, H_f), 4.48 (m, 3H, H_m, H_q), 4.27 (m, 1H, H_m), 4.16 (t, J = 8.4 Hz, 2H, H_a), 4.12 (s, 3H, H_t), 2.58 (s, 3H, H_d), 2.46 (s, 3H, H_c), 2.29 (s, 3H, H_h), 2.23 (s, 3H, H_j), 2.09 (s, 3H, H_l), 2.02 (m, 2H, H_o), 1.82 (m, 2H, H_p), 1.75 (s, 3H, H_n) **^{13}C-NMR** (δ, ppm, 100 MHz, $CDCl_3$): 170.68 (C=O ribityl acetate), 170.28 (C=O ribityl acetate), 169.75 (C=O ribityl acetate), 169.66 (C=O ribityl acetate), 159.91 (C=O flavin core), 155.01 (C=O flavin core), 149.09 (N-C=N flavin core), 147.93 (C-CH_3 flavin core), 137.67 (C-CH_3 flavin core), 137.18 (C-H imidazole), 135.35 (N=C-C=O flavin core), 134.74 (N-C=C aromatic flavin core), 132.56 (C-H aromatic flavin core), 131.29 (N-C=C aromatic flavin core), 123.60 (C-H imidazole), 122.49 (C-H imidazole), 115.62 (C-H aromatic flavin core), 70.31 (C-H ribityl), 69.07 (C-H ribityl), 65.77 (C-H ribityl), 61.79 (C-H ribityl), 49.06 (CH_2 close to N), 44.66 (CH_2 ribityl), 40.36 (CH_2-N bromo butyl), 27.51 (CH_2-CH_2 bromo butyl), 24.01 (CH_2-CH_2 bromo butyl), 21.47 (CH_3 aromatic flavin core), 21.07 (CH_3 acetate ribityl), 20.80 (CH_3 acetate ribityl), 20.70

(CH_3 acetate ribityl), 20.37 (CH_3 acetate ribityl), 19.43 (CH_3 aromatic flavin core) **ESI-MS (+)** m/z $[M\text{-}Br^-]^+$ calc. 681.71 found 681.41.

Dimethyl 2,2'-bipyridine-4,4'-dicarboxylate (L21)

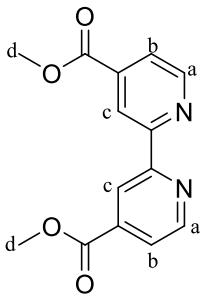

2,2'-bipyridine-4,4'-dicarboxylic acid (0.2 g, 0.82 mmol) was dissolved in 10 ml of methanol. A large excess of thionyl chloride was added. The reaction was refluxed overnight. The solvent was removed under reduced pressure, 10 ml of ethyl acetate was added and extracted with $NaHCO_{3\,(aq)}$ (3x10 ml) and dried under vacuum. The pure product was obtained without any further purification. White solid. **Yield**: 71% **^{1}H-NMR** (δ, ppm, 400 MHz, $CDCl_3$): 9.02 (m, 2H, H_c), 8.91 (m, 2H, H_a), 7.96 (m, 2H, H_b), 4.03 (s, 6H, H_d) **^{13}C-NMR** (δ, ppm, 100 MHz, $CDCl_3$): present in literature [166] **ESI-MS (+)** m/z $[M+H^+]^+$ calc. 273.26 found 273.20 m/z **CHNS analysis**: $C_{14}H_{12}N_2O_4$: calculated C: 61.76, H: 4.44, N: 10.29. Found: C: 61.11, H: 4.33, N: 9.85.

4'-(methoxycarbonyl)-[2,2'-bipyridine]-4-carboxylic acid (L22)

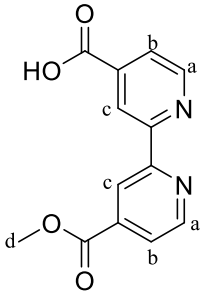

L21 (0.3 g, 1.1 mmol, 1 eq.) and KOH (0.061 g, 1.1 mmol, 1 eq.) were dissolved in a mixture 1:1 of methanol/THF. The reaction was refluxed for 2 hours. The solvent was removed under reduced pressure, 10 ml of water was added, and the aqueous phase was extracted with dichloromethane. The aqueous phase was acidified with few drops of $HCl_{(aq.)}$ up to the formation of a white solid. This solid was washed with hot ethyl acetate and the solvent was removed. The pure product was obtained without any further purification. White solid. **Yield**: 19% **^{1}H-NMR** (δ, ppm, 400 MHz, DMSO-D_6): 8.94 (m, 2H, H_c), 8.85 (m, 2H, H_a), 7.94 (m, 2H, H_b), 3.96 (s, 3H, H_d) **^{13}C-NMR** (δ, ppm, 100 MHz, $CDCl_3$): present in literature [166] **ESI-MS (+)** m/z $[M+H^+]^+$ calc. 259.23 found 259.30 m/z **CHNS analysis**: $C_{14}H_{12}N_2O_4$: calculated C: 60.47, H: 3.90, N: 10.85. Found: C: 61.05, H: 4.12, N: 9.99.

4-(2,5-dioxopyrrolidin-1-yl) 4'-methyl [2,2'-bipyridine]-4,4'-dicarboxylate (L23)

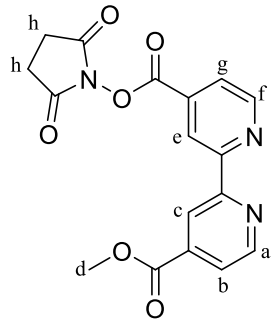

The same procedure used for compound **L17** was applied by reacting compound **L22** (0.2 g, 0.77 mmol, 1 eq.) with EDC (0.148 g, 0.77 mmol, 1 eq.) and N-hydroxysuccinimide (0.089, 0.77 mmol, 1 eq.). White solid. **Yield**: 75% **^{1}H-NMR** (δ, ppm, 400 MHz, $CDCl_3$): 9.13 (s, 1H, H_e), 9.01 (s, 1H, H_c), 8.98 (d, J = 4.9 Hz, 1H, H_f), 8.89 (d, J = 4.9 Hz, 1H, H_a), 8.00 (dd, J = 4.9 Hz, J' = 1.6 Hz, 1H, H_g), 7.96 (dd, J = 4.9 Hz, J' = 1.6 Hz, 1H, H_b), 4.03 (s, 3H, H_d), 2.97 (s, 4H, H_e) **^{13}C-NMR** (δ, ppm, 100 MHz, $CDCl_3$): 171.75 (C=O succinimide), 168.21 (C=O ester), 167.74 (C=O ester), 161.46 (C quaternary bipyridine close to carbonyl), 160.98 (C quaternary bipyridine close to carbonyl), 157.21 (C quaternary bipyridine close to N), 156.67 (C quaternary bipyridine close to N), 152.35 (C-H bipyridine close to N), 151.16 (C-H bipyridine close to N), 123.83 (C-H bipyridine), 118.51 (C-H bipyridine), 55.36 (methyl ester), 25.87 (CH_2 succinimide) **ESI-MS (+)** m/z $[M+H^+]^+$ calc. 356.31 found 356.15 m/z $[M-C_4H_4NO_2]^+$ calc. 257.06 found 257.35 **CHNS analysis**: $C_{17}H_{13}N_3O_6$: calculated C: 57.47, H: 3.69, N: 11.83. Found: C: 58.21, H: 3.85, N: 11.49.

Riboflavin tetra-acetylated N-(4'-(methoxycarbonyl)-[2,2'-bipyridine]-4-amide) (L24)

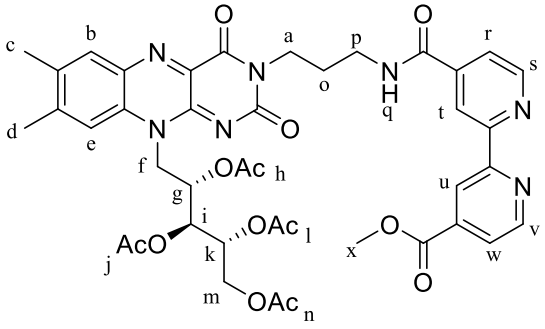

The same procedure used for compound **L18** was applied by reacting compound **L16** (0.032 g, 0.053 mmol, 1 eq.) with **L23** (0.095 g, 0.27 mmol, 5 eq.). Yellow sticky solid. **Yield**: 40% **^{1}H-NMR** (δ, ppm, 400 MHz, $CDCl_3$): 8.98 (s, 1H, H_t), 8.90 (m, 3H, H_v, H_u, H_s), 8.06 (s, 1H, H_b), 7.93 (d, J = 4.9 Hz, 1H, H_w), 7.88 (d, J = 4.9 Hz, 1H, H_r), 7.86 (m, 1H, H_q), 7.59 (s, 1H, H_e), 5.70 (s, 1H, H_g), 5.49 (m, 1H, H_i), 5.43 (m, 1H, H_k), 4.97 (bs, 2H, H_f), 4.48 (dd, J = 12.4 Hz, J' = 2.8 Hz, 1H, H_m), 4.28 (m, 3H, H_m, H_a), 4.02 (s, 3H, H_x), 3.52 (s, 2H, H_p), 2.59 (s, 3H, H_d), 2.47 (s, 3H, H_c), 2.29 (s, 3H, H_h), 2.23 (s, 3H, H_j), 2.12 (m, 2H, H_o), 2.09 (s, 3H, H_o), 1.76 (s, 3H, H_n) **^{13}C-NMR** (δ, ppm, 100 MHz, $CDCl_3$): 170.65 (C=O ribityl acetate), 170.29 (C=O ribityl acetate), 169.82 (C=O ribityl acetate), 165.57 (HN-C=O bipyridine), 165.21 (CH_3O-C=O bipyridine), 160.46 (C=O flavin core), 155.48 (C=O flavin core), 149.98 (C-CH_3 flavin core), 149.19 (N-C=N flavin core), 143.38 (C quaternary pyridine close to carbonyl), 138.77 (C quaternary pyridine close to carbonyl), 137.04 (C-CH_3 flavin core), 135.32 (N=C-C=O flavin core), 134.91 (N-C=C aromatic flavin core), 132.95 (C-H aromatic flavin core), 131.26 (N-C=C aromatic flavin core), 123.25 (C-H bipyridine close to N), 121.84 (C-H bipyridine close to N), 120.79 (C-H bipyridine), 118.94 (C-H bipyridine), 115.47 (C-H aromatic flavin core), 70.39 (C-H ribityl), 69.06 (C-H ribityl), 61.87 (C-H ribityl), 52.79

(methyl ester), 44.64 (CH_2 ribityl), 39.19 (CH_2-N propyl), 36.47 (CH_2-NH amide), 27.40 (CH_2 propyl), 21.51 (CH_3 aromatic flavin core), 21.04 (CH_3 acetate ribityl), 20.80 (CH_3 acetate ribityl), 20.71 (CH_3 acetate ribityl), 20.35 (CH_3 acetate ribityl), 19.49 (CH_3 aromatic flavin core) **ESI-MS (+)** m/z $[M+Na^+]^+$ calc. 863.82 found 863.96 m/z.

Dichloro(p-cymene)ruthenium(II) dimer

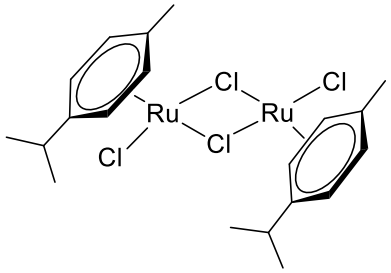

1.0 g of $RuCl_3 \cdot nH_2O$ was dissolved in 10 mL of ethanol, then a large excess of α-phellandrene (3 mL) was added. The reaction was refluxed for 6 hours. At the end, 10 mL of pentane were added to precipitate the product which was collected by filtration, washed with diethyl ether (3 x 5 mL) and dried under vacuum. Dark red crystals. **Yield**: Quantitative **^{1}H-NMR** (δ, ppm, 400 MHz, $CDCl_3$): 5.35 (d, J = 6.0 Hz, 2H), 5.49 (d, J = 6.0 Hz, 2H) **^{13}C-NMR** (δ, ppm, 100 MHz, $CDCl_3$): 101.23 (C quaternary p-cymene), 96.76 (C quaternary p-cymene), 81.31 (C-H aromatic p-cymene), 80.54 (C-H aromatic p-cymene), 30.64 (CH_3 p-cymene), 22.17 (CH_3 isopropyl p-cymene), 18.95 (CH isopropyl p-cymene).

13.2 Intermediate complexes: monodentate pyridine ligands

General synthetic procedure for the intermediate complexes with pyridine-like monodentate ligand

$[(\eta^6\text{-p-Cym})RuCl_2]_2$ (1 eq.) and the monodentate ligand (2 eq.) were dissolved in dichloromethane dry in a Schlenk flask with nitrogen atmosphere. The mixture was stirred for 5 hours, then diethyl ether was added, and the solution was left al -4°C overnight. The precipitate was collected by filtration, washed with cold diethyl ether and dried under vacuum.

$[(\eta^6\text{-p-cym})Ru(L1)Cl_2]$ (I1)

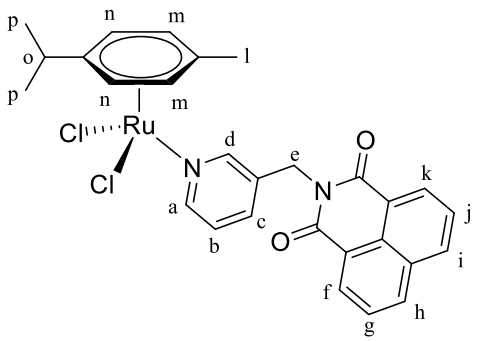

$[(\eta^6\text{-p-Cym})RuCl_2]_2$ (0.36 g, 1.26 mmol), **L1** (0.38 g, 0.63 mmol). **Yield**: 83%. **^{1}H-NMR** (δ, ppm, 400 MHz, $CDCl_3$): 9.36 (d, J = 2.0 Hz, 1H, H_d), 8.95 (dd, J = 5.8, J' = 1.4 Hz, 1H, H_a), 8.66 (dd, J = 7.3, J' = 1.1 Hz, 2H, H_f, H_k), 8.28 (dd, J = 7.3, J' = 1.2 Hz, 2H, H_h, H_i), 7.95 (m, 1H, H_b), 7.81 (dd, J = 8.2, J' = 7.3 Hz, 2H, H_g, H_j), 7.25 (dd, J = 7.9,

J' = 5.7 Hz, 1H, H_c), 5.46 (d, J = 5.9 Hz, 2H, H_n), 5.39 (s, 2H, H_e), 5.28 (d, J = 5.9 Hz, 2H, H_m), 3.03 (m, 1H, H_o), 2.15 (s, 3H, H_l), 1.31 (d, J = 7.0 Hz, 6H, H_p) **^{13}C-NMR** (δ, ppm, 100 MHz, $CDCl_3$): 164.12 (C=O imides), 156.75 (C-H pyridine close to N), 153.37 (C-H pyridine close to N), 138.40 (C-H pyridine), 134.51 (C-H naphthalene), 134.19 (C quaternary naphthalene), 131.67 (C-H naphthalene), 128.15 (C quaternary pyridine), 127.10 (C-H naphthalene), 124.15 (C-H pyridine), 122.14 (C quaternary naphthalene), 103.58 (C quaternary p-cymene), 96.96 (C quaternary p-cymene), 82.65 (C-H aromatic p-cymene), 82.61 (C-H aromatic p-cymene), 40.81 (CH_2 bridge), 30.62 (CH_3 p-cymene), 22.27 (CH_3 isopropyl p-cymene), 18.09 (CH isopropyl p-cymene) **ESI-MS (+)** m/z calc 559,04 found 559,16 **CHNS analysis**: $C_{28}H_{26}N_2O_2Cl_2Ru$: calculated: C: 56.57, H: 4.41, N: 4.71. Found: C: 54.74, H: 4.30, N: 5.13.

[(η^6-p-cym)Ru(L2)Cl$_2$] (I2)

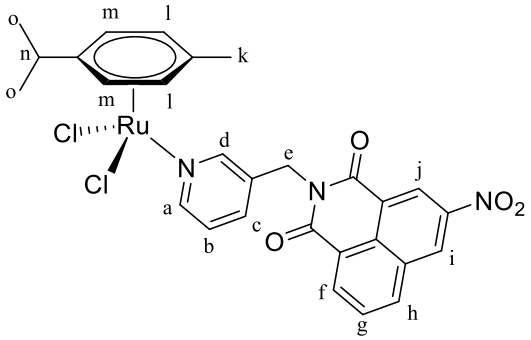

[(η^6-p-Cym)RuCl$_2$]$_2$ (0.15 g, 0.24 mmol), **L2** (0.16 g, 0.48 mmol). Orange solid. **Yield**: 85% **^{1}H-NMR** (δ, ppm, 400 MHz, $CDCl_3$): 9.35 (d, J = 2.1 Hz, 2H, H_d, H_j), 9.18 (d, J = 2.2 Hz, 1H, H_i), 8.97 (d, J = 5.7 Hz, 1H, H_a), 8.83 (d, J = 5.7 Hz, 1H, H_f), 8.47 (d, J = 8.3 Hz, 1H, H_h), 7.98 (m, 2H, H_b, H_g), 7.26 (s, 1H, H_c), 5.46 (d, J = 5.8 Hz, 2H, H_m), 5.40 (s, 2H, H_e), 5.28 (d, J = 5.8 Hz, 2H, H_l), 3.03 (m, 1H, H_n), 2.16 (s, 3H, H_k), 1.33 (d, J = 6.9 Hz, 6H, H_o) **^{13}C-NMR** (δ, ppm, 100 MHz, $CDCl_3$): 163.25 (C=O imides), 162.34 (C=O imides), 156.94 (C-H pyridine close to N), 153.43 (C-H pyridine close to N), 148.13 (C quaternary naphthalene close to NO_2), 138.94 (C-H naphthalene), 138.35 (C-H pyridine), 136.98 (C-H naphthalene), 134.73 (C-H naphthalene), 134.52 (C-H pyridine), 130.57 (C quaternary naphthalene), 129.86 (C quaternary pyridine), 129.12 (C-H naphthalene), 129.04 (C-H naphthalene), 124.83 (C quaternary naphthalene), 124.21 (C quaternary naphthalene), 124.01 (C quaternary naphthalene), 103.69 (C quaternary p-cymene), 96.99 (C quaternary p-cymene), 82.63 (C-H aromatic p-cymene), 40.74 (CH_2 bridge), 30.58 (CH_3 p-cymene), 22.26 (CH_3 isopropyl p-cymene), 18.07 (CH isopropyl p-cymene) **ESI-MS (+)** m/z $[M-Cl]^+$ calc 604.05 found 604.22 **CHNS analysis**: $C_{28}H_{25}N_3O_4Cl_2Ru$: calculated: C: 52.59, H: 3.94, N: 6.57. Found: C: 52.06, H: 3.93, N: 6.26.

[(η^6-p-cym)Ru(L4)Cl$_2$] (I3)

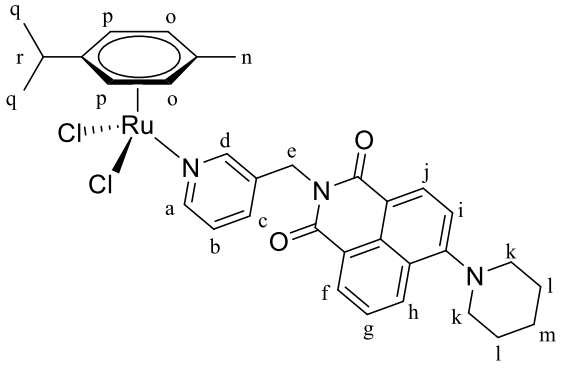

[(η^6-p-Cym)RuCl$_2$]$_2$ (0.10 g, 0.16 mmol), **L4** (0.12 g, 0.32 mmol). Orange solid. **Yield**: 89% **^{1}H-NMR** (δ, ppm, 400 MHz, $CDCl_3$): 9.34 (d, J = 1.9 Hz, 1H, H_d), 8.93 (dd, J = 5.6, J' = 1.4 Hz, 1H, H_a), 8.61 (dd, J = 7.3, J' = 1.2 Hz, 1H,

H_f), 8.53 (d, J = 8.1 Hz, 1H, H_j), 8.43 (dd, J = 8.5, J' = 1.2 Hz, 1H, H_h), 7.94 (dt, J = 7.9, J' = 1.7 Hz, 1H, H_b), 7.71 (dd, J = 8.5, J' = 7.3 Hz, 1H, H_g), 7.22 (m, 2H, H_c, H_i), 5.46 (d, J = 5.9 Hz, 2H, H_p), 5.37 (s, 2H, H_e), 5.28 (d, J = 5.9 Hz, 2H, H_o), 3.27 (m, 4H, H_k), 3.00 (m, 1H, H_r), 2.13 (s, 3H, H_n), 1.90 (m, 4H, H_l), 1.76 (d, *J* = 5.8 Hz, 2H, H_m), 1.30 (d, J = 6.9 Hz, 6H, H_q) **^{13}C-NMR** (δ, ppm, 100 MHz, $CDCl_3$): 164.48 (C=O imides), 163.92 (C=O imides), 157.82 (C quaternary naphthalene piperidine), 156.79 (C-H pyridine close to N), 153.13 (C-H pyridine close to N), 138.31 (C-H pyridine), 134.47 (C-H pyridine), 133.15 (C quaternary naphthalene), 131.40 (C-H naphthalene), 131.23 (C-H naphthalene), 130.07 (C quaternary pyridine), 126.26 (C quaternary naphthalene), 125.44 (C-H naphthalene), 124.11 (C-H naphthalene), 122.71 (C quaternary naphthalene), 115.23 (C quaternary naphthalene), 114.79 (C-H naphthalene), 103.62 (C quaternary p-cymene), 97.03 (C quaternary p-cymene), 82.63 (C-H aromatic p-cymene), 54.56 (CH_2 piperidine close to N), 40.60 (CH_2 bridge), 30.61 (CH_3 p-cymene), 26.21 (CH_2 piperidine), 24.32 (CH_2 piperidine), 22.27 (CH_3 isopropyl p-cymene), 18.07 (CH isopropyl p-cymene) **ESI-MS (+)** m/z $[M\text{-}Cl]^+$ calc 642,18 found 642,13 **CHNS analysis**: $C_{33}H_{35}N_3O_2Cl_2Ru$: calculated: C: 58.49, H: 5.21, N: 10.46. Found: C: 57.92, H: 5.04, N: 10.26.

[(η^6-p-cym)Ru(L8)Cl$_2$] (I4)

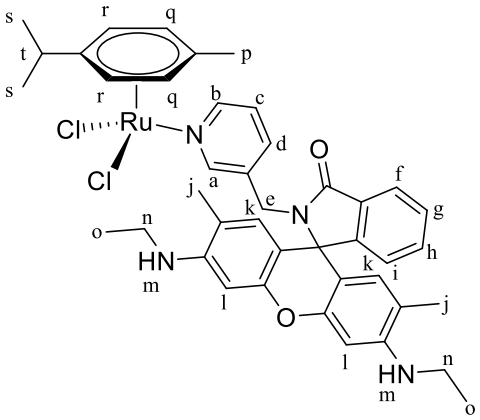

$[(\eta^6\text{-p-Cym})RuCl_2]_2$ (0.077 g, 0.131 mmol, 1 eq.), **L8** (0.127 g, 0.254 mmol, 2 eq.). Purple solid. **Yield**: 90% **^{1}H-NMR** (δ, ppm, 400 MHz, $CDCl_3$): 8.76 (bs, 1H, H_a), 8.69 (d, J = 5.6 Hz, 1H, H_b), 7.99 (d, J = 7.2 Hz, 1H, H_i), 7.50 (m, 2H, H_g, H_h), 7.22 (bs, 1H, H_d), 7.06 (d, J = 6.8 Hz, 1H, H_f), 6.92 (bs, 1H, H_c), 6.36 (s, 2H, H_l), 6.12 (s, 2H, H_k), 5.37 (d, J = 6 Hz, 2H H_q), 5.21 (d, J = 5.6 Hz, 2H, H_r), 4.30 (s, 2H, H_e), 3.23 (bs, 4H, H_n), 3.05 (m, 1H, H_t), 2.13 (s, 3H, H_p), 1.86 (s, 6H, H_j), 1.34 (m, 12H, H_o, H_s) **^{13}C-NMR** (δ, ppm, 100 MHz, $CDCl_3$): 168.63 (C quaternary amide), 155.08 (C-H pyridine close to N), 153.61 (C quaternary rhodamine close to O), 152.21 (C-H pyridine close to N), 151.60 (C quaternary rhodamine close to NH), 137.77 (C quaternary rhodamine), 134.70 (C quaternary rhodamine), 132.96 (C-H pyridine), 130.30 (C quaternary pyridine), 128.67 (C-H rhodamine), 128.29 (C-H pyridine), 123.90 (C-H rhodamine), 123.06 (C-H rhodamine), 123.01 (C quaternary rhodamine), 118.24 (C-H rhodamine), 104.19 (C-H rhodamine), 103.85 (C quaternary p-cymene), 96.56 (C quaternary p-cymene), 96.40 (C-H rhodamine), 83.02 (C-H aromatic p-cymene), 81.92 (C-H aromatic p-cymene), 65.27 (C quaternary rhodamine), 41.04 (CH_2 bridge) ,38.43 (CH_2 NH ethyl rhodamine), 30.61 (CH_3 p-cymene), 22.29 (CH_3 isopropyl p-cymene), 18.07 (CH isopropyl p-cymene), 16.75 (CH_3 NH ethyl rhodamine), 14.70 (CH_3 rhodamine) **ESI-MS (+)** m/z $[M\text{-}Cl]^+$ calc 775.38 found 775.27 **CHNS analysis**: $C_{42}H_{46}N_4O_2Cl_2Ru$: calculated: C: 62.22, H: 5.72, N: 6.91. Found: C: 60.22, H: 5.45, N: 6.24.

[(η^6-p-cym)Ru(L18)Cl$_2$] (I5)

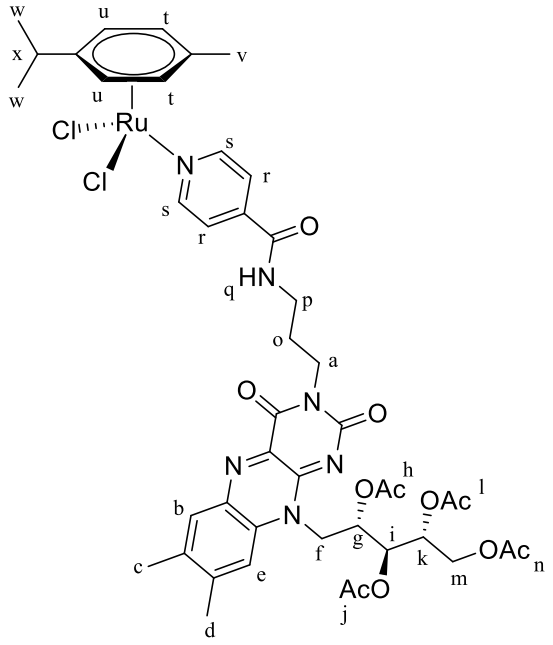

[(η^6-p-Cym)RuCl$_2$]$_2$ (0.034 g, 0.056 mmol, 1 eq.), **L8** (0.079 g, 0.112 mmol, 2 eq.). Orange solid. **Yield**: 59% **^{1}H-NMR** (δ, ppm, 400 MHz, CDCl$_3$): 9.16 (d, J = 6 Hz, 2H, H$_s$), 8.07 (s, 1H, H$_b$), 8.03 (t, J = 6.4 Hz, 1H, H$_q$), 7.82 (d, J = 6 Hz, 2H, H$_r$), 7.60 (s, 1H, H$_e$), 5.68 (s, 1H, H$_g$), 5.48 (m, 4H, H$_i$, H$_k$, H$_t$), 5.27 (d, J = 6 Hz, 2H, H$_u$), 4.99 (bs, 2H, H$_f$), 4.48 (d, J = 12.4 Hz, 1H, H$_m$), 4.29 (dd, J = 12.4 Hz, J' = 5.6 Hz, 1H, H$_m$), 4.23 (s, 2H, H$_a$), 3.48 (m, 2H, H$_p$), 3.00 (m, 1H, H$_x$), 2.58 (s, 3H, H$_d$), 2.47 (s, 3H, H$_c$), 2.30 (s, 3H, H$_h$), 2.24 (s, 3H, H$_j$), 2.12 (s, 3H, H$_v$), 2.10 (s, 5H, H$_l$, H$_o$), 1.75 (s, 3H, H$_n$), 1.33 (d, J = 9.6 Hz, 6H, H$_w$) **^{13}C-NMR** (δ, ppm, 100 MHz, CDCl$_3$): 170.68 (C=O ribityl acetate), 170.26 (C=O ribityl acetate), 169.79 (C=O ribityl acetate), 169.64 (C=O ribityl acetate), 167.54 (HN-C=O pyridine), 160.54 (C=O flavin core), 155.59 (C=O flavin core), 150.23 (C-H pyridine close to nitrogen), 149.57 (N-C=N flavin core), 147.13 (C-CH$_3$ flavin core), 141.83 (C quaternary pyridine close to carbonyl), 137.16 (C-CH$_3$ flavin core), 135.61 (C-H pyridine close to amide), 135.27 (N=C-C=O flavin core), 135.04 (N-C=C aromatic flavin core), 132.93 (C-H aromatic flavin core), 131.31 (N-C=C aromatic flavin core), 115.52 (C-H aromatic flavin core), 103.97 (C quaternary p-cymene), 99.42 (C quaternary p-cymene), 85.11 (C-H aromatic p-cymene), 81.37 (C-H aromatic p-cymene), 70.42 (C-H ribityl), 69.18 (C-H ribityl), 69.11 (C-H ribityl), 61.99 (C-H ribityl), 44.69 (CH$_2$ ribityl), 39.15 (CH$_2$-N propyl), 36.36 (CH$_2$-NH amide), 30.33 (CH$_3$ p-cymene), 27.27 (CH$_2$ propyl), 22.41 (CH$_3$ isopropyl p-cymene), 21.52 (CH$_3$ aromatic flavin core), 21.03 (CH$_3$ acetate ribityl), 20.79 (CH$_3$ acetate ribityl), 20.72 (CH$_3$ acetate ribityl), 20.33 (CH$_3$ acetate ribityl), 19.50 (CH$_3$ aromatic flavin core), 18.87 (CH isopropyl p-cymene) **ESI-MS (+)** m/z [M-C$_{11}$H$_{19}$O$_6$]$^+$ calc 730.12 found 730.17 **CHNS analysis**: C$_{44}$H$_{52}$N$_6$O$_{11}$Cl$_2$Ru: calculated: C: 52.18, H: 5.17, N: 8.30. Found: C: 51.69, H: 5.34, N: 8.12.

13.3 Intermediate complexes: monodentate carbene ligands

General synthetic procedure for the intermediate complexes with carbene monodentate ligand

The synthesis of the carbene complexes is divided in two steps. In the first step, the imidazolium salt (2 eq.) and Ag$_2$O (1 eq.) were dissolved in acetonitrile dry in a Schlenk flask with nitrogen atmosphere. The mixture was heated at 40°C for 4 hours. The linear complex silver-carbene is formed during this step, with the formation of an equivalent of AgI, a white precipitate. In the second step the [(η^6-p-Cym)RuCl$_2$]$_2$ (1 eq.) is

added, with acetonitrile, in the reaction mixture. The reaction was stirred for 24 hours at room temperature. In this step, the desired ruthenium-carbene complex is formed, with the formation of a second equivalent of AgI. After 24 hours the reaction is stopped, diethyl ether was added, and the solution was left al -4°C overnight. The precipitate was collected by filtration, washed with cold diethyl ether, and dried under vacuum.

[(η^6-p-cym)Ru(L9)Cl$_2$] (I6)

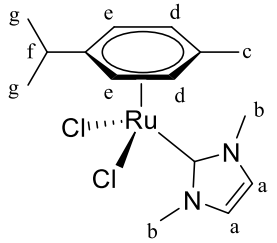

[(η^6-p-Cym)RuCl$_2$]$_2$ (0.349 g, 0.570 mmol, 1 eq.), **L9** (0.254g, 1.14 mmol, 2 eq.) and Ag_2O (0.132 g, 0.568 mmol, 1 eq.). Black solid. **Yield**: 79% **^{1}H-NMR** (δ, ppm, 400 MHz, $CDCl_3$): 6.99 (s, 2H, H_a), 5.42 (d, J = 8 Hz, 2H, H_d), 5.15 (d, J = 8 Hz, 2H, H_e), 4.01 (s, 6H, H_b), 2.96 (m, 1H, H_f), 2.09 (s, 3H, H_c), 1.27 (d, J = 9.6 Hz, 6H, H_g) **^{13}C-NMR** (δ, ppm, 100 MHz, $CDCl_3$): 173.37 (C quaternary carbene), 123.77 (C-H carbene), 108.90 (C quaternary p-cymene), 99.32 (C quaternary p-cymene), 84.78 (C-H p-cymene), 82.80 (C-H p-cymene), 39.57 (CH_3 carbene), 30.81 (CH_3 p-cymene), 22.52 (CH_3 isopropyl p-cymene), 18.67 (C-H isopropyl p-cymene), 1.03 (CH_3 carbene) **ESI-MS (+)** m/z [M-Cl]$^+$ calc 367.88 found 367.14 **CHNS analysis**: $C_{15}H_{23}N_2Cl_2Ru$: calculated: C: 44.67, H: 5.75, N: 6.95. Found: C: 44.53, H: 5.78, N: 5.67.

[(η^6-p-cym)Ru(L12)Cl$_2$] (I7)

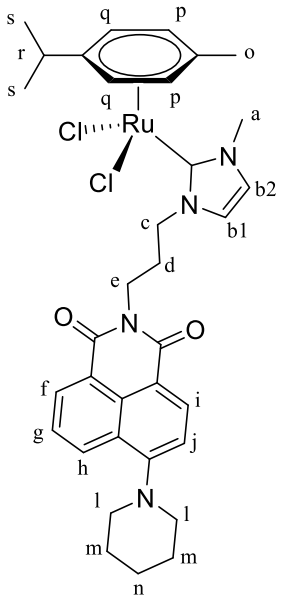

[(η^6-p-Cym)RuCl$_2$]$_2$ (0.058 g, 0.094 mmol, 1 eq.), **L12** (0.1 g, 0.19 mmol, 2 eq.) and Ag_2O (0.022 g, 0.094 mmol, 1 eq.). Orange solid. **Yield**: 83% **^{1}H-NMR** (δ, ppm, 400 MHz, $CDCl_3$): 8.57 (d, J = 7.2 Hz, 1H, H_f), 8.50 (d, J = 8.1 Hz, 1H, H_i), 8.40 (d, J = 8.4 Hz, 1H, H_h), 7.68 (t, J = 8.5, 1H, H_g), 7.18 (d, J = 8.1 Hz, 1H, H_j), 7.13 (d, J = 1.9 Hz, 1H, H_{b2}), 6.98 (d, J = 1.9 Hz, 1H, H_{b1}), 5.27 (m, 2H, H_p), 5.06 (m, 2H, H_q), 4.73 (bs, 1H, H_c), 4.30 (t, J = 6.8 Hz, 2H, H_e), 4.14 (bs, 1H, H_c), 3.95 (s, 3H, H_a), 3.25 (bs, 4H, H_l), 2.66 (m, 1H, H_r), 2.39 (bs, 1H, H_d), 2.20 (bs, 1H, H_d), 1.89 (bs, 7H, H_m, H_o), 1.74 (bs, 2H, H_n), 1.11 (d, J = 9.6 Hz, 6H, H_s) **^{13}C-NMR** (δ, ppm, 100 MHz, $CDCl_3$): 174.24 (C quaternary carbene), 164.97 (C=O imide), 164.49 (C=O imide), 157.29 (C-N piperidine quaternary), 132.54

(C-H naphthalene), 130.92 (C quaternary naphthalene), 130.62 (C quaternary naphthalene), 130.19 (C-H naphthalene), 126.34 (C-H naphthalene), 125.35 (C quaternary naphthalene), 124.06 (C-H imidazole), 123.44 (C quaternary naphthalene), 121.31 (C-H imidazole), 116.26 (C quaternary naphthalene), 114.70 (C-H naphthalene), 108.45 (C quaternary p-cymene), 99.98 (C quaternary p-cymene), 84.76 (C-H p-cymene), 83.69 (C-H p-cymene), 54.59 (CH_2 piperidine close to N)**,** 49.78 (CH_2 close to N), 39.49 (CH_3 methyl imidazole), 37.60 (CH_2 close to N), 30.60 (CH_3 p-cymene), 30.35 (CH_2 propyl), 26.25 (CH_2 piperidine), 24.35 (CH_2 piperidine), 18.52 (C-H isopropyl p-cymene) **ESI-MS (+)** m/z $[M\text{-}Cl]^+$ calc 672.25 found 672.98 **CHNS analysis**: $C_{34}H_{42}N_4O_2Cl_2Ru$: calculated: C: 57.46, H: 5.96, N: 7.88. Found: C: 56.79, H: 5.25, N: 6.90.

13.4 Intermediate complexes: bidentate ligands

General synthetic procedure for the intermediate complexes with the bidentate ligands

$[(\eta^6\text{-p-Cym})RuCl_2]_2$ (1 eq.), the bidentate ligand (2 eq.) and KPF_6 (2 eq.) were dissolved in methanol dry in a Schlenk flask with nitrogen atmosphere. The mixture was stirred for 4 hours, and during the reaction KCl is formed like white precipitate. The KCl is separated with filtration then diethyl ether was added, and the solution was left al -4°C overnight. The precipitate was collected by filtration, washed with cold diethyl ether and dried under vacuum.

$[(\eta^6\text{-p-cym})Ru(N,N'\text{-bpy})Cl](PF_6)$ (I8)

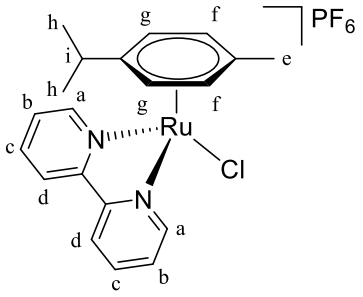

$[(\eta^6\text{-p-Cym})RuCl_2]_2$ (0.150 g, 0.25 mmol, 1 eq.), 2,2'-bipyridine (0.076 g, 0.49 mmol, 2 eq.) and KPF_6 (0.090 g, 0.49 mmol, 2 eq.). Yellow solid. **Yield**: 71% **^{1}H-NMR** (δ, ppm, 400 MHz, CD_6CO): 9.63 (d, J = 5.6, 2H, H_a), 8.65 (d, J = 8.4, 2H, H_d), 8.36 (m, 2H, H_b), 7.85 (m, 2H, H_c), 6.27 (d, J = 6.0, 2H, H_f), 6.02 (d, J = 6.0, 2H, H_g), 2.80 (m, 1H, H_i), 2.33 (s, 3H, H_e), 1.12 (d, J = 7.2 Hz, 6H, H_h) **^{13}C-NMR** (δ, ppm, 100 MHz, CD_6CO): 155.76 (C-H bipyridine close to N), 154.91 (C quaternary bipyridine), 139.91 (C-H bipyridine), 127.65 (C-H bipyridine), 123.75 (C-H bipyridine), 105.10 (C quaternary p-cymene), 103.88 (C quaternary p-cymene), 86.75 (C-H p-cymene), 84.49 (C-H p-cymene), 30.96 (CH_3 p-cymene), 21.35 (CH_3 isopropyl p-cymene), 17.96 (C-H isopropyl p-cymene) **ESI-MS (+)** m/z $[M\text{-}CH_3PF_6]^+$ calc. 427.05 found 427.17 **CHNS analysis**: $C_{20}H_{22}N_2PF_6ClRu$: calculated: C: 42.00, H: 3.88, N: 4.90. Found: C: 41.41, H: 3.46, N: 4.39.

[(η^6-p-cym)Ru(N,N'-phen)Cl](PF$_6$) (I9)

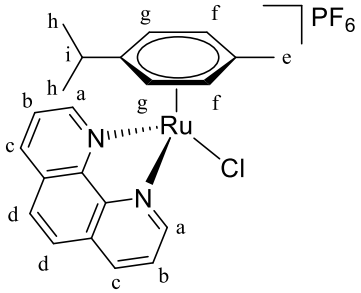

[(η^6-p-Cym)RuCl$_2$]$_2$ (0.3 g, 0.49 mmol, 1 eq.), 1,10-phenantroline (0.194 g, 0.98 mmol, 2 eq.) and KPF$_6$ (0.18 g, 0.98 mmol, 2 eq.). Orange solid. **Yield**: 81% **^{1}H-NMR** (δ, ppm, 400 MHz, CD$_6$CO): 9.69 (dd, J = 5.2 Hz, J' = 1.2 Hz, 2H, H$_a$), 8.59 (dd, J = 8 Hz, J' = 1.2 Hz, 2H, H$_c$), 8.07 (dd, J = 8.4 Hz, J' = 5.2 Hz, 2H, H$_b$), 8.04 (s, 2H, H$_d$), 6.06 (d, J = 6.4 Hz, 2H, H$_f$), 5.87 (d, J = 6.4 Hz, 2H, H$_g$), 2.74 (m, 1H, H$_i$), 2.24 (s, 3H, H$_e$), 1.08 (d, J = 9.6 Hz, 6H, H$_h$) **^{13}C-NMR** (δ, ppm, 100 MHz, CD$_6$CO): 155.67 (C-H phenanthroline close to N), 138.79 (C-H phenanthroline), 130.70 (C quaternary phenanthroline), 127.64 (C-H phenanthroline), 126.43 (C-H phenanthroline), 105.41 (C quaternary p-cymene), 85.99 (C-H p-cymene), 84.37 (C-H p-cymene), 30.96 (CH$_3$ p-cymene), 21.33 (CH$_3$ isopropyl p-cymene), 17.88 (C-H isopropyl p-cymene) **ESI-MS (+)** m/z [M-CH$_3$PF$_6$]$^+$ calc. 451.05 found 451.16 **CHNS analysis**: $C_{22}H_{22}N_2PF_6ClRu$: calculated: C: 44.34, H: 3.72, N: 4.70. Found: C: 44.41, H: 3.93, N: 4.65.

[(η^6-p-cym)Ru(N,N'-L7)Cl](PF$_6$) (I10)

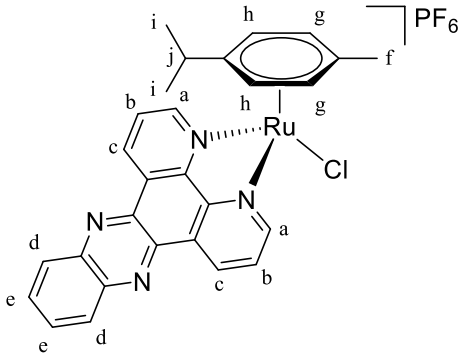

[(η^6-p-Cym)RuCl$_2$]$_2$ (0.3 g, 0.49 mmol, 1 eq.), **L7** (0.277 g, 0.98 mmol, 2 eq.) and KPF$_6$ (0.18 g, 0.98 mmol, 2 eq.). Orange solid. **Yield**: 78% **^{1}H-NMR** (δ, ppm, 400 MHz, CD$_6$CO): 9.78 (dd, J = 5.2 Hz, J' = 1.2 Hz, 2H, H$_a$), 9.72 (dd, J = 8 Hz, J' = 1.2 Hz, 2H, H$_c$), 8.32 (q, J = 3.6 Hz, 2H, H$_d$), 8.20 (dd, J = 8.4 Hz, J' = 5.6 Hz, 2H, H$_e$), 8.00 (q, J = 3.6 Hz, 2H, H$_e$), 6.15 (d, J = 6.4 Hz, 2H, H$_g$), 5.94 (d, J = 6.4 Hz, 2H, H$_h$), 2.81 (m, 1H, H$_j$), 2.32 (s, 3H, H$_f$), 1.13 (d, J = 9.6 Hz, 6H, H$_i$) **^{13}C-NMR** (δ, ppm, 100 MHz, CD$_6$CO): 155.67 (C-H dppz close to N), 148.33 (C quaternary dppz close to N), 142.08 (C quaternary dppz), 138.86 (C quaternary dppz), 135.45 (C-H dppz), 132.33 (C-H dppz), 129.90 (C quaternary dppz), 129.37 (C-H dppz), 127.70 (C-H dppz), 106.07 (C quaternary p-cymene), 103.13 (C quaternary p-cymene), 86.10 (C-H p-cymene), 84.77 (C-H p-cymene), 31.04 (CH$_3$ p-cymene), 21.46 (CH$_3$ isopropyl p-cymene), 18.00 (C-H isopropyl p-cymene) **ESI-MS (+)** m/z [M-CH$_3$PF$_6$]$^+$ calc. 553.05 found 553.18 **CHNS analysis**: $C_{28}H_{24}N_4PF_6ClRu$: calculated: C: 48.18, H: 3.47, N: 8.03. Found: C: 47.66, H: 3.40, N: 7.65.

[(η^6-p-cym)Ru(N,N'-L6)Cl](PF$_6$) (I11)

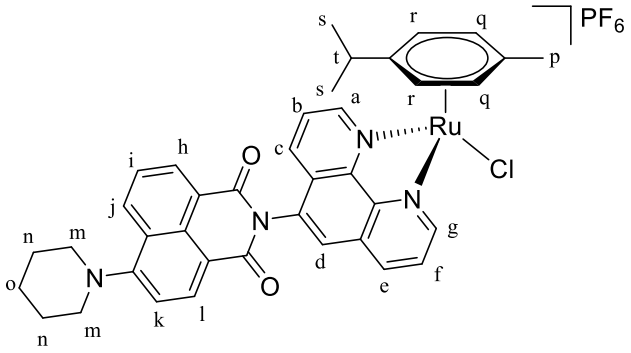

[(η^6-p-Cym)RuCl$_2$]$_2$ (0.1 g, 0.16 mmol, 1 eq.), **L6** (0.15 g, 0.33 mmol, 2 eq.) and KPF$_6$ (0.06 g, 0.33 mmol, 2 eq.). Orange solid. **Yield**: 82% **^{1}H-NMR** (δ, ppm, 400 MHz, CD_6CO): 9.76 (m, 2H, H_a, H_g), 8.62 (m, 1H, H_h), 8.58 (m, 1H, H_l), 8.50 (d, J = 8.4 Hz, 1H, H_e), 8.43 (t, J = 9.2 Hz, 1H, H_i), 8.34 (m, 1H, H_c), 8.03 (s, 1H, H_d), 7.96 (m, 1H, H_k), 7.81 (m, 1H, H_j), 7.68 (t, J = 8.4 Hz, 1H, H_b), 7.35 (t, J = 8.4 Hz, 1H, H_f), 6.12 (d, J = 5.9 Hz, 1H, H_q), 6.08 (d, J = 5.8 Hz, 1H, H_r), 5.90 (t, J = 5.4 Hz, 2H, H_r, H_q), 3.40 (bs, 4H, H_m), 2.77 (m, 1H, H_t), 2.23 (s, 3H, H_p), 2.01 (bs, 4H, H_n), 1.82 (bs, 2H, H_n), 1.11 (m, 6H, H_s) **^{13}C-NMR** (δ, ppm, 100 MHz, CD_6CO): 164.37 (C=O imide), 163.79 (C=O imide), 158.08 (C-N piperidine quaternary), 156.35 (C-H phenanthroline close to N), 156.07 (C-H phenanthroline close to N), 146.33 (C quaternary phenanthroline close to N), 145.74 (C quaternary phenanthroline close to N), 138.95 (C quaternary phenanthroline), 135.06 (C quaternary phenanthroline), 133.68 (C-H phenanthroline), 132.84 (C-H naphthalene), 131.53 (C-H phenanthroline), 131.10 (C quaternary naphthalene), 130.69 (C quaternary naphthalene), 129.67 (C-H naphthalene), 129.16 (C-H phenanthroline), 128.67 (C quaternary phenanthroline), 126.76 (C-H phenanthroline), 126.76 (C-H naphthalene), 126.40 (C-H naphthalene), 125.70 (C quaternary naphthalene), 123.15 (C quaternary naphthalene), 115.57 (C quaternary naphthalene), 115.00 (C-H naphthalene), 105.95 (C quaternary p-cymene), 102.60 (C quaternary p-cymene), 86.04 (C-H p-cymene), 85.98 (C-H p-cymene), 84.75 (C-H p-cymene), 84.62 (C-H p-cymene), 54.38 (CH_2 piperidine close to N),31.04 (CH_3 p-cymene), 26.03 (CH_2 piperidine), 24.12 (CH_2 piperidine) 21.48 (CH_3 isopropyl p-cymene), 21.37 (CH_3 isopropyl p-cymene), 17.84 (C-H isopropyl p-cymene) **ESI-MS (+)** m/z [M-CH_3PF_6]$^+$ calc. 729.26 found 729.25 **CHNS analysis**: $C_{39}H_{36}N_4PF_6ClRu$: calculated: C: 53.58, H: 4.15, N: 6.41. Found: C: 52.19, H: 3.86, N: 5.95.

13.5 Final complexes

General synthetic procedure for the final complexes

The monodentate intermediate complex (1 eq.) was dissolved in CH_2Cl_2 dry in a Schlenk flask with nitrogen atmosphere. At the same time AgTfO (2eq.) was dissolved in dry MeOH in nitrogen atmosphere, and then it was dropped slowly into the ruthenium complex solution. The solution became turbid immediately and it was stirred for 2 h at room temperature, covering the flask with aluminum foil to keep the solution in dark conditions. Then, the AgCl formed was removed filtering the solution in a Schlenk filter and the clear solution obtained was dropped in a Schlenk flask with the bidentate ligand (1 eq.). The mixture was stirred overnight always in nitrogen and dark environment. In the end, diethyl ether was added, and the solution was left al -4°C overnight. The precipitate was collected by filtration, washed with cold diethyl ether, and dried under vacuum.

[(η^6-p-cym)Ru(N,N'-bpy)(L1)](SO$_3$CF$_3$)$_2$ (C1)

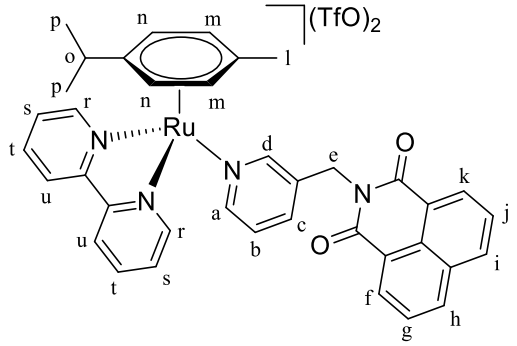

I1 (0.10 g, 0.17 mmol, 1 eq.), AgTfO (0.09 g, 0.34 mmol, 2 eq.) and 2,2'-bipyridine (0.03 g, 0.17 mmol, 1 eq.). Orange solid. **Yield**: 77% **^{1}H-NMR** (δ, ppm, 400 MHz, DMSO-D$_6$): 9.88 (dd, J = 5.7, J' = 1.4 Hz, 2H, H$_r$), 8.51 (ddd, J = 8.3, J' = 3.7, J'' = 1.3 Hz, 5H, H$_a$, H$_u$, H$_f$, H$_k$), 8.46 (d, J = 1.1 Hz, 1H, H$_d$), 8.37 (d, J = 5.5 Hz, 1H, H$_c$), 8.29 (td, J = 7.9, J = 1.4 Hz, 2H, H$_s$), 7.96 (m, 4H, H$_j$, H$_i$, H$_h$, H$_g$), 7.91 (dd, J = 8.2, J' = 7.3 Hz, 2H, H$_t$), 7.43 (dd, J = 7.9, J' = 5.7 Hz, 1H, H$_b$), 6.66 (d, J = 6.3 Hz, 2H, H$_m$), 6.27 (d, J = 6.3 Hz, 2H, H$_n$), 5.16 (s, 2H, H$_e$), 2.41 (m, 1H, H$_n$), 1.78 (s, 3H, H$_l$), 0.82 (d, J = 6.9 Hz, 6H, H$_p$) **^{1}H-NMR** (δ, ppm, 400 MHz, CDCl$_3$): 10.32 (d, J = 5.5 Hz, 2H, H$_r$), 8.76 (d, J = 5.7 Hz, 1H, H$_a$), 8.63 (s, 1H, H$_d$), 8.50 (d, J = 7.2 Hz, 2H, H$_u$), 8.25 (d, J = 8.4 Hz, 2H, H$_k$, H$_f$), 8.21 (t, J = 7.8 Hz, 2H, H$_s$), 8.11 (m, 4H, H$_t$, H$_h$, H$_i$), 7.93 (d, J = 9.0 Hz, 1H, H$_c$), 7.79 (t, J = 8 Hz, H$_g$, H$_j$), 7.42 (t, J = 7.4 Hz, 1H, H$_b$), 6.54 (d, J = 6.3 Hz, 2H, H$_m$), 6.45 (d, J = 6.3 Hz, 2H, H$_n$), 5.26 (s, 2H, H$_e$), 2.42 (m, 1H, H$_o$), 1.87 (s, 3H, H$_l$), 0.93 (d, J = 6.8 Hz, 6H, H$_p$) **^{13}C-NMR** (δ, ppm, 100 MHz, CDCl$_3$): 163.71 (C=O imides), 158.05 (C-H bipyridine close to N), 156.38 (C-H pyridine close to N), 153.18 (C-H pyridine close to N), 140.63 (C quaternary bipyridine), 138.42 (C-H pyridine), 134.81 (C-H naphthalene), 133.70 (C quaternary naphthalene), 131.86 (C-H naphthalene), 130.62 (C quaternary pyridine), 127.09 (C-H naphthalene), 123.44 (C-H pyridine), 121.87 (C quaternary naphthalene), 102.70 (C quaternary p-cymene), 92.36 (C quaternary p-cymene), 85.16 (C-H aromatic p-cymene), 40.30 (CH_2 bridge), 31.05 (CH_3 p-cymene), 22.27 (CH_3 isopropyl p-cymene), 18.03 (CH isopropyl p-cymene) **ESI-MS (+)** m/z [M-TfO$^-$] $^+$ m/z calc. 829.84 found 829.14 **CHNS analysis**: $C_{40}H_{34}N_4O_8S_2F_6Ru$: calculated: C: 49.13, H: 3.50, N: 5.73, S: 6.56. Found: C: 48.51, H: 3.87, N: 5.25, S: 6.43.

[(η^6-p-cym)Ru(N,N'-bpy)(L2)](SO$_3$CF$_3$)$_2$ (C2)

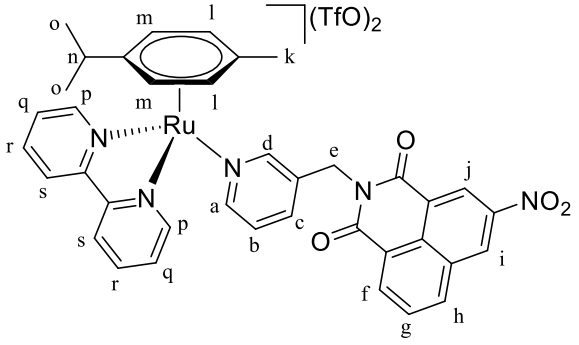

I2 (0.050 g, 0.078 mmol, 1 eq.), AgTfO (0.040 g, 0.156 mmol, 2 eq.) and 2,2'-bipyridine (0.012 g, 0.078 mmol, 1 eq.). Red solid. **Yield**: 71% **^{1}H-NMR** (δ, ppm, 400 MHz, DMSO-D$_6$): 9.89 (d, J = 6.2 Hz, 1H, H$_p$), 9.53 (s, 1H, H$_j$), 8.89 (s, 1H, H$_i$), 8.82 (d, J = 8.1 Hz, 1H, H$_a$), 8.64 (d, J = 7.4 Hz, 1H, H$_f$), 8.57 (s, 1H ,H$_d$), 8.54 (d, J = 9.0 Hz, 2H, H$_s$), 8.37 (d, J = 5.5 Hz, 1H, H$_c$), 8.32 (t, J = 6.2 Hz, 2H, H$_q$), 8.09 (t, J = 8.1 Hz, 1H, H$_g$), 8.00 (s, 3H, H$_r$, H$_h$), 7.44 (t, J = 7.4 Hz, 1H, H$_b$), 6.68 (d, J = 6.3 Hz, 2H, H$_l$), 6.27 (d, J = 6.3 Hz, 2H, H$_m$), 5.17 (s, 2H, H$_e$), 2.45 (m, 1H, H$_n$), 1.77 (s, 3H, H$_k$), 0.81 (d, J = 6.8 Hz, 6H, H$_o$) **^{1}H-NMR** (δ, ppm, 400 MHz, CDCl$_3$): 10.40 (d, J = 5.6 Hz, 2H, H$_p$), 9.14 (s, 1H, H$_j$), 9.06 (s, 1H, H$_i$), 8.78 (s, 2H, H$_s$), 8.72 (d, J = 8.1 Hz, 1H, H$_a$), 8.45 (d, J = 7.4 Hz, 1H, H$_f$), 8.27 (t, J = 6.2 Hz, 2H, H$_q$), 8.18 (t, J = 6.2 Hz, 2H, H$_r$), 8.12 (d, J = 5.5 Hz, 2H, H$_d$, H$_h$), 7.98 (t, J = 8.1 Hz, 1H, H$_g$), 7.90 (t,

J = 5.5 Hz, 1H, H_c), 7.43 (t, J = 7.4 Hz, 1H, H_b), 6.50 (m, 4H, H_l, H_m), 5.34 (s, 2H, H_e), 2.43 (m, 1H, H_n), 1.90 (s, 3H, H_k), 0.94 (d, J = 6.8 Hz, 6H, H_o) **^{13}C-NMR** (δ, ppm, 100 MHz, $CDCl_3$): 162.45 (C=O imides), 162.15 (C=O imides), 158.21 (C-H bipyridine close to N), 154.51 (C-H pyridine close to N), 154.01 (C-H pyridine close to N), 146.68 (C quaternary naphthalene close to NO_2), 140.69 (C quaternary bipyridine), 140.09 (C-H pyridine), 136.51 (C-H naphthalene), 136.33 (C-H naphthalene), 134.87 (C-H naphthalene), 131.15 (C-H pyridine), 130.77 (C quaternary naphthalene), 130.43 (C-H bipyridine), 129.48 (C quaternary pyridine), 129.33 (C-H naphthalene), 127.47 (C-H naphthalene), 124.24 (C quaternary naphthalene), 123.99 (C quaternary naphthalene), 123.85 (C quaternary naphthalene), 123.09 (C-H bipyridine), 103.98 (C quaternary p-cymene), 92.35 (C-H aromatic p-cymene), 84.85 (C-H aromatic p-cymene), 40.63 (CH_2 bridge), 31.12 (CH_3 p-cymene), 22.36 (CH_3 isopropyl p-cymene), 21.93 (CH_3 isopropyl p-cymene), 18.05 (CH isopropyl p-cymene) **ESI-MS (+)** m/z $[M\text{-}TfO^-]^+$ m/z calc. 873.85. found 874.23 **CHNS analysis**: $C_{40}H_{33}N_5O_{10}S_2F_6Ru$: calculated: C: 46.97, H: 3.25, N: 6.85, S: 6.27. Found: C: 45.19, H: 3.41, N: 6.30, S: 6.26.

[(η^6-p-cym)Ru(N,N'-bpy)(L4)](SO$_3$CF$_3$)$_2$ (C3)

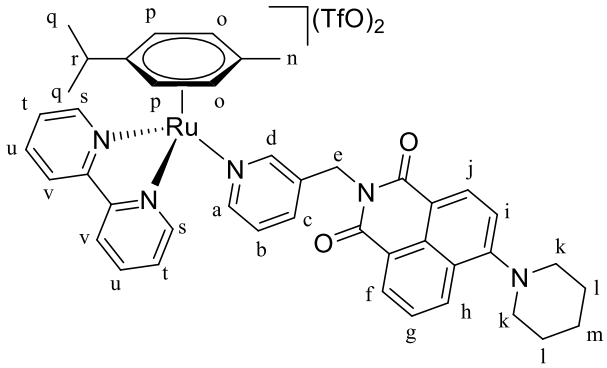

I3 (0.12 g, 0.17 mmol, 1 eq.), AgTfO (0.09 g, 0.35 mmol, 2 eq.) and 2,2'-bipyridine (0.03 g, 0.17mmol, 1 eq.). Orange solid. **Yield**: 91% **^{1}H-NMR** (δ, ppm, 400 MHz, DMSO-D_6): 9.87 (d, J = 5.5 Hz, 2H, H_s), 8.51 (m, 3H, H_a, H_d, H_f), 8.44 (dd, J = 7.8, J = 6.4 Hz, 2H, H_t), 8.35 (m, 2H, H_j, H_h), 8.29 (t, J = 7.9 Hz, 2H, H_u), 7.95 (t, J = 7.0 Hz, 3H, H_v, H_c), 7.84 (m, 1H, H_g), 7.43 (m, 1H, H_b), 7.33 (d, J = 8.3 Hz, 1H, H_i), 6.66 (d, J = 6.2 Hz, 2H, H_p), 6.27 (d, J = 6.3 Hz, 2H, H_o), 5.13 (s, 2H, H_e), 3.24 (s, 4H, H_k), 2.45 (m, 1H, H_r), 1.84 (s, 4H, H_l), 1.78 (s, 3H, H_n), 1.69 (s, 2H, H_m), 0.82 (d, J = 6.9 Hz, 6H, H_q) **^{1}H-NMR** (δ, ppm, 400 MHz, $CDCl_3$): 10.24 (d, J = 5.7 Hz, 2H, H_s), 8.76 (d, J = 5.5 Hz, 1H, H_a), 8.56 (s, 1H, H_d), 8.41 (t, J = 6.2 Hz, 2H, H_t), 8.35 (d, J = 8.1 Hz, 1H, H_f), 8.20 (m, 4H, H_v, H_h, H_j), 8.07 (t, J = 6.2 Hz, 2H, H_u), 7.93 (d, J = 7.4 Hz, 1H, H_c), 7.69 (d, J = 8.5, 1H, H_g), 7.40 (t, J = 7.4 Hz, 1H, H_b), 7.24 (d, J = 8.2 Hz, 1H, H_i), 6.52 (d, J = 6.3 Hz, 2H, H_o), 6.42 (d, J = 6.3 Hz, 2H, H_p), 5.20 (s, 2H, H_e), 3.29 (s, 4H, H_k), 2.41 (m, 1H, H_r), 1.92 (bs, 4H, H_l), 1.86 (s, 3H, H_n), 1.77 (s, 2H, H_m), 0.92 (d, J = 6.8 Hz, 6H, H_q) **^{13}C-NMR** (δ, ppm, 100 MHz, $CDCl_3$): 163.91 (C=O imides), 163.05 (C=O imides), 157.35 (C quaternary naphthalene piperidine), 154.78 (C-H bipyridine close to N), 153.04 (C-H pyridine close to N), 140.68 (C quaternary bipyridine), 140.39 (C-H pyridine close to N), 136.81 (C-H pyridine), 133.04 (C-H pyridine), 131.55 (C-H naphthalene), 131.07 (C-H naphthalene), 130.42 (C quaternary naphthalene), 130.35 (C-H bipyridine), 129.47 (C quaternary pyridine), 127.35 (C-H bipyridine), 125.73 (C quaternary naphthalene), 125.31 (C-H naphthalene), 123.67 (C-H bipyridine), 122.36 (C-H naphthalene), 122.11 (C quaternary naphthalene), 119.26 (C quaternary naphthalene), 116.00 (C-H naphthalene), 109.26 (C quaternary p-cymene), 103.45 (C quaternary p-cymene), 92.42 (C-H aromatic p-cymene), 85.00 (C-H aromatic p-cymene), 55.21 (CH_2 piperidine close to N), 40.23 (CH_2 bridge), 31.24 (CH_3 p-cymene), 25.75 (CH_2 piperidine), 23.66 (CH_2 piperidine), 22.19 (CH_3 isopropyl p-cymene), 17.94 (CH isopropyl p-cymene) **ESI-MS (+)** m/z $[M\text{-}TfO^-]^+$ m/z calc. 911.98. found 912.49 **CHNS analysis**: $C_{45}H_{43}N_5O_8S_2F_6Ru$: calculated: C: 50.94, H: 4.09, N: 6.60, S: 6.04. Found: C: 48.86, H: 4.05, N: 6.14, S: 5.99.

[(η^6-p-cym)Ru(N,N'-bpy)(L8)](SO$_3$CF$_3$)$_2$ (C4)

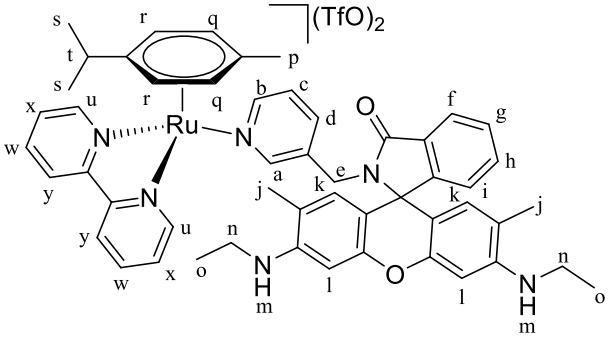

I4 (0.183 g, 0.23 mmol, 1 eq.), AgTfO (0.116 g, 0.45 mmol, 2 eq.) and 2,2'-bipyridine (0.035 g, 0.23 mmol, 1 eq.). Purple solid. **Yield**: 45% **^{1}H-NMR** (δ, ppm, 400 MHz, DMSO-D_6): 9.83 (d, J = 5.2 Hz, 2H, H_u), 8.65 (d, J = 8 Hz, 2H, H_y), 8.53 (s, 1H, H_a), 8.40 (t, J = 7.9 Hz, 2H, H_w), 8.09 (d, J = 4.8 Hz, 1H, H_b), 8.05 (t, J = 6.4 Hz, 2H, H_x), 7.90 (d, J = 6.4 Hz, 1H, H_f), 7.53 (m, 2H, H_g, H_h), 7.09 (d, J = 8.4 Hz, 1H, H_d), 7.00 (t, J = 5.6 Hz, 1H, H_c), 6.91 (d, J = 7.6 Hz, 1H, H_i), 6.63 (d, J = 6.4 Hz, 2H, H_q), 6.14 (d, J = 6.4 Hz, 2H, H_r), 6.07 (s, 2H, H_l), 5.60 (s, 2H, H_k), 4.98 (t, J = 5.2 Hz, 2H, H_m), 4.14 (s, 2H, H_e), 3.05 (q, J = 6.8 Hz, 4H, H_n), 2.36 (m, 1H, H_t), 1.58 (s, 3H, H_p), 1.48 (s, 6H, H_j), 1.18 (t, J = 7.2 Hz, 6H, H_o), 0.79 (d, J = 6.8 Hz, 6H, H_s) **^{1}H-NMR** (δ, ppm, 400 MHz, $CDCl_3$): 10.16 (d, J = 5.2 Hz, 2H, H_u), 8.61 (d, J = 8 Hz, 2H, H_y), 8.43 (s, 1H, H_a), 8.25 (m, 3H, H_w, H_b), 8.09 (t, J = 6.4 Hz, 2H, H_x), 7.88 (m, 1H, H_f), 7.51 (m, 2H, H_g, H_h), 7.06 (m, 1H, H_d), 7.00 (m, 1H, H_c), 6.75 (d, J = 7.6 Hz, 1H, H_i), 6.48 (d, J = 6.4 Hz, 2H, H_q), 6.33 (d, J = 6.4 Hz, 2H, H_r), 5.85 (s, 2H, H_l), 4.04 (s, 2H, H_e), 3.53 (m, 2H, H_m), 3.23 (q, J = 6.8 Hz, 4H, H_n), 2.39 (m, 1H, H_t), 1.36 (s, 6H, H_j), 1.20 (t, J = 7.2 Hz, 6H, H_o), 0.91 (d, J = 6.8 Hz, 6H, H_s) **^{13}C-NMR** (δ, ppm, 100 MHz, $CDCl_3$): 167.89 (C quaternary amide), 157.05 (C-H bipyridine close to N), 154.78 (C-H pyridine close to N), 152.80 (C quaternary rhodamine close to O), 152.57 (C quaternary rhodamine close to NH), 151.89 (C-H pyridine close to N), 147.66 (C quaternary bipyridine), 141.07 (C-H bipyridine), 137.42 (C quaternary rhodamine), 133.29 (C quaternary rhodamine), 130.06 (C-H pyridine), 128.62 (C quaternary pyridine), 128.62 (C-H rhodamine), 128.13 (C-H bipyridine), 124.29 (C-H rhodamine), 122.74 (C-H rhodamine), 122.37 (C quaternary rhodamine), 118.26 (C-H rhodamine), 108.41 (C quaternary p-cymene), 104.77 (C-H rhodamine), 104.72 (C quaternary p-cymene), 96.46 (C quaternary p-cymene), 91.98 (C-H rhodamine), 85.22 (C-H aromatic p-cymene), 81.92 (C-H aromatic p-cymene), 65.56 (C quaternary rhodamine), 40.73 (CH_2 bridge), 38.44 (CH_2 NH ethyl rhodamine), 31.02 (CH_3 p-cymene), 22.15 (CH_3 isopropyl p-cymene), 17.81 (CH isopropyl p-cymene), 16.57 (CH_3 NH ethyl rhodamine), 14.51 (CH_3 rhodamine) **ESI-MS (+)** m/z [M-TfO$^-$]$^+$ calc. 936.01 found 1037,99 **CHNS analysis**: $C_{54}H_{54}N_6O_8S_2F_6Ru$: calculated: C: 54.31, H: 4.56, N: 7.04, S: 5.37 Found: C: 52.90, H: 4.61, N: 6.75, S: 5.51.

[(η^6-p-cym)Ru(N,N'-phen)(L4)](SO$_3$CF$_3$)$_2$ (C5)

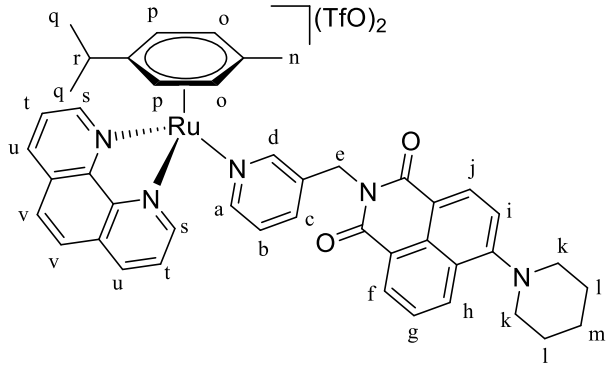

I3 (0.046 g, 0.068 mmol, 1 eq.), AgTfO (0.035 g, 0.136 mmol, 2 eq.) and 1,10-phenantroline (0.014 g, 0.068 mmol, 1 eq.). Orange solid. **Yield**: 80% **^{1}H-NMR** (δ, ppm, 400 MHz, DMSO-D_6): 10.28 (d, J = 5.3 Hz, 2H, H_s), 8.92 (d, J = 8 Hz, 2H, H_u), 8.50 (s, 1H, H_a), 8.42 (m, 2H, H_f, H_j), 8.38 (d, J = 7.1 Hz, 1H, H_d), 8.31 (m, 3H, H_g, H_b, H_c), 8.19 (s, 2H, H_v), 7.83 (m, 2H, H_t), 7.33 (m, 2H, H_i, H_h), 6.73 (d, J = 6.4 Hz, 2H, H_o), 6.39 (d, J = 6.4 Hz, 2H, H_p), 5.06 (s, 2H, H_e), 3.22 (bs, 4H, H_k), 2.38 (m, 1H, H_r), 1.83 (bs, 4H, H_l), 1.80 (s, 3H, H_n), 1.67 (bs, 2H, H_m), 0.68 (d, *J* = 6.9 Hz, 6H, H_q) **^{1}H-NMR** (δ, ppm, 400 MHz, $CDCl_3$): 10.68 (d, J = 5.2 Hz, 2H, H_s), 8.81 (d, J = 6 Hz, 1H, H_a), 8.71 (d, J = 8.4 Hz, 2H, H_u), 8.56 (s, 1H, H_d), 8.43 (d, J = 8 Hz, 2H, H_t), 8.37 (d, J = 8 Hz, 2H, H_f, H_h), 8.32 (d, J = 8.4 Hz, 1H, H_j), 8.03 (s, 2H, H_v), 7.81 (d, J = 6 Hz, 1H, H_c), 7.68 (t, J = 8 Hz, 1H, H_g), 7.31 (t, J = 8 Hz, 1H, H_b), 7.20 (d, J = 8.4 Hz, 1H, H_i), 6.64 (d, J = 6.4 Hz, 2H, H_o), 6.55 (d, J = 6.4 Hz, 2H, H_p), 5.11 (s, 2H, H_e), 3.26 (s, 4H, H_k), 2.33 (m, 1H, H_r), 1.91 (bs, 4H, H_l), 1.88 (s, 3H, H_n), 1.75 (bs, 2H, H_m), 0.80 (d, J = 9.6 Hz, 6H, H_q) **^{13}C-NMR** (δ, ppm, 100 MHz, $CDCl_3$): 163.80 (C=O imides), 163.20 (C=O imides), 157.97 (C quaternary naphthalene piperidine), 153.35 (C-H phenanthroline close to N), 152.82 (C-H pyridine close to N), 145.51 (C-H phenanthroline), 140.51 (C-H pyridine close to N), 139.64 (C quaternary phenanthroline), 136.90 (C-H pyridine), 133.07 (C-H pyridine), 131.36 (C-H naphthalene), 131.22 (C-H naphthalene), 130.63 (C-H phenanthroline), 130.46 (C quaternary naphthalene), 129.65 (C quaternary pyridine), 128.61 (C quaternary phenanthroline), 127.95 (C-H phenanthroline), 127.26 (C quaternary naphthalene), 125.84 (C quaternary naphthalene), 125.57 (C-H naphthalene), 122.48 (C-H naphthalene), 122.02 (C quaternary naphthalene), 119.30 (C quaternary naphthalene), 115.11 (C-H naphthalene), 105.26 (C quaternary p-cymene), 91.22 (C quaternary p-cymene), 85.05 (C-H aromatic p-cymene), 54.67 (CH_2 piperidine close to N), 39.95 (CH_2 bridge), 31.07 (CH_3 p-cymene), 26.00 (CH_2 piperidine), 22.10 (CH_3 isopropyl p-cymene), 18.05 (CH isopropyl p-cymene) **ESI-MS (+)** m/z [M-TfO^-]$^+$ calc. 936.01 found 936.33 **CHNS analysis**: $C_{49}H_{49}N_5O_8S_2F_6Ru$: calculated: C: 52.78, H: 4.43, N: 6.28, S: 5.75. Found: C: 52.17, H: 3.87, N: 5.94, S: 5.63.

[(η^6-p-cym)Ru(N,N'-L7)(L4)](SO$_3$CF$_3$)$_2$ (C6)

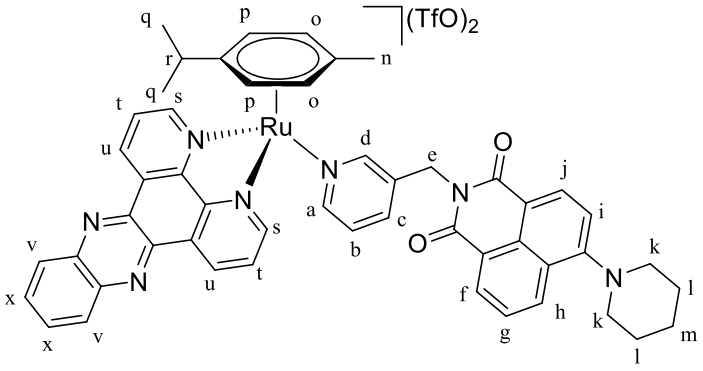

I3 (0.211 g, 0.311 mmol, 1 eq.), AgTfO (0.16 g, 0.623 mmol, 2 eq.) and **L7** (0.088 g, 0.311 mmol, 1 eq.). Orange solid. **Yield**: 68% **^{1}H-NMR** (δ, ppm, 400 MHz, DMSO-D_6): 10.34 (dd, J = 6.4 Hz, J' = 0.8 Hz, 2H, H_s), 9.75 (dd, J = 9.6 Hz, J' = 1.2 Hz, 2H, H_u), 8.55 (d, J = 5.2 Hz, 1H, H_a), 8.49 (m, 4H, H_f, H_h, H_x), 8.44 (s, 1H, H_d), 8.28 (m, 2H, H_v), 8.19 (m, 2H, H_t), 8.13 (d, J = 8 Hz, 1H, H_i), 7.87 (d, J = 7.6 Hz, 1H, H_c), 7.71 (dd, J = 16 Hz, J' = 7.6 Hz, 1H, H_g), 7.39 (dd, J = 14 Hz, J' = 6 Hz, 1H, H_b), 7.14 (d, J = 8.4 Hz, 1H, H_j), 6.83 (d, J = 6.4 Hz, 2H, H_o), 6.44 (d, J = 6.8 Hz, 2H, H_p), 5.04 (s, 2H, H_e), 3.04 (s, 4H, H_k), 2.68 (m, 1H, H_r), 1.85 (s, 3H, H_n), 1.78 (m, 4H, H_l), 1.66 (m, 2H, H_m), 0.82 (d, J = 6.8 Hz, 6H, H_q) **^{1}H-NMR** (δ, ppm, 400 MHz, $CDCl_3$): 10.72 (dd, J = 6.4 Hz, J' = 0.8 Hz, 2H, H_s), 9.90 (dd, J = 9.6 Hz, J' = 1.2 Hz, 2H, H_u), 8.93 (d, J = 5.2 Hz, 1H, H_a), 8.57 (t, J = 9.6 Hz, 2H, H_t), 8.47 (m, 3H, H_d, H_x), 8.17 (d, J = 8 Hz, 1H, H_i), 8.12 (m, 3H, H_v, H_f), 8.02 (d, J = 8.2 Hz, 1H, H_f), 7.82 (d, J = 7.6 Hz, 1H, H_c), 7.37 (m, 2H, H_g, H_b), 6.88 (d, J = 8.4 Hz, 1H, H_j), 6.74 (d, J = 6.4 Hz, 2H, H_o), 6.61 (d, J = 6.8 Hz, 2H, H_p), 5.09 (s, 2H, H_e), 3.08 (s, 4H, H_k), 2.49 (m, 1H, H_r), 1.97 (s, 3H, H_n), 1.84 (m, 4H, H_l), 1.71 (m, 2H, H_m), 0.92 (d, J = 6.8 Hz, 6H, H_q) **^{13}C-NMR** (δ, ppm, 100 MHz, $CDCl_3$): 162.40 (C=O imides), 160.86 (C=O imides), 158.55 (C quaternary naphthalene piperidine), 152.84 (C-H pyridine close to N), 147.77 (C-H dppz close to N), 143.03 (C quaternary

dppz close to N), 139.91 (C quaternary dppz), 138.54 (C-H pyridine close to N), 136.98 (C-H pyridine), 132.88 (C quaternary naphthalene), 132.78 (C quaternary dppz), 131.28 (C-H pyridine), 130.85 (C quaternary dppz), 130.39 (C-H dppz), 129.92 (C-H naphthalene), 129.88 (C-H dppz), 129.13 (C quaternary pyridine), 127.57 (C-H dppz), 126.89 (C quaternary naphthalene), 125.80 (C quaternary naphthalene), 125.08 (C-H naphthalene), 123.85 (C-H naphthalene), 122.04 (C-H dppz), 121.71 (C quaternary naphthalene), 117.86 (C quaternary naphthalene), 116.59 (C-H naphthalene), 108.72 (C quaternary p-cymene), 91.63 (C quaternary p-cymene), 85.17 (C-H aromatic p-cymene), 54.67 (CH_2 piperidine close to N), 40.06 (CH_2 bridge), 31.22 (CH_3 p-cymene), 25.95 (CH_2 piperidine), 22.28 (CH_3 isopropyl p-cymene), 18.15 (CH isopropyl p-cymene) **ESI-MS (+)** m/z [M-TfO^-]$^+$ calc. 1038.10 found 1037.99 **CHNS analysis**: $C_{53}H_{45}N_7O_8S_2F_6Ru$: calculated: C: 53.62, H: 3.82, N: 8.26, S: 5.40 Found: C: 51.00, H: 3.78, N: 7.59, S: 6.04.

[(η^6-p-cym)Ru(N,N'-L6)(L4)](SO_3CF_3)$_2$ (C7)

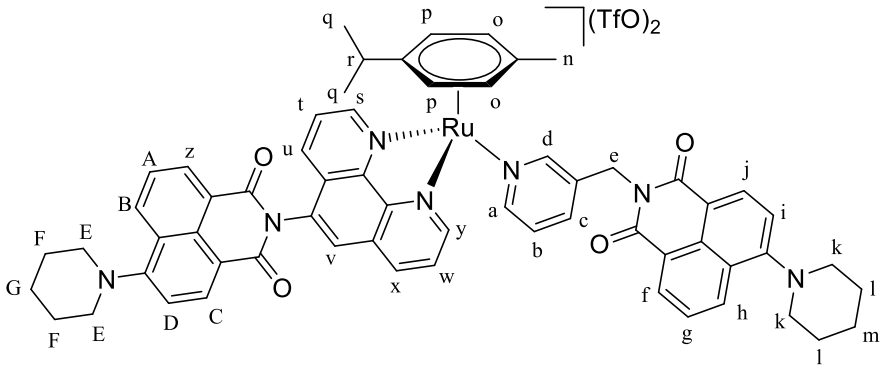

I3 (0.1 g, 0.148 mmol, 1 eq.), AgTfO (0.076 g, 0.295 mmol, 2 eq.) and **L4** (0.068 g, 0.148 mmol, 1 eq.). Orange solid. **Yield**: 54% **^{1}H-NMR** (δ, ppm, 400 MHz, DMSO-D_6): 10.40 (d, J = 5.2 Hz, 1H, H_s), 10.34 (d, J = 5.2 Hz, 1H, H_y), 9.00 (d, J = 8 Hz, 1H, H_d), 8.93 (dd, J = 12.4 Hz, J' = 4 Hz, 1H, H_a), 8.65 (s, 1H, H_v), 8.54 (m, 3H, H_f, H_j, H_z), 8.41 (m, 4H, H_c, H_h, H_t, H_C), 8.25 (t, J = 8.4 Hz, 2H, H_x, H_B), 8.15 (m, 1H, H_b), 7.91 (m, 2H, H_A, H_D), 7.77 (m, 1H, H_g), 7.41 (t, J = 7.6 Hz, 2H, H_i, H_u), 7.21 (dd, J = 10 Hz, J' = 4.4 Hz, 1H, H_w), 6.78 (t, J = 10 Hz, 2H, H_o), 6.53 (dd, J = 16.8 Hz, J' = 6.8 Hz, 2H, H_p), 5.12 (s, 2H, H_e), 3.30 (bm, 4H, H_E), 3.11 (bm, 4H, H_k), 2.43 (m, 1H, H_r), 1.88 (bm, 4H, H_F), 1.84 (s, 3H, H_n), 1.78 (bm, 4H, H_l), 1.72 (bm, 2H, H_G), 1.63 (bm, 2H, H_m), 0.74 (t, J = 12.8 Hz, 6H, H_q) **^{1}H-NMR** (δ, ppm, 400 MHz, $CDCl_3$): 10.72 (d, J = 5.3 Hz, 1H, H_s), 10.67 (d, J = 4.9 Hz, 1H, H_y), 8.78 (s, 1H, H_d), 8.71 (bs, 1H, H_u), 8.68 (d, J = 8.2 Hz, 1H, H_a), 8.52 (m, 3H, H_f, H_j, H_z), 8.47 (d, J = 7.0 Hz, 1H, H_C), 8.38 (m, 2H, H_t, H_h), 8.32 (m, 2H, H_x, H_B), 8.27 (m, 1H, H_b), 7.99 (s, 1H, H_v), 7.92 (d, J = 7.9 Hz, 1H, H_D), 7.75 (m, 1H, H_g), 7.60 (m, 1H, H_i), 7.32 (t, J = 8.4 Hz, 1H, H_A), 7.12 (bs, 1H, H_w), 6.65 (d, J = 6.2 Hz, 1H, H_o), 6.58 (d, J = 6.2 Hz, 1H, H_o), 6.52 (m, 2H, H_p), 5.16 (s, 2H, H_e), 3.33 (bs, 4H, H_E), 3.18 (bs, 4H, H_k), 2.30 (m, 1H, H_r), 1.92 (bm, 4H, H_F), 1.85 (bm, 4H, H_l), 1.82 (s, 3H, H_n), 1.77 (bm, 2H, H_G), 1.70 (bm, 2H, H_m), 0.79 (t, J = 12.8 Hz, 6H, H_q) **^{13}C-NMR** (δ, ppm, 100 MHz, $CDCl_3$): 164.54 (C=O imide), 164.01 (C=O imide), 163.83 (C=O imide), 163.37 (C=O imide), 159.08 (C-N piperidine quaternary), 158.71 (C-N piperidine quaternary), 153.96 (C-H phenanthroline close to N), 152.92 (C-H pyridine close to N), 152.63 (C-H phenanthroline close to N), 146.24 (C quaternary phenanthroline close to N), 145.47 (C quaternary phenanthroline close to N), 141.00 (C quaternary phenanthroline), 139.33 (C-H pyridine close to N), 137.11 (C-H pyridine), 135.00 (C quaternary phenanthroline), 134.11 (C-H phenanthroline), 133.46 (C quaternary naphthalene), 133.06 (C-H naphthalene), 132.41 (C-H phenanthroline), 132.08 (C-H pyridine), 131.47 (C quaternary naphthalene), 130.93 (C quaternary naphthalene), 129.75 (C-H naphthalene), 129.53 (C-H naphthalene), 129.04 (C-H phenanthroline), 128.85 (C quaternary pyridine), 128.58 (C quaternary phenanthroline), 127.42 (C quaternary naphthalene), 126.29 (C-H phenanthroline), 125.97 (C quaternary naphthalene), 125.73 (C-H naphthalene), 125.54 (C-H naphthalene), 125.44 (C quaternary naphthalene), 122.49 (C-H naphthalene), 122.17 (C quaternary naphthalene), 122.04 (C quaternary naphthalene), 119.17 (C quaternary naphthalene), 115.35 (C-H naphthalene), 114.96 (C quaternary naphthalene), 114.01 (C-H naphthalene), 108.24 (C quaternary p-cymene), 105.47 (C quaternary p-cymene), 91.31 (C-H p-cymene), 85.32 (C-H p-cymene), 54.61

(CH_2 piperidine close to N), 39.96 (CH_2 bridge), 31.22 (CH_3 p-cymene), 26.14 (CH_2 piperidine), 24.26 (CH_2 piperidine), 22.21 (CH_3 isopropyl p-cymene), 22.11 (CH_3 isopropyl p-cymene), 18.08 (C-H isopropyl p-cymene) **ESI-MS (+)** m/z $[M\text{-}TfO^-]^+$ calc. 1214.32 found 1214.24 **CHNS analysis**: $C_{64}H_{59}N_7O_{10}S_2F_6Ru$: calculated: C: 56.30, H: 4.36, N: 7.18, S: 4.70 Found: C: 53.37, H: 4.09, N: 6.77, S: 4.68.

$[(\eta^6\text{-p-cym})Ru(N,N'\text{-phen})(L9)](SO_3CF_3)_2$ (C8)

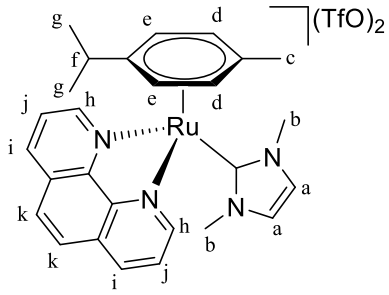

I6 (0.098 g, 0.24 mmol, 1 eq.), AgTfO (0.125 g, 0.48 mmol, 2 eq.) and 1,10-phenantroline (0.048 g, 0.24 mmol, 1 eq.). Orange solid. **Yield**: 51% **^{1}H-NMR** (δ, ppm, 400 MHz, DMSO-D_6): 10.21 (d, J = 4.4 Hz, 2H, H_h), 8.97 (d, J = 8 Hz, 2H, H_i), 8.27 (s, 2H, H_k), 8.15 (m, 2H, H_j), 7.25 (s, 2H, H_a), 6.75 (d, J = 6.4 Hz, 2H, H_d), 6.39 (d, J = 6.4 Hz, 2H, H_e), 3.47 (s, 3H, H_b), 2.60 (m, 1H, H_f), 1.96 (s, 3H, H_c), 0.73 (d, J = 9.6 Hz, 6H, H_g) **^{1}H-NMR** (δ, ppm, 400 MHz, $CDCl_3$): 10.64 (d, J = 4.4 Hz, 2H, H_h), 8.64 (d, J = 7.2 Hz, 2H, H_i), 8.29 (m, 2H, H_j), 8.06 (s, 2H, H_k), 6.90 (s, 2H, H_a), 6.76 (d, J = 6.4 Hz, 2H, H_d), 6.44 (d, J = 6.4 Hz, 2H, H_e), 3.72 (s, 3H, H_b), 2.60 (m, 1H, H_f), 2.03 (s, 3H, H_c), 0.82 (d, J = 9.6 Hz, 6H, H_g) **^{13}C-NMR** (δ, ppm, 100 MHz, $CDCl_3$): 160.51 (C quaternary carbene), 146.25 (C-H phenanthroline close to N), 138.89 (C-H phenanthroline), 130.67 (C-H phenanthroline), 127.79 (C quaternary phenanthroline), 126.68 (C-H carbene), 125.60 (C quaternary phenanthroline), 102.53 (C quaternary p-cymene), 95.99 (C quaternary p-cymene), 88.94 (C-H p-cymene), 82.03 (C-H p-cymene), 40.01 (CH_3 carbene), 31.23 (CH_3 p-cymene), 22.33 (CH_3 isopropyl p-cymene), 18.83 (C-H isopropyl p-cymene), 1.04 (CH_3 carbene) **ESI-MS (+)** m/z $[M\text{-}TFO^-]^+$ calc. 661.71 found 661.22 **CHNS analysis**: $C_{30}H_{35}N_4O_6S_2F_6Ru$: calculated: C: 43.58, H: 4.27, N: 6.78, S: 7.76. Found: C: 43.05, H: 3.49, N: 6.57, S: 6.87.

$[(\eta^6\text{-p-cym})Ru(N,N'\text{-phen})(L12)](SO_3CF_3)_2$ (C9)

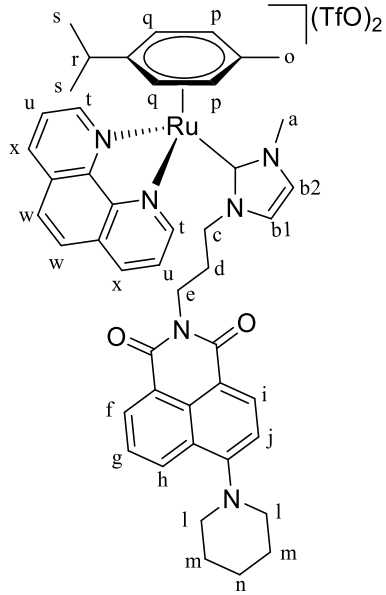

I7 (0.091 g, 0.128 mmol, 1 eq.), AgTfO (0.066 g, 0.256 mmol, 2 eq.) and 1,10-phenantroline (0.025 g, 0.128 mmol, 1 eq.). Orange solid. **Yield**: 67% **^{1}H-NMR** (δ, ppm, 400 MHz, DMSO-D_6): 10.31 (d, J = 4.7 Hz, 1H, H_t), 10.24 (d, J = 5.0 Hz, 1H, H_t), 8.97 (t, J = 11.9 Hz, 2H, H_i, H_f), 8.53 (d, J = 8.2 Hz, 1H, H_u), 8.46 (d, J = 8.5 Hz, 2H,

H_x), 8.28 (m, 3H, H_g, H_w), 8.19 (m, 1H, H_h), 7.86 (t, J = 8.5, 1H, H_u), 7.44 (s, 1H, H_{b2}), 7.36 (d, J = 8.4 Hz, 1H, H_j), 7.29 (s, 1H, H_{b1}), 6.82 (d, J = 5.9 Hz, 1H, H_p), 6.73 (d, J = 5.8 Hz, 1H, H_q), 6.47 (d, J = 6.0 Hz, 2H, H_p), 6.30 (d, J = 6.0 Hz, 2H, H_q), 4.28 (m, 1H, H_c), 4.14 (m, 1H, H_c), 4.03 (m, 1H, H_e), 3.92 (m, 1H, H_e), 3.23 (bs, 4H, H_l), 2.61 (m, 1H, H_r), 1.96 (s, 3H, H_o), 1.85 (s, 4H, H_m), 1.69 (bs, 2H, H_n), 1.59 (m, 1H, H_d), 1.33 (m, 1H, H_d), 0.80 (d, J = 6.9 Hz, 3H, H_s), 0.71 (d, J = 6.9 Hz, 3H, H_s) **^{1}H-NMR** (δ, ppm, 400 MHz, $CDCl_3$): 10.59 (d, J = 5.5 Hz, 2H, H_t), 8.77 (d, J = 8.9 Hz, 1H, H_u), 8.69 (d, J = 8.2 Hz, 1H, H_f), 8.50 (m, 2H, H_x), 8.44 (d, J = 8.1 Hz, 1H, H_i), 8.38 (d, J = 9.5 Hz, 1H, H_h), 8.26 (dd, J = 8.2, 5.5 Hz, 1H, H_g), 8.07 (s, 2H, H_w), 7.68 (t, J = 8.5, 1H, H_u), 7.33 (d, J = 2.0 Hz, 1H, H_{b2}), 7.18 (d, J = 8.1 Hz, 1H, H_j), 6.96 (d, J = 1.9 Hz, 1H, H_{b1}), 6.83 (d, J = 5.9 Hz, 1H, H_p), 6.73 (d, J = 5.8 Hz, 1H, H_q), 6.42 (t, J = 5.4 Hz, 2H, H_p, H_q), 4.33 (m, 1H, H_c), 4.25 (m, 1H, H_c), 4.14 (m, 1H, H_e), 3.94 (m, 1H, H_e), 3.71 (s, 3H, H_a), 3.25 (bs, 4H, H_l), 2.59 (m, 1H, H_r), 1.90 (bs, 7H, H_m, H_o), 1.75 (bs, 2H, H_n), 1.42 (m, 2H, H_d), 0.82 (d, J = 6.9 Hz, 3H, H_s), 0.78 (d, J = 6.9 Hz, 3H, H_s) **^{13}C-NMR** (δ, ppm, 100 MHz, $CDCl_3$): 164.46 (C quaternary carbene), 164.45 (C=O imide), 163.94 (C=O imide), 160.01 (C-H phenanthroline close to N), 159.09 (C-H phenanthroline close to N), 157.73 (C-N piperidine quaternary), 146.40 (C-H phenanthroline), 146.23 (C-H phenanthroline), 132.97 (C-H naphthalene), 131.20 (C quaternary naphthalene), 131.14 (C quaternary naphthalene), 130.89 (C-H phenanthroline), 128.02 (C quaternary phenanthroline), 127.92 (C quaternary phenanthroline), 126.40 (C quaternary phenanthroline), 126.30 (C quaternary phenanthroline), 126.10 (C-H naphthalene), 125.40 (C quaternary naphthalene), 123.58 (C-H imidazole), 122.53 (C quaternary naphthalene), 122.39 (C-H imidazole), 119.21 (C quaternary naphthalene), 115.02 (C-H naphthalene), 112.98 (C quaternary p-cymene), 109.59 (C quaternary p-cymene), 93.80 (C-H p-cymene), 84.18 (C-H p-cymene), 54.52 (CH_2 piperidine close to N)**,** 48.83 (CH_2 close to N), 39.96 (CH_3 methyl imidazole), 36.94 (CH_2 close to N), 31.17 (CH_3 p-cymene), 29.60 (CH_2 propyl), 26.25 (CH_2 piperidine), 24.30 (CH_2 piperidine), 22.31 (CH_3 isopropyl p-cymene), 22.21 (CH_3 isopropyl p-cymene), 18.75 (C-H isopropyl p-cymene) **ESI-MS (+)** m/z [M- TfO^-]$^+$ calc. 967.07 found 967.19 **CHNS analysis**: $C_{48}H_{49}N_6O_8S_2F_6Ru$: calculated: C: 51.61, H: 4.42, N: 7.52, S: 5.74. Found: C: 50.83, H: 3.79, N: 7.73, S: 5.41.

[(η^6-p-cym)Ru(N,N'-phen)(L18)](SO$_3$CF$_3$)$_2$ (C10)

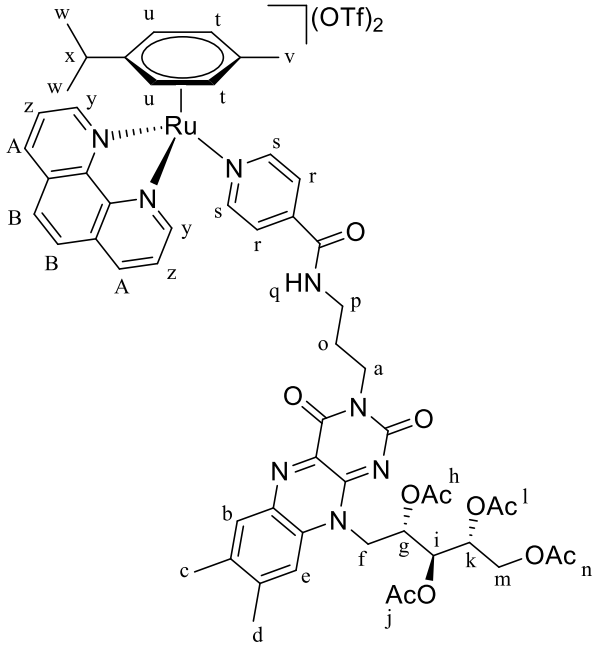

I5 (0.099 g, 0.098 mmol, 1 eq.), AgTfO (0.05 g, 0.195 mmol, 2 eq.) and 1,10-phenantroline (0.019 g, 0.098 mmol, 1 eq.). Dark green solid. **Yield**: 22% **^{1}H-NMR** (δ, ppm, 400 MHz, DMSO-D_6): 10.30 (d, J = 5.8 Hz, 2H, H_y), 9.04 (d, J = 7.8 Hz, 1H, H_A), 8.90 (d, J = 8.1 Hz, 1H, H_A), 8.80 (m, 1H, H_q), 8.75 (d, J = 6.2 Hz, 1H, H_s), 8.66 (d, J = 5.9 Hz, 1H, H_s), 8.39 (m, 2H, H_z), 8.29 (s, 2H, H_B), 7.96 (s, 1H, H_b), 7.93 (d, J = 7.1 Hz, 1H, H_r), 7.85 (d, J = 5.1 Hz,

1H, H_r), 7.78 (s, 1H, H_e), 6.73 (d, J = 5.9 Hz, 1H, H_t), 6.37 (d, J = 6.7 Hz, 1H, H_t), 6.19 (d, J = 6.5 Hz, 1H, H_u), 5.87 (d, J = 6.8 Hz, 1H, H_u), 5.47 (m, 2H, H_g, H_i), 5.32 (m, 1H, H_k), 5.08 (bs, 2H, H_f), 4.90 (m, 1H, H_f), 4.37 (m, 1H, H_m), 4.23 (m, 1H, H_m), 3.96 (bs, 2H, H_a), 2.42 (s, 3H, H_c), 2.20 (s, 6H, H_h, H_j), 2.01 (s, 6H, H_l, H_v), 1.86 (m, 2H, H_o), 1.60 (bs, 3H, H_n), 0.70 (d, J = 6.9 Hz, 6H, H_w) **^{1}H-NMR** (δ, ppm, 400 MHz, $CDCl_3$): 10.57 (dd, J = 5.2 Hz, J' = 1.2 Hz, 2H, H_y), 8.80 (d, J = 6 Hz, 2H, H_s), 8.58 (dd, J = 8 Hz, J' = 1.2 Hz, 2H, H_A), 8.09 (m, 3H, H_z, H_b), 8.02 (s, 2H, H_B), 7.97 (m, 1H, H_q), 7.90 (d, J = 6 Hz, 2H, H_r), 7.62 (s, 1H, H_e), 6.58 (d, J = 6.2 Hz, 1H, H_t), 6.48 (d, J = 6.1 Hz, 2H, H_t), 6.03 (d, J = 5.8 Hz, 1H, H_u), 5.80 (d, J = 5.8 Hz, 1H, H_u), 5.69 (s, 1H, H_g), 5.51 (s, 1H, H_i), 5.45 (m, 1H, H_k), 5.01 (bs, 2H, H_f), 4.48 (m, 1H, H_m), 4.25 (m, 3H, H_m, H_a), 3.45 (m, 2H, H_p), 2.72 (m, 1H, H_x), 2.60 (s, 3H, H_d), 2.48 (s, 3H, H_c), 2.29 (s, 3H, H_h), 2.25 (s, 3H, H_v), 2.24 (s, 3H, H_j), 2.10 (s, 5H, H_l, H_o), 1.77 (s, 3H, H_n), 1.05 (d, J = 9.6 Hz, 6H, H_w) **^{13}C-NMR** (δ, ppm, 100 MHz, $CDCl_3$): 170.68 (C=O ribityl acetate), 170.24 (C=O ribityl acetate), 169.71 (C=O ribityl acetate), 169.63 (C=O ribityl acetate), 164.00 (HN-C=O pyridine), 160.56 (C=O flavin core), 155.59 (C=O flavin core), 153.32 (C-H phenanthroline close to N), 151.72 (C-H pyridine close to nitrogen), 149.31 (N-C=N flavin core), 148.56 (C-CH_3 flavin core), 144.84 (C quaternary pyridine close to carbonyl), 145.62 (C-H phenanthroline), 140.12 (C quaternary phenanthroline), 137.12 (C-CH_3 flavin core), 136.79 (C-H pyridine close to amide), 135.26 (N=C-C=O flavin core), 135.12 (N-C=C aromatic flavin core), 133.03 (C-H aromatic flavin core), 131.34 (N-C=C aromatic flavin core), 130.71 (C-H phenanthroline), 128.53 (C quaternary phenanthroline), 127.90 (C-H phenanthroline), 115.72 (C-H aromatic flavin core), 107.35 (C quaternary p-cymene), 94.29 (C quaternary p-cymene), 88.29 (C-H aromatic p-cymene), 70.32 (C-H ribityl), 69.79 (C-H ribityl), 69.35 (C-H ribityl), 62.00 (C-H ribityl), 54.66 (CH_2 piperidine close to N), 44.72 (CH_2 ribityl), 39.91 (CH_2 bridge), 39.43 (CH_2-N propyl), 36.74 (CH_2-NH amide), 31.15 (CH_3 p-cymene), 27.23 (CH_2 propyl), 26.03 (CH_2 piperidine), 22.16 (CH_3 isopropyl p-cymene), 21.59 (CH_3 aromatic flavin core), 21.10 (CH_3 acetate ribityl), 20.76 (CH_3 acetate ribityl), 20.69 (CH_3 acetate ribityl), 20.33 (CH_3 acetate ribityl), 19.59 (CH_3 aromatic flavin core), 18.07 (CH isopropyl p-cymene) **ESI-MS (+)** m/z [M- TfO^-]$^+$ calc. 1271.27 found 1271.33 **CHNS analysis**: $C_{58}H_{60}N_8O_{17}S_2F_6Ru$: calculated: C: 49.05, H: 4.26, N: 7.89, S: 5.51. Found: C: 48.80, H: 4.01, N: 8.02, S: 5.63.

[(η^6-p-cym)Ru(N,N'-L24)(L4)](SO$_3$CF$_3$)$_2$ (C11)

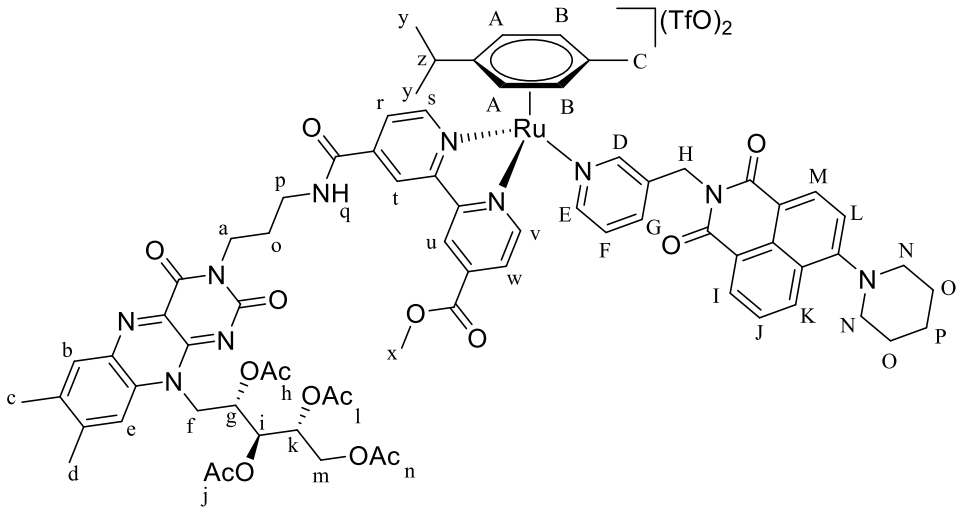

I3 (0.014 g, 0.021 mmol, 1 eq.), AgTfO (0.011 g, 0.043 mmol, 2 eq.) and **L24** (0.018 g, 0.021 mmol, 1 eq.). Dark green solid. **Yield**: 59% **^{1}H-NMR** (δ, ppm, 400 MHz, DMSO-D_6): 10.08 (m, 1H, H_v), 9.71 (m, 1H, H_s), 9.15 (bs, 2H, H_u, H_t), 9.04 (s, 1H, H_E), 8.97 (s, 1H, H_D), 8.93 (s, 1H, H_l), 8.87 (s, 1H, H_M), 8.61 (bs, 2H, H_r, H_w), 8.32 (bs, 2H, H_G, H_J), 8.13 (s, 1H, H_K), 8.10 (s, 1H, H_b), 7.92 (s, 1H, H_L), 7.89 (m, 1H, H_q), 7.77 (bs, 1H, H_F), 7.75 (s, 1H, H_e), 6.72 (s, 1H, H_B), 6.34 (s, 1H, H_B), 6.29 (s, 1H, H_A), 6.06 (s, 1H, H_A), 5.48 (m, 2H, H_g, H_i), 5.33 (m, 1H, H_k), 5.13 (s, 2H, H_H), 5.09 (bs, 2H, H_f), 4.38 (m, 1H, H_m), 4.23 (m, 1H, H_m), 4.01 (bs, 5H, H_a, H_x), 3.19 (s, 2H, H_p), 2.42 (s, 3H,

H_c), 2.25 (s, 6H, H_h, H_j), 2.01 (s, 3H, H_l,), 1.93 (m, 2H, H_o), 1.80 (bs, 7H, H_C, H_O), 1.67 (bs, 2H, H_P), 1.59 (s, 3H, H_n), 0.97 (d, J = 6.9 Hz, 3H, H_y), 0.83 (d, J = 6.9 Hz, 3H, H_y) **^{1}H-NMR** (δ, ppm, 400 MHz, $CDCl_3$): 10.41 (m, 1H, H_v), 9.59 (m, 1H, H_s), 8.84 (bs, 2H, H_u, H_t), 8.66 (m, 2H, H_D, H_l), 8.57 (m, 3H, H_r, H_w, H_M), 8.48 (m, 2H, H_J, H_K), 8.24 (bs, 1H, H_G), 8.05 (s, 1H, H_b), 7.96 (m, 1H, H_q), 7.63 (s, 1H, H_e), 7.38 (bs, 1H, H_F), 6.63 (s, 1H, H_B), 6.50 (s, 1H, H_B), 6.09 (s, 1H, H_A), 5.89 (s, 1H, H_A), 5.72 (s, 1H, H_g), 5.48 (m, 2H, H_i, H_k), 5.19 (s, 2H, H_H), 5.06 (bs, 2H, H_f), 4.52 (dd, J = 12.4 Hz, J' = 2.8 Hz, 1H, H_m), 4.26 (m, 3H, H_m, H_a), 4.05 (s, 3H, H_x), 3.56 (s, 2H, H_p), 3.37 (bs, 4H, H_N), 2.74 (m, 1H, H_z), 2.59 (s, 3H, H_d), 2.47 (s, 3H, H_c), 2.29 (s, 3H, H_h), 2.23 (s, 3H, H_j), 2.12 (m, 2H, H_o), 2.09 (s, 3H, H_o), 1.84 (bs, 4H, H_O), 1.76 (s, 6H, H_n, H_C), 1.69 (s, 2H, H_P), 0.86 (m, 6H, H_y) **^{13}C-NMR** (δ, ppm, 100 MHz, $CDCl_3$): 170.71 (C=O ribityl acetate), 170.32 (C=O ribityl acetate), 169.81 (C=O ribityl acetate), 165.57 (HN-C=O bipyridine), 165.23 (CH_3O-C=O bipyridine), 162.31 (C=O imides), 160.92 (C=O imides), 160.39 (C=O flavin core), 157.91 (C quaternary naphthalene piperidine), 156.03 (C=O flavin core), 153.17 (C-H pyridine close to N), 150.03 (C-CH_3 flavin core), 149.74 (N-C=N flavin core), 148.12 (C-H bipyridine close to N), 144.96 (C-H bipyridine close to N), 143.92 (C quaternary bipyridine close to N), 143.00 (C quaternary bipyridine close to carbonyl), 139.04 (C quaternary bipyridine close to carbonyl), 138.72 (C-H pyridine close to N), 137.13 (C-CH_3 flavin core), 136.87 (C-H pyridine), 135.41 (N=C-C=O flavin core), 134.82 (N-C=C aromatic flavin core), 133.05 (C-H aromatic flavin core), 132.90 (C quaternary naphthalene), 131.25 (C-H pyridine), 131.13 (N-C=C aromatic flavin core), 129.93 (C-H naphthalene), 129.10 (C quaternary pyridine) 126.81 (C quaternary naphthalene), 125.84 (C quaternary naphthalene), 125.11 (C-H naphthalene), 123.80 (C-H naphthalene), 121.70 (C quaternary naphthalene), 120.82 (C-H bipyridine), 119.01 (C-H bipyridine), 117.79 (C quaternary naphthalene), 116.65 (C-H naphthalene), 115.51 (C-H aromatic flavin core), 108.81 (C quaternary p-cymene), 93.58 (C quaternary p-cymene), 84.29 (C-H aromatic p-cymene), 70.42 (C-H ribityl), 69.21 (C-H ribityl), 62.14 (C-H ribityl), 54.71 (CH_2 piperidine close to N), 52.73 (methyl ester), 44.63 (CH_2 ribityl), 40.35 (CH_2 bridge), 39.22 (CH_2-N propyl), 36.44 (CH_2-NH amide), 31.19 (CH_3 p-cymene), 27.39 (CH_2 propyl), 25.95 (CH_2 piperidine), 22.34 (CH_3 isopropyl p-cymene), 21.50 (CH_3 aromatic flavin core), 21.06 (CH_3 acetate ribityl), 20.80 (CH_3 acetate ribityl), 20.73 (CH_3 acetate ribityl), 20.32 (CH_3 acetate ribityl), 19.51 (CH_3 aromatic flavin core), 18.13 (CH isopropyl p-cymene) **ESI-MS (+)** m/z $[M\text{-}C_{25}H_{42}O_{13}NSF_3]^+$ calc. 1111.54 found 1111.79 **CHNS analysis**: $C_{76}H_{78}N_{10}O_{21}S_2F_6Ru$: calculated: C: 52.26, H: 4.50, N: 8.02, S: 3.67. Found: C: 52.83, H: 5.33, N: 7.57, S: 3.27.

14 Biological protocols, kinetics calculations and methods

14.1 DNA binding studies

CD titrations. Circular dichroism (CD) spectra were recorded at 25 °C on a Jasco J-715 spectropolarimeter with buffer compensation; each spectrum is the average of three independent measurements. 1 cm path-length quartz cuvettes were used. Disodium salt of calf thymus DNA (CT DNA) (Sigma) was used as received and stored at 4 °C. Solutions of DNA in 10 mM of PBS (pH=7.4) 137 mM NaCl, 2.7 mM KCl gave a ratio of UV absorbance at 260 and 280 nm, A260/A280, of 1.9, indicating that the DNA was sufficiently free of protein. The concentration of stock solutions of DNA expressed in moles of nucleotide phosphate [NP] was

determined by UV absorbance at 260 nm. The extinction coefficient, ε_{260}, was taken as 6600 M^{-1} cm^{-1} [166]. Stock solutions were stored at 4 °C and used after no more than 4 days. Metal complexes were dissolved in DMSO. The final concentration of DMSO in the buffered solution never exceeds 5%.

Atomic Force Microscopy. AFM experiments were conducted using a 965 bp linear DNA template obtained by PCR from plasmid pNEB193 and suitable primers under standard reaction conditions. The DNA fragment was gel purified by electroelution using an Elutrap apparatus (Schleicher & Schuell, Keene NH), phenol/chloroform extracted, ethanol precipitated and resuspended in 5 mM Tris-HCl pH 7.4. The DNA concentration was determined by absorbance at 260 nm. A solution of 40 nM DNA was incubated for one hour at room temperature in the presence of increasing concentrations, 1 µM, 10 µM, 100 µM and 1 mM, of the thiosemicarbazone compounds. The reaction was diluted 20-times in deposition buffer (4 mM HEPES pH 7.4, 10 mM NaCl, 2 mM $MgCl_2$) and immediately deposited onto freshly-cleaved. After 2 minutes of incubation the mica surface was rinsed with milliQ water and dried with nitrogen. AFM imaging was performed with the tapping mode in air using a Nanoscope IIIA microscope (Digital Instruments). Images were collected with a scan size of 2 µm at a scan rate of 2.5 lines per second. DNA contour length measurements were performed as previously described [168] using the following contour length estimator: L = (0.963ne + 1.362no) × S/W, where “ne” and “no” are the number of even and odd chain codes respectively, S is the image scan size, W is the image width in pixels

14.2 Aflatoxin production inhibition assay

A high throughput procedure performed in a multi-well plate was used to assess aflatoxin accumulation in a coconut milk-derived medium (CCM). The effect on aflatoxin biosynthesis was assessed by the microplate fluorescence-based procedure described by Degola and co-workers [169]. Standard flat-bottom 96-well microplates were used. Suspensions of conidia were diluted to the appropriate concentrations and brought to the final concentration of 5×10^2 conidia/well; cultures were set in a final volume of 200 µL/well of CCM medium added with TSs. The plates were incubated in the dark under stationary conditions for up to 6 days at 25 °C. Aflatoxin accumulation was monitored by fluorescence emission determination: readings were performed directly from the bottom of wells of the culture plate with a microplate reader (TECAN SpectraFluor Plus, Männedorf, Switzerland) using the following parameters: λ_{exc} = 360 nm; λ_{em} = 465 nm; manual gain = 83; lag time = 0 µs; number of flashes = 3; and integration time = 200 µs.

14.3 Mycelial growth inhibition assay

Conidia suspensions, obtained from 14-21-day solid cultures [YES medium: 2% (w⁄v) yeast extract, 5% (w⁄v) sucrose, 2% (w⁄v) agar], were extimated for concentration (OD_{600}). Determination of A. flavus radial growth was performed in YES solid medium amended with: three single spots (5 µL of a 10^7 conidia/mL suspension each) of fungal strain were equidistant inoculated in 90-mm Petri dishes, plates were incubated for 4 days at 25 °C and the mycelial growth was evaluated daily by measuring the reverse of colonies along two orthogonal diameters. Radial growth was expressed as cm/day ± SD. Additionally, conidial germination rate and post-germination hyphal outgrowth were assessed by analyzing changes in optical density of spore suspensions

over time: in a 96 well microtiter plate 104 spores were inoculated in a final volume of 200 µL of YES liquid medium amended with TSs and incubated at 28 °C. The optical density at 620 nm (OD_{620}) was recorded for each well every 120 min with a microplate reader (MULTISKAN EX, Thermo Electron Corporation, Vantaa, Finland) without shaking. Samples were inoculated in triplicate. Biomass variation was also determined: fresh or dry mycelium weight was obtained, for each sample, withdrawing the mycelium from eight wells of the microplate and pooling them. The pooled mycelia were then blotted dry on clean paper and weighed (fresh weight determination) and then incubated at 80 °C for 48 h before dry weight determination. Samples were inoculated in triplicate.

14.4 Tables of the kinetics rate calculations

Complex C1	Complex integral - signal of methylene group 5.16 ppm	Free ligand integral - signal of methylene group 5.32 ppm	Sum of integrals	Complex (%)	Free ligand %	[Complex]	Reference signal 7.43 ppm
t 0h	2.03	0	2.03	100%	0%	100% = 3mM	
t 1h	1.71	0.38	2.09	81.82%	18.18%	81.82% = 2.45mM	
t 3h	1.43	0.87	2.30	62.17%	37.83%	62.17% = 1.86mM	
t 5h	0.89	0.91	1.80	49.44%	50.56%	49.44% = 1.48mM	
t 8h	0.63	1.19	1.82	34.61%	65.38%	34.61% = 1.04mM	

Complex C2	Complex integral - signal of methylene group 5.17 ppm	Free ligand integral - signal of methylene group 5.30 ppm	Sum of integrals	Complex (%)	Free ligand %	[Complex]	Reference signal 9.53 ppm
t 0h	1.96	0	1.96	100%	0%	100% = 3mM	
t 1h	1.44	0.44	1.88	76.60%	23.40%	76.60% = 2.30mM	
t 3h	1.27	0.53	1.80	70.56%	29.44%	70.56% = 2.12mM	
t 5h	1.19	0.57	1.76	67.61%	32.39%	67.61% = 2.03mM	
t 8h	1.18	0.63	1.81	65.19%	34.81%	65.19% = 1.96mM	

Complex C3	Complex integral - signal of methylene group 5.13 ppm	Free ligand integral - signal of methylene group 5.27 ppm	Sum of integrals	Complex (%)	Free ligand %	[Complex]	Reference signal 1.84 ppm
t 0h	1.89	0	1.89	100%	0%	100% = 3mM	
t 1h	0.72	1.40	2.12	33.96%	66.04%	33.96% = 1.02mM	
t 3h	0.48	1.71	2.19	21.92%	78.08%	21.92% = 0.66mM	
t 5h	0.26	1.84	2.10	12.38%	87.62%	12.38% = 0.37mM	
t 8h	0.17	1.94	2.11	8.06%	91.94%	8.06% = 0.24mM	

Complex C5	Complex integral - signal of methylene group 5.04 ppm	Free ligand integral - signal of methylene group 5.27 ppm	Sum of integrals	Complex (%)	Free ligand %	[Complex]	Reference signal 1.68 ppm
t 0h	1.92	0	1.92	100%	0%	100% = 3mM	
t 1h	0.77	1.23	2.00	38.50%	61.50%	38.50% = 1.15mM	
t 3h	0.21	1.57	1.78	11.80%	88.20%	11.80% = 0.354mM	
t 5h	0.17	1.85	2.02	8.41%	91.59%	8.41% = 0.252mM	
t 8h	0.14	1.98	2.12	6.60%	93.40%	6.60% = 0.198mM	

Complex C6	Complex integral - signal of methylene group 5.04 ppm	Free ligand integral - signal of methylene group 5.27 ppm	Sum of integrals	Complex (%)	Free ligand %	[Complex]	Reference signal 1.68 ppm
t 0h	1.95	0	1.95	100%	0%	100% = 3mM	
t 1h	1.82	0.21	2.03	89.65%	10.35%	89.65% = 2.69mM	
t 3h	1.57	0.53	2.10	74.76%	25.24%	74.76% = 2.12mM	
t 5h	1.29	0.76	2.05	69.93%	37.07%	69.93% = 2.03mM	

t 8h	0.98	0.92	1.90	51.58%	48.42%	51.58% = 1.96mM	

Complex C7	Complex integral - signal of methylene group 5.12 ppm	Free ligand integral - signal of methylene group 5.27 ppm	Sum of integrals	Complex (%)	Free ligand %	[Complex]	Reference signal 1.88 ppm
t 0h	1.74	0	1.74	100%	0%	100% = 3mM	
t 1h	0.89	0.94	1.83	48.63%	51.37%	48.63% = 1.46mM	
t 3h	0.54	1.48	2.02	26.73%	73.27%	26.73% =0.80mM	
t 5h	0.36	1.45	1.81	19.89%	80.11%	19.89% = 0.60mM	
t 8h	0.22	1.62	1.84	11.96%	88.04%	11.96% = 0.36mM	

14.5 General methods

Materials. Anhydrous solvents were dried and stored over molecular sieves (3 Å), all other reagents and solvents were used as received. Reactions performed under an inert atmosphere were carried out using Schlenk glassware using nitrogen as the inert gas.

NMR Measurements. NMR experiments were performed on a Brüker Avance 400 MHz instrument at 298 K. Chemical shifts are quoted in ppm relative to tetramethylsilane, (δH=2.50) The spectra are processed with the software MestrReNova.

UV Measurements. UV-visible experiments were performed on a Spectrophotometer UV/Vis/NIR Lambda 750 and for the data elaboration the software Origin was utilized.

Fluorescence Measurements. Fluorescence experiments were performed on a spectrophotometer Fluoromax-3 and for the data elaboration the software Origin was utilized.

IR Analysis. The infrared spectra are obtained with a FT-IR spectrometer Spectrum Two with the wavelength range of 8,300 – 350 cm^{-1}.

ESI analysis. The mass spectra were recorded with an ESI spectrometer Acquity Waters Ultraperformance spectrometer with an SQD (Single Quadrupole Deterctor), associated with an UPLC Acquity Waters (Source Temperature (°C) 150; Desolvation Temperature (°C) 300; Cone Gas Flow (L/Hr) 100; Desolvation Gas Flow (L/Hr) 480; Solvent Flow (mL/min) 0.2; Capillary voltage (kV) 3; Cone voltage (V) -20/-50).

CNHS elemental analysis. Elemental analysis was performed on a Termo Fischer Scientific FlashSmart CHNS.

15 References

1 Anastassopoulou, J. and Theophanides. *Bioinorg. Chem,* **1995**, 459, 209–218.

2 Thompson, K. H. In *Encyclopedia of Inorganic Chemistry*; King, R. B., Ed.; John Wiley & Sons Ltd.: Chichester, UK, **2011**; Chapter 1, pp 1−10.

3 Magner, L. N. *A History of Medicine*, 2nd ed.; Taylor & Francis Group, LLC: Boca Raton, FL, **2005**.

4 Orvig, C. and Abrams, M. *J. Chem. Rev*, **1999**, 99, 2201.

5 Ehrlich, P. and Bertheim, A. *Ber. Dtsch. Chem. Ges.* **1912**, 45, 756.

6 Mjos, D. K. and Orvig, C. *Chem. Rev.* **2014**, 114, 4540−4563.

7 Alderden, R. A. *et al. Chem. Educ.* **2006**, 83, 728.

8 Lippert, B., Ed. Cisplatin - Chemistry and Biochemistry of a Leading Anticancer Drug, 1st ed.; Wiley-VCH: Weinheim, Germany, **1999**.

9 Berners-Price, S. J.; Appleton, T. G. In Platinum-Based Drugs in Cancer Therapy; Kelland, L., Farrell, N. P., Eds.; Humana Press Inc.: Totowa, NJ, **2000**; pp 3−35.

10 Reedijk, J. *Chem. Rev.* **1999**, 99, 2499.

11 Wang, D.; Lippard, S. J. *Nat. Rev. Drug Discovery*, **2005**, 4, 307.

12 Dilruba, S. *et al*. *Cancer Chemother. Pharmacol*. **2016**, 77(6), 1103-24.

13 Sigel, A.; Sigel, H.; Sigel, R. K. *Metal Ions in Biological Systems & Metal Ions in Life Sciences*; various books and numerous chapters.

14 Pelosi, G. *The Open Crystallography Journal*, **2010**, 3, 16-28.

15 French, F. A. *Cancer Res*, **1965**, 25, 1454-8.

16 Brockman, R. W. *et al*. *Proc. Soc. Exp. Biol. Med.* **1970**, 133, 609-14.

17 Shao, J. *et al*. *Mol. Cancer Ther.* **2006**, 5, 586-92.

18 Hall, I. H. *et al*. *Pharmazie*. **2000**, 55, 937-41.

19 Yuan, J. *et al*. *Blood*. **2004**, 104, 1450-8.

20 Bisceglie, F. *et al*. *Metallomics*, **2019**, 11(10), 1729-1742.

21 Kang, G. *et al*. *Science*. **2020**, 368, 424-427.

22 Agrawal, K. C. *et al*. *J*. *Med*. *Chem*. **1974**, 17, 631-5.

23 Zaltariov, M. F. *et al*. *Inorg. Chem.* **2017**, 56, 3532−3549.

24 Antholine, W. E. *et al*. *J. Med. Chem.* **1976**, 19, 339- 41.

25 Gorrini, C. *et al*. Nat. *Rev. Drug. Discov.* **2013**, 12, 931–47.

26 Malarz, K. *et al Oncotarget* **2018**, 9(25), 17689–17710.

27 Sîrbu, A. *et al*. *Dalton Trans.* **2017**, 46, 3833-3847.

28 Nitiss, J. L. *Nature Reviews Cancer* **2009**,9, 327–337.

29 Chen, J. *et al*. *Toxicol. Appl. Pharmacol.* **2004**, 197, 40-8.

30 Pessoto, F. S. *et al*. *Oxidative Medicine and Cellular Longevity*. **2015**, 1-15.

31 Wang, C. and Youle, R. J. *Annu Rev Genet.* **2009**, 43, 95–118.

32 Khobta, A. and Epe, B. *Mutat. Res-Fund. Mol. M.* **2012**, 736, 5-14.

33 Karaczyn, A. A. *et al. Ann. Clin. Lab. Sci.* **2009**, 39, 251-26.

34 Karaczyn, A. A. *et al*. *Chem. Res. Toxicol*. **2003**, 16, 1555-1559.

35 Bal, W. *Et al. Chem. Res. Toxicol.* **1998**, 11, 1014-1023.

36 Panagiotou, K. *et al*. *Bioinorg. Chem. Appl*. **2008**, 80-85.

37 Belicchi-Ferrari, M. *et al. Polyhedron* **2007**, 26, 5150-5161.

38 Belicchi-Ferrari, M. *et al. J Inorg Biochem*. **2002**, 90, 113-126.

39 Buschini, A. *et al. J Inorg Biochem*. **2009**, 103, 666-677.

40 Belicchi-Ferrari, M. *et al. J. Inorg. Biochem*. **2010**, 104, 199-206.

41 Pelosi, G. *et al. J. Med. Chem*. **2010**, 53, 8765-8769.

42 Bisceglie, F. *et al. J. Inorg. Biochem*. **2012**, 116, 195-203.

43 Bisceglie, F. *et al. Metallomics.* **2013**, 5, 1510-1518.

44 Buschini, A. *et al. Metallomics*. **2014**, 6, 783-792.

45 Ivanov, V. I. *et al. Biopolymers*, **1973**, 12, 89–110.

46 Benns, B. G. *et al. Appl Microbiol.* **1960**, 8(6), 353-356.

47 Araújo Neto, L. N. *et al. Chem Biol Interact.* **2017**, 272, 172-181.

48 Abbas, H. K. *et al. Toxin Rev.* **2009**, 28, 142–153.

49 Wu, F. *et al. Annu. Rev. Food Sci. Technol.* **2014**, *5*, 351–372.

50 Ishikawa, A. T. *Toxins* **2017**, 9(11), 374.

51 Chawanthayatham, S. *et al. PNAS* **2017**, 114(15), 3101-3109.

52 Jayashree, T. and Subramanyam, C. *Free Radical Biology & Medicine*, **2000**, 29, 981–985.

53 Kim, J. H. *et al. International Journal of Food Microbiology,* 2008, 122, 49–60.

54 Huang, J. Q. *et al. International Journal of Food Microbiology,* **2009**, 130, 17–21.

55 Reverberi, M. *et al. Applied Microbiology and Biotechnology,* **2012**, 95, 1293–1304.

56 Roze, L. V. *et al. Annu. Rev. Food Sci. Technol.* **2013**, 4, 293–311.

57 Yu, J. *et al.* Applied and environmental microbiology, **2004**, 70, 1253–1262.

58 Degola, F. *et al. International Journal of Food Microbiology*, **2015**, 200, 104–111.

59 Degola, F. *et al. Appl. Microbiol. Biotechnol.* **2017**, 101, 6683–6696.

60 Rogolino, D. *et al. ScientIfic Reports* **2017**, 7, 11214.

61 Bisceglie, F. *et al. Scientifc Reports*, **2020**, 10, 17686.

62 Orsoni, N. *et al. Int. J. Mol. Sci.* **2020**, 21, 8681.

63 Kim, J. H. *et al. Molecules*, **2013**, 18, 1564-1581.

64 Sakuda, S. *et al. Toxins*, **2014**, 6, 1193-1200.

65 Kim, J. H. *et al. Appl Microbiol Biotechnol*, **2005**, 67, 807–815.

66 Kim, J. H. *et al. International Journal of Food Microbiology*, **2008**, 122, 49–60.

67 Dallabona, C. *et al. Molecules,* **2019**, 24, 2971.

68 Alexandre, A. *et al. Biochim. Biophys. Acta.* **1984**, 767, 120–129.

69 Jones, G. *et al. J. Mol. Biol.* **1997**, 267, 727-748.

70 De Graaf, C. *et al. J. Med. Chem.* **2005**, 48, 2308–2318.

71 Nissink, J.W.M. *et al. Proteins* **2002**, 49, 457–471.

72 Cotton, S.A., *Chemistry of Precious Metals*, Blackie Academic and Professional, **1997**, London.

73 Orellana, G. *et al. Inorganic Chemistry*, **1990**, 29, 4, 882-885.

74 Brevard, C. and Granger, P. *Inorganic Chemistry*, **1983**, 22, 3, 532-535.

75 Metal Complexes in Cancer Chemotherapy, ed. B. K. Keppler, VCH, Weinheim, 1993.

76 Fricker, S. B. *Dalton Trans.*, **2007**, 4903.

77 Reedijk, J. *Platinum Met. Rev.*, **2008**, 52,2.

78 Allardayce, C. S. and Dyson, P. J. *Platinum Met. Rev.*, **2001**, 45, 62.

79 Kostova, J. *Curr.Med.Chem.*, **2006**, 13, 1085.

80 Sava, G. *et al. Dalton Trans.*, **2011**, 40, 9069-9075.

81 Allardyce, C. S. *et al. Appl. Organomet. Chem.*, **2005**, 19,1.

82 Durig, J. R. *et al. Chem. Biol. Interact.*, **1976**, 13, 287.

83 Clarke, M. J. *Met. Ions Biol. Syst.*, **1980**, 11, 231.

84 Clarke, M. J. *Coordination Chemistry Reviews*, **2003**, 236, 209-233.

85 Kelman, A. D. *et al. Clin. Hematol. Oncol.*, **1977**, 7, 274–288.

86 Keller, H. and Keppler, B. USPatent, **1989**, 4843069; Keppler, B. K. *et al. Complexes in Cancer Chemotherapy*, VCH, Weinheim, **1993**, p. 187.

87 Trondl, R. *et al. Chem. Sci.,* **2014**, 5, 2925-2932.

88 Mestroni, Alessio, E. and Sava, G. Int. Patent, **1998**, PCT C 07F 15/00, A61K 31/28, WO 98/00431; Sava, S. *et al. Metal Complexes Complexes in Cancer Chemotherapy*, VCH, Weinheim, **1993**, p. 157.

89 Allardyce, C. S *et al. Chem. Commun.,* **2001**, 1396.

90 R. E. Morris, R. E. *et al. J. Med. Chem.*, **2001**, 44, 3616.

91 Süss-Fink, G. *Dalt. Trans.,* **2010**, 39, 1673–1688.

92 Murray, B. S. *et al. Coord. Chem. Rev.*, **2016**, 306, 86–114.

93 Zhang, Y. *et al.* Acta Pharm. Sinica B, **2018**, 8(1), 34-50.

94 Mari, C. *et al. Chem. Sci.* **2015**, 00, 1–27.

95 Mari, C. *et al.* **2015**, 69, 176–181.

96 Arias-Rotondo, D. M. and McCusker, J. K. *Chem. Soc. Rev.* **2016**, 45, 5803–5820.

97 Chen, Y. *et al. Dalt. Trans.* **2014**, 43, 15375–15384.

98 White, J. K. *et al. Inorganica Chim. Acta*, **2017**, 454, 7–20.

99 Luis, E. T. *et al. Polyhedron,* **2018.**

100 Triesscheijn, M. *et al.* **2006**, 1034–1044.

101 Karioti, A. and Bilia, A. R. *Int. J. Mol. Sci.* **2010**, 11(2), 562-594.

102 Höckel, M. and Vaupel, P. *J. Natl. Cancer Inst.,* **2001**, 93, 266–276

103 Cosse, J. P. and Michiels, C. *Anti-Cancer Agents Med. Chem.,* **2008**, 8, 790–797.

104 K. L. Eales, K. E. R. Hollinshead and D. A. Tennant, *Oncogenesis*, **2016**, 5.

105 Bonnet, S. *Dalton Trans.*, **2018**, 47, 10330.

106 Howerton, B. S*. et al. J. Am. Chem. Soc.* **2012**, 134, 20, 8324–8327.

107 Qu, F. *et al. Inorg. Chem.* **2017**, 56, 13, 7519–7532.

108 Van Houten, J. and Watts, R. J. *J. Am. Chem. Soc.* **1976**, 98, 4853.

109 Howerton, B. S. *et al. J. Am. Chem. Soc.* **2012**, 134, 8324−8327.

110 White, J. K. *et al. Inorganica Chim. Acta* **2017**, 454, 7–20.

111 Gill, T. P. and Mann, K. R. *Organometallics* **1982**, 1, 485−488.

112 Schrenk, J. L. *et al. Inorg. Chem.* **1983**, 22, 4047−4049.

113 McNair, A. M. *et al. Inorg. Chem.* **1984**, 23, 2633−1640.

114 Pizarro, A. M. *et al.* In Topics in Organometallic Chemistry; Jaouen, G., Metzler-Nolte, N., Eds.; Springer-Verlag: Berlin, **2010**; Vol. 32, 21−56.

115 Wang, F. *et al. Proc. Natl. Acad. Sci. U.S.A.* **2005**, 102, 18269−18274.

116 Yan, Y. K. *et al. Chem. Commun.* **2005**, 4764–4776.

117 Betanzos-Lara, S. *et al. Chem. Commun.* **2009**, 6622−6624.

118 Betanzos-Lara, S. *et al. Organometallics* **2012**, 31, 3466−3479.

119 Tandon, R. *et al. Chem. Rec.* **2017**, 17, 956-993.

120 Jia, X. *et al. Pure Appl. Chem.* **2014**, 86, 1237-1246.

121 Gopikrishna, P. *et al. ACS Appl. Mater. Interfaces* **2018**, 10, 12081-12111.

122 Bacchi, A. *et al. ChemistrySelect* **2017**, 2, 7000 – 7007.

123 Duke, R. M. *et al. Chem. Soc. Rev.* **2010**, 39, 3936–3953.

124 Grepioni, F. *et al. Journal of Materials Chemistry* **2015**, 3, 9425.

125 Borenfreund, A. *et al. Annals of the New York Academy of Sciences* **1975**, 164- 171.

126 Keiser, G. Optical Fibers for Biomedical Applications, Handbook of Optical Fibers, **2019**, 1069-1095.

127 Dąbrowski, J. M. and Arnaut, L. G. *Photochem. Photobiol. Sci.*, **2015**, 14, 1765-1780.

128 Beija, M. *et al. Chem. Soc. Rev.* **2009**, 38, 2410–2433.

129 Drexhage, K. H. *J. Res. Natl. Bur. Stand.* **1976**, 80A, 421–428.

130 Drexhage, K. H. *Laser Focus*, **1973**, 9, 35–39.

131 Bogen, S. T. *et al. J. Chem. Soc. Faraday Trans.* **1998**, 94, 2435–2440.

132 Quitevis, E. L. *et al. J. Phys. Chem.* **1993**, 97, 5762–5769.

133 Zhou, Z. G. *et al. Chem. Commun.* **2008**, 3387–3389.

134 Liu, W. M. *et al. J. Am. Chem. Soc.* **2008**, 130, 1274–1284.

135 Hara, C. *et al. Brain Cell Biology*, **2006**, 35, 229–237.

136 Carrone, G. *et al. J. Phys. Chem. A* **2014**, 118, 10416−10424.

137 Bhat, S. S. *et al. Journal of Inorganic Biochemistry* **2020,** 203, 110903.

138 Liu, J. *et al. Inorg. Chem.* **2001**, 40, 5045-5050.

139 Nolan, P. S. *N-Heterocyclic Carbenes: Effective Tools for Organometallic Synthesis*, Wiley-VCH, **2014**.

140 Enders, D. *et al. Chem. Rev.* **2007**, 107, 5606–5655.

141 Díez-González, S. *et al. Chem. Rev.* **2009**, 109, 3612–3676.

142 Luan, X. *et al.* **2011**, N- Heterocyclic Carbenes in Transition Metal Catalysis and Organocatalysis, vol. 32 (ed. C.S.J. Cazin), Springer, Netherlands.

143 Samojłowicz, C. *et al. Chem. Rev.* **2009**, 109, 3708.

144 Samuel, B. and Blechert, S. **2006**, N-Heterocyclic Carbenes in Synthesis (ed. S.P. Nolan), Wiley-VCH Verlag GmbH & Co. KGaA, Weinheim.

145 Vougioukalakis, G.C. and Grubbs, R.H. *Chem. Rev.* **2009**, 110, 1746.

146 Lam, N. Y. S. *et al. Inorg. Chem.* **2018**, 57, 14427−14434.

147 Onar, G. *et al. Journal of Organometallic Chemistry*, **2019**, 886, 48-56.

148 Chen, C. *et al. European Journal of Medicinal Chemistry*, **2020**, 203, 112605.

149 Egorova, K. S. *et al. Chem. Rev.* **2017**, 117, 7132−7189.

150 Malhotra, S. V. and Kumar, V. *Bioorganic & Medicinal Chemistry Letters*, **2010**, 20, 581–585.

151 Chen, H. L. *et al. J. Chin. Chem. Soc.* **2014**, 61, 763-769.

152 Edwards, A. M. **2014**, 1146, 3–13.

153 Regensburg, U. **2018**, 1–17.

154 Alonso-de Castro, S. *et al. Angew. Chem. Int. Ed.* **2018**, 57, 3143 –3147.

155 Alonso-de Castro, S. *et al. Chem. Sci.* **2017**, 8, 4619–4625.

156 Gurruchaga-Pereda, J. *et al. ACS Catal.* **2020**, 10, 187−196.

157 Alonso-de Castro, S. *et al. Scientific Reports*, **2018**, 8, 17198.

158 Baarda, I. F. and Metzler, D. E. *Biochim. Biophys. Acta* **1961**, 50, 463–471.

159 Franco *et al. Eur. J. Inorg. Chem.* **2015**, 296–304.

160 Langdon-Jones, E. E. *et al. European Journal of Inorganic Chemistry,* **2017**, 44, 5279 – 5287.

161 McQuaid *et al. Chem. Commun.,* **2019**, 55, 9116-9119.

162 Gardner *et al. J. Org. Chem.* **2015**, 80, 9794−9797.

163 Metternich *et al. Chem. Eur.J.* **2018**, 24, 4228 –4233.

164 Singh, G. *et al. Chem. Eur. J.* 2020, 26,1989 –2001.

165 Foth, P. J. *et al. Org. Lett.*, **2020***,* 22, 16, 6682–6686.

166 Kai-Hsuan, C. *et al. ChemMedChem*, **2011**, 6, 759 – 764.

167 Reichmann, M. E *et al. J Am Chem Soc* **1954**, 76, 30473053.

168 Rivetti, C. *Cytom Part A*, **2009**, 75A, 854-861.

169 Degola, F. *et al. Letters in Applied Microbiology* **2012**, 55, 82–89.